FLRW COSMOLOGY WITH HYBRID SCALE FACTOR
IN $f(R, L_m)$ GRAVITY

 Vasudeo Patil[a], **Jeevan Pawde**[a], **Rahul Mapari**[b*], **Sachin Waghmare**[c]

[a] *Department of Mathematics, Arts, Science and Commerce College, Chikhaldara, Dist. Amravati (MS), India-444807*
[b] *Department of Mathematics, Government Science College, Gadchiroli (MS), India-442605*
[c] *Department of Mathematics, Tulshiram Gaikwad Patil College of Engg. & Technology, Nagpur(MS), India-441122*
Corresponding Author e-mail: r.v.mapari@gmail.com

In this paper, we aim to describe the cosmic late-time acceleration of the Universe in $f(R, L_m)$ gravity framework proposed by Harko (2010) with the help of an equation of state for strange quark matter. To achieve this, we adopt a specific form of $f(R, L_m)$ gravity as $f(R, L_m) = \frac{R}{2} + L_m^n$, where n is arbitrary constants. Here we utilize a hybrid scale factor to resolve the modified field equations in the context of $f(R, L_m)$ gravity for an isotropic and homogeneous Friedmann–Lemaître–Robertson–Walker (FLRW) metric in presence of strange quark matter (SQM). Also, we analyze the dynamics of energy density, pressure and the state finder parameters and explained the distinctions between our model and the current dark energy models in the presence of SQM. We observed a transition from an accelerating to a decelerating phase in the Universe, followed by a return to an accelerating phase at late times. Also, we analyzed the state finder diagnostic as well equation of state parameter and found that the model exhibited quintessence-like behavior. The conclusion drawn from our investigation was that the proposed $f(R, L_m)$ cosmological model aligns well with recent observational studies and effectively describes the cosmic acceleration observed during late times.

Keywords: *FLRW Cosmological Model; $f(R, L_m)$ gravity; Strange Quark Matter; Hybrid Scale Factor*

PACS: 04.20.-q; 04.20.Jb; 04.50.Kd

1. INTRODUCTION

In the twentieth century, the late-time accelerated expansion of the Universe has been a puzzling cosmic mystery that has caused controversy among researchers. Some astronomical and cosmological observations, including Supernovae Ia (SN Ia) [1, 2, 3, 4, 5], Cosmic Microwave Background (CMB) [6, 7], Baryon Acoustic Oscillations (BAO) in galaxy clustering [8, 9], Large Scale Structure (LSS) [10, 11] and Wilkinson Microwave Anisotropy Probe (WMAP) [12], all point to the conclusion that the Universe is presently experiencing accelerated expansion. This contradicts the prevailing theory of General Relativity (GR) on a large scale. During the early stages of the Big Bang, radiation played a significant role in driving the expansion of the Universe. As Universe expanded and cooled, matter took over, leading to a matter-dominated phase. However, recent observations suggest that we are now in a new era where "Dark Energy" (DE) is the dominant force influencing the expansion of the Universe. The exact mechanism behind this faster expansion is still under debate. To overcome this problem, researchers have proposed various alternative theories with one of the most common being modified gravity theories (MGT). These MGTs provide alternative explanations for the cosmic acceleration and serve as potential substitutes for GR.

Buchadahl (1970) introduced most favorite modified gravity as $f(R)$ gravity which provided a way to extend Einstein's universal theory of relativity. This theory was developed to explain the rapid expansion of the Universe and formation of its structures. Some $f(R)$ models were considered in [13, 14] for their ability to pass regional tests and incorporate concepts of dark energy and inflation. Additionally, it was speculated that $f(R)$ gravity models could potentially describe galactic dynamics of large test particles without the need for dark matter [15, 16, 17, 18, 19].

Harko and Lobo (2010) recently proposed the $f(R, L_m)$ gravity theory, where $f(R, L_m)$ is a function of Lagrangian matter density (L_m) and Ricci scalar (R). This theory represents the most general form of Riemann-space gravitational theories. In $f(R, L_m)$ gravity, test particles experience non-geodesic motion with additional forces perpendicular to their four-velocity vectors [20]. Some researchers found that the $f(R, Lm)$ gravity models open up new possibilities that extend beyond the algebraic structure observed in the Hilbert-Einstein action [21]. The energy conditions in $f(R, Lm)$ are broad and versatile, encompassing both the familiar energy conditions in General Relativity and $f(R)$ gravity. These conditions allow for arbitrary couplings, non-minimal couplings, and non-couplings between matter and geometry [22]. The mass-radius relationship is explored within the non-minimal geometry-matter coupling $f(R, Lm)$ gravity through investigating the simplest case as

$f = R + L_m + RL_m$, where the gravitational field is coupled to the matter field and the coupling constant [23]. The $f(R, L_m)$ cosmological model concurs with present observations and effectively predicts late-time cosmic acceleration for the FRW metric [24]. Some researchers [25] investigate a transit dark energy cosmological model in $f(R, Lm)$ gravity and using observational constraints, they establish a significant relationship between energy density parameters. The anisotropic nature of the Universe has been explored in $f(R, L_m)$ gravity for spatially homogeneous and isotropic FRW cosmological model and determine the present phase of the Universe [26]. The FRW metric solutions in $f(R, L_m)$ gravity successfully evade the Big-Bang singularity and can predict cosmic acceleration without relying on a cosmological constant owing to the geometry-matter coupling terms in the Friedmann-like equations [27]. Incorporating bulk viscosity, the $f(R, L_m)$ cosmological model offers a robust explanation for recent observations, effectively capturing the cosmic expansion scenario [28]. Certain scholars have explored wormhole solutions within the framework of $f(R, L_m)$ gravity and derived the field equations for the general $f(R, L_m)$ function, considering the static as well spherically symmetric Morris-Thorne wormhole metric [29].

The hybrid scale factor plays a crucial role in achieving viable cosmic dynamics without relying on any specific relationship between the pressure and energy density of the Universe in teleparallel gravity[30, 31]. Some authors [32] have obtained the exact solutions for LRS Bianchi-I metric in presence of holographic dark energy using hybrid expansion law. Some scholars used a hybrid scale factor to investigate the shearing, non-rotating and expanding character of the cosmos, which approaches anisotropy over large values of time t [33]. The $(n + 2)$ dimensional flat FRW Universe in the framework of general theory of relativity has been investigated utilizing hybrid expansion law with thick domain wall and bulk viscous fluid [34]. Certain scholars successfully tackled the Einstein field equations for strange quark matter to explore a 5-dimensional cosmological model discussed the dynamic aspects of concerning solution [35]. The Kantowski-Sachs cosmological model has been explored in the $f(R)$ theory of gravity with quark and strange quark matter and found that the spatial volume V is finite at $t = 0$, expands as t increases and becomes infinitely large as $t \to \infty$ [36]. Certain authors have successfully derived the solution for gravitational field equations using a power law relationship between the metric potentials and equation of state (EoS) [37].

Building upon the aforementioned investigations, many scholars have extensively studied FRW cosmological models, investigating their behavior concerning different energy sources and using hybrid expansion law as well strange quark matter in various modified gravity scenarios. These dedicated authors have sought to unveil the dynamic and cosmological properties of our Universe [38, 39, 40, 41, 42, 43, 44, 45, 46, 47, 48].

2. FORMALISM OF $f(R, L_m)$ GRAVITY

The $f(R, Lm)$ gravity model proposed by Harko and Lobo (2010) [20] is a generalization of the $f(R)$ gravity whose action is given by

$$S = \int f(R, L_m)\sqrt{-g}d^4x \tag{1}$$

Here $f(R, L_m)$ is a function of Ricci scalar R and Lagrangian of the matter density L_m.
One can acquire the Ricci scalar R by contracting the Ricci tensor R_{ij} as

$$R = g^{ij}R_{ij} \tag{2}$$

where the Ricci-tensor is given by

$$R_{ij} = \partial_\kappa \Gamma^\kappa_{ij} - \partial_j \Gamma^\kappa_{\kappa i} + \Gamma^\lambda_{ij}\Gamma^\kappa_{\lambda\kappa} - \Gamma^\kappa_{j\lambda}\Gamma^\lambda_{\kappa i} \tag{3}$$

Here $\Gamma^i_{j\kappa}$ represents the components of well-known Levi-Civita connection as indicated by

$$\Gamma^i_{j\kappa} = \frac{1}{2}g^{i\lambda}\left[g_{\kappa\lambda,j} + g_{\lambda j,\kappa} - g_{j\kappa,\lambda}\right] \tag{4}$$

The corresponding field equations of $f(R, L_m)$ gravity can be derived by varying the action (1) with respect to g_{ij} as,

$$f_R R_{ij} + (g_{ij}\Box - \nabla_i\nabla_j) f_R - \frac{1}{2}(f - f_{L_m}L_m)g_{ij} = \frac{1}{2}f_{L_m}T_{ij} \tag{5}$$

Where, $f_R = \frac{\delta f(R,L_m)}{\delta R}$, $f_{L_m} = \frac{\delta f(R,L_m)}{\delta L_m}$, $\Box = \nabla_i\nabla^j$ and T_{ij} is the Stress-energy momentum tensor for perfect fluid, given by

$$T_{ij} = \frac{-2}{\sqrt{-g}}\frac{\delta(\sqrt{-g}L_m)}{\delta g^{ij}} \tag{6}$$

By contracting the field Eq. (5), we find the relationship between Ricci scalar R, matter Lagrangian density L_m and T trace of the stress-energy-momentum tensor T_{ij} as

$$Rf_R + 3\Box f_R - (f - f_{L_m}L_m) = \frac{1}{2}f_{L_m}T \tag{7}$$

where $\Box F = \frac{1}{\sqrt{-g}}\partial_i\left(\sqrt{-g}g^{ij}\partial_j F\right)$ for any function of F

Now by taking covariant derivative of Eq. (5), one can acquire the following result as

$$\nabla^i T_{ij} = 2\nabla^i ln(f_{L_m})\frac{\partial L_m}{\partial g^{ij}} \tag{8}$$

3. THE MOTION EQUATIONS IN $f(R, L_m)$ GRAVITY

According to the most recent observations of Planck collaboration (2013) [49], our Universe is isotropic and homogeneous at larger scales. Therefore, to explore the current cosmological model we consider the flat Friedman-Lematre-Robertson-Walker (FLRW) metric of the form,

$$ds^2 = -dt^2 + a^2\left(dx^2 + dy^2 + dz^2\right) \tag{9}$$

Where $a(t)$ is the scale factor that signifies the expanding nature of the Universe at a time t.

For metric (9), the non-zero components of Christoffel symbols are

$$\Gamma_{ij}^0 = a\dot{a}\delta_{ij}, \Gamma_{0j}^k = \Gamma_{j0}^k = \frac{\dot{a}}{a}\delta_j^k, \quad for \ \ i,j,k = 1,2,3 \tag{10}$$

With the help of (4), the non zero components of Ricci tensor are given by

$$R_{00} = -3\frac{\ddot{a}}{a}, \qquad R_{11} = R_{22} = R_{33} = a\ddot{a} + 2\dot{a}^2 \tag{11}$$

Hence, the Ricci-scalar (R) associated with line element (9) is found as

$$R = 6\left[\frac{\ddot{a}}{a} + \frac{\dot{a}^2}{a^2}\right] = 6\left[\dot{H} + H^2\right] \tag{12}$$

where $H = \frac{\dot{a}}{a}$ is the Hubble parameter.

As the quark gluon plasma served as a perfect fluid, the energy momentum tensor (EMT) for strange quark matter (SQM) is given by

$$T_{ij} = \left(\rho_{sq} + p_{sq}\right)u_i u_j + p_{sq}g_{ij} \tag{13}$$

Here ρ_{sq} and p_{sq} are energy density and thermodynamic pressure of the SQM. and $u^i = (1,0,0,0)$ components of co-moving four velocity vectors in cosmic fluid with $u_i u^j = 0$ and $u_i u^i = -1$.
.

$$\rho_{sq} = \rho_q + B_c \qquad p_{sq} = p_q - B_c \tag{14}$$

Following the assumption that quarks are non-interacting and massless particles, an the pressure is approximated by an EoS of the form

$$p_q = \frac{\rho_q}{3} \tag{15}$$

Therefore, $p_{sq} = \frac{1}{3}\left(\rho_{sq} - \rho_0\right)$ is the linear EoS for SQM with ρ_0 is the density at zero pressure. If $\rho_0 = 4B_c$, the EoS for strange quark matter in the bag is reduced to

$$p_{sq} = \frac{\rho_{sq} - 4B_c}{3} \tag{16}$$

where, B_c is the bag constant.

The modified Friedmann equations which describe the dynamics of Universe in $f(R, L_m)$ gravity are given by

$$3H^2 f_R + \frac{1}{2}\left(f - Rf_R - f_{L_m}L_m\right) + 3H\dot{f_R} = \frac{1}{2}f_{L_m}\rho_{sq} \tag{17}$$

and

$$\dot{H} + 3H^2 f_R - \ddot{f_R} - 3H\dot{f_R} + \frac{1}{2}\left(f_{L_m}L_m - f\right) = \frac{1}{2}f_{L_m}p_{sq} \tag{18}$$

The overhead dot (.) depicts the derivative corresponding to time t.

4. COSMOLOGICAL SOLUTIONS FOR $f(R, L_m)$ GRAVITY

To examine the dynamics of Universe we employ the functional form of $f(R, L_m)$ gravity [26, 28, 29] of the form

$$f(R, L_m) = \frac{R}{2} + L_m^n \tag{19}$$

where n is any arbitrary constants and one can retain to standard Friedmann equations of GR for $n = 1$

For this particular functional form of $f(R, Lm)$ gravity, we have considered $Lm = \rho$ [50] and hence, for matter-dominated Universe, the Friedmann equations (17) and (18) yields,

$$2\dot{H} + 3H^2 = (n-1)\rho_{sq}^n - n\rho^{n-1}p_{sq} \tag{20}$$

and

$$3H^2 = (2n-1)\rho_{sq}^n \tag{21}$$

5. HYBRID SCALE FACTOR

The hybrid scale factor presents a transition in the cosmic evolution, shifting from early deceleration to late-time acceleration. In the early phase, the cosmic dynamics are dominated by power law behavior, while in the late phase, the exponential factor takes over. In the early stages of the Universe, the scale factor becomes zero, implying the absence of an initial singularity. Consequently, the chosen scale factor yields a time-dependent deceleration parameter, which effectively characterizes the transition of the Universe over time.

Therefore, to derive exact solutions for Friedmann equations (20) & (21) which involves three unknowns namely H, ρ_{sq} and p_{sq}, we employed the hybrid scale factor [51, 52, 53] as

$$a = e^{\alpha t} t^\eta \tag{22}$$

where, α and η

are positive constants. Also, when $\eta = 0$, the scale factor reverts to the exponential law and when $\alpha = 0$, the scale factor reduces to the power law.

So with this scale factor, we found the following time dependent kinematical properties as,
The Spatial Volume (V) given by

$$V = a^3 = \left(e^{\alpha t} t^\eta\right)^3 \tag{23}$$

The deceleration parameter (q) plays a crucial role in understanding the past and future evolution of the Universe. In cosmology, the deceleration parameter (q) is a measure of the rate at which expansion of the Universe is changing. For a universe dominated by matter and radiation, $q > 0$, indicating a decelerating expansion. On the other hand, if the Universe is dominated by dark energy with negative pressure, the $q < 0$, implying an accelerating expansion.
The Deceleration Parameter (q) is

$$q = -1 + \frac{\eta}{(\alpha t + \eta)^2} \tag{24}$$

The Hubble Parameter (H),

$$H = \frac{\alpha t + \eta}{t} \tag{25}$$

Scalar Expansion (θ)

$$\theta = 3H = 3\left(\frac{\alpha t + \eta}{t}\right) \tag{26}$$

Using Equ. (25) in Equ. (21) we obtained
Energy Density (ρ_{sq}) for SQM as

$$\rho_{sq} = \left[\frac{1}{(2n-1)}\left(\frac{\alpha t + \eta}{t}\right)^2\right]^{\frac{1}{n}} \tag{27}$$

Pressure (p_{sq}) for SQM is

$$p_{sq} = \frac{2}{n}\frac{\eta}{t^2}\left[\frac{1}{(2n-1)}\left(\frac{\alpha t + \eta}{t}\right)^2\right]^{\frac{n-1}{n}} - \frac{1}{(2n-1)}\left(\frac{\alpha t + \eta}{t}\right)^2 \tag{28}$$

The equation of state (EoS) for SQM is

$$\omega = \frac{p_{sq}}{\rho_{sq}} = \frac{\frac{2}{n}\frac{\eta}{t^2}\left[\frac{1}{(2n-1)}\left(\frac{\alpha t + \eta}{t}\right)^2\right]^{\frac{n-1}{n}} - \frac{1}{(2n-1)}\left(\frac{\alpha t + \eta}{t}\right)^2}{\left[\frac{1}{(2n-1)}\left(\frac{\alpha t + \eta}{t}\right)^2\right]^{\frac{1}{n}}} \tag{29}$$

from Equ. (14) the density and pressure for quark matter is given by

$$\rho_q = \left[\frac{1}{(2n-1)}\left(\frac{\alpha t + \eta}{t}\right)^2\right]^{\frac{1}{n}} - B_c \tag{30}$$

and

$$p_q = \frac{2}{n}\frac{\eta}{t^2}\left[\frac{1}{(2n-1)}\left(\frac{\alpha t + \eta}{t}\right)^2\right]^{\frac{n-1}{n}} - \frac{1}{(2n-1)}\left(\frac{\alpha t + \eta}{t}\right)^2 + B_c \tag{31}$$

6. STATEFINDERS DIAGNOSTIC

Statefinder parameters are cosmological diagnostic tools used to study the expansion dynamics of the Universe. They were introduced as a way to probe the nature of dark energy, the mysterious force driving the accelerated expansion of the Universe. These statefinder parameters were proposed by Sahni et al. (2003) in their paper titled "Statefinder—a new geometrical diagnostic of dark energy" [54]. During this research they were discusses how these parameters can be useful in distinguishing between various dark energy models, including quintessence and cosmological constant models, by examining their trajectories in the $\{r, s\}$ plane. By measuring these statefinder parameters from observational data, cosmologists can gain insights into the nature of dark energy and fate of the Universe, helping to test and refine our understanding of the fundamental laws governing the cosmos.

The statefinder pair $\{r, s\}$ is defined as

$$r = \frac{\ddot{a}}{aH^3} \tag{32}$$

and

$$s = \frac{r-1}{3(q - \frac{1}{2})} \tag{33}$$

We analyze the statefinder parameters (r, s) for our cosmological $f(R, L_m)$ model. The values $(r, s) = (1, 0)$ and $(1, 1)$ are representative of the ΛCDM (Lambda Cold Dark Matter) and CDM (Cold Dark Matter) models, respectively. However, $s > 0$ and $r < 1$ correspond to dark energy (DE) models, such as the phantom and quintessence models. On the other hand, when $r > 1$ and $s < 0$, it reflects the behavior of the Chaplygin gas model.

With the help of Equ. (22), (24) and (25), above equations can be written as

$$r = 1 - \frac{3\eta}{(\alpha t + \eta)^2} + \frac{2\eta}{(\alpha t + \eta)^3} \tag{34}$$

$$s = \frac{2\eta[3\eta(\alpha t + \eta) - 2\eta]}{3(\alpha t + \eta)\left[3(\alpha t + \eta)^2 - 2\eta\right]} \tag{35}$$

When time (t) is zero, the statefinder pair attains the values

$$\{r, s\} = \left\{1 - \frac{3\eta - 2}{\eta^2}, \frac{2}{3\eta}\right\}$$

From the figure we have observed that,

- Figure 1, clearly demonstrates that the average scale factor and spatial volume maintain a constant value at the initial time point ($t = 0$). However, as time progresses, both parameters show a steady and consistent growth, eventually extending towards infinity for prolonged periods (t). This remarkable observation indicates an ongoing and continuous expansion of the Universe.

- From Figure 2, it is depict that the deceleration parameter (q) decreases as cosmic time increases and approaches -1 for large values of t, indicating the accelerating phase of the Universe which coincident with the observations of type Ia supernovae [2].

- In Figure 3, it is shown that both the Hubble parameter and scalar expansion parameters exhibit diversity during the early stages of the Universe. As time approaches infinity, these parameters tend to zero. The graph indicates that the Universe initially experienced rapid and infinite expansion, but later settled into a constant expansion rate during a later epoch.

- Figure 4 exhibits the variation of pressure from significantly large negative values to reaching zero intriguing negative pressure phenomenon is commonly referred to as dark energy (DE), playing a crucial role in driving the accelerated expansion of Universe.

- According to Figure 5, the energy density fallows an interesting trend, starting with a substantial value initially. However, as time progresses, the energy density gradually diminishes and eventually approaches zero as $t \to \infty$. This striking behavior strongly suggests the expansion of Universe.

- The Figure 6 depicts the evolution of equation of state (EoS) over time (t). It illustrates a transition from an accelerating to a decelerating phase, eventually returning to an accelerating phase of the Universe over late time.
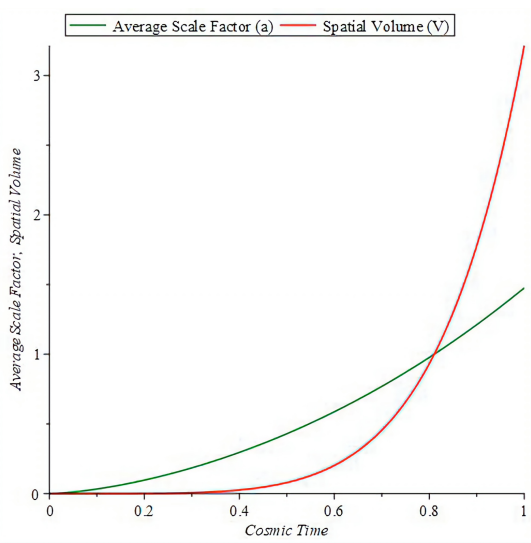

Figure 1. Variation of Average Scale Factor (a) & Volume (V) against Cosmic Time (t) for $\alpha = 0.5$ and $\eta = 1.5$
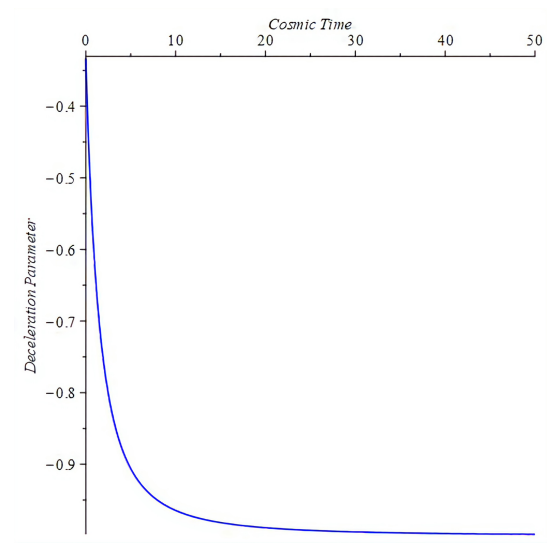

Figure 2. Variation of Deceleration Parameter (q) against Cosmic Time (t) for $\alpha = 0.5$ and $\eta = 1.5$
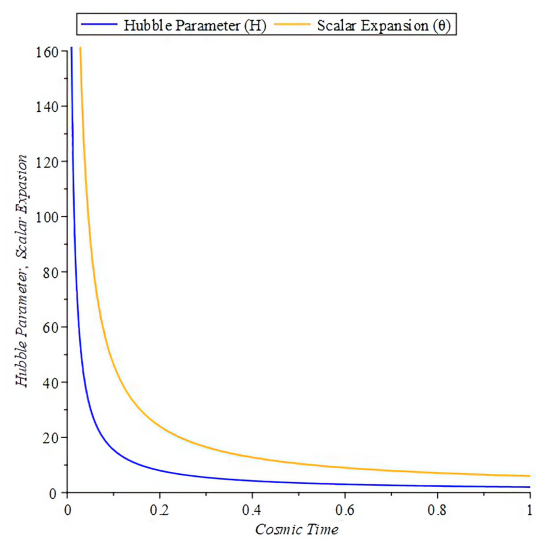

Figure 3. Variation of Hubble Parameter (H) & Scalar Expansion (θ) against Cosmic Time (t) for $\alpha = 0.5$ and $\eta = 1.5$
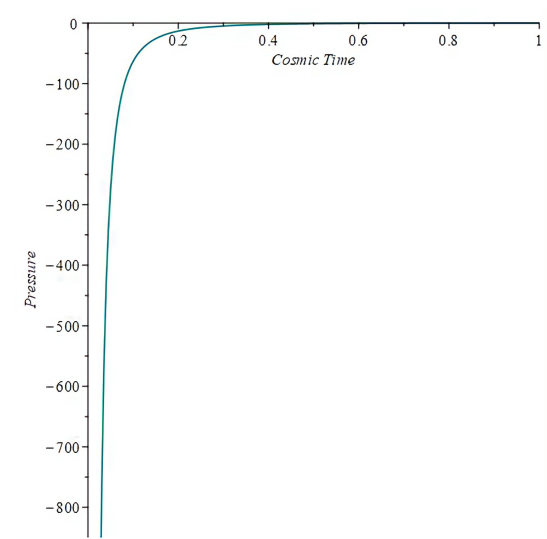

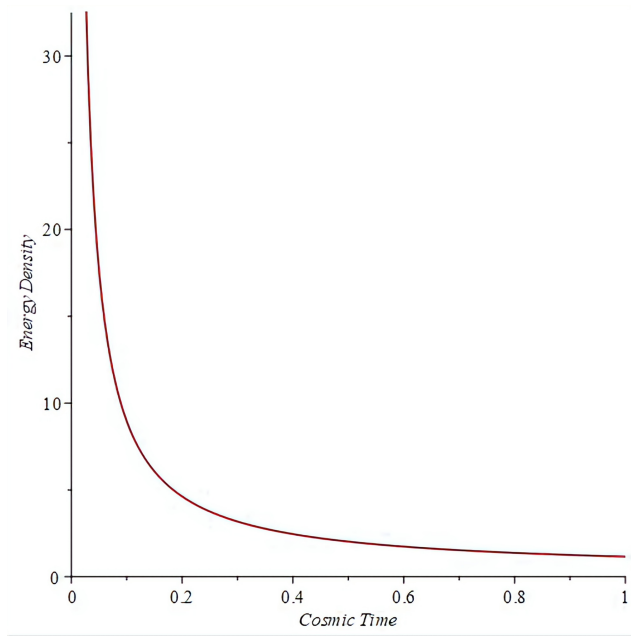**Figure 4.** Variation of Pressure (P) against Cosmic Time (t) for $\alpha = 0.5$ and $\eta = 1.5$

Figure 5. Variation of Energy Density (ρ) against Cosmic Time (t) for α=0.5 and $\eta = 1.5$
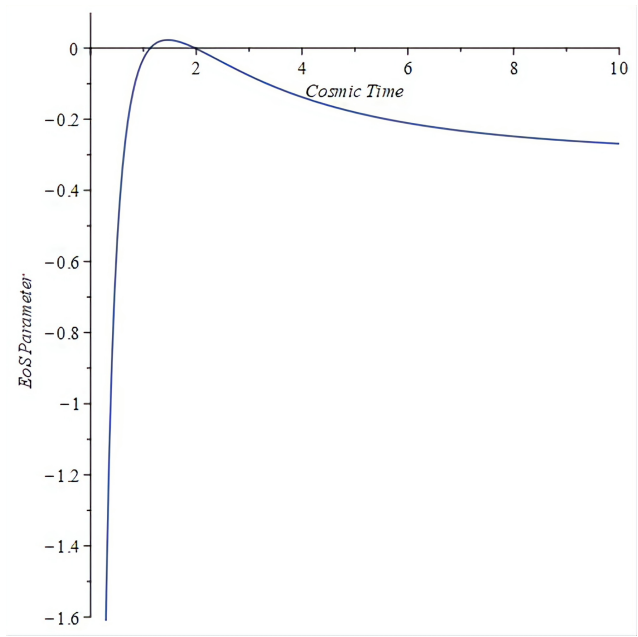

Figure 6. Variation of Equations of state Parameter (EoS) against Cosmic Time(t) for $\alpha = 0.5$ and $\eta = 1.5$
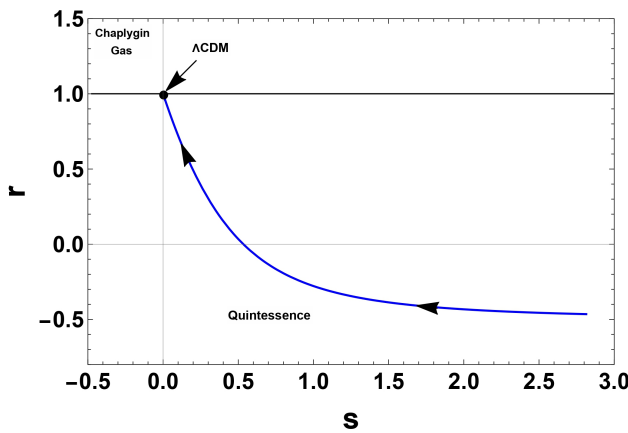

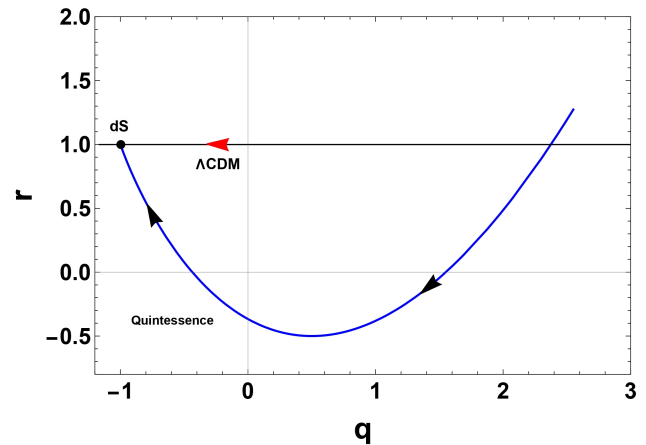**Figure 7.** Evolution trajectory of $r - s$ Plane

Figure 8. Evolution trajectory of $r - q$ Plane

- Yet it is clear from the aforementioned traits that the evolutionary trajectories split depending on different parameter choices and vary from one model to another. Particularly noteworthy is Figure 7, which shows how to plot the $r - s$ planes. Compared to looking at the r and s evolution separately, analyzing the $r - s$ plane is clearer. This clarity is very helpful when comparing various cosmological models. Given this situation, the $r - s$ planes' usefulness increases because of their clear evolutionary paths and obvious directional cues, which make differentiating between discrepancies easier.

- Figure 8 is a $r - q$ plane, which vividly demonstrate the consistency with the characteristics deliberated upon in this section. Moreover, it is noteworthy that the most suitable-fit model within this category showcases the capacity to transition from an initial phase of decelerating expansion to a subsequent phase of cosmic acceleration in the late stages of the Universe's evolution.

- We have observed from Figure 7 and 8 that, in the long run, they both have a tendency to evolve in a way that resembles a ΛCDM model, i.e., $\{r, s\} = \{1, 0\}$ and $\{q, r\} = \{-1, 1\}$ in future.

7. DISCUSSION AND CONCLUDING REMARKS

In this article, we investigates the late-time cosmic accelerated expansion of the Universe using a specific form of $f(R, L_m)$ gravity as non-linear model, $f(R, L_m) = \frac{R}{2} + L_m^n$, where n is free model parameter. During this study we derived the motion equations for the isotropic and homogeneous FLRW cosmological model with

strange quark matter (SQM). We have obtained cosmological model using hybrid scale factor and exhibited a smooth transition of the Universe from accelerating phase to decelerated phase and retain to accelerating phase.

The results of this study are extremely persuasive, leading to the formulation of the subsequent conclusions:

- We have noted that the average scale factor and spatial volume (V) remain bounded around $t = 0$, progressively expanding as time (t) advances, ultimately approaching an infinitely large value as $t \to \infty$, as depicted in Figure 1. This signifies that the expansion of the Universe initiates with a finite volume, progressively extending as time unfolds and results matched with [55, 56, 57].

- The deceleration parameter (q) is a measure of the rate at which the expansion of Universe is changing over time (t). It is used to describe the acceleration or deceleration of the universe's expansion under the influence of gravitational forces and other factors. In our study, we observed the deceleration parameter (q) is decreasing function of cosmic time (t) and approaches -1, it suggests that the expansion of the universe is accelerating, and we got the ΛCDM model.

- We noticed that, the Hubble parameter (H) and scalar expansion (θ) both initially have large value and as time progresses i.e. $t \to \infty$, the values of H and θ approaches to zero. This reflects that, in the initial moments after the Big Bang, the Universe expanded rapidly and as time progresses the expansion rate begins to decreases which is good agreement with results [58, 59].

- Our study reveals that the Universe's pressure for SQM (p_{sq}) experiences growth with cosmic time (t). It starts at a highly negative value and gradually approaches zero at the current epoch. Recent cosmological findings attribute the Universe's accelerated expansion to dark energy, characterized by negative pressure. Consequently, the model aligns well with observations of the type Ia Supernovae [1].

- In the study, it was determined that the energy density for SQM (ρ_{sq}) consistently remains positive and decreases as cosmic time. Initially, the energy density remained constant during the early epoch. The Universe could potentially reach a steady state in the distant future, as the (ρ_{sq}) tends to diminish significantly over extended periods of time.

- Initially, as time (t) approaches zero, the cosmological model exhibits a Phantom phase with $\omega < -1$, signifying an accelerated expansion. After a finite period, the model converges towards $\omega = -1$, representing the cosmological constant (Λ) and aligning with the ΛCDM model, characterized by continued accelerated expansion. Subsequently, the model enters the quintessence region with $\omega > -1$, maintaining this state for a certain duration. Beyond $t = 1.1$, the model transitions from an accelerating to a decelerating phase (for transition phase of the universe one can refer [60]), but it later reverts to an accelerating phase. Ultimately, the model reenters the quintessence region, where it persists during late times.

- In the present paradigm, we have conducted an assessment of the statefinder parameters and subsequently depicted the graphical representations of the $r - s$ and $r - q$ planes. Our investigation has yielded results indicating that $\{r, s\} = \{1, 0\}$ and $\{q, r\} = \{-1, 1\}$ respectively, providing a striking manifestation that the current model aligns closely with the characteristics of the de Sitter point, a foundational feature of the ΛCDM cosmological framework.

ORCID

🆔 **Vasudeo Patil**, https://orcid.org/0000-0002-0442-3962; 🆔 **Jeevan Pawde**, https://orcid.org/0000-0001-8068-6265; 🆔 **Rahul Mapari**, https://orcid.org/0000-0002-5724-9734; 🆔 **Sachin Waghmare**, https://orcid.org/0000-0001-5316-0540

REFERENCES

[1] A.G. Riess et al., Astron. J. **116**, 1009 (1998). https://doi.org/10.1086/300499

[2] S. Perlmutter et al., Astrophys. J. **517**, 565 (1999). https://doi.org/10.1086/307221

[3] S. Perlmutter et al., Astrophys. J. **483**, 565 (1997). https://doi.org/10.1086/304265

[4] P.M. Garnavich et al., Astrophys. J. **509**, 74 (1998). https://doi.org/10.1086/306495

[5] P.S. Letelier, Phys. Rev. D , **28**, 2414 (1983). https://doi.org/10.1103/PhysRevD.28.2414

[6] D.N. Spergel et al., ApJS, **148**, 175-194 (2003). https://doi.org/10.1086/377226

[7] D.N. Spergel et al., Astrophys. J. Suppl., **170**, 377 (2007). https://doi.org/10.1086/513700

[8] D.J. Eisenstein et al., Astrophys. J. **633**, 560-576 (2005). https://doi.org/10.1086/466512

[9] W.J. Percival, et al., Mon. Not. Roy. Astron. Soc. **381**, 1053-1066 (2007). https://doi.org/10.1111/j.1365-2966.2007.12268.x

[10] T. Koivisto, and D.F. Mota, Phys. Rev. D, **73**, 083502 (2006). https://doi.org/10.1103/PhysRevD.73.083502

[11] S.F. Daniel, Phys. Rev. D, **77**, 103513 (2008). https://doi.org/10.1103/PhysRevD.77.103513

[12] G. Hinshaw, et al., ApJS, **208**, 19 (2013). https://doi.org/10.1088/0067-0049/208/2/19

[13] S. Nojiri, and S.D. Odintsov, Phys. Rev. D, **68**, 123512 (2003). https://doi.org/10.1103/PhysRevD.68.123512

[14] S. Nojiri, et al., Phys. Lett. B, **657**, 238-245 (2007). https://doi.org/10.1016/j.physletb.2007.10.027

[15] S. Capozziello, V.F. Cardone, and A. Troisi, JCAP, **0608**, 001 (2006). [*CrossRef*]

[16] A. Borowiec, W. Godlowski, and M. Szydlowski, Int. J. Geom. Meth. Mod. Phys. **4**, 183-196 (2007). https://doi.org/10.1142/S0219887807001898

[17] C.F. Martins, et al., Phys. Rev. Lett. **98**, 151301 (2007). https://doi.org/10.1111/j.1365-2966.2007.12273.x

[18] C.G. Boehmer, T. Harko, and F.S.N. Lobo, Astropart.Phys. **29**, 386-392 (2008). https://doi.org/10.1016/j.astropartphys.2008.04.003

[19] T.P. Sotiriou, and V. Faraoni, Rev. Mod. Phys. **82**, 451 (2010). https://doi.org/10.1103/RevModPhys.82.451

[20] T. Harko, and F.S.N. Lobo, Eur. Phys. J. C, **70**, 373-379 (2010). https://doi.org/10.1140/epjc/s10052-010-1467-3

[21] F.S.N. Lobo, and T. Harko, (2012). https://doi.org/10.48550/arXiv.1211.0426

[22] J. Wang, and K. Liao, Class. Quantum Grav. **29**, 215016 (2012). https://doi.org/10.48550/arXiv.1211.0426

[23] R.V. Lobato, G.A. Carvalho, and C.A. Bertulani, Eur. Phys. J. C, **81**, 1013 (2021). https://doi.org/10.1140/epjc/s10052-021-09785-3 [*CrossRef*]

[24] L.V. Jaybhaye, R. Solanki, S. Mandal, and P.K. Sahoo, Phys. Lett. B, **831**, 137148 (2022). https://doi.org/10.1016/j.physletb.2022.137148

[25] A. Pradhan, D.C. Maurya, G.K. Goswami, and A. Beesham, International Journal of Geometric Methods in Modern Physics, **20**(06), 2350105 (2022). https://doi.org/10.1142/S0219887823501050

[26] N.S. Kavya, V. Venkatesha, S. Mandal, and P.K. Sahoo, Physics of the Dark Universe, **38**, 101126 (2022). https://doi.org/10.1016/j.dark.2022.101126

[27] B.S. Gonçalves, P.H.R.S. Moraes, and B. Mishra, (2023) https://doi.org/10.48550/arXiv.2101.05918

[28] L.V. Jaybhaye, et al., Universe, **9**(4), 163 (2023). https://doi.org/10.3390/universe9040163

[29] R. Solanki, et al., Chin. J. Phys. **85**, 74 (2023). https://doi.org/10.1016/j.cjph.2023.06.005

[30] V.M. Raut, Prespacetime J. **11**(7), 608-616 (2020). https://prespacetime.com/index.php/pst/article/view/1740/1640

[31] S.K. Tripathy, B. Mishra, M. Khlopov, and S. Ray, IJMPD, **30** (16), 2140005 (2021). https://doi.org/10.1142/S0218271821400058

[32] A.Y. Shaikh, et al., New Astronomy, **80**, 101420 (2020). https://doi.org/10.1016/j.newast.2020.101420

[33] D.R.Manekar, S.R. Bhoyar, and H. Kumar, Sch. J. Phys. Math. Stat. **8**(4), 82-87 (2021). https://doi.org/10.36347/sjpms.2021.v08i04.001

[34] V.G. Mete, V.S. Deshmukh, D.V. Kapse, and V.S. Bawane, Prespacetime J. **14**(3), 309-315 (2023). https://prespacetime.com/index.php/pst/issue/view/143

[35] G.S. Khadekar, and R. Shelote, Int. J. Theor. Phys. **51**, 1442–1447 (2012). https://doi.org/10.1007/s10773-011-1020-7

[36] K.S. Adhav, A.S. Bansod, and S.L. Munde, Open Phys. **13**, 90-95 (2015). https://doi.org/10.1515/phys-2015-0010

[37] D.D. Pawar, S.P. Shahare, Y.S. Solanke, and V.J. Dagwal, Indian J. Phys. **95**, 10 (2021). https://doi.org/10.1515/phys-2015-0010

[38] V.R. Patil, J.L. Pawde, and R.V. Mapari, IJIERT, **9**(4), 92-101 (2022). https://doi.org/10.17605/OSF.IO/QABKV

[39] P.K. Agrawal, and D.D. Pawar, J. Astrophys. and Astronomy, **38**(2), (2017). https://doi.org/10.1007/s12036-016-9420-y

[40] A.Y. Shaikh, A.S. Shaikh, and K.S. Wankhade, Pramana J. Phys. **95**(19), (2021). https://doi.org/10.1007/s12043-020-02047-z

[41] P.K. Sahoo, and B. Mishra, Turkish J. Phys. **39**(1), 43-53 (2015). https://doi.org/10.3906/fiz-1403-5

[42] P.K. Sahoo, P. Sahoo, B.K. Bishi, and S. Aygü, New Astronomy, **60**(1), 80-87 (2018). https://doi.org/10.1016/j.newast.2017.10.010

[43] A.Y. Shaikh, S.V. Gore, and S.D. Katore, Bulg. J. Phys. **49**(4), 340–361 (2022). https://doi.org/10.55318/bgjp.2022.49.4.340

[44] S.H. Shekh, and V.R. Chirde, Gen. Rel. and Grav. **51**(87), 340–361 (2019). https://doi.org/10.1007/s10714-019-2565-7

[45] V.R. Chirde, S.P. Hatkar, and S.D. Katore, Int. J. Mod. Phys. D, **29**(8), 2050054 (2020). https://doi.org/10.1142/S0218271820500546

[46] D.D. Pawar, R.V. Mapari, V.M. Raut, Bulg. J. Phys. **48**, 225–235 (2021).

[47] V.R. Patil, J.L. Pawde, R.V. Mapari, and P.A. Bolke, East Eur. J. Phys. **3**, 62–74 (2023). https://doi.org/10.26565/2312-4334-2023-3-04

[48] S. Jokweni, V. Singh, and A. Beesham, Phys. Sci. Forum, **7**(12), (2023). https://doi.org/10.3390/ECU2023-14037

[49] Planck Collaboration, Astronomy & Astrophys. **571** (A16) (2014). https://doi.org/10.1051/0004-6361/201321591

[50] T. Harko, F.S.N. Lobo, J.P. Mimoso, and D. Pavón, Eur. Phys. J. C, **75**, 386 (2015). https://doi.org/10.1051/0004-6361/201321591

[51] B. Mishra, S.K. Tripathy, and P.P. Ray, Eur. Phys. J. C, **75**, 386 (2015). https://doi.org/10.1007/s10509-018-3313-2

[52] S.K. Tripathy et al., Phys.Dark Univ.**30**, 100722 (2020). https://doi.org/10.1016/j.dark.2020.100722

[53] B. Mishra, S.K. Tripathy, and S. Tarai, Mod. Phys. Lett. **33**(9), 1850052 (2018). https://doi.org/10.1142/S0217732318500529

[54] V. Sahni, et al., U. Alam, JETP Lett. **77**(9), 201 (2003). https://doi.org/10.1134/1.1574831

[55] D.D. Pawar, R.V. Mapari, and J.L. Pawde, Pramana J. Phys. **95**(10), (2021). https://doi.org/10.1007/s12043-020-02058-w

[56] P.P. Khade, Jordan J. Phys. **16**(1), 51-63 (2023). https://doi.org/10.47011/16.1.5

[57] D.D. Pawar, R.V. Mapari, and P.K. Agrawal, J. Astrophys. Astr. **40**(13), (2019). https://doi.org/10.1007/s12036-019-9582-5

[58] V.R. Patil, S.K. Waghmare, P.A. Bolke, Bull. Cal. Math. Soc. **115**(2), 159-170 (2023).

[59] J.S. Wath, and A.S. Nimkar, Bulgarian J. Phys. **50**, 255-264 (2023). https://doi.org/10.55318/bgjp.2023.50.3.255

[60] D.D. Pawar, and R.V. Mapari, Journal of Dynamical Systems and Geometric Theories, **20**(1), 115-136 (2022). https://doi.org/10.1080/1726037X.2022.2079268

КОСМОЛОГІЯ FLRW ІЗ ГІБРИДНИМ МАСШТАБНИМ КОЕФІЦІЄНТОМ У $f(R, L_m)$ ГРАВІТАЦІЇ

Васудео Патіл[a], **Дживан Павде**[a], **Рахул Мапарі**[b], **Сачін Вагмаре**[c]

[a] *Департамент математики, мистецтв, науки та торгівлі коледжу Чікхалдара*
округ Амраваті (MS), Індія-444807

[b] *Департамент математики, Державний науковий коледж, Гадчіролі (MS), Індія-442605*

[c] *Факультет математики, Тулширам Гайквад Патіл коледж англійської мови та технолоій,*
Нагпур (MS), Індія-441122

У цій статті ми маємо за мету описати пізнє космічне прискорення Всесвіту в гравітаційній системі $f(R, L_m)$, запропонованій Харко (2010) за допомогою рівняння стану дивної кваркової матерії. Щоб досягти цього, ми приймаємо певну форму сили тяжіння $f(R, L_m)$ як $f(R, L_m) = \frac{R}{2} + L_m^n$, де n є довільна константа. Тут ми використовуємо гібридний масштабний коефіцієнт для вирішення модифікованих рівнянь поля в контексті гравітації $f(R, L_m)$ для ізотропної та однорідної метрики Фрідмана–Леметра–Робертсона–Уокера (FLRW) у присутності дивної кваркової матерії (SQM). Крім того, ми аналізуємо динаміку щільності енергії, тиску і параметрів шукача стану та пояснюємо відмінності між нашою моделлю та поточними моделями темної енергії за наявності SQM. Ми спостерігали перехід від фази прискорення до фази уповільнення у Всесвіті, а потім повернення до фази прискорення у пізніший час Крім того, ми проаналізували діагностику визначника стану та рівняння параметрів стану та виявили, що модель продемонструвала квінтесенційну поведінку. Наше дослідження дійшло висновку, що запропонована космологічна модель $f(R, L_m)$ добре узгоджується з нещодавніми спостережними дослідженнями та ефективно описує космічне прискорення, яке спостерігалося в останні часи.

Ключові слова: *космологічна модель; $f(R, L_m)$ гравітація; дивна кваркова матерія; гібридний масштабний фактор*

SPECTRAL AND TIMING STUDY OF THE NEWLY DETECTED ULTRALUMINOUS X-RAY SOURCES IN NGC 3585 USING DIFFERENT *CHANDRA* OBSERVATIONS

 S. Rita Devi[a*], **A. Senorita Devi**[b], **Atri Deshamukhya**[a]

[a] Assam University, Silchar, Assam, India
[b] Manipur University, Canchipur, Manipur, India
[*] Corresponding Author e-mail: sinamrita26@gmail.com

The present work aims to study the previously unstudied Ultraluminous X-ray sources (ULXs) in the galaxy NGC 3585 at its various epochs of *Chandra* observation. We report here the detection of two new ULXs viz. CXOUJ111306.0-264825 (X-1) and CXOUJ111325.3-264732 (X-2) with their bolometric luminosity $> 10^{39} erg\ s^{-1}$ in its various *Chandra* observations. X-1 was found to be a spectrally hard ULX in both the epochs where it was detected. However in the ULX, X-2, a slight hardening of the spectra was observed within a period of 17 years. Assuming isotropic emission and explained by disk blackbody model, the spectrally softer epoch of X-2 with an inner disk temperature, $kT_{in} \sim 0.79$ keV and bolometric luminosity $\sim 2.51 \times 10^{39} erg\ s^{-1}$ implies for X-2 to be powered by a compact object, necessarily a black hole of mass, $M_{BH} \sim 44.85^{+82.11}_{-25.92} M_{\odot}$ accreting at ~ 0.42 times the Eddington limit. The Lightcurve of X-1 and X-2 binned at 500s, 1ks, 2ks and 4ks has shown no signature of short-term variability in both the ULXs in kilo-seconds time scales. Overall, both the detected ULXs seem to be almost static sources both in long-term (years) as well as short-term (kilo-seconds) time scales with the presently available *Chandra* Observations.

Keywords: *Accretion; Accretion disks; Galaxies: individual(NGC 3585); X-rays: binaries*

PACS: 97.10.Gz, 98.52.-b: 98.56.Ew, 95.85.Nv, 97.80.Jp

1. INTRODUCTION

Ultraluminous X-ray sources (ULXs) are defined as point-like, non nuclear X-ray sources with an X-ray luminosity exceeding the Eddington limit for a 20 $M_{\odot}$ black hole (BH) [1]. ULXs have X-ray luminosity $\geq 10^{39}$ erg s^{-1}, which may even rise upto 10^{42} erg s^{-1} in the 0.5-10.0 keV energy range. In early days, these X-ray detected in the external galaxies with isotropic luminosities $\geq 10^{39}$ erg s^{-1} were unclear and they were thought to be - underluminous accreting supermassive black holes (SMBH) or overluminous X-ray binaries (XRBs) located near the galactic nucleus, or rather a totally new class of astrophysical object [2]. The first such individual luminous X-ray sources were detected in nearby external spiral galaxies by the Einstein satellite in the 0.3 - 4.0 keV energy range [3]. Since their first discovery with the Einstein Observatory [4], ULX remained mysterious object for more than two decades. The mass accretion rate in ULXs and also the mass of the compact object harbored by ULXs have been controversial, and still it is in debate. However recent observations with Chandra, XMM-Newton, NuSTAR etc. have given clear visions of these sources by detecting many of its kind. Now many ULXs, above 1800 in numbers, have been detected and its population is also well studied [5, 6, 7, 8, 9, 10].

Various models came up to explain the high luminosities of ULXs, such as - (i) Super-Eddington accretion onto stellar mass blackholes with mass, $M_{BH} \approx 10 M_{\odot}$ [11, 12], (ii) sub-Eddington accretion on to Intermediate mass blackholes with masses, $M_{BH} \sim 10^2 - 10^5$ $M_{\odot}$ [13, 14] and (iii) relativistic and geometric beaming from an anisotropic super-critical accretor [15, 16].

In its early days, ULXs were considered to be extragalactic X-ray binaries (XRBs) with stellar-mass black hole (BH) accretors [17] like the XRBs observed in our own galaxy. From their spectral and variability studies, they were suggested to be accreting compact objects in binary systems. Later again, ASCA X-ray spectral studies of many ULXs gave the evidence that they display the characteristics of accreting blackholes. ULX spectra are now studied more precisely by using high quality data from various missions such as that of XMM-Newton, NuSTAR, also data from the very high resolution detectors of Chandra etc.. Advanced studies of ULX spectra and variability of individual sources indicate that some ULXs can represent different spectral states in analogy with those observed in X-ray binaries [7]. Again in some ULXs, transitions of luminosity were also observed such as that of XMMU J004243.6+412519 in M31 which changed from X-ray binary state ($L_x \sim 2 \times 10^{38} erg\ s^{-1}$) to ultraluminous state ($L_x \sim 10^{39} erg\ s^{-1}$) and then returned to binary state [18].

These transitions suggest that ULXs can also be an ultraluminous state of accreting compact objects like XRBs. Also in many ULXs, spectral state transitions between two spectral states have been reported such as that in NGC 1313 X-1 [19] and in NGC 247 where spectral state transition occur from soft ULX to super-soft ULX in the brightest ULX source [20]. All these clearly points towards some ULXs being quite closely related to black hole binaries. If ULX sources are indeed accreting compact objects, then their very high luminosity should favor them to harbor massive (stellar mass) black holes. Afterwards, many future works have given the evidence for these ULXs to be powered by accretion on to stellar mass black holes, such as that of Avdan et al.(2016) [21] who studied X-ray and optical properties of the ULX, X-6, in the nearby galaxy NGC 4258 (M106). They reported that the compact object in this ULX is most likely a stellar-mass black hole. Singha and Devi (2017)[22] studied the spectra of the ULXs in NGC 5643 and NGC 7457 and reported that some ULXs were found to be accreting at a sub-Eddington rate and some ULXs were accreting at super-Eddington rate on to stellar mass BHs. They also studied seven ULXs in NGC 2276 and they suggested that the compact objects associated with these seven sources are in the stellar mass BH range [23].

Although the high luminosity of some ULXs were well explained by stellar mass black holes, some ULXs which are very luminous, having luminosities above 10^{41} erg s^{-1}, could not be explained by super-Eddington accretion onto stellar mass black holes. Indeed, they require black hole mass greater than the stellar mass to explain their high luminosities. Black holes having mass range, $M_{BH} \sim 10^2 - 10^4$ M$_\odot$ are called intermediate-mass black holes (IMBHs) and it express the missing component of the black hole mass spectrum in the gap between those of stellar mass black holes found in Galactic X-ray binaries and those associated with active galactic nuclei (AGN), $M_{BH} \sim 10^6 - 10^9$M$_\odot$ [24]. Farrell et al (2009) [25] discovered the most luminous hyper luminous X-ray source (HLX), HLX-1, in the spiral galaxy ESO 243-49 having peak luminosity of the order of 10^{42} erg s^{-1}. Their analysis suggest that HLX-1 harbour black hole with mass, M, 3000 M$_\odot$ < M < 10^5 M$_\odot$ which is the range of IMBHs. The review of Miller & Colbert (2004)[26] and Miller (2005)[27] discussed various arguements regarding the evidence for IMBHs in ULXs. Many other bright ULXs such as M82 X-1 [28, 29], M51 ULX-7 [30] and NGC 2276–3c [31] also give evidence for ULXs harboring IMBHs. Many other such HLXs with bolometric luminosity greater than 10^{41} erg s^{-1} such as the HLXs reported in Singha and Devi (2019)[14] highly points towards these extremely luminous X-ray sources to be powered by accretion on to IMBH. Sanatombi et al. (2023)[32] reported the super-soft ULX, CXOUJ132943.3+471135, in the galaxy M51 to harbor a black hole with mass $\sim 10^4 M_\odot$ where they have also reported that even with extreme beaming case, the mass of the black hole harbored by this source is $\sim 10^3 M_\odot$.

Another breakthrough discovery for ULX model is the ULX pulsar. Pulsations are recently detected in many ULXs, so they are also sometimes modelled as an accreting system in which the compact object is a neutron star with mass $\sim$ 1 - 2 M$_\odot$, accreting at extreme super-Eddington rates. NuSTAR observations of the starburst galaxy M82 reported the first ULX pulsations [33], later on many other ULXs were confirmed to present pulsations [34, 35, 36, 37]. Doroshenko et al.(2020)[38] reported the first Galactic pulsating ULX - Swift J0243.6+6124. King et al. (2023)[16] has reported for a kind of recently reported system in which some high mass X-ray binaries (HMXBs) ocassionally becomes ULXs like the system A0538-66. Here, they pointed out that a normal Be X-ray Binary which is a HMXB, makes regular transitions between normal Be X-ray binary states to PULXs and back again. These Be X-ray binaries in their PULXs states have very high super-Eddington accretions even though they behave as normal Be X-ray systems when it is in its usual Be X-ray binary state. Thus, in recent years, deep X-ray studies of ULXs have shown that the ULX population is dominated by supercritical accretors which may be either a stellar mass BH or a neutron star. However, the ULX population appears to remain heterogeneous with some candidate Intermediate mass black hole (IMBH) also.

In this paper, we present the spectral study of the non-nuclear X-ray point sources in NGC 3585 from all its available *Chandra* observations. The NGC 3585 group is known to include NGC 3585 itself, which is an E6 galaxy and the brightest galaxy in the group [39]. NGC 3585 has not been studied extensively in X-rays. In this work, we also investigate for any signature of kiloseconds variability of the sources detected. Also, we have investigated for any long term variability of the point sources at the available different epochs of *Chandra* observation of NGC 3585. The distance to the galaxy, NGC 3585, is adopted to be 20 Mpc [40].

The observation and data analysis are described in Section 2. Results and discussion are presented in Section 3 and summarized in Section 4.

2. OBSERVATION AND DATA ANALYSIS

In the present work, we have carried out spectral and timing analysis of the point sources in NGC 3585 as detected by *Chandra* ACIS-S detector. NGC 3585 has been observed by Chandra ACIS-S detector five times-first in the year 2001 (Obs ID 2078), second in the year 2008(Obs ID 9506) and then three times in the year 2018 (Obs ID 19332, Obs ID 21034, Obs ID 21035). The detail *Chandra* observational log of NGC 3585 is given in Table 1. The data reduction and analysis were done using CIAO 4.14 and HEASOFT 6.30.1. For each of the observation data sets, using acis_set_ardlib, observation-specific bad pixel lists were set in the ardlib parameterfile. Figure 1 shows a three-color X-ray image of the galaxy NGC 3585 which is created by using CIAO

Table 1. Chandra ACIS-S Observation log for NGC 3585

Galaxy	Distance (Mpc)	ObsId*	Exposure (ks)	Observation Year	N(≥ 100)**
NGC 3585	20.0	2078	36	2001-06-03	2
		9506	60	2008-03-11	1
		19332	62	2018-03-13	1
		21034	30	2018-03-14	-
		21035	30	2018-03-15	-

*ObsID - *Chandra* Observation ID ; **N-number of sources with net counts ≥ 100

tools dmcopy and dmimg2jpg. The soft X-rays with energy $\approx (0.3 - 1.0 keV)$, medium X-rays $\approx (1.0 - 2.0 keV)$ and hard X-rays $\approx (2.0 - 8.0 keV)$ are represented in red, green and blue respectively. X-ray point sources were extracted from the level 2 event lists by using the CIAO source detection tool *Wavdetect*. Using a combination of CIAO tools and calibration data, the source (and background) spectrum were extracted. Spectra were grouped and rebinned so that each bin had a minimum of 15 counts. The spectral analysis was done using spectral fitting package XSPEC version 12.12.1, available in the Heasoft package. Sources with counts ≥ 100 are chosen for the spectral analysis so that spectral parameters could be constrained properly while using two-parameter model. With this criteria, we detected two new Ultraluminous X-ray sources - CXOUJ111306.0-264825 (X-1) and CXOUJ111325.3-264732 (X-2). The spectra of the two sources are fitted in the energy range 0.3 -8.0 keV using two empirical spectral models - the absorbed power law and an absorbed disk-blackbody. XSPEC model-*phabs* was used to take into account the absorption in the spectrum. While fitting the spectra, the hydrogen column density (n_H) was generally set free to vary, however for those cases when the estimated n_H was much lower than the average Galactic value, it was frozen to the Galactic value $\sim 4.96 \times 10^{20} cm^{-2}$. Since the number of counts in each sectrum was typically low, C statistics were used for the analysis. A measure of the goodness of fit is determined by C-stat/(degrees of freedom(dof)), which should be approximately one. The intrinsic bolometric luminosity is a good parameter for the study and identification of the ULXs, so from the model parameters and the distance to the galaxy, the bolometric luminosity of the point sources are estimated for the disk-blackbody model. However for power-law model, the luminosity in the 0.3-8.0 keV range are estimated.

Using the disk blackbody model, the mass of the compact object harboured by the ULXs can be indirectly estimated. So, for ULXs at few mega parsec, to roughly estimate the black hole mass, we assume the inner-disk radius, $R_{in} \sim 10 \, GM/c^2$. The inner disk radius, R_{in} is then computed from normalization of the disk black body component using the distance to the source D=20 Mpc, and taking the viewing angle, cos i=0.5, and color factor, f=1.7 [14]. Thus the mass of the compact object harbored by the corresponding ULX is estimated.
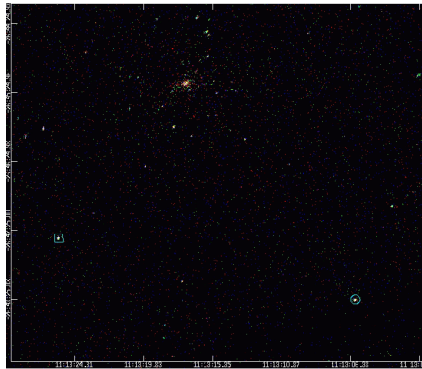

Figure 1. Three-colour X-ray image of NGC 3585 (ObsID 2078): Red represents soft X-ray emission (0.3–1 keV), green represents medium-hard X-rays (1-2 keV) and blue denotes hard X-rays (2-8 keV). X-1 is represented by the circle in cyan and X-2 by the box in cyan.

3. RESULTS AND DISCUSSION

Two new Ultraluminous X-ray sources - CXOUJ111306.0-264825 (X-1) and CXO-UJ111325.3-264732 (X-2) were identified whose details are tabulated in Table 2. Both the sources were estimated to have X-ray luminosities, $L_x, \geq 10^{39}$ erg s^{-1}, probably considered both the sources to be ULX. The spectral properties of the ULX sources as estimated by the two models are tabulated in Table 3.

Table 2. Details of the X-ray sources

| Source	Source name	R.A.*	Decl.**	ObsId	Counts
X-1	CXOUJ111306.0-264825	+11:13:06.04	-26:48:25.34	2078	220
				9506	358
X-2	CXOUJ111325.3-264732	+11:13:25.32	-26:47:31.67	2078	142
				19332	124

*R.A - in (hours, minutes and seconds); **Decl. in (degrees, arcminutes and arcseconds)

Table 3. Spectral properties of the two ULXs (X-1 and X-2)

		Powerlaw				Disk-blackbody			
Source	Obs Id.	n_H	Γ	$\log(L_x)$	$Cstat$/dof	n_H	KT_{in}	$\log(L_x)$	$Cstat$/dof
		$(10^{22} cm^{-2})$		(ergs s^{-1})		$(10^{22} cm^{-2})$	keV	(ergs s^{-1})	
(1)	(2)	(3)	(4)	(5)	(6)	(7)	(8)	(9)	(10)
X-1	2078	0.0496*	$1.69^{+0.20}_{-0.18}$	$39.44^{+0.06}_{-0.07}$	13.78/10	0.0496*	$0.98^{+0.25}_{-0.23}$	$39.69^{+0.07}_{-0.08}$	34.19/10
X-1	9506	$0.07^{+0.09}_{-0.06}$	$1.74^{+0.34}_{-0.24}$	$39.50^{+0.05}_{-0.03}$	12.31/19	0.0496*	$0.95^{+0.16}_{-0.16}$	$39.69^{+0.04}_{-0.05}$	26.37/19
X-2	2078	$0.27^{+0.19}_{-0.16}$	$2.65^{+0.73}_{-0.63}$	$39.46^{+0.34}_{-0.19}$	4.64/5	$0.03^{+0.11}_{-0.03}$	$0.79^{+0.26}_{-0.18}$	$39.42^{+0.08}_{-0.05}$	6.40/5
X-2	19332	$0.53^{+0.72}_{-0.48}$	$2.17^{+0.97}_{-0.78}$	$39.33^{+0.53}_{-0.18}$	5.83/4	$0.07^{+0.48}_{-0.06}$	$1.34^{+0.68}_{-0.45}$	$39.37^{+0.09}_{-0.06}$	6.63/4

* Freeze to the Galactic hydrogen Column density $\sim 4.96 \times 10^{20} cm^{-2}$

Columns: (1): Source (2): Observation ID. (3): n_H, equivalent hydrogen column density. (4): Γ,the powerlaw photon index. (5):(L_x),X-ray luminosity in the 0.3 -8.0 keV energy range, (6): Cstat/Degrees of freedom. (7): n_H, equivalent hydrogen column density. (8): KT_{in},the inner disk temperature. (9):(L_x), bolometric X-ray luminosity. (10):Cstat/Degrees of freedom.

The observed normalized net count distribution of these sources as fitted with powerlaw model and disk blackbody model are shown in Figure 2 and Figure 3. The detail study and findings of the the two newly detected ULXs are discussed below.
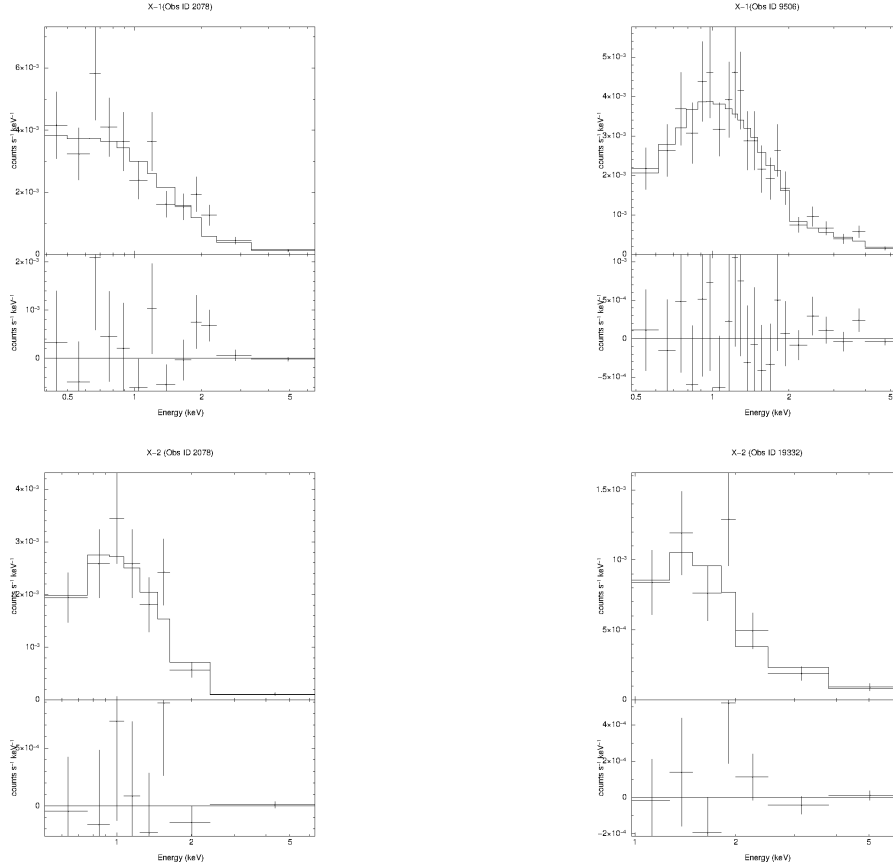
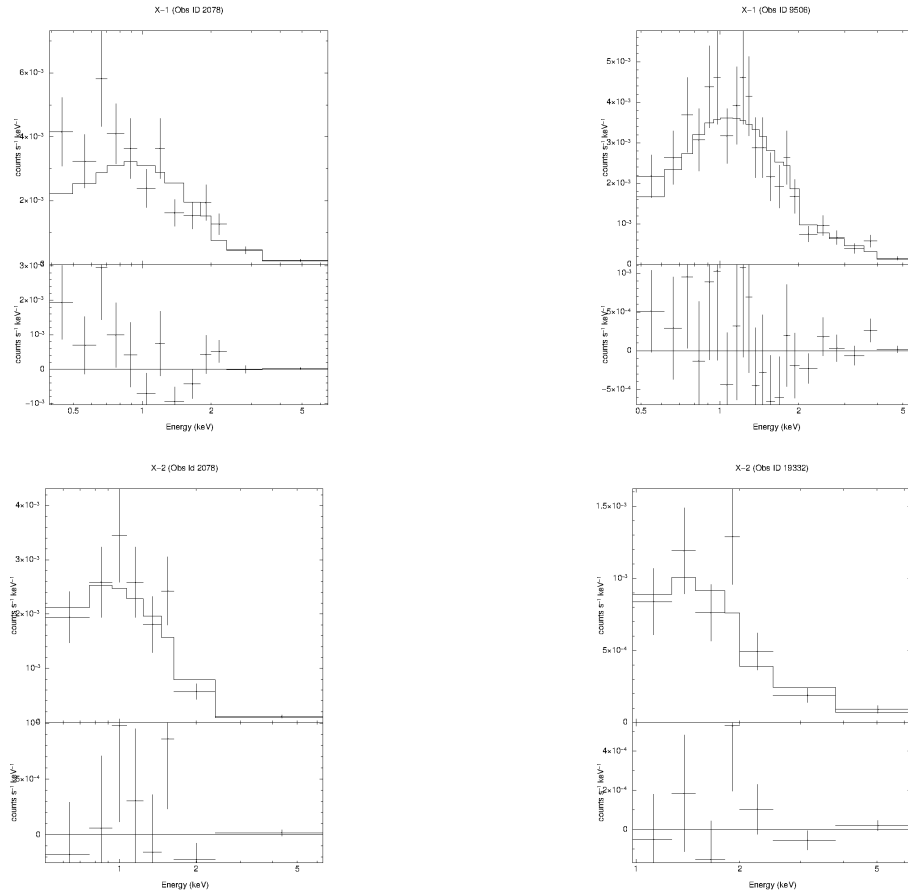**Figure 2.** Powerlaw Spectra of the two ULXs (X-1 and X-2) at different epochs

Figure 3. Disk blackbody Spectra of the two ULXs (X-1 and X-2) at different epochs

3.1. CXOUJ111306.0-264825 (X-1)

CXOUJ111306.0-264825 (X-1) has been detected in two of the *Chandra* observations of NGC 3585. In the year 2001 observation (ObsId 2078), the spectrum of X-1 is found to prefer the powerlaw model than the disk blackbody model. In this epoch of observation, X-1 is found to be spectrally hard with a powerlaw photon index (Γ) $\sim$ 1.69. However, both the models estimate the X-ray luminosity of this source to be in the ULX range with few times 10^{39} erg s^{-1}. After a period of 7 years in the year 2008 observation (ObsId 9506) also, the spectrum of X-1 remains hard with powerlaw photon index (Γ) $\sim$ 1.74, while the inner disk temperature (kT_{in}), as explained by the disk blackbody model remains around $\sim$ 1 keV in both the observations. In the later observation, both the models could well explain the spectra of X-1, but with a slight preference to the disk blackbody model. In both the two epochs, the luminosity of X-1 is almost consistent.

The radiative mechanism of this hard ULX, X-1, may be due to inverse comptonization of soft photons near the accretion disk. But, if we try to explain the spectra of X-1 with the disk blackbody model as being seen to slightly prefer this model in the case of ObsID 9506, then with the assumption of isotropic emission, the mass of the compact object harbored by this ULX is estimated to be in the stellar mass BH which is likely accreting at sub-Eddington rate.

3.2. CXOUJ111325.3-264732 (X-2)

CXOUJ111325.3-264732 (X-2) has been detected in four *Chandra* observations - ObsId 2078 of the year 2001, ObsIds 19332, 21034 and 21035 of the year 2018. However the net source counts in the observations - ObsIds 21034 and 21035 were only 57 and 38 respectively. So due to this very low counts, the spectrum could not be fitted properly as the number of variable parameters exceeds the number of bins. Hence for the present study, we consider the spectra of X-2 only in the two epochs of observation with ObsIds - 2078 and 19332. The spectra of X-2 can equally be well explained by both the models in both these epochs of observations. In the year 2001 observation, its spectra was relatively soft with an inner disk temperature, $kT_{in} \sim$ 0.79 keV as
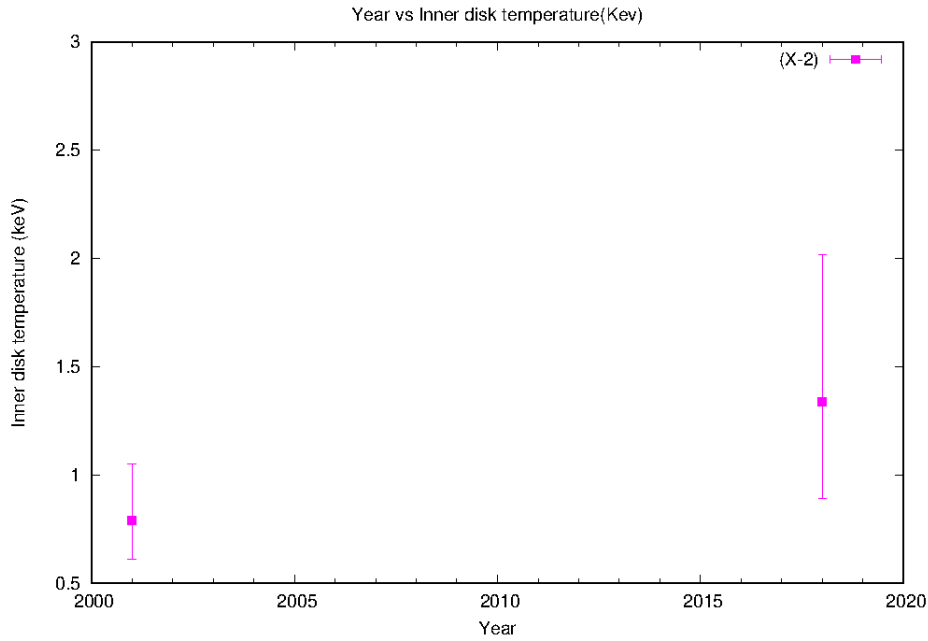
Figure 4. Spectral state transitions in X-2

explained by the disk blackbody model, which after a period of nearly 17 years in the ObsId 19332, the spectra becomes slightly harder with $kT_{in} \sim 1.34$ keV (Figure 4).

However, within error limits, this hardening of the spectrum within a period of 17 years is not very significant. In both the epochs of observation, the powerlaw photon index(Γ) ≈ 2, within error limits. The luminosity of X-2 almost remain consistent in both the epochs. With the assumption of isotropic emission and explain by disk blackbody model, the spectral parameters of X-2 in its relatively softer state with $kT_{in} \sim 0.79$ keV and bolometric luminosity $\sim 2.51 \times 10^{39} erg\ s^{-1}$(ObsId 2078), estimates a black hole of mass, $M_{BH} \sim 44.85^{+82.11}_{-25.92} M_{\odot}$ accreting at ~ 0.42 times the Eddington limit.

3.3. Temporal property of the ULXs

As investigated in its various epochs of observation, the two detected ULXs were found to have no long-term variability in their luminosity . Bachetti et al.(2014)[33] reported for a variable ULX spatially coincident with a pulsating neutron star whose X-ray luminosity can reach upto $1.8 \times 10^{40} erg\ s^{-1}$ in the 0.3 -10 keV range. This implies for certain variable ULXs to be neutron star candidates which are super-accretors. As such, to check the presence of any short-term/kiloseconds variability for the two ULXs detected in the present study, temporal analysis was carried out. The lightcurve of X-1 and X-2 binned over 0.5, 1, 2 and 4 ks for each of the *Chandra* observations in which these two ULXs are detected, are shown in Figure 5 and Figure 6 respectively.

For CXOUJ111306.0-264825 (X-1), in all these time bins, the probability for the count rate being a constant during the observation with ObsID 2078 is all greater than 0.045 and that in the observation with ObsID 9506 is all > 0.31. Likewise for CXOUJ111325.3-264732 (X-2) also, in all these time bins, the probability for the count rate being a constant during the observation with ObsID 2078 is all > 0.73 and that in the observation with ObsID 19332 is all > 0.24. For, the sources to be variable, their variability probability should be $\geq 99\%$ or rather the probability for their count rate being constant should be less than 0.01 (1 %), which is not so in case of X-1 and X-2 in the present study. This clearly shows the absence of any short-term variability in kilo-seconds time-scales in both the two newly detected ULXs- CXOUJ111306.0-264825 and CXOUJ111325.3-264732 with the currently available Chandra data. So, it is indicative that these two ULXs in NGC 3585 is more likely to be static sources both in long-term (years) as well as short-term (kiloseconds) scales.

However, due to limited timing capabilities of many sensitive X-ray instruments aboard X-ray satellites, the transient nature of pulsations of many variable sources have eluded detections. So, a more detail future work with high quality data from other missions may enable us to ascertain the real physical nature of these two ULXs and many more such ULXs in more details.
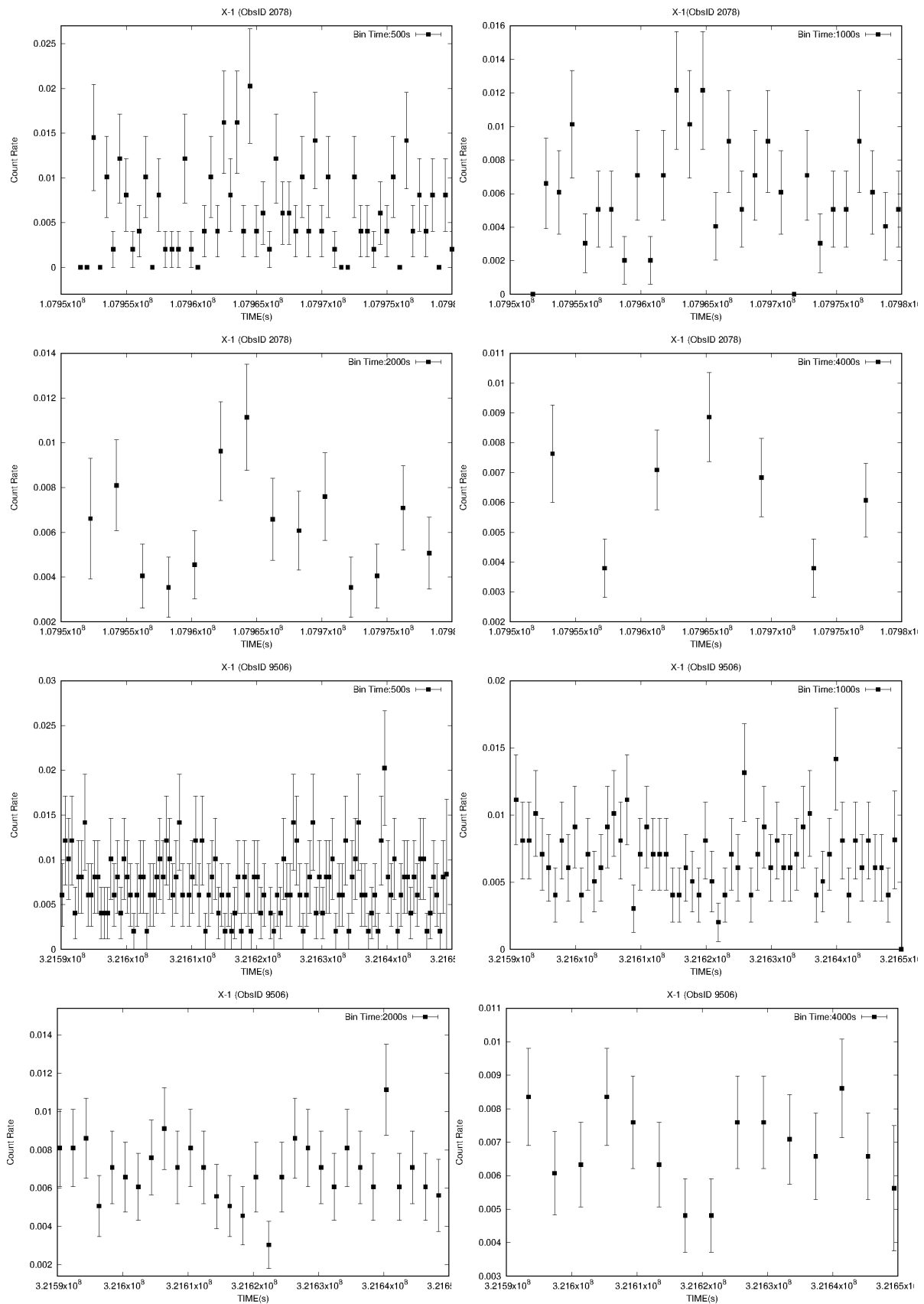
Figure 5. Lightcurve of CXOUJ111306.0-264825 (X-1) in its two epochs - ObsID 2078 and ObsId 9506, in different time bins (500 s, 1000 s, 2000 s and 4000 s)
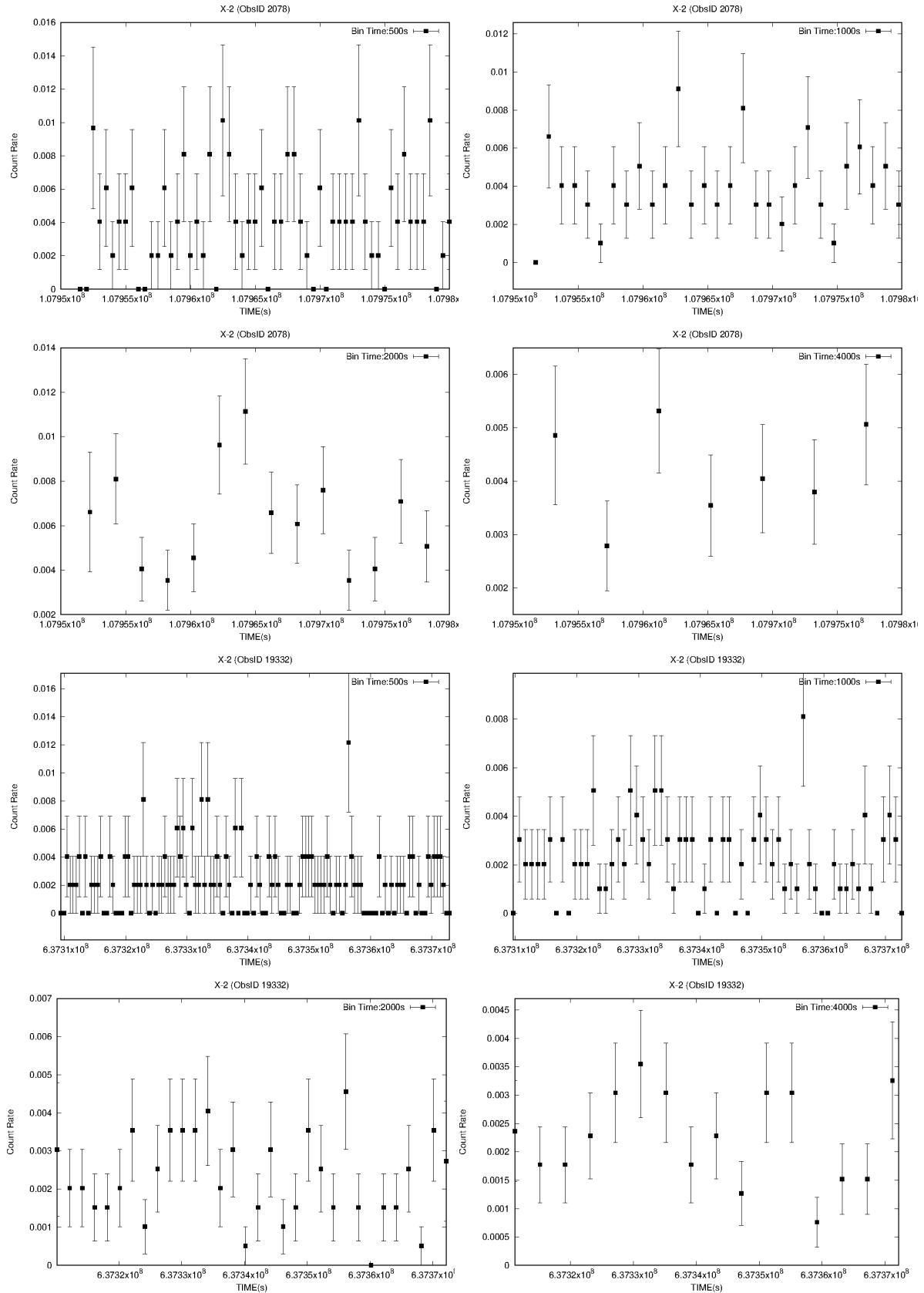
Figure 6. Lightcurve of CXOUJ111325.3-264732 (X-2) in its two epochs - ObsID 2078 and ObsId 19332, in different time bins (500 s, 1000 s, 2000 s and 4000 s)

4. CONCLUSION

We present the results of spectral and timing analysis of the X-ray point sources in the galaxy NGC 3585 as observed by *Chandra* in different epochs. NGC 3585 is least studied in X-rays and the point sources in NGC 3585 are hardly reported. Two point sources- CXOUJ111306.0-264825 (X-1) and CXOUJ111325.3-264732 (X-2) with net source count > 100 were detected and thus considered for the present study. The spectra of the two sources were fitted with two empirical models - the absorbed power law and an absorbed disk black-body. The ULX source, X-1, was observed in two *Chandra* observational epochs with a gap of nearly 7 years. In both the epochs, X-1 is found to be spectrally hard with an inner disk temperature, $kT_{in} \sim 1$ keV as explained by the disk blackbody model and a powerlaw photon index, $\Gamma, \sim 1.69$ as explained by the powerlaw model.

However in both the epochs, its bolometric luminosity was nearly constant at around $4.89 \times 10^{39} erg \ s^{-1}$, showing an absence of long term variability with the available *Chandra* data. ULX source, X-2, is being studied here in two *Chandra* epochs at a gap of nearly 17 years. X-2 seem to have some sort of spectral hardening within a period of 17 years, however this hardening of the spectrum is not very significant within error limits. In both the epochs, X-2 also have almost nearly consistent bolometric luminosity around $2.51 \times 10^{39} erg \ s^{-1}$, thereby showing no evidence of long term variability in years scale. The spectral parameters of X-2 in its relatively softer state with $kT_{in} \sim 0.79$ keV (ObsId 2078), estimates a black hole of mass, $M_{BH} \sim 44.85^{+82.11}_{-25.92} M_{\odot}$ accreting at sub-Eddington limit. Timing analysis of both X-1 and X-2 reveals no short-term/kilo-seconds variability in these two ULXs. Hence with the available *Chandra* data, both the two detected ULXs seems to be nearly static sources both in long-term as well as short-term scales. However, a more detail future work with high quality data from other missions may enable us to ascertain the real physical nature of these two ULXs and many more such ULXs.

ORCID

S. Rita Devi, https://orcid.org/0000-0002-0663-1538; **A. Senorita Devi**, https://orcid.org/0000-0001-9971-4262; **Atri Deshamukhya**, https://orcid.org/0000-0003-4350-6645

REFERENCES

[1] S.N. Fabrika, K.E. Atapin, A.S. Vinokurov, and O.N. Sholukhova, "Ultraluminous X-Ray Sources," Astrophy. Bulle. **76**, 6-38 (2021). https://doi.org/10.1134/S1990341321010077

[2] E.J.M. Colbert, R. Petre, E.M. Schlegel, and S.D. Ryder, "Soft X-Ray Emission from the Spiral Galaxy NGC 1313," Astrophys.J. **446**, 177 (1995). https://doi.org/10.1086/175777

[3] G. Fabbiano, D.-W. Kim, and G. Trinchieri, "An X-Ray Catalog and Atlas of Galaxies," Astrophys. J Suppl. Ser. **80**, 531-644 (1992). https://ui.adsabs.harvard.edu/link_gateway/1992ApJS...80..531F/doi:10.1086/191675

[4] G. Fabbiano, "X Rays From Normal Galaxies," Ann. Rev. Astron. Astrophys. **27**, 87-138 (1989). https://doi.org/10.1146/annurev.aa.27.090189.000511

[5] D.A. Swartz, K.K. Ghosh, A.F. Tennant, and K. Wu,"The Ultra-Luminous X-ray Source Population from the Chandra Archive of Galaxies," Astrophys. J. Suppl. Ser. **154**, 519 (2004). https://ui.adsabs.harvard.edu/link_gateway/2004ApJS..154..519S/doi:10.48550/arXiv.astro-ph/0405498

[6] A.S. Devi, R. Misra, V. Agrawal, and K.Y. Singh, "The dependence of the estimated luminosities of ULX on spectral models," Astrophys. J. **664**, 458-466 (2007). https://doi.org/10.48550/arXiv.0704.1107

[7] P. Kaaret, H. Feng, and T. Roberts, "Ultraluminous X-Ray Sources," Ann. Rev. of Astro. and Astrophy. **55**, 303-341 (2017). https://doi.org/10.1146/annurev-astro-091916-055259

[8] H.P. Earnshaw, T.P. Roberts, M.J. Middleton, D.J. Walton, and S. Mateos, "A new, clean catalogue of extragalactic non-nuclear X-ray sources in nearby galaxies," Mon. Not. R. Astron. Soc. **483**, 5554–5573 (2019). https://doi.org/10.1093/mnras/sty3403

[9] K. Kovlakas, A. Zezas, J.J. Andrews, A. Basu-Zych, T. Fragos, A. Hornschemeier, B. Lehmer, and A. Ptak, "A census of ultraluminous X-ray sources in the local Universe," Mon. Not. R. Astron. Soc. **498**(4), 4790–4810 (2020). https://doi.org/10.1093/mnras/staa2481

[10] D.J. Walton, A.D.A. Mackenzie, H. Gully, N.R. Patel, T.P. Roberts, H.P. Earnshaw, and S. Mateos, "A multimission catalogue of ultraluminous X-ray source candidates," Mon. Not. R. Astron. Soc. **509**(2), 1587–1604 (2022). https://doi.org/10.1093/mnras/stab3001

[11] J. Poutanen, G. Lipunova, S. Fabrika, A. G. Butkevich, and P. Abolmasov, "Supercritically accreting stellar mass black holes as ultraluminous X-ray sources," Mon. Not. R. Astron. Soc. **377**, 1187–1194 (2007). https://doi.org/10.1111/j.1365-2966.2007.11668.x

[12] E.S. Mukherjee, D.J. Walton, M. Bachetti, F.A. Harrison, D.Barret, E. Bellm, S.E. Boggs, et al., "A Hard X-Ray Study of Ultraluminous X-ray Source NGC 5204 X-1 with NuSTAR and XMM-Newton," Astrophys. J. **808**, 64 (2015). https://doi.org/10.1088/0004-637X/808/1/64

[13] O. Godet, B. Plazolles, T. Kawaguchi, J. Lasota, D. Barret, S. Farrell, V. Braito, M. Servillat, N. Webb, and N. Gehrels, Astrophys. J. **752**, 34 (2012). https://ui.adsabs.harvard.edu/link_gateway/2012ApJ...752...34G/doi:10.48550/arXiv.1204.3461

[14] A.C. Singha, and A.S. Devi, "Bimodal Distribution of the Hyperluminous X-ray Sources," Acta Astrono. **69**, 339–360 (2019). https://doi.org/10.32023/0001-5237/69.4.3

[15] A.R. King, M.B. Davies, M.J. Ward, G. Fabbiano, and M. Elvis, "Ultraluminous X-Ray Sources in External Galaxies," Astrophys. J. **552**, L109–L112 (2001). https://doi.org/10.48550/arXiv.astro-ph/0104333

[16] A.R. King, J.P. Lasota, and M. Middleton, "Ultraluminous X-ray sources," New Astron. Rev. **96**, 101672 (2023). https://doi.org/10.1016/j.newar.2022.101672

[17] S.A. Rappaport, P. Podsiadlowski, and E. Pfahl, "Stellar-mass black hole binaries as ultraluminous X-ray sources," Mon. Not. R. Astron. Soc. **356**, 401–414 (2005). https://doi.org/10.1111/j.1365-2966.2004.08489.x

[18] M.J. Middleton, J.C.A. Miller-Jones, S. Markoff, R. Fender, M. Henze, N. Hurley-Walker, Anna M. M. Scaife, et al., "Bright radio emission from an ultraluminous stellar-mass microquasar in M 31," Nature. **493**, 187–190 (2013). https://doi.org/10.1038/nature11697

[19] H. Feng, and P. Kaaret, "Spectral State Transitions of the Ultraluminous X-Ray Sources X-1 and X-2 in NGC 1313," Astrophys. J. **650**, L75 (2006). https://ui.adsabs.harvard.edu/link_gateway/2006ApJ...650L..75F/doi:10.1086/508613

[20] C. Pinto, R. Soria, D.J. Walton, A. D'Ai, F. Pintore, P. Kosec, W.N. Alston, et al., "XMM-Newton campaign on the ultraluminous X-ray source NGC 247 ULX-1: outflows," Mon. Not. R. Astron. Soc. **505**, 5058–5074 (2021). https://doi.org/10.1093/mnras/stab1648

[21] H. Avdan, S. Avdan, A. Akyuz, S. Balman, N. Aksaker, and I. Akkaya Oralhan, "X-RAY SPECTRAL AND OPTICAL PROPERTIES OF A ULX IN NGC 4258 (M106)," Astrophy. J. **828**, 105 (2016). https://doi.org/10.3847/0004-637X/828/2/105

[22] A.C. Singha, and A.S. Devi, "Study of X-ray point sources in NGC 5643 and NGC 7457 with Chandra," Astrophys. Space Sci. **362**, 1-9 (2017). https://doi.org/10.1007/s10509-017-3189-6

[23] A.C. Singha, and A.S. Devi, "Spectral and Temporal Analysis of Ultraluminous X-ray Sources in NGC 2276," Acta Astronomica, **71**, 261–279 (2021). https://doi.org/10.32023/0001-5237/71.4.1

[24] D. Richstone, E.A. Ajhar, R. Bender, G. Bower, A. Dressler, S.M. Faber, A.V. Filippenko, et al., "Supermassive Black Holes and the Evolution of Galaxies," Nature, **395**, A14 (1998). https://doi.org/10.48550/arXiv.astro-ph/9810378

[25] S.A.Farrell, N.A. Webb, D. Barret, O. Godet, and J.M. Rodrigues, "An intermediate-mass black hole of over 500 solar masses in the galaxy ESO 243-49," Nature, **460**, 73-75 (2009). https://doi.org/10.1038/nature08083

[26] M.C. Miller, and E.J.M. Colbert, Int. J. Mod. Phys. D. **13**, 1–64 (2004). https://doi.org/10.1142/S0218271804004426

[27] J.M. Miller, "Present Evidence for Intermediate Mass Black Holes in ULXs and Future Prospects," Astrophys. Space Sci. **300**, 227–238 (2005). https://doi.org/10.1007/s10509-005-1181-z

[28] H. Feng, and P. Kaaret, "Identification of the X-Ray Thermal Dominant State in an Ultraluminous X-Ray Source in M82," The Astrophy. J. Let. **712**, L169–L173 (2010). https://doi.org/10.1088/2041-8205/712/2/L169

[29] D.R. Pasham, T.E. Strohmayer, and R.F. Mushotzky, "A 400-solar-mass black hole in the galaxy M82," Nature, **513**, 74–76 (2014). https://doi.org/10.1038/nature13710

[30] H.M. Earnshaw, T.P. Roberts, L.M. Heil, M. Mezcua, D.J. Walton, C. Done, F.A. Harrison, et al., "A variable ULX and possible IMBH candidate in M51a,"Mon. Not. R. Astron. Soc. **456**, 3840-3854 (2016). https://doi.org/10.1093/mnras/stv2945

[31] M. Mezcua, T.P. Roberts, A.P. Lobanov, and A.D. Sutton, "The powerful jet of an off-nuclear intermediate-mass black hole in the spiral galaxy NGC 2276," Mon. Not. R. Astron. Soc. **448**, 1893–1899 (2015). https://doi.org/10.1093/mnras/stv143

[32] T. Sanatombi, A.S. Devi, and K.Y. Singh, "Spectral study of the Ultraluminous X-ray sources in M51 at different epochs of Chandra observation," Chin. J. of Phys. **83**, 579–598 (2023), https://doi.org/10.1016/j.cjph.2023.04.010

[33] M. Bachetti, F. Harrison, D. Walton, B. Grefenstette, D. Chakrabarty, F. Fürst, D. Barret, A. Beloborodov, et al., "An ultraluminous X-ray source powered by an accreting neutron star," Nature, **514**, 202-212 (2014). https://doi.org/10.1038/nature13791

[34] G.L. Israel, A. Papito, P. Esposito, L. Stella, L. Zampieri, A. Belfiore, G.A.R. Castillo, et al., "Discovery of a 0.42-s pulsar in the ultraluminous X-ray source NGC 7793 P13," Mon. Not. R. Astron. Soc. **466**, L48-L52 (2017). https://doi.org/10.1093/mnrasl/slw218

[35] S. Carpano, F. Haberl, C. Maitra, and G. Vasilopoulos, "Discovery of pulsations from NGS 300 ULX1 and its fast period evolution," Mon. Not. R. Astron. Soc. **476**, L45-49 (2018). https://doi.org/10.1093/mnrasl/sly030

[36] R. Sathyaprakash, T.P. Roberts, D.J. Walton, F. Fuerst, M. Bachetti, C. Pinto, W.N. Alston, et al., "The discovery of weak coherent pulsations in the ultraluminous X-ray source NGC 1313 X-2," Mon. Not. R. Astron. Soc. **488**, L35-40 (2019). https://doi.org/10.1093/mnrasl/slz086

[37] G.A.R. Castillo, G.L. Israel, A. Belfiore, F. Bernardini, P. Esposito, F. Pintore, et al., "Discovery of a 2.8 s pulsar in a 2 d orbit High-Mass X-ray Binary powering the Ultraluminous X-ray source ULX-7 in M51," Astrophys.J. **895**, 60 (2020). https://doi.org/10.48550/arXiv.1906.04791

[38] V. Doroshenko, S. Tsygankov, J. Long, A. Santangelo, S. Molkov, A. Lutovinov, L.D. Kong, et al., "First characterization of Swift J1845.7–0037 with NuSTAR," Astron and Astroph. **634**, A89 (2020). https://doi.org/10.1051/0004-6361/201937036

[39] G. de Vaucouleurs, *Third Reference Catalogue of Bright Galaxies*, (Springer, Berlin, 1991).

[40] A. Bogdan, and M. Gilfanov, "Soft band *X/K* luminosity ratios for gas-poor early-type galaxies," Astron and Astroph. **512**, A16 (2010). https://doi.org/10.1051/0004-6361/200913651

СПЕКТРАЛЬНЕ ТА ЧАСОВЕ ДОСЛІДЖЕННЯ НЕЩОДАВНО ВИЯВЛЕНИХ ДЖЕРЕЛ УЛЬТРАСВІТОВОГО РЕНТГЕНІВЬСОГО ВИПРОМІНЮВАННЯ В NGC 3585 З ВИКОРИСТАННЯМ РІЗНИХ *Chandra* СПОСТЕРЕЖЕНЬ

С. Ріта Деві[a], **А. Сеньорита Деві**[b], **Атрі Дешамухья**[a]

[a] *Ассамський університет, Сілчар, Ассам, Індія*
[b] *Маніпурський університет, Канчіпур, Маніпур, Індія*

Ця робота має на меті вивчити раніше невивчені джерела ультрасвітового рентгенівського випромінювання (ULX) у галактиці NGC 3585 у різні епохи її спостереження *Chandra*. Тут ми повідомляємо про виявлення двох нових ULX, а саме. CXOUJ111306.0-264825 (X-1) і CXOUJ111325.3-264732 (X-2) з їхньою болометричною світністю $> 10^{39}~s^{-1}$ у різних спостереженнях *Chandra* . Було виявлено, що X-1 є спектрально жорстким ULX в обидві епохи, коли він був виявлений. Проте в ULX, X-2 спостерігалося невелике посилення спектрів протягом 17 років. Припускаючи ізотропне випромінювання та пояснюючи модель чорного тіла диска, спектрально м'якша епоха X-2 із внутрішньою температурою диска $kT_{in} \sim 0{,}79$ кеВ і болометричною світністю $\sim 2{,}51 \times 10^{39}~s^{-1}$ означає, що X-2 живиться від компактного об'єкта, обов'язково чорної діри з масою $M_{BH} \sim 44{,}85^{+82,11}_{-25,92} M_\odot$ збільшується у $\sim 0{,}42$ рази від межі Еддінгтона. Крива світла X-1 і X-2, згрупована на 500 с, 1 кс, 2 тис. і 4 тис. Загалом обидва виявлені ULX є майже статичними джерелами як у довгостроковому (роки), так і в короткостроковому (кілосекунди) часовому масштабі з наявними на даний момент спостереженнями *Chandra*.
Ключові слова: *акреція, акреаційні диски; галактики: окремі (NGC 3585); рентгенівські промені: бінарні*

KINEMATIC CALCULATION OF THE ^{16}O(γ,4α) REACTION†

 Serhii Afanasiev*

National Science Center "Kharkov Institute of Physics and Technology"
1, Akademicheskaya St., 61108, Kharkiv, Ukraine
**Corresponding Author e-mail: afanserg@kipt.kharkov.ua*

The event distribution over the excitation energy of a system of two α-particles (E$_x$) is measured for the reaction ^{16}O(γ,4α). It is found that an intermediate excited ^{8}Be nucleus is formed, and the channels of the ^{8}Be nucleus ground state (GS) formation are extracted. After the separation of the GS ^{8}Be nucleus, a broad maximum with a center at ~ 3 MeV appears in the distribution of E$_x$, which may correspond to the first excited state of the ^{8}Be nucleus. There are two possible channels for the formation of this state in the reaction - $\gamma + {}^{16}$O $\rightarrow \alpha_1 + {}^{12}$C* $\rightarrow \alpha_1 + \alpha_2 + {}^8$Be* $\rightarrow \alpha_1 + \alpha_2 + \alpha_3 + \alpha_4$ and $\gamma + {}^{16}$O $\rightarrow {}^8$Be* $+ {}^8$Be* $\rightarrow (\alpha_1 + \alpha_2) + (\alpha_3 + \alpha_4)$. Each decay mode is reduced to several two-particle systems. For a comprehensive study of the channel for the formation of the first excited state of the ^{8}Be nucleus in the ^{16}O(γ,4α) reaction, a kinematic model for calculating the parameters of α-particles has been developed. The model is based on the assumption of a sequential two-particle decay with the formation of intermediate excited states of ^{8}Be and ^{12}C nuclei. For the kinematic model of the ^{16}O(γ,4α) reaction, a graphical application was created in the Python programming language. The matplotlib library is used for data visualization. To generate random values, a set of functions from the standard random library of the Python programming language is used. Monte Carlo simulations of several distributions for one parameter with a given numerical function were performed. Several excited states of the ^{12}C and ^{8}Be nuclei can contribute to the reaction. The created scheme allows us to choose the relative contribution for each channel of decay, as well as the contribution of a separate level in each channel. To correctly comparison of the experimental data and the results of the kinematic calculation, the α-particles were sorted by energy in such a way that $T^1_{sort} > T^2_{sort} > T^3_{sort} > T^4_{sort}$. As a result of comparing the experimental and calculated data, it was determined that predominantly occurs the process $\gamma + {}^{16}$O $\rightarrow \alpha_1 + {}^{12}$C* $\rightarrow \alpha_1 + \alpha_2 + {}^8$Be* $\rightarrow 4\alpha$ with the formation of the ^{12}C nucleus in states with E$_0$ = 13.3 MeV, E$_0$ = 15.44 MeV, and the 1st excited state of the ^{8}Be nucleus with E$_0$ = 3.04 MeV. The conditions for the identification of α-particles in the experiment for each decay of the stage are determined.

Keywords: *photonuclear reactions; diffusion chamber; the excited states of ^{8}Be and ^{12}C nuclei*

PACS: 25.20.-x

1. INTRODUCTION

The study of photonuclear reactions of total α-decay is of particular interest for studying the properties of virtual α-cluster structures in nuclei [1, 2], their influence on the mechanism of nuclear reactions and on the dynamics of α-synthesis in the Universe [3]. In particular, the study of ^{8}Be, ^{12}C, and ^{16}O nuclei as 2-, 3-, and 4-α-cluster structures, respectively, is important for estimating the abundance of elements in the Universe through the process of stellar nucleosynthesis. The α-shaped cluster is the most probable because it has the highest binding energy and is compact enough to fit into the inter-nucleon distance in the nucleus [4]. In addition, the α-particle is a crucial ingredient in the concept of the Ikeda diagram [5], where highly clustered states are predicted by excitation energies around energy thresholds for decay into specific cluster channels.

In recent years, the interest in understanding the structure of α-cluster nuclei (^{12}C and ^{16}O) has been significantly renewed and numerous theoretical calculations have been performed using various non-relativistic macroscopic and microscopic methods - the antisymmetrized molecular dynamics (AMD) [6], the fermionic molecular dynamics (FMD) [7], the Bose-Einstein condensate cluster model [8], the no-core shell model [9], the algebraic cluster model (ACM) [10] and others. Despite the general agreement on the structure of the ground state of nuclei, there is no consensus on the structure of the excited states of the nucleus. The models do not necessarily contradict each other; it is just that each model is too narrow in scope.

Also, in theoretical calculations, there are differences in the interpretation of the reaction mechanism, taking into account the possible realization of partial channels: 4α, $\alpha + {}^{12}$C*, ^{8}Be*$+ {}^8$Be*.

The experimental study of the ^{16}O(γ,4α) reaction has been repeatedly carried out under irradiation of nuclear photographic plates with both monochromatic γ-quanta from reverse reactions and radioactive sources, and exposed to a beam of bremsstrahlung photons [11-15]. The previously obtained data have low statistics and a significant scatter over the full cross section. In the study of the reaction, the relative contribution of the channels for the formation of intermediate excited states of ^{8}Be nuclei was mainly estimated.

In the present work, we continue [16, 17] the study of the $^{16}O(\gamma,4\alpha)$ reaction. The results given here were obtained by using a diffusion chamber [17] placed in a magnetic field and exposed to a beam of bremsstrahlung photons, their endpoint energy being 150 MeV. Earlier, a narrow near-threshold maximum was found in the excitation energy distribution of the 2α-particle system for all events, which corresponds to the formation of the ground state (GS) of the ^8Be nucleus. In [16], a partial channel for the formation of the ground state was identified and it was determined (distribution by the excitation energy of the 3α-particle system) that an intermediate excited state of the ^{12}C nucleus could be formed in two levels ($E_0 = 7.65$ MeV and 10.3 MeV).

The excitation energy of a system of several α-particles (n) was defined as

$$E_x(n \cdot \alpha) = M^{eff} - (n \cdot m_\alpha - Q_{n\cdot\alpha}) \tag{1}$$

where M^{eff} is their effective mass, m_α is the mass of the α-particle, and $Q_{n\cdot\alpha}$ is the decay threshold. The histograms in Fig.1 shows the distribution of the dependence of events on the excitation energy for: a) two α-particles $E_x(2\alpha)$ and b) three α-particles $E_x(3\alpha)$. In Fig.1 shows the distributions of events without combinations that correspond to the formation of GS [16].

For the four final α-particles, there are 6 combinations of 2α-particle system (one resonant and 5 background) and 4 combinations of 3α-particle system (one resonant and 3 background). From these combinations, for each event, it is impossible to choose in advance a combination that can correspond to the production of excited ^8Be and ^{12}C nuclei. Therefore, the distributions in Fig.1 shows all values of the combinations for each event.
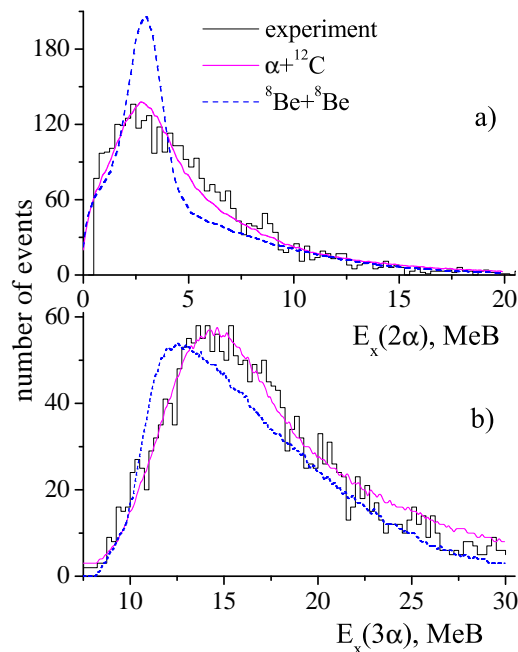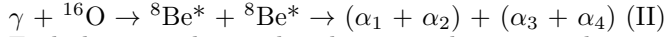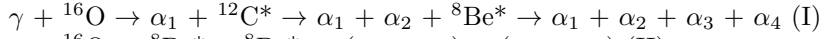

Figure 1. Distribution of events by excitation energy: a) 2α-particles, b) 3α-particles.

It should be noted that in Figs.1a and 1b, no obvious resonance structure is observed and all possible combinations lie in a wide range both in terms of $E_x(2\alpha)$ and $E_x(3\alpha)$.

2. METHOD OF KINEMATIC CALCULATION OF THE $^{16}O(\gamma,4\alpha)$ REACTION

To determine the decay channel and reliably identification of α-particles in the experiment, a program for calculating the kinematic parameters of α-particles was created. Under the assumption of sequential decay with the formation of intermediate excited states, multiple reactions can be represented as a sequence of two-particle acts. In this case, the calculation of the reaction kinematics can be reduced to several tasks of generating particle parameters. In the system of the center of mass of a two-particle reaction, the kinematics is determined by the fact that, regardless of the specific type of interaction, the reaction products scatter at an angle of 180° and have an equal modulus momentum, and their energies depend only on the masses of the particles and the total energy of the system. For the reaction of $^{16}O(\gamma,4\alpha)$, sequential two-particle decay is possible via two channels:

$\gamma + {}^{16}\text{O} \rightarrow \alpha_1 + {}^{12}\text{C*} \rightarrow \alpha_1 + \alpha_2 + {}^{8}\text{Be*} \rightarrow \alpha_1 + \alpha_2 + \alpha_3 + \alpha_4$ (I)

$\gamma + {}^{16}\text{O} \rightarrow {}^{8}\text{Be*} + {}^{8}\text{Be*} \rightarrow (\alpha_1 + \alpha_2) + (\alpha_3 + \alpha_4)$ (II)

Each decay mode is reduced to several two-particle systems:

- $(\gamma + {}^{16}\text{O})$ – the initial,
- $(\alpha_1 + {}^{12}\text{C*})$ or $({}^{8}\text{Be*} + {}^{8}\text{Be*})$ – the first intermediate,
- $(\alpha_2 + {}^{8}\text{Be*})$ – the second intermediate,
- $(\alpha + \alpha)$ – the final.

The mathematical calculation is based on the literature data on the parameters of the levels of ^{12}C and ^{8}Be nuclei and the corresponding assumptions about the angular distributions in the center of mass (c.m.) of the reaction and the particles in a system at rest (s.r.) of the intermediate nucleus.

For the kinematic model of the ^{16}O(γ,4α) reaction, a graphical application was created in the Python programming language on the platform of the Tkinter graphics library.

The matplotlib library is used for data visualization.

To generate random values, a set of functions from the standard random library of the Python programming language is used. Monte Carlo simulations of several distributions for one parameter with a given numerical function were performed.

For the initial system, the distribution of the number of events from the energy of γ-quanta $N(E_\gamma)$ was taken from this experiment, and random values of E_γ were generated by the random.choice() function.

Several excited states of the ^{12}C and ^{8}Be nuclei can contribute to the reaction. The created scheme allows us to choose the relative contribution for each channel (I) or (II), as well as the contribution of a separate level in each channel. For this purpose, the random.randint(0,100) function was used, which creates arbitrary, uncorrelated numbers evenly distributed in the range from 0 to 100.

The excitation curves $f(E_x)$ of the states of the nuclei ^{12}C and ^{8}Be were taken as Gaussian functions with the maximum position E_0 and the half-width at half-height Γ from the compilation of spectroscopic data. Random values were generated by the random.gauss(E_0,Γ) function.

In Fig.1a shows that the events are concentrated at $E_0(2\alpha) \sim 3$ MeV, which coincides with the 1st excited state of the ^{8}Be nucleus ($E_0 = 3.04$ MeV, $\Gamma = 1.5$ MeV [18]). To describe $E_0(3\alpha)$ in Fig.1b, two broad levels of the ^{12}C nucleus with $E_0 = 13.3$ MeV, $\Gamma = 1.7$ MeV and $E_0 = 15.44$ MeV, $\Gamma = 1.77$ MeV were chosen [19]. These levels have spin-parity 4^+ and 2^+ with isotopic spin T = 0, which is important for α-particle decay.

The parameters of the particles at the first intermediate stage were determined. In the non-relativistic approximation, in the case of a two-particle channel, the law of conservation of energy is $E_\gamma = T_{P1} + T_{P2} + E_x + Q$, where T is the kinetic energy of particles P_1 and P_2 ($P_1 = \alpha_1$, $P_2 = {}^{12}$C or $P_1 = {}^{8}$Be, $P_2 = {}^{8}$Be), E_x is the excitation energy of the intermediate particle ($E_x({}^{12}$C) in the case of channel (I) or $E_x = E_x({}^{8}\text{Be}_1) + E_x({}^{8}\text{Be}_2)$ for channel (II)), and Q is the energy threshold of the corresponding channel.

Using a two-particle channel and an unambiguous connection between the particles, we obtain:

$$T_{P1} = \frac{M_{P1}}{M_{P1} + M_{P2}}(E_\gamma - Q - E_x) \qquad (2)$$

The polar (θ) and azimuthal (ϕ) angles were generated and the kinematic parameters P_1 and P_2 in the c.m. were fully determined.

At the second stage, the kinematic parameters of the decaying particles were determined in a similar way, but in the s.r. of the intermediate excited nucleus (^{12}C* $\rightarrow \alpha_2 + {}^{8}$Be* for channel (I) or ${}^{8}\text{Be}_1 \rightarrow \alpha_1 + \alpha_2$ and ${}^{8}\text{Be}_2 \rightarrow \alpha_3 + \alpha_4$ for channel (II)). Using the value of the intermediate excited nucleus in c.m. determined at the first stage of decay, the parameters of decaying particles were also converted to c.m.

If necessary, at the third stage, the kinematic parameters of the final decaying particles were determined in the s.r. of the next intermediate excited nucleus (for channel (I), the final two-particle system ^{8}Be $\rightarrow \alpha_3 + \alpha_4$, which were converted to c.m. using the parameters of the excited nucleus determined at the second decay stage according to the above scheme.

Further, for both channels, the kinematic parameters of α-particles were converted from the c.m. reaction to the laboratory reference frame and the laws of conservation of energy and momentum were checked. An event was considered to be formed if it complied with these conservation laws.

In Figs.1a and b, the solid curve represents the distributions of all combinations of 2α- and 3α-systems for channel (I), and the dashed curve for channel (II). We generated 10^6 events for each of the channels. The results of the kinematic modeling are normalized by the area per experiment. It is clear from the figures that qualitatively the simulation results for channel (I) better describe the experimental data.

3. SORTING α-PARTICLES BY ENERGY. ANGULAR AND ENERGY CORRELATIONS OF $\alpha\alpha$-PARTICLE PAIRS

To correctly comparison of the experimental data and the results of the kinematic calculation, the α-particles were sorted by energy in such a way that $T_{sort}^1 > T_{sort}^2 > T_{sort}^3 > T_{sort}^4$.

Consider the relative contribution of the sorted α-particles to the total reaction energy, which was defined as $T_0 = E_\gamma - Q$, where Q is the energy threshold of the reaction under study. The experimental value of the energy T^{aver} was determined for particles falling into the MeV interval T_0, the points are placed in the middle of the interval. In Fig.2 shows the distribution of T^{aver}: squares for T^1_{sort}, circles for T^2_{sort}, triangles for T^3_{sort}, and stars for T^4_{sort}.

The linear function fit was performed and the coefficients of the relative contribution of particles to the total energy were determined to be 0.409, 0.303, 0.190, and 0.098 for T^1_{sort}, T^2_{sort}, T^3_{sort}, T^4_{sort}, respectively. It should be noted both the linear dependence of the distributions and some consistency (change to ~ 0.1) in these coefficients.

The results of the kinematic calculation with the above sorting procedure are shown in Fig.2 - solid lines for channel (I) and dashed lines for channel (II). The figure shows that qualitatively, for all 4 α-particles, the best agreement is observed in the case of channel (I).
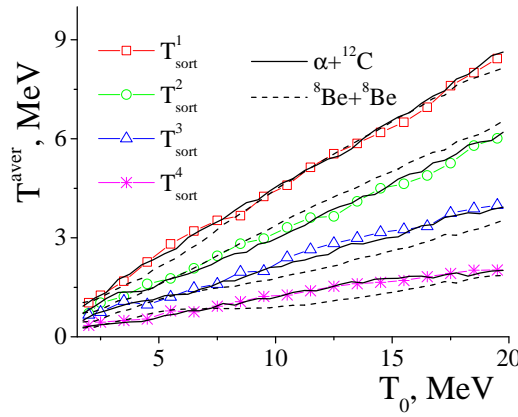

Figure 2. Distribution of events by the average energy of the α-particles. Dots - experimental value, solid lines - channel (I), dashed lines - channel (II).

For a more detailed comparison of the modeling results, a comparison was chosen by the angle of departure and relative energy of the α-particles pair. Two maximum and two minimum pairs were chosen as reference pairs: $(\alpha^1_{sort}, \alpha^2_{sort})$ and $(\alpha^3_{sort}, \alpha^4_{sort})$, which may show different types of dependencies.

The angle of departure of two α-particles (i and j) was defined as

$$\theta_{ij} = \frac{\vec{P}_i \cdot \vec{P}_j}{|P_i| \cdot |P_j|} \tag{3}$$

where $\mathbf{P}$ is the momentum vector of α-particles, and P is their momentum modulus.

The relative energy of a pair of α-particles was determined as

$$\varepsilon_{ij} = \frac{T_i + T_j}{T_0} \tag{4}$$

In Fig.3a, the dots represent the distribution of the dependence of the number of events on the angle of departure of the 2α-particle system $\theta_{\alpha\alpha}$, and Fig.3b - the distribution of events by the relative energy of the 2α-particle system $\varepsilon_{\alpha\alpha}$. Open points are $\alpha^1_{sort}+\alpha^2_{sort}$, closed points are $\alpha^3_{sort}+\alpha^4_{sort}$. The solid lines represent the results of the calculation within the channel (I), and the dashed lines represent the results of the calculation within the channel (II). The modeling results are normalized to the experiment by area.

The general conclusion can be drawn as follows: the distributions within channel (I) are in good agreement with the experimental data, while the distributions within channel (II) for both $\theta_{\alpha\alpha}$ and $\varepsilon_{\alpha\alpha}$ differ in terms of the position of the maxima.

4. IDENTIFICATION OF α-PARTICLES IN THE DECAY CHANNEL OF THE ^{16}O$(\gamma, \alpha)^{12}$C* REACTION

After choosing the most probable decay channel, the main task is to identify α-particles in the experiment, taking into account the fact that a sequential two-particle decay is taking place. It should be noted that this decay leads to a direct relationship of the kinematic parameters in the c.m. reaction. At the first intermediate
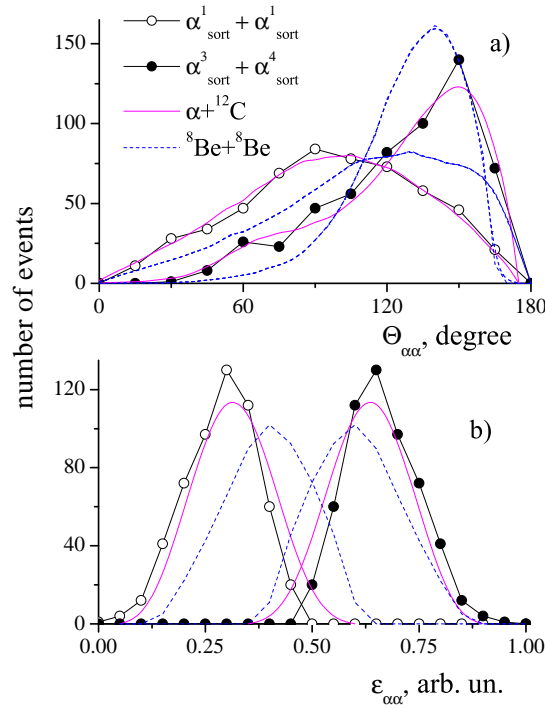
Figure 3. a) distribution of events by the angle of departure of the 2α-particle system, b) distribution of events by the relative energy of the 2α-particle system. Solid lines - channel (I), dashed lines - channel (II).

stage for $T_{\alpha1}$ from Eq.(2):

$$T_{\alpha1} = \frac{M_{12C}}{M_{\alpha} + M_{12C}}(E_{\gamma} - Q_{\alpha12C} - E_x(^{12}C)) \tag{5}$$

There is also a relationship at the second intermediate stage:

$$T_{\alpha2} + T_{8Be} - \frac{M_{\alpha}}{M_{12C}}T_{\alpha1} = E_x(^{12}C)) - E_x(^8Be)) - Q_{\alpha8Be} \tag{6}$$

where M_{12C} – the mass of carbon, and $Q_{\alpha12C} = 7.16$ MeV and $Q_{\alpha8Be} = 7.37$ MeV – the decay thresholds of the $^{16}O \rightarrow \alpha + ^{12}C$ and $^{12}C \rightarrow \alpha + ^8Be$ reactions, respectively. The discrete levels of ^8Be ($E_0 = 3.04$ MeV) and ^{12}C ($E_0 = 13.3$ MeV and $E_0 = 15.44$ MeV) [18, 19] lead to the appearance of some special values of α-particle energy. Thus, at low E_{γ}, one should expect a small $T_{\alpha1}$ (Eq. 5); and with the growth of E_{γ}, there is a significant increase in the value of $T_{\alpha1}$ and, accordingly, a change in the growth rate of $T_{\alpha2}$ (Eq. 6).

In Fig. 4a shows the distribution of the average energy (T^{aver}) of α-particles depending on the total energy T_0 in channel (I) - $\gamma + ^{16}O \rightarrow \alpha_1 + ^{12}C^* \rightarrow \alpha_1 + \alpha_2 + ^8Be^* \rightarrow \alpha_1 + \alpha_2 + \alpha_3 + \alpha_4$. In this figure, unlike to Fig.2, the numbering of α-particles corresponds to their sequence of formation. The distribution is shown for: $T_{\alpha1}$ - squares, $T_{\alpha2}$ - circles, $T_{\alpha3}$ - triangles, $T_{\alpha4}$ - stars.

The average energy distributions of α-particles can be divided into three intervals: $T_0 < 7$ MeV, $T_0 = 7$–11 MeV, and $T_0 > 11$ MeV. And while there is a certain regularity in the behavior of the distributions in the first and third intervals, the second interval is characterized by a sharp increase in the relative contribution coefficient of $T_{\alpha1}$. The behavior of α_2-, α_3-, α_4-particles is due to the fact that they are formed in the process of decay of discrete levels of ^{12}C and ^8Be nuclei. Therefore, their dependence has a low growth rate.

At the first stage of the identification, the conditions for the identification of two α-particles (α_3, α_4) forming the ^8Be nucleus in the 1st excited state with $E_0 = 3.04$ MeV were chosen.

All α-particles are reliably identified at $T_0 < 7$ MeV: - the α_1-particle has the minimum energy, while the α_3, α_4-particles have the maximum energy (their distributions are close in value).

Furthermore, the figure shows that at $T_0 > 11$ MeV, all α-particles are also reliably identified: the α_1-particle already has the maximum energy, while α_3-, α_4-particles have the minimum energy.

In the range of 7-11 MeV, the α_2-particle has the maximum energy. In the narrow interval (9-11 MeV), when E_{γ} - $Q_{\alpha12C} > E_x(^{12}C)$ (Eq. (5)), the relative contribution of the α_1-particle increases rapidly and all
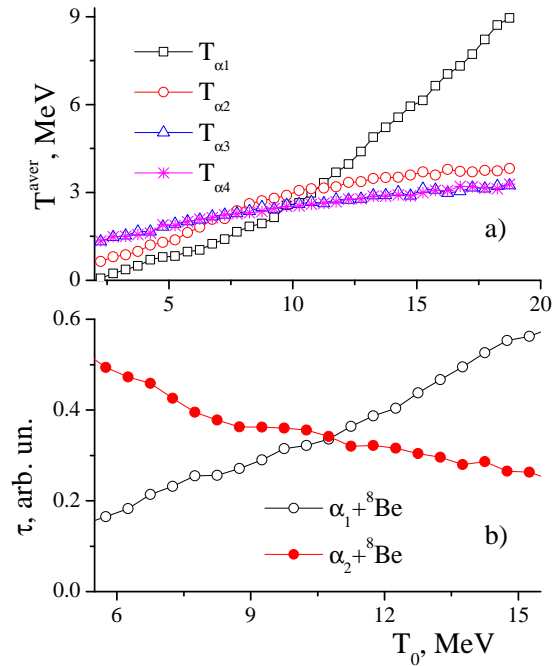
Figure 4. a) distribution of events by the average energy of α-particles in the channel $\alpha + {}^{12}$C*, b) distribution of the relative magnitude of τ from the total energy T_0.

α-particles account for the same contribution of total energy. It was assumed that a pair of α-particles (α_3, α_4) is the pair with an excitation energy closer to $E_0({}^8\text{Be}) = 3.04$ MeV. Statistically, less than 7% of all events are in this range.

Thus, at the first stage of identification, two α-particles corresponding to the formation of the ^{8}Be nucleus were identified with high confidence.

At the second stage, the angle of departure in the $\alpha_1 + \alpha_2 + {}^8$Be system ($\theta_{ij}$) was used to correctly identify α_1- and α_2-particles. At low energies ($T_0 < 11$ MeV), the $\alpha_2 + {}^8$Be the angle of departure should be larger (since the two-particle decay ^{12}C* $\rightarrow \alpha_2 + {}^8$Be occurs) and, obviously, larger than the $\alpha_1 + {}^8$Be scattering angle, which is close to the phase distribution. At high energies ($T_0 > 11$ MeV), due to the high energy of $T_{\alpha 1}$ and to fulfill the laws of conservation of energy and momentum, the angle of departure of $\alpha_1 + {}^8$Be is already larger than the angle of departure of $\alpha_2 + {}^8$Be.

In Fig. 4b shows the distribution by the relative value of $\tau = \varepsilon_{ij} \cdot \theta_{ij}/180°$, where ε_{ij} and θ_{ij} were determined by (Eq. 3) and (Eq. 4), respectively. For the correctness of comparison, the angle of departure was normalized to 180°. Open circles are for the pair $\alpha_1 + {}^8$Be, closed circles are for the pair $\alpha_2 + {}^8$Be. As expected, the distributions have different angles of change and, therefore, the α_1- and α_2-particles can be separated in different T_0 intervals: at $T_0 < 10.5$ MeV - $\tau(\alpha_1 + {}^8\text{Be}) > \tau(\alpha_1 + {}^8\text{Be})$, and conversely at $T_0 > 10.5$ MeV.

Thus, conditions were obtained under which experimental α-particles can be identified with high confidence in the decay channel $\alpha_1 + {}^{12}$C* $\rightarrow \alpha_1 + \alpha_2 + {}^8$Be* $\rightarrow \alpha_1 + \alpha_2 + \alpha_3 + \alpha_4$.

In Fig. 5 shows the experimental [16, 17] distribution of events by excitation energy: a) 2α-particles, b) 3α-particles. The distributions were obtained using the set of conditions defined above for the identification of α-particles. Compared to Fig.1, only resonant combinations are shown.

The fitting with Gaussian functions was performed and the positions of the maxima and their widths were determined: $E_0(2\alpha) = 3.06 \pm 0.22$ MeV, $\Gamma = 1.95 \pm 0.14$ MeV (Fig. 5a); $E_0{}^1(3\alpha) = 13.13 \pm 0.26$ MeV, $\Gamma^1 = 1.64 \pm 0.31$ MeV and $E_0{}^2(3\alpha) = 15.56 \pm 0.27$ MeV, $\Gamma^2 = 1.86 \pm 0.33$ MeV (Fig. 5b), which are consistent with the data of spectroscopic studies [18, 19] within the error.

5. CONCLUSION

In the ^{16}O(γ,4α) reaction, a detailed study of the formation of final particles has been performed. For the events, after the channel for the formation of the ground state of the ^{8}Be nucleus has been isolated, distributions

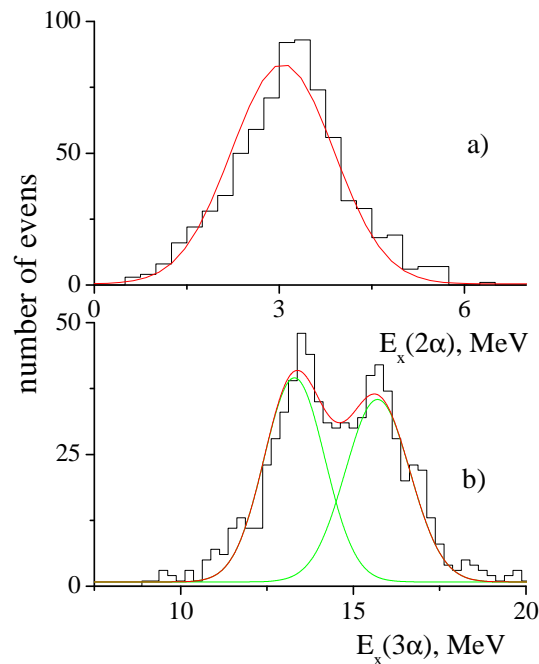**Figure 5.** Distribution of events by excitation energy: a) 2α-particles, b) 3α-particles. The decay channel $\gamma + {}^{16}\mathrm{O} \to \alpha_1 + {}^{12}\mathrm{C}^* \to \alpha_1 + \alpha_2 + {}^8\mathrm{Be}^* \to \alpha_1 + \alpha_2 + \alpha_3 + \alpha_4$.

of 2 and 3 combinations of α-particles have been constructed. Due to the inseparability of α-particles, it is difficult to separate the resonant combination from the background ones.

To determine the most probable decay channel and identify the particles at each stage of decay, a kinematic model of the $^{16}\mathrm{O}(\gamma,4\alpha)$ reaction was created assuming a sequential two-particle process with the formation of intermediate excited states of $^8\mathrm{Be}$ and $^{12}\mathrm{C}$ nuclei. To compare the experimental data and modeling results, α-particles were sorted by energy $\mathrm{T}^1_{sort} > \mathrm{T}^2_{sort} > \mathrm{T}^3_{sort} > \mathrm{T}^4_{sort}$ in both data sets (experimental and calculated).

It was determined that the experimental data can be mainly described within the process $\gamma + {}^{16}\mathrm{O} \to \alpha_1 + {}^{12}\mathrm{C}^* \to \alpha_1 + \alpha_2 + {}^8\mathrm{Be}^* \to \alpha_1 + \alpha_2 + \alpha_3 + \alpha_4$ with the formation of the $^{12}\mathrm{C}$ nucleus in states with $\mathrm{E}_0 = 13.3$ MeV, $\mathrm{E}_0 = 15.44$ MeV, and the 1st excited state of the $^8\mathrm{Be}$ nucleus with $\mathrm{E}_0 = 3.04$ MeV.

The identification of α-particles corresponding to each stage of the chosen decay process was performed.

ORCID

Serhii Afanasiev, https://orcid.org/0000-0003-1682-4621

REFERENCES

[1] Y. Kanada-En'yo, Prog. Theor. Phys. **117**, 947 (2001), https://doi.org/10.1143/PTP.117.655.

[2] S.A. Sofianos, R.M. Adam, and V.B. Belyaev, Phys. Rev. C, **84**, 064304 (2011), https://doi.org/10.1103/PhysRevC.84.064304. (in Ukrainian)

[3] V. Liccardo, M. Malheiro, M.S. Hussein, B.V. Carlson, and T. Frederico, Eur. Phys. J. A, **54**, 221 (2018), https://doi.org/10.1140/epja/i2018-12648-5

[4] D. Brink, J.J. Castro, Nucl. Phys. A, **216**, 109 (1973), https://doi.org/10.1016/0375-9474(73)90521-6

[5] K. Ikeda, H. Horiuchi, and S. Saito, Prog. Theor. Phys. Suppl. **68**, 1 (1980), https://doi.org/10.1143/PTPS.68.1

[6] Y. Funaki, T. Yamada, H. Horiuchi, G. Röpke, P. Schuck, and A. Tohsaki, Phys. Rev. Lett. **101**(8), 082502 (2008), https://doi.org/10.1103/PhysRevLett.101.082502

[7] M. Chernykh, H. Feldmeier, H. Neff, P. von Neumann-Cosel, and A. Richter, Phys. Rev. Lett. **98**, 032501 (2007), https://doi.org/10.1103/PhysRevLett.98.032501

[8] Y. Funaki, H. Horiuchi, W. Von Oertzen, G. Röpke, P. Schuck, A. Tohsaki, and T. Yamada, Phys. Rev. C, **80**, 064326 (2009), https://doi.org/10.1103/PhysRevC.80.064326

[9] R. Roth, J. Langhammer, A. Calci, S. Binder, and P. Navrátil, Phys. Rev. Lett. **107**, 072501 (2011), https://doi.org/10.1103/PhysRevLett.107.072501

[10] R. Bijker and F. Iachello, Phys. Rev. Lett. **112**, 152501 (2014), https://doi.org/10.1103/PhysRevLett.112.152501

[11] F.K. Goward and J.J. Wilkins, Proc. Phys. Soc. A, **65**, 671 (1952), 10.1088/0370-1298/65/8/114

[12] C.H. Millar, Can. J. Phys. **31**, 723 (1953), https://doi.org/10.1139/p53-068

[13] J.P. Roalsvig, Can. J. Phys. **43**, 330 (1965), https://doi.org/10.1139/p65-030

[14] M. Elaine Toms, Nucl. Phys. **54**, 625 (1964), https://doi.org/10.1016/0029-5582(64)90439-0

[15] R.A. Golubev and V.V. Kirichenko, Nucl. Phys. A, **587**, 241 (1995), https://doi.org/10.1016/0375-9474(94)00789-P

[16] Sergey Afanas'ev, The Journal of Kharkiv National University, Physical series "Nucleus, Particles, Fields", **1025**(4), 4 (2012), https://periodicals.karazin.ua/eejp/article/view/13573

[17] S.N. Afanasyev, Ukr. J. Phys. **64**, 787 (2019), https://doi.org/10.15407/ujpe64.9.787

[18] D.R. Tilley, J.H. Kelley, J.L. Godwin, D.J. Millener, J.E. Purcell, C.G. Sheu, and H.R. Weller, Nucl. Phys. A, **745**, 155 (2004), https://doi.org/10.1016/j.nuclphysa.2004.09.059

[19] F. Ajzenberg-Selove, Nucl. Phys. A, **506**, 1 (1990), https://doi.org/10.1016/0375-9474(90)90271-M

КІНЕМАТИЧНИЙ РОЗРАХУНОК РЕАКЦІЇ ^{16}O(γ,4α)
Сергій Афанасьєв

Національний Науковий Центр "Харківський Фізико-Технічний Інститут",
вул. Академічна, 1, Харків, 61108, Україна

В реакції ^{16}O(γ,4α) виміряно розподіл подій за енергією збудження (E$_x$) системи двох α-частинок. Визначено, що утворюється проміжне збуджене ядро ^{8}Be, виділено канал утворення основного стану (ОС) ядра ^{8}Be. Після виділення ОС ядра ^{8}Be у розподілі за E$_x$ проявляється широкий максимум з центром при $\sim$ 3 МеВ, що може відповідати першому збудженому стану ядра ^{8}Be. В реакції можливо два каналу утворення цього стану - γ + ^{16}O $\rightarrow \alpha_1$ + ^{12}C* $\rightarrow \alpha_1$ + α_2 + ^{8}Be* $\rightarrow \alpha_1$ + α_2 + α_3 + α_4 і γ + ^{16}O $\rightarrow$ ^{8}Be* + ^{8}Be* $\rightarrow (\alpha_1 + \alpha_2) + (\alpha_3 + \alpha_4)$. Кожна мода розпаду зводиться до кількох двочастинкових систем. Для комплексного дослідження каналу утворення першого збудженого стану ядра ^{8}Be в реакції ^{16}O(γ,4α) розроблено кінематичну модель розрахунку параметрів α-частинок. Модель створено в припущенні послідовного двочастинкового розпаду ядра ^{16}O з утворенням проміжних збуджених станів ядер ^{8}Be і ^{12}C. Для кінематичної моделі реакції ^{16}O(γ,4α) створено графічне застосування мовою програмування Python. Для візуалізації даних використовується бібліотека matplotlib. Для генерації випадкових значень використовується набір функцій стандартної бібліотеки random мови програмування Python. Проводилося моделювання методом Монте-Карло кількох розподілів за одним параметром із заданою чисельною функцією. У реакції можливий вклад декількох збуджених станів ядер ^{12}C і ^{8}Be. Створена схема, що дозволяє вибирати відносний вклад як для кожного каналу розпада, так і вклад окремого рівня в кожному каналі. Для коректного порівняння експериментальних даних і результатів кінематичного розрахунку було виконано сортування α-частинок за енергією таким чином, що T$^1_{sort}$ > T$^2_{sort}$ > T$^3_{sort}$ > T$^4_{sort}$. У результаті порівняння експериментальних і розрахункових даних визначено, що переважно йде процес γ + ^{16}O $\rightarrow \alpha_1$ + ^{12}C* $\rightarrow \alpha_1$ + α_2 + ^{8}Be* $\rightarrow 4\alpha$ з утворенням ядра ^{12}C у станах з E$_0$ = 13.3 МеВ, E$_0$ = 15.44 МеВ та першого збудженого стану ядра ^{8}Be з E$_0$ = 3.04 МеВ. Визначено умови для ідентифікації α-частинок в експерименті на відповідність кожному етапу розпаду.

Ключові слова: *фотоядерні реакції; дифузійна камера; збуджені стани ядер ^{8}Be і ^{12}C*

ESTIMATION OF NUCLEAR MASS FORMULAS COEFFICIENTS USING LEAST-SQUARES METHOD BASED ON GAUSS-SEIDEL SCHEME: A COMPARATIVE STUDY BETWEEN THREE MODELS

 Hadj Mouloudj[a,b*], **Benyoucef Mohammed-Azizi**[a,c], **Oussama Zeggai**[d,e], **Abdelkader Ghalem**[b,f], **Alla Eddine Toubal Maamar**[g]

[a] *Laboratoire de Physique des Particules et Physique Statistique, Ecole Normale Supèrieure-Kouba, B.P. 92, Vieux-Kouba 16050, Algiers, Algeria*
[b] *Department of Physics, Faculty of Exact Sciences and Informatics, Hassiba Benbouali University, Chlef, Algeria*
[c] *University of Bechar, Bechar 08000, Algeria*
[d] *Department of Common Core, Faculty of Exact Sciences and Informatics, Hassiba Benbouali University, Chlef, Algeria*
[e] *Research Unit of Materials and Renewable Energies (URMER), Abou Bekr Belkaïd University, Tlemcen 13000, Algeria*
[f] *Mechanics and Energetics Laboratory, Chlef 02100, Algeria*
[g] *Department of Electrical Systems Engineering, Faculty of Technology, University of M'hamed Bougara of Boumerdes, Boumerdes 35000, Algeria*
Corresponding Author e-mail: h.mouloudj@univ-chlef.dz

This paper presents the analysis and implementation of the least-squares method based on the Gauss-Seidel scheme for solving nuclear mass formulas. The least-squares method leads to the solution of the system by iterations. The main advantages of the discussed method are simplicity and high accuracy. Moreover, the method enables us to process large data quickly in practice. To demonstrate the effectiveness of the method, implementation using the FORTRAN language is carried out. The steps of the algorithm are detailed. Using 2331 nuclear masses with $Z \geq 8$ and $N \geq 8$, it was shown that the performance of the liquid drop mass formula with six parameters improved in terms of root mean square (r.m.s. deviation equals 1.28 MeV), compared to the formula of liquid drop mass with six parameters without microscopic energy, deformation energy and congruence energy (r.m.s. deviation equals 2.65 MeV). The nuclear liquid drop model is revisited to make explicit the role of the microscopic corrections (shell and pairing). Deformation energy and the congruence energy estimate have been used to obtain the best fit. It is shown that the performance of the new approach is improved by a model of eight parameters, compared to the previous model of six parameters. The obtained r.m.s. result for the new liquid drop model in terms of masses is equal to 1.05 MeV.

Keywords: *Nuclear masses; Numerical methods; Binding energy; Shell correction; Pairing correction*

PACS: 02.60.-x, 02.60.Cb, 02.60.Ed, 21.10.Dr, 21.60.-n, 31.15.Ct

1. INTRODUCTION

The determination of nuclear masses is one of the most crucial tools for accessing the binding energy within the nucleus, and therefore the total of all forces affecting the interior of the nucleus. Experimentally, there are a number of techniques for measuring masses in the fundamental as well as the excited state. When discussing the mass models, we're interested exclusively in theoretical models intended to calculate the nuclear masses of all bonded nuclei. At different levels, these models require experimental values for their calculations. The purpose of these models is to predict all quantities related to the nucleus: mass, binding energy or deformation energy, separation energy....etc. The three most common categories of existing models are: semi-empirical, macroscopic-microscopic and microscopic, plus two models of a different type [1]. These models have a property that applies to all nuclei globally with Z, $N \geq 8$. Among the models there are: SEMF: The Semi-Empirical Mass Formula and the LDM: Liquid-Drop Model. The macroscopic-microscopic models include the MS-LD: Myers and Świątecki model [2], a Strutinsky-type approach [3], the FRDM: Finite-Range Droplet Model, the FRLDM: Möller's Finite-Range Liquid-Drop Model [4], the TF: Thomas-Fermi nuclear model [5] or the ETFSI: Extended Thomas-Fermi plus Strutinsky Integral [6], and the LSDM: Lublin-Strasbourg Drop Model [7]. The models that are only microscopic are: Hartree-Fock-Bogoliubov (HFB21) approach [8], that employs Skyrme interactions, and the HFB strategy, utilizing the advantage of Gogny forces (GHFB) [9]. With the existence of two other models proving its effectiveness in nuclear mass calculations: the model of DZ: Duflo and Zuker [10] and that of KTUY: Koura et al. [11].

In nuclear physics, the first SEMF, known as the Weizsäcker formula or the Bethe-Weizsäcker formula [12], is used to estimate atomic mass in relation to mass number A and atomic number Z. The SEMF was proposed

by Carl Friedrich Von Weizsäcker, in 1935 [13], [14], where the nucleus is seen as a liquid droplet containing protons and neutrons moving in a disorderly fashion. SEMF's reference formula for all macroscopic approaches has been able to retrieve a large number of nucleus properties such as nuclear masses, binding energies, separation energies, nuclear fission, although it does not provide for magic numbers. Next, a significant improvement in the LDM liquid droplet model was made after the incorporation of phenomenological microscopic corrections to the macroscopic terms. In fact, Myers and Świątecki took (made) the first step in this approach in 1966, who added layer correction and pairing corrections to the binding energy of the liquid drop [2]. This new microscopic-macroscopic model was very successful in reproducing nuclear data (masses, quadrupole moments, heights of fission barriers, ...etc.), when the layer corrections were more precisely evaluated using a method proposed by Strutinsky [15], [16], and the matching correction obtained in the Bardeen-Cooper-Schrieffer (BCS) approximation [2], [17], this introduced a simple algebraic layer correction, plus an attribution to a "clustering" effect of the novel equidistant distribution of individual particle levels, subsequently generating a series of gap band intervals at the observed magic numbers. In addition to this microscopic addition, Myers-Świątecki's final mass formula featured an empirical odd-even correction (pairing coefficient), and diverged from spherical symmetry through the incorporation of a shape dependence into the surface and Coulomb terms of Von Weizsäcker's semi-empirical equation.

Later, Strutinsky's theorem [3] appeared, that can be seen as an approximation of the Hartree-Fock (HF) approach [18], which offers an even more stringent microscopic formulation of Strutinsky's layer correction method [19]. Total binding energy is now decomposed into a macroscopic term and a microscopic term (denoting the layer and the pairing corrections), both of which are a function not only of A and Z, it also depends on a set of deformation parameters β, featuring the shape of the core. The significance of these upgrades was astonishing since the squared deviation (r.m.s) between theory and experiment decreased [20].

Recently years, a significant number of studies have been published on the subject of nuclear masses such as the published papers [21]–[27]. Interestingly, to date no researcher has discussed the proposed LDM formula of eight parameters with making a comparison between three models. Hence this work aim to presents the LDM formula of six parameters, the LDM formula of six parameters without (microscopic energy, deformation energy, and congruence energy), and the proposed LDM formula of eight parameters. The idea is based on adding two coefficients to the six-parameter LDM formula, which are the shell correction coefficient and the pairing correction coefficient. Correction coefficients are added to improve the root mean square value. Then, the Least Squares Method (LSM) is implemented to determine the parameters of the theoretical formulas. LSM is one of the widely employed methods for data fitting [24], where the method for different experimental cases is detailed in [28]. Two categories of least-squares problems can be distinguished: linear and non-linear, based on whether all unknown residuals are linear or non-linear. In statistical regression analysis, the linear least-squares problem has a closed-form solution.

The non-linear problem is generally solved by iterative refinement, where each iteration approximating the system by a linear system, so the basic calculation is similar in both cases [29]. This work is very significant considering the following merits: (1) an improved LDM formula of eight parameters is proposed. (2) A comparison between three liquid-drop models and comparison with other previous works are discussed. (3) A step-by-step tutorial for determining the parameters of nuclear masses formulas is presented using the least squares method. This paper will add to the information contained in the previous studies and give a new perspective about the application of the LSM with improved nuclear masses formulas.

This paper is divided into five sections, the second of which describes the implemented three liquid drop mass formulas. Next, principle of the least squares method is presented. In the fourth section, the theoretical and experimental results are shown and compared. Finally, the fifth section provides the conclusions of the study.

2. DESCRIPTION OF THE LIQUID DROP MASS MODELS

In this section, three LDM models are detailed; the six parameters LDM formula, the six parameters LDM formula without (microscopic energy, deformation energy, and congruence energy), and the proposed eight parameters LDM formula.

2.1. The six parameters liquid drop mass formula

In nuclear physics, the liquid drop mass formula is well known. LDM sometimes called the Liquid Drop Model, or Myers-Świątecki Liquid Drop (MS-LD) formula, it was developed by Von Weizsäcker [12], [30]. In accordance with the usual rules of the liquid drop model approaches, the mass of an atom with Z protons and N neutrons is described by the following relation [2], [5].

$$
\begin{aligned}
M_{theo}(Z, N, def) \;=\; & ZM_H + NM_n - 0.00001433Z^{2.39} \\
& + b_{vol}\left(1 - k_{vol}I^2\right)A \\
& + b_{surf}\left(1 - k_{surf}I^2\right)A^{2/3} \\
& + b_{coul}\,Z^2/A^{1/3} \;-\; f_p Z^2/A \\
& + E_{shell}(Z, N) + E_{pair}(Z, N) + E_{def}(Z, N) + E_{cong}(Z, N)
\end{aligned}
\tag{1}
$$

Where:

A, Z and N: are the numbers of atoms, protons and neutrons, respectively (A = Z + N).

M_H is the hydrogen-atom mass excess, $M_H = 7.288970613$ MeV

M_n is the neutron mass excess, $M_n = 8.071317133$ MeV.

$Z^{2.39}$: is the binding energy of electrons.

$b_{vol}(1 - k_{vol}I^2)A$: is the volume energy term.

$b_{surf}(1 - k_{surf}I^2)A^{2/3}$: is the surface energy term.

$b_{coul}(Z^2/A^{1/3})$: is the Coulomb energy term.

$f_p(Z^2/A)$: is the Proton form-factor correction to the Coulomb energy term.

b_{coul}, R_0, e^2: are quantities defined by:

$$
b_{coul} = \frac{3}{5}\frac{e^2}{R_0}
\tag{2}
$$

R_0: is the nuclear-radius constant, its value $R_0 = 1.16$ fm.

e^2: electronic charge squared, its value $e^2 = 1.4399764$ MeV.fm.

I: is the relative neutron excess, defined by:

$$
I = \frac{N - Z}{N + Z}
\tag{3}
$$

$E_{def}(Z, N)$: is the deformation energy, the difference between a nucleus's macroscopic energy at equilibrium deformation and its energy if it were spherical [7]. The deformation energy is given by:

$$
E_{def}(Z, N) = E(\beta) - E(\beta = 0)
\tag{4}
$$

β: is a set of parameters defining the deformation of the nucleus, $\beta = 0$ representing the spherical deformation (undeformed nucleus).

$E_{cong}(Z, N)$: is the congruence energy is described as:

$$
E_{cong}(Z, N) = -10\exp\left(-4.2\,|I|\right)
\tag{5}
$$

$E_{shell}(Z, N)$, and $E_{pair}(Z, N)$: are the corrections of shell and pairing, respectively.

The microscopic energy is given by:

$$
E_{micro}(Z, N) = E_{shell}(Z, N) + E_{pair}(Z, N)
\tag{6}
$$

E_{micro} containing the contributions from shell and paring effects coming from the protons and neutrons. For simplifying the calculation, we put:

$$
\begin{aligned}
U(Z, N, def) \;=\; & E_{shell}(Z, N) + E_{pair}(Z, N) + E_{def}(Z, N) + E_{cong}(Z, N) \\
& + ZM_H + NM_n - 0.00001433\,Z^{2.39}
\end{aligned}
\tag{7}
$$

So, the model of the standard liquid drop can be expressed as follows:

$$
\begin{aligned}
M_{theo}(Z, N, def) \;=\; & b_{vol}\left(1 - k_{vol}I^2\right)A \\
& + b_{surf}\left(1 - k_{surf}I^2\right)A^{2/3} \\
& + b_{coul}\,Z^2/A^{1/3} - f_p Z^2/A \\
& + U(Z, N, def)
\end{aligned}
\tag{8}
$$

In literature, the least squares method is one of the best methods for solving the liquid drop model Eq. (1) in order to find the six parameters (b_{vol}, k_{vol}, b_{surf}, k_{surf}, b_{coul}, f_p), the steps of the method are illustrated in the next section, and results are discussed in the 4th section.

2.2. The six parameters liquid drop mass formula without (microscopic energy, deformation energy, and congruence energy)

In this part, we eliminate microscopic energy (the corrections of shell and pairing), deformation energy, and congruence energy to observe their impact on the root-mean-square value. So, the new liquid drop model can be expressed as follows:

$$
\begin{aligned}
M_{theo}(Z, N, def) \quad = \quad & ZM_H + NM_n - 0.00001433 Z^{2.39} \\
& + b_{vol} \left(1 - k_{vol} I^2\right) A \\
& + b_{surf} \left(1 - k_{surf} I^2\right) A^{2/3} \\
& + b_{coul} Z^2/A^{1/3} \; - \; f_p Z^2/A
\end{aligned}
\tag{9}
$$

In order to find the six parameters (b_{vol}, k_{vol}, b_{surf}, k_{surf}, b_{coul}, f_p), the Least Squares Method (LSM) is used. The steps of the method are illustrated in the next section, and results are discussed in the 4th section.

2.3. The proposed eight parameters liquid drop mass formula

In this part, we add two coefficients to the previous equation Eq.1, which are the shell correction coefficient b_{sh} and the pairing correction coefficient b_{pa}. The microscopic corrections for pairing and shell effects treated as in Ref. [23]. Correction coefficients are added to improve the root mean square value. So, the new liquid drop model is described by the following relation:

$$
\begin{aligned}
M_{theo}(Z, N, def) \quad = \quad & ZM_H + NM_n - 0.00001433 Z^{2.39} \\
& + b_{vol} \left(1 - k_{vol} I^2\right) A \\
& + b_{surf} \left(1 - k_{surf} I^2\right) A^{2/3} \\
& + b_{coul} Z^2/A^{1/3} \; - \; f_p Z^2/A \\
& + b_{sh} E_{shell}(Z, N) + b_{pa} E_{pair}(Z, N) + E_{def}(Z, N) + E_{cong}(Z, N)
\end{aligned}
\tag{10}
$$

The Least Squares Method (LSM) is used to find the eight parameters (b_{vol}, k_{vol}, b_{surf}, k_{surf}, b_{coul}, f_p, b_{sh}, b_{pa}). The steps of the method are illustrated in the next section, and results are discussed in the 4th section.

3. THE LEAST SQUARES METHOD

The Least Squares Method is traditionally credited to Carl Friedrich Gauss, with origins dating back to 1795 [31], [32]. LSM finds utility across a range of scientific disciplines including statistics, geodesy, economics, optimization and more. The current study suggests utilizing LSM for optimizing the semi-empirical mass formula, or formulas with similar characteristics. Examples of models in this category include: (a) The FRDM and the FRLDM, which involve comprehensive calculations of shell and pairing corrections, along with consideration of various nuclear deformations [33], (b) The "Pomorski-Dudek Model" with shell and pairing corrections [7], (c) The "Royer Model" with shell and pairing corrections but no nuclear deformation [34], and (d) The "Myers Droplet Model based on the Thomas-Fermi Approximation" with or without shell correction [35]. These nuclear mass formulas play a vital role in assessing certain ground-state properties, nuclear reactions, and predicting the neutron/proton drip lines. All these formulas can be optimized using the same method, which is described by the following procedure.

A) **Define the root mean square deviation (R.M.S).**

The root mean square deviation (R.M.S) is defined by:

$$
R.M.S = err(b_{vol}, k_{vol}, b_{surf}, k_{surf}, b_{coul}, f_p) = \frac{1}{n} \sum_{i=1}^{i_{\max}} \left[M_{\exp}(i) - M_{theo}(i)\right]^2
\tag{11}
$$

where:

n: is the total number of nuclides.

$M_{theo}(i)$: are the mass computed at a specific value of Z and N.

$M_{exp}(i)$: are experimental values of nuclear mass that calculated using the mass excess values found in on the recent updated Atomic Mass Evaluation, i.e. AME table, published in [36]. $M_{exp}(i)$ are given with MeV by the following formula:

$$
M_{\exp}(i) = Mass\, excess + A \,.\, u
\tag{12}
$$

u: The atomic mass unit, $1u = 931.49410242$ MeV.

B) **Replacing the $M_{theo}(i)$ by its expression in the RMS deviation formula.**

In this step, we calculate $M_{theo}(i)$ by the given Eq.8, and replace results in Eq. 11. So, the root mean square deviation is described by:

$$R.M.S = \frac{1}{n} \sum_{i=1}^{i_{\max}} \begin{pmatrix} M_{\exp}(i) - b_{vol}\left(1 - k_{vol}I_i^2\right)A_i - b_{surf}\left(1 - k_{surf}I_i^2\right)A_i^{2/3} - \\ b_{coul}Z_i^2/A_i^{1/3} \quad + f_p Z_i^2/A_i \quad - U_i\left(Z_i, N_i, def\right) \end{pmatrix}^2 \tag{13}$$

C) **Define the objective.**

According to LSM, the goal is to reduce the error in Eq. 11 to a minimum, thus:

$$\frac{\partial err\left(b_{vol}, k_{vol}, b_{surf}, k_{surf}, b_{coul}, f_p\right)}{\partial\chi\big|_{\chi = b_{vol},\, \cdots\, , f_p}} = 0 \tag{14}$$

D) **Construction of the model.**

The equations of model are given by:

$$\begin{cases} \frac{\partial err}{\partial b_{vol}} & = & -2\sum_{i=1}^{i_{\max}}\left(M_{\exp}(i) - M_{theo}(i)\right)\frac{\partial M_{theo}(i)}{\partial b_{vol}} & = 0 \\[2mm] \frac{\partial err}{\partial k_{vol}} & = & -2\sum_{i=1}^{i_{\max}}\left(M_{\exp}(i) - M_{theo}(i)\right)\frac{\partial M_{theo}(i)}{\partial k_{vol}} & = 0 \\[2mm] \frac{\partial err}{\partial b_{surf}} & = & -2\sum_{i=1}^{i_{\max}}\left(M_{\exp}(i) - M_{theo}(i)\right)\frac{\partial M_{theo}(i)}{\partial b_{surf}} & = 0 \\[2mm] \frac{\partial err}{\partial k_{surf}} & = & -2\sum_{i=1}^{i_{\max}}\left(M_{\exp}(i) - M_{theo}(i)\right)\frac{\partial M_{theo}(i)}{\partial k_{surf}} & = 0 \\[2mm] \frac{\partial err}{\partial b_{coul}} & = & -2\sum_{i=1}^{i_{\max}}\left(M_{\exp}(i) - M_{theo}(i)\right)\frac{\partial M_{theo}(i)}{\partial b_{coul}} & = 0 \\[2mm] \frac{\partial err}{\partial f_p} & = & -2\sum_{i=1}^{i_{\max}}\left(M_{\exp}(i) - M_{theo}(i)\right)\frac{\partial M_{theo}(i)}{\partial f_p} & = 0 \end{cases} \tag{15}$$

Where:

$$\begin{cases} \frac{\partial M_{\text{theo}}(i)}{\partial b_{\text{vol}}} = \sum_{i=1}^{i_{\max}}\left(A_i\left(1 - k_{\text{vol}}I_i^2\right)\right) \\[2mm] \frac{\partial M_{\text{theo}}(i)}{\partial k_{\text{vol}}} = -\sum_{i=1}^{i_{\max}}\left(b_{\text{vol}}A_i I_i^2\right) \\[2mm] \frac{\partial M_{\text{theo}}(i)}{\partial b_{\text{surf}}} = \sum_{i=1}^{i_{\max}}\left(A_i^{2/3}\left(1 - k_{\text{surf}}I_i^2\right)\right) \\[2mm] \frac{\partial M_{\text{theo}}(i)}{\partial k_{\text{surf}}} = -\sum_{i=1}^{i_{\max}}\left(b_{\text{surf}}A_i^{2/3}I_i^2\right) \\[2mm] \frac{\partial M_{\text{theo}}(i)}{\partial b_{\text{coul}}} = \sum_{i=1}^{i_{\max}}\left(Z_i^2/A_i^{1/3}\right) \\[2mm] \frac{\partial M_{\text{theo}}(i)}{\partial f_p} = -\sum_{i=1}^{i_{\max}}\left(Z_i^2/A_i\right) \end{cases} \tag{16}$$

E) **Solve the equations of model.**

Solutions of the model given by Eq. (15) are determined as follow:

$$b_{\text{vol}} = \cfrac{\begin{pmatrix} \sum_i A_i M_{\exp}(i) - b_{\text{surf}}\sum_i A_i^{5/3} + k_{\text{surf}}b_{\text{surf}}\sum_i A_i^{5/3}I_i^2 - \\ b_{\text{coul}}\sum_i A_i^{2/3}Z_i^2 + f_p\sum_i Z_i^2 - \sum_i A_i U_i - k_{\text{vol}}\sum_i A_i I_i^2 M_{\exp}(i) + \\ k_{\text{vol}}b_{\text{surf}}\sum_i A_i^{5/3}I_i^2 - k_{\text{vol}}k_{\text{surf}}b_{\text{surf}}\sum_i A_i^{5/3}I_i^4 + \\ k_{\text{vol}}b_{\text{coul}}\sum_i A_i^{2/3}I_i^2 Z_i^2 - k_{\text{vol}}f_p\sum_i I_i^2 Z_i^2 + k_{\text{vol}}\sum_i A_i I_i^2 U_i \end{pmatrix}}{\sum_i A_i^2 - 2k_{\text{vol}}\sum_i A_i^2 I_i^2 + k_{\text{vol}}^2\sum_i A_i^2 I_i^4} \tag{17}$$

$$k_{\text{vol}} = \cfrac{\begin{pmatrix} -\sum_i A_i I_i^2 M_{\exp}(i) + b_{\text{vol}}\sum_i A_i^2 I_i^2 + b_{\text{surf}}\sum_i A_i^{5/3}I_i^2 - k_{\text{surf}}b_{\text{surf}}\sum_i A_i^{5/3}I_i^4 + \\ b_{\text{coul}}\sum_i A_i^{2/3}I_i^2 Z_i^2 - f_p\sum_i I_i^2 Z_i^2 + \sum_i A_i I_i^2 U_i \end{pmatrix}}{b_{\text{vol}}\sum_i A_i^2 I_i^4} \tag{18}$$

$$
b_{\text{surf}} = \frac{\left(\begin{array}{l} \sum_i A_i^{2/3} M_{\exp}(i) - b_{\text{vol}} \sum_i A_i^{5/3} + k_{\text{vol}} b_{\text{vol}} \sum_i A_i^{5/3} I_i^2 - b_{\text{coul}} \sum_i A_i^{1/3} Z_i^2 + \\[2mm] f_p \sum_i A_i^{-1/3} Z_i^2 - \sum_i A_i^{2/3} U_i - k_{\text{surf}} \sum_i A_i^{2/3} I_i^2 M_{\exp}(i) + \\[2mm] k_{\text{surf}} b_{\text{vol}} \sum_i A_i^{5/3} I_i^2 - k_{\text{surf}} k_{\text{vol}} b_{\text{vol}} \sum_i A_i^{5/3} I_i^4 + k_{\text{surf}} b_{\text{coul}} \sum_i A_i^{1/3} I_i^2 Z_i^2 - \\[2mm] k_{\text{surf}} f_p \sum_i A_i^{-1/3} I_i^2 Z_i^2 + k_{\text{surf}} \sum_i A_i^{2/3} I_i^2 U_i \end{array}\right)}{\sum_i A_i^{4/3} - 2 k_{\text{surf}} \sum_i A_i^{4/3} I_i^2 + k_{\text{surf}}^2 \sum_i A_i^{4/3} I_i^4} \tag{19}
$$

$$
k_{\text{surf}} = \frac{\left(\begin{array}{l} -\sum_i A_i^{2/3} I_i^2 M_{\exp}(i) + b_{\text{vol}} \sum_i A_i^{5/3} I_i^2 - k_{\text{vol}} b_{\text{vol}} \sum_i A_i^{5/3} I_i^4 + \\[2mm] b_{\text{surf}} \sum_i A_i^{4/3} I_i^2 + b_{\text{coul}} \sum_i A_i^{1/3} I_i^2 Z_i^2 - f_p \sum_i A_i^{-1/3} I_i^2 Z_i^2 + \sum_i A_i^{2/3} I_i^2 U_i \end{array}\right)}{b_{\text{surf}} \sum_i A_i^{4/3} I_i^4} \tag{20}
$$

$$
b_{\text{coul}} = \frac{\left(\begin{array}{l} \sum_i A_i^{-1/3} Z_i^2 M_{\exp}(i) - b_{\text{vol}} \sum_i A_i^{2/3} Z_i^2 + k_{\text{vol}} b_{\text{vol}} \sum_i A_i^{2/3} I_i^2 Z_i^2 - b_{\text{surf}} \sum_i A_i^{1/3} Z_i^2 + \\[2mm] k_{\text{surf}} b_{\text{surf}} \sum_i A_i^{1/3} I_i^2 Z_i^2 + f_p \sum_i A_i^{-4/3} Z_i^4 - \sum_i A_i^{-1/3} Z_i^2 U_i \end{array}\right)}{\sum_i A_i^{-2/3} Z_i^4} \tag{21}
$$

$$
f_p = \frac{\left(\begin{array}{l} -\sum_i A_i^{-1} Z_i^2 M_{\exp}(i) + b_{\text{vol}} \sum_i Z_i^2 - k_{\text{vol}} b_{\text{vol}} \sum_i Z_i^2 I_i^2 + b_{\text{surf}} \sum_i A_i^{-1/3} Z_i^2 - \\[2mm] k_{\text{surf}} b_{\text{surf}} \sum_i A_i^{-1/3} I_i^2 Z_i^2 + b_{\text{coul}} \sum_i A_i^{-4/3} Z_i^4 + \sum_i A_i^{-1} Z_i^2 U_i \end{array}\right)}{\sum_i A_i^{-2} Z_i^4} \tag{22}
$$

The Gauss-Seidel approach involves performing successive calculations of $(b_{vol}, k_{vol}, b_{surf}, k_{surf}, b_{coul}, f_p)$. At each iteration, the new value supersedes the previous one. Use Eq. (17) to determine the unknowns by an iterating sequence, where we choose the initial values $(b_{vol}^0, k_{vol}^0, b_{surf}^0, k_{surf}^0, b_{coul}^0, f_p^0)$ appropriately, the steps are as follows:

$$
\begin{cases}
\left(b_{vol}^0, k_{vol}^0, b_{surf}^0, k_{surf}^0, b_{coul}^0, f_p^0\right) & \to & b_{vol}^1 \\[1mm]
\left(b_{vol}^1, k_{vol}^0, b_{surf}^0, k_{surf}^0, b_{coul}^0, f_p^0\right) & \to & k_{vol}^1 \\[1mm]
\left(b_{vol}^1, k_{vol}^1, b_{surf}^0, k_{surf}^0, b_{coul}^0, f_p^0\right) & \to & b_{surf}^1 \\[1mm]
\left(b_{vol}^1, k_{vol}^1, b_{surf}^1, k_{surf}^0, b_{coul}^0, f_p^0\right) & \to & k_{surf}^1 \\[1mm]
\left(b_{vol}^1, k_{vol}^1, b_{surf}^1, k_{surf}^1, b_{coul}^0, f_p^0\right) & \to & b_{coul}^1 \\[1mm]
\left(b_{vol}^1, k_{vol}^1, b_{surf}^1, k_{surf}^1, b_{coul}^1, f_p^0\right) & \to & f_p^1 \\[3mm]
\left(b_{vol}^1, k_{vol}^1, b_{surf}^1, k_{surf}^1, b_{coul}^1, f_p^1\right) & \to & b_{vol}^2 \\[1mm]
\left(b_{vol}^2, k_{vol}^1, b_{surf}^1, k_{surf}^1, b_{coul}^1, f_p^1\right) & \to & k_{vol}^2 \\[1mm]
\left(b_{vol}^2, k_{vol}^2, b_{surf}^1, k_{surf}^1, b_{coul}^1, f_p^1\right) & \to & b_{surf}^2 \\[1mm]
\left(b_{vol}^2, k_{vol}^2, b_{surf}^2, k_{surf}^1, b_{coul}^1, f_p^1\right) & \to & k_{surf}^2 \\[1mm]
\left(b_{vol}^2, k_{vol}^2, b_{surf}^2, k_{surf}^2, b_{coul}^1, f_p^1\right) & \to & b_{coul}^2 \\[1mm]
\left(b_{vol}^2, k_{vol}^2, b_{surf}^2, k_{surf}^2, b_{coul}^2, f_p^1\right) & \to & f_p^2 \\[3mm]
\left(b_{vol}^2, k_{vol}^2, b_{surf}^2, k_{surf}^2, b_{coul}^2, f_p^2\right) & \to & b_{vol}^3 \\[1mm]
\quad\vdots & \quad\vdots & \vdots \\
\quad\cdots & \quad\cdots & \cdots
\end{cases} \tag{23}
$$

F) Update the values.

The process is repeated till convergence is reached, i.e. until a stable set $(b_{vol}^k, k_{vol}^k, b_{surf}^k, k_{surf}^k, b_{coul}^k, f_p^k)$ after a sufficient number k of rounds, where k is a whole number.

4. RESULTS AND DISCUSSION

The LSM is made with FORTRAN code to solve the equations systems Eq. 8, Eq. 9, and Eq. 10 for 2331 nuclides. The achieved results are discussed in this section. Table 1 demonstrates the coefficients obtained using LSM for the discussed three models. $(SP - LDM)_1$: The Six Parameters LDM formula. $(SP - LDM)_2$: The Six Parameters LDM formula without (microscopic energy, deformation energy, and congruence energy. $(EP - LDM)$: The proposed Eight Parameters LDM formula.

Table 1. The coefficients obtained using LSM for the discussed three models.

Coefficients (MeV)	$(SP - LDM)_1$	$(SP - LDM)_2$	$(EP - LDM)$
b_{vol}	-15.9727	-15.5986	-16.0498
k_{vol}	1.8397	1.6954	1.8272
b_{surf}	19.8832	18.9262	20.3437
k_{surf}	1.9206	1.5061	1.8925
b_{coul}	0.7327	0.7231	0.7390
f_p	1.2344	2.0543	1.4446
b_{sh}	-	-	0.7275
b_{pa}	-	-	0.6637
RMS	**1.28**	**2.65**	**1.05**

Table 2 demonstrates the obtained values versus iterations for the proposed eight parameters LDM Formula. Figures 1a, 1b, 2a, 2b, 3a, 3b, 4a, 4b depict the convergence of the eight coefficients $b_{vol}, k_{vol}, b_{surf}, k_{surf}, b_{coul}, f_p, b_{sh}, b_{pa}$, respectively.

Table 2. Iterations and convergence of the eight coefficients formula.

Iterations	b_{vol}	k_{vol}	b_{surf}	k_{surf}	b_{coul}	f_p	b_{sh}	b_{pa}
50	-14.641376	1.428979	11.660317	-1.163253	0.615636	-3.215885	1.174006	1.226985
100	-14.644251	1.483173	11.849770	-0.891092	0.600652	-3.450187	1.040020	0.985133
150	-14.644095	1.523160	11.929214	-0.605908	0.598580	-3.431418	1.030725	0.960194
300	-14.643833	1.613897	12.185625	0.088771	0.596867	-3.240858	1.021870	0.929168
500	-14.647650	1.689492	12.587653	0.723691	0.598327	-2.852138	1.005048	0.896717
700	-14.658353	1.733695	13.025564	1.143882	0.602349	-2.394916	0.985021	0.870226
1000	-14.688660	1.768886	13.703765	1.541319	0.610902	-1.689191	0.953279	0.837541
1500	-14.773100	1.792807	14.806025	1.893609	0.627683	-0.629695	0.903030	0.794445
4000	-15.410877	1.818667	18.649300	2.180657	0.698445	1.792211	0.757456	0.683832
7000	-15.896930	1.826270	20.206447	2.018919	0.733131	1.874165	0.720209	0.657450
10000	-16.040475	1.827507	20.432650	1.922742	0.740038	1.596387	0.721804	0.659292
50000	-16.049779	1.827150	20.343749	1.892542	0.739009	1.444598	0.727491	0.663692
100000	-16.049779	1.827150	20.343749	1.892542	0.739009	1.444598	0.727491	0.663692
500000	-16.049779	1.827150	20.343749	1.892542	0.739009	1.444598	0.727491	0.663692
1000000	-16.049779	1.827150	20.343749	1.892542	0.739009	1.444598	0.727491	0.663692
10000000	-16.049779	1.827150	20.343749	1.892542	0.739009	1.444598	0.727491	0.663692
50000000	-16.049779	1.827150	20.343749	1.892542	0.739009	1.444598	0.727491	0.663692
100000000	-16.049779	1.827150	20.343749	1.892542	0.739009	1.444598	0.727491	0.663692

The experimental values of nuclear mass are calculated using the mass excess equation given by Eq. 12. The experimental masses values are taken from the recently updated Atomic Mass Evaluation, i.e. AME table, published in [36]. The number of total iterations was set at 100,000,000 (100 million of iterations) to illustrates the convergence of parameters. However, despite the number of iterations, the execution time is of the order
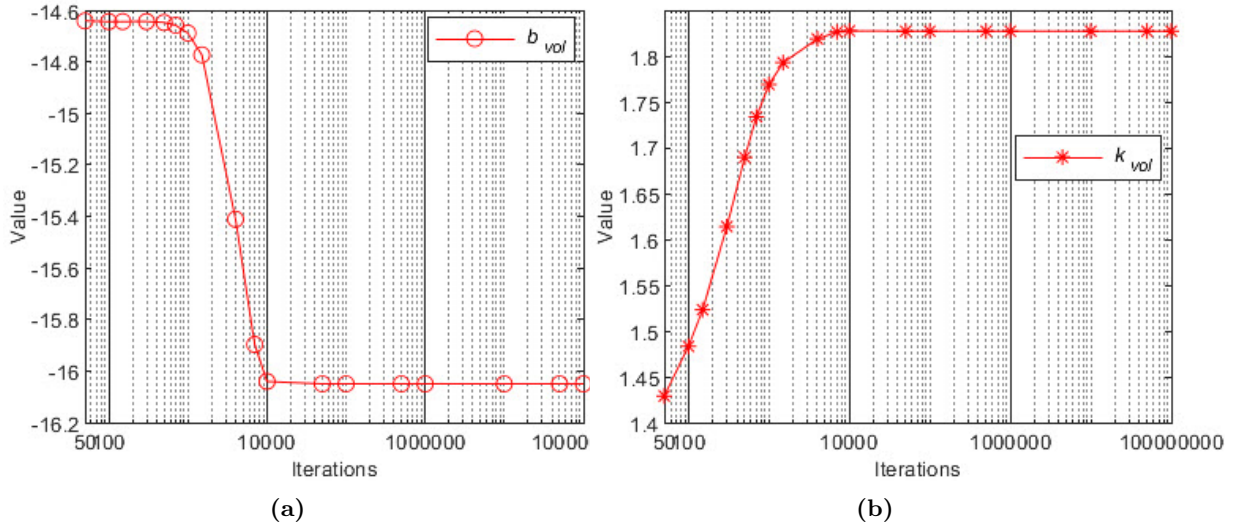
Figure 1. Convergence of b_{vol}, and k_{vol} coefficients versus iterations.
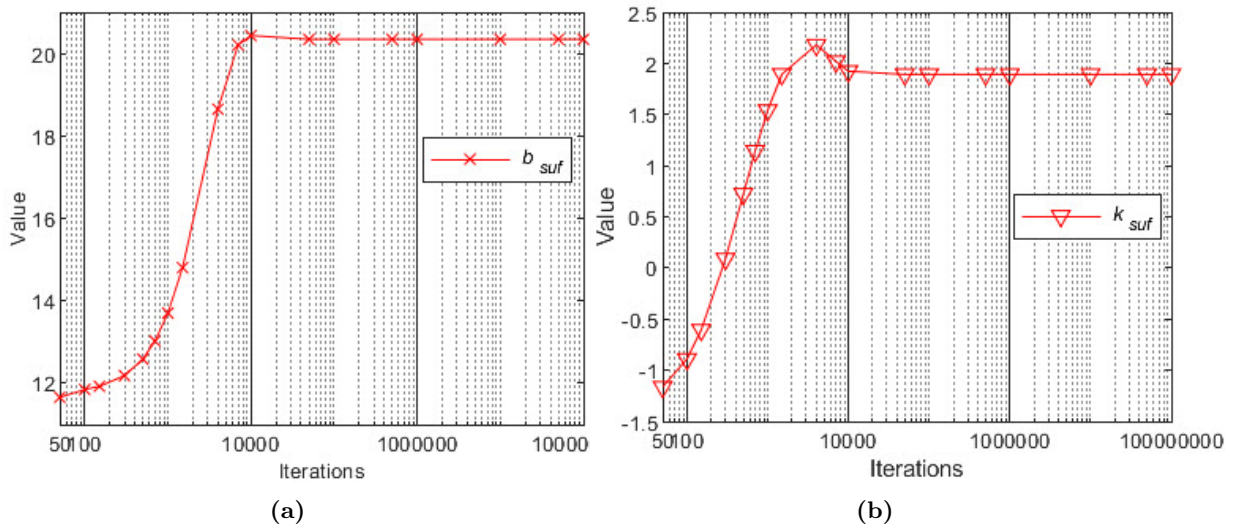

Figure 2. Convergence of b_{surf}, and k_{surf} coefficients versus iterations.

of a few seconds for this case where only eight quantities varied. Coefficient values were recorded for a certain number of iterations (see Table 1). Results for all the eight coefficients are stable from 50,000 iterations onwards. Here, stability is defined by requiring that the 6 digits after the decimal point no longer change. With these stabilized values, we obtain a root-mean-square deviation given by Eq. 11, i.e. 1.05 MeV in the nuclear mass. As a result, shell and pairing corrections are necessary in these kinds of formulas. Root mean square deviation of 0.864 MeV has been achieved in our improved equation, published in [27], (which is not the subject of our study in this paper). On the other part, it should be pointed out that the direct comparison between the different types of mass formulas proposed in the literature is only a relative significance, as very often the "basis", i.e. the set and number of nuclei aren't the same. Other factors come into consideration, such as the fact that microscopic corrections are model-dependent. What's more, in some serious calculations, the root mean square deviation is weighted by a measurement error,... etc. The root mean square deviation can be improved by increasing the number of corrective terms and the introduction of the shell and pairing corrections.

5. CONCLUSION

A new liquid drop model of eight parameters has been proposed in this paper. The main advantage of this proposed model is adding only two coefficients to the common six parameters model to improve the root mean square value. A comparative analysis of the proposed model with some proposed models in literature have been presented. A simple and fast algorithm based on the least squares method is used to find the eight
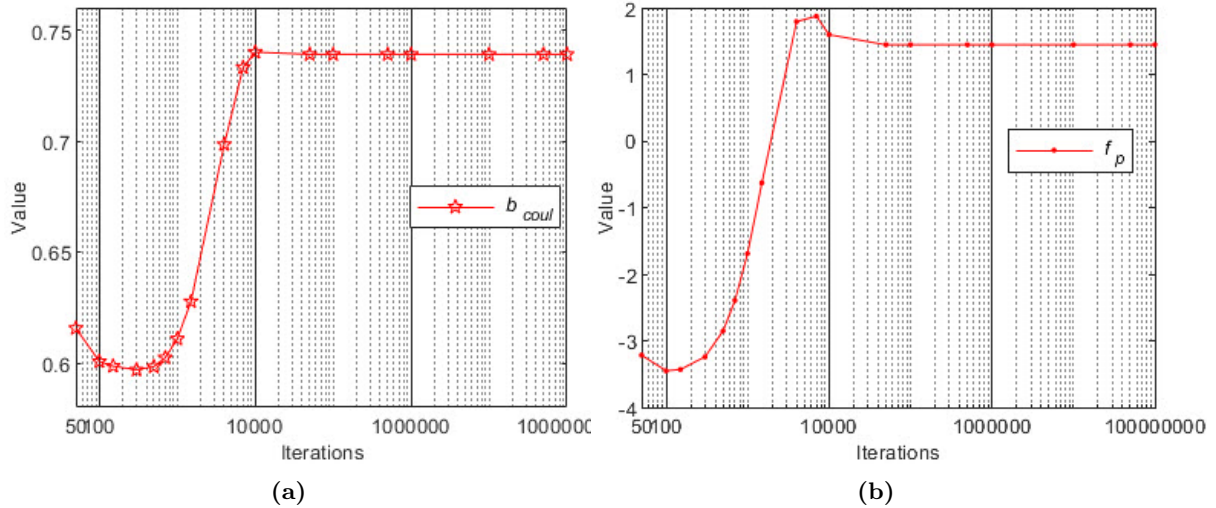
Figure 3. Convergence of b_{coul}, and f_p coefficients versus iterations.
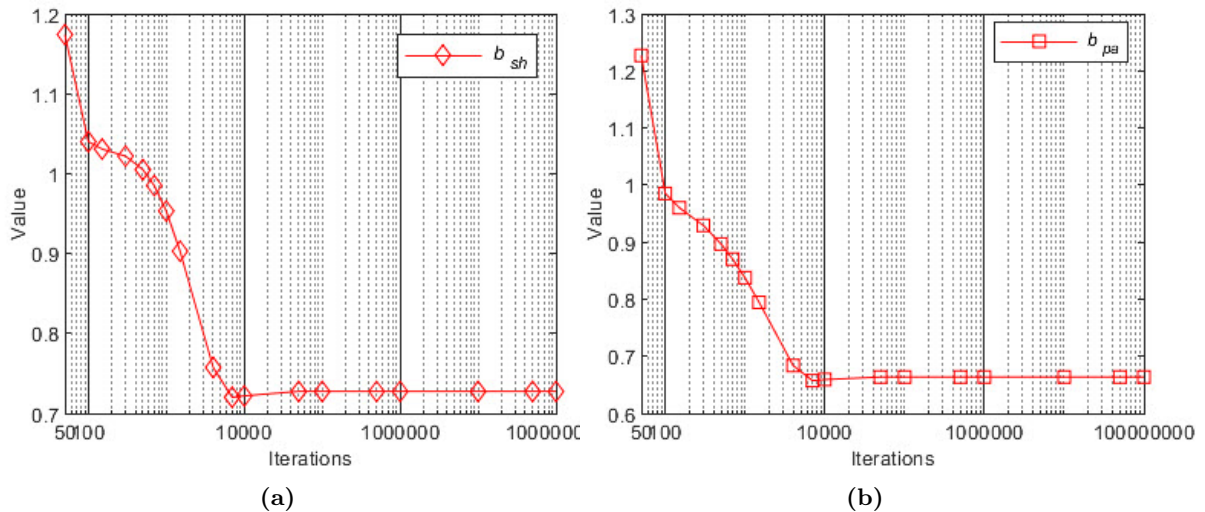
Figure 4. Convergence of b_{sh}, and b_{pa} coefficients versus iterations.

parameters. The steps of the method are described in detail, where it is characterized by the maximum of simplicity in the procedure. The performance of the proposed model was verified using developed FORTRON program and checked with experimental nuclear DATA from Atomic Mass Data Center. A close concordance between theoretical and experimental values has been obtained. The results demonstrate that r.m.s. value for the new liquid drop model in terms of masses is equal to 1.05 MeV. Also, finding a mathematical formula for a liquid drop model that is close to reality is still a good problem for research because this will open way to new perspectives in the study of nuclei. The results of the present work join a growing body of literature in the field of theoretical physics, and the information presented opens new avenues for further studies on other models.

ORCID

Hadj Mouloudj, https://orcid.org/0009-0006-0376-9642; Benyoucef Mohammed-Azizi, https://orcid.org/0000-0002-9980-058X; Oussama Zeggai, https://orcid.org/0000-0002-9850-3559; Abdelkader Ghalem, https://orcid.org/0000-0001-6308-3753; Alla Eddine Toubal Maamar, https://orcid.org/0000-0002-0738-0048

REFERENCES

[1] P. Möller, and A.J. Sierk, International Journal of Mass Spectrometry, **349–350**, 19 (2013). https://doi.org/10.1016/j.ijms.2013.04.008.

[2] W.D. Myers, and W.J. Świątecki, Nuclear Physics, **81**, 1 (1966). https://doi.org/10.1016/0029-5582(66)90639-0.

[3] V.M. Strutinsky, Nuclear Physics A, **95**, 420 (1967). https://doi.org/10.1016/0375-9474(67)90510-6.

[4] P. Möller, J.R. Nix, W.D. Myers, and W.J. Świątecki, "Nuclear Ground-State Masses and Deformations," Atomic Data Nucl. Data Tables, 185-381, 59 (1995).

[5] W.D. Myers and W.J. Świątecki, Nuclear Physics A, **601**, 141 (1996). https://doi.org/10.1016/0375-9474(95)00509-9.

[6] A.K. Dutta, J.-P. Arcoragi, J.M. Pearson, R. Behrman, and F. Tondeur, Nuclear Physics A, **458**, 77 (1986). https://doi.org/10.1016/0375-9474(86)90283-6.

[7] K. Pomorski and J. Dudek, Phys. Rev. C, **67**, (2003). https://doi.org/10.1103/PhysRevC.67.044316.

[8] S. Goriely, N. Chamel, and J.M. Pearson, Phys. Rev. C, **82**, (2010). https://doi.org/10.1103/physrevc.82.035804.

[9] S. Goriely, S. Hilaire, M. Girod, and S. Péru, Phys. Rev. Lett. **102**, (2009). https://doi.org/10.1103/physrevlett.102.242501.

[10] J. Duflo, and A.P. Zuker, Phys. Rev. C, **52**, R23 (1995). https://doi.org/10.1103/physrevc.52.r23.

[11] H. Koura, T. Tachibana, M. Uno, and M. Yamada, Progress of Theoretical Physics, **113**, 305 (2005). https://doi.org/10.1143/ptp.113.305.

[12] C.F.V. Weizsacker, Z. Physik, **96**, 431 (1935). https://doi.org/10.1007/bf01337700.

[13] J. Bleck-Neuhaus, *Elementare Teilchen*, (Springer Berlin Heidelberg, 2010), https://doi.org/10.1007/978-3-540-85300-8.

[14] ZEUS Collaboration, M. Derrick, et al., Z. Phys. C - Particles and Fields, **63**, 391 (1994), https://doi.org/10.1007/bf01580320.

[15] A. Bohr, B.R. Mottelson, and D. Pines, Phys. Rev. **110**, 936 (1958), https://doi.org/10.1103/physrev.110.936.

[16] S.G. Nilsson, C.F. Tsang, A. Sobiczewski, Z. Szymański, S. Wycech, C. Gustafson, I.-L. Lamm, P. Möller, and B. Nilsson, Nuclear Physics A, **131**, 1 (1969), https://doi.org/10.1016/0375-9474(69)90809-4.

[17] H. Olofsson, S. Åberg, and P. Leboeuf, Phys. Rev. Lett. **100**, (2008), https://doi.org/10.1103/physrevlett.100.037005.

[18] M. Brack, and P. Quentin, Physics Letters B, **56**, 421 (1975), https://doi.org/10.1016/0370-2693(75)90401-3.

[19] G.G. Bunatian, V.M. Kolomietz, and V.M. Strutinsky, Nuclear Physics A, **188**, 225 (1972), https://doi.org/10.1016/0375-9474(72)90058-9.

[20] D. Lunney, J.M. Pearson, and C. Thibault, Rev. Mod. Phys. **75**, 1021 (2003), https://doi.org/10.1103/revmodphys.75.1021.

[21] F.F.A. Al-dawdy, and F.M.A. Al-jomaily, Arab Journal of Nuclear Sciences and Applications, **55**, 150 (2022), https://doi.org/10.21608/ajnsa.2022.135860.1574.

[22] F. Al-jomaily and R. Abdullateef, Arab Journal of Nuclear Sciences and Applications, **55**, 62 (2021), https://doi.org/10.21608/ajnsa.2021.75297.1471.

[23] B. Mohammed-Azizi, Int. J. Mod. Phys. C, **21**, 681 (2010), https://doi.org/10.1142/s0129183110015415.

[24] M.M.A. Vahid, M. Mohsen, A.M. Bagher, Nuclear Science, **2**, 11 (2010), https://doi.org/10.11648/j.ns.20170201.13.

[25] S.Cht. Mavrodiev, *Nuclear Theory*, edited by M. Gaidarov, and N. Minkov, (HeronPress, Sofia, 2016). **35**, 288 (2016).

[26] H. Zhang, J. Dong, N. Ma, G. Royer, J. Li, and H. Zhang, Nuclear Physics A, **929**, 38 (2014), https://doi.org/10.1016/j.nuclphysa.2014.05.019.

[27] B. Mohammed-Azizi and H. Mouloudj, Int. J. Mod. Phys. C, **33**, (2021), https://doi.org/10.1142/s0129183122500760.

[28] H.R. Vega-Carrillo, and H. René, Revista Mexicana de Física, **35**(4), 591 (1989), https://doi.org/10.48779/0egn-1c86.

[29] P.R. Chowdhury, C. Samanta, and D.N. Basu, Mod. Phys. Lett. A, **20**, 1605 (2005), https://doi.org/10.1142/s021773230501666x.

[30] H.A. Bethe, and R.F. Bacher, Rev. Mod. Phys. **8**, 82 (1936), https://doi.org/10.1103/RevModPhys.8.82.

[31] S.M. Stigler, Ann. Statist. **9**, (1981), https://doi.org/10.1214/aos/1176345451.

[32] P.C. Hansen, V. Pereyra, and G. Scherer. *Handbook of Least Squares Data Fitting with Applications*, (Johns Hopkins University Press, 2013)

[33] P. Möller, A.J. Sierk, T. Ichikawa, and H. Sagawa, Atomic Data and Nuclear Data Tables, **109–110**, 1 (2016), https://doi.org/10.1016/j.adt.2015.10.002.

[34] G. Royer, Nuclear Physics A, **807**, 105 (2008), https://doi.org/10.1016/j.nuclphysa.2008.04.002.

[35] W.D. Myers, *Droplet Model of Atomic Nuclei*, (Plenum Publishing Corporation, 1977). https://escholarship.org/content/qt7bn59935/qt7bn59935.pdf

[36] Atomic Mass Data Center AMDC, International Atomic Energy Agency - Nuclear Data Section, https://www-nds.iaea.org/amdc/

ОЦІНКА КОЕФІЦІЄНТІВ ЯДЕРНОЇ МАСИ ЗА ДОПОМОГОЮ МЕТОДУ НАЙМЕНШИХ КВАДРАТІВ НА ОСНОВІ СХЕМИ ГАУССА-ЗЕЙДЕЛЯ: ПОРІВНЯЛЬНЕ ДОСЛІДЖЕННЯ МІЖ ТРЬОМА МОДЕЛЯМИ

Хадж Мулудж[a,b], **Бенюсеф Мохаммед-Азізі**[a,c], **Усама Зеггай**[d,e], **Абделькадер Галем**[b,f], **Алла Еддін Тубал Маамар**[g]

[a] *Лабораторія фізики елементарних частинок і статистичної фізики, Вища педагогічна школа Коуби, Стара-Коуба 16050, Алжир*

[b] *Факультет фізики, факультет точних наук та інформатики, Університет Хасіба Бенбуалі, Шлеф, Алжир*

[c] *Університет Бешар, Бешар 08000, Алжир*

[d] *Відділ загального ядра, факультет точних наук та інформатики, Університет Хасіба Бенбуалі, Шлеф, Алжир*

[e] *Дослідницький відділ матеріалів і відновлюваних джерел енергії (URMER), Університет Абу Бекр Белкайд, Тлемсен 13000, Алжир*

[f] *Лабораторія механіки та енергетики, Шлеф 02100, Алжир*

[g] *Кафедра інженерії електричних систем, технологічний факультет, Університет М'хамеда Бугара в Бумердесі, Бумердес 35000, Алжир*

У цій статті представлено аналіз та реалізацію методу найменших квадратів на основі схеми Гаусса-Зейделя для розв'язування формул ядерної маси. Метод найменших квадратів приводить до розв'язку системи шляхом ітерацій. Основними перевагами розглянутого методу є простота і висока точність. Крім того, метод дозволяє нам швидко обробляти великі дані на практиці. Для демонстрації ефективності методу виконано реалізацію на мові FORTRAN. Деталізовано кроки алгоритму. Використовуючи 2331 ядерну масу з $Z \geq 8$ і $N \geq 8$, було показано, що продуктивність формули маси рідкої краплі з шістьма параметрами покращилася в термінах середньоквадратичного кореня (середньоквадратичне відхилення дорівнює 1,28 МеВ), порівняно з формулою маси краплі рідини з шістьма параметрами без мікроскопічної енергії, енергії деформації та енергії конгруентності (середньоквадратичне відхилення дорівнює 2,65 МеВ). Модель краплі ядерної рідини переглянуто, щоб чітко виясните роль мікроскопічних поправок (оболонка та спарення). Енергія деформації та оцінка енергії конгруентності були використані для отримання найкращої відповідності. Показано, що ефективність нового підходу покращується за допомогою моделі восьми параметрів порівняно з попередньою моделлю шести параметрів. Отримане середньоквадратичне значення Результат для нової моделі рідкої краплі в термінах мас дорівнює 1,05 МеВ.

Ключові слова: *ядерні маси; чисельні методи; енергія зв'язку; корекція оболонки; виправлення пар*

DIFFUSION OF HIGH-ENERGY NEGATIVELY CHARGED PARTICLES IN THE FIELD OF ATOMIC STRINGS OF AN ORIENTED CRYSTAL

 Igor V. Kyryllin[a,b*], **Mykola F. Shul'ga**[a,b], **Oleksandr P. Shchus**[b,a]

[a] Akhiezer Institute for Theoretical Physics, National Science Center "Kharkiv Institute of Physics and Technology"
Akademichna Str., 1, Kharkiv, 61108, Ukraine
[b] V.N. Karazin Kharkiv National University, 4, Svoboda Sq., Kharkiv, 61022, Ukraine
∗Corresponding Author e-mail: i.kyryllin@gmail.com

The work analyzes the dependence of the diffusion index of high-energy negatively charged particles on the energy of their transverse motion in oriented crystal. The crystal had an axial orientation relative to the direction of particle incidence. The analysis was carried out using the example of π^- mesons with a momentum of 100 GeV/c that impinged on a silicon crystal, which corresponds to the conditions achievable on secondary beam of the the CERN SPS accelerator. The analysis showed that the dependence under consideration is not monotonic. It has a minimum in the energy region slightly exceeding the value of the potential energy of particles at the saddle point of the potential of crystal atomic strings. At higher values of the energy of transverse motion of particles $E_\perp$, the diffusion index increases with increasing $E_\perp$, due to the increase of the average absolute value of the velocity of particle motion in the plane orthogonal to the crystal axis, near which motion takes place. The increase in the diffusion index at low values of $E_\perp$ is associated with the manifestation of incoherent scattering of particles on thermal vibrations of crystal atoms. The analysis carried out in the work is of interest both for a deeper understanding of the process of high-energy negatively charged particle beams passage through oriented crystals, and for improving methods for charged particle beams steering with a help of straight and bent oriented crystals.

Keywords: *Channeling; High-energy charged particle; Diffusion; Oriented crystal*

PACS: 61.85.+p

1. INTRODUCTION

In 1963, M.T. Robinson and O.S. Oen [1] based on computer simulations showed that the orientation of the crystal has a significant effect on the nature of fast charged particles diffusion in the crystal. Since then, orientation effects in the scattering of particles in crystals have been studied for many decades. In 1965, J. Lindhard [2] developed a theory of the channeling phenomenon, which describes a motion of fast charged particles at a small angle to crystal atomic strings or crystal atomic planes. With such motion, the impact parameter changes slightly when the particle is scattered on neighboring atoms of the string or plane, and correlations in the scattering on neighboring crystal lattice atoms become significant. Due to such correlations, coherent effects in the scattering of charged particles on crystal atomic strings and planes arise. Correlations in scattering allow positively charged particles to move in a crystal without approaching close distances to atomic strings and planes, since at small distances the field of atomic nuclei is not completely screened by the field of atomic electrons (especially if some of the electrons are valence) and positively charged particles are repelled from the nuclei of neighboring atoms in the same direction. The fact that positively charged particles, when moving at a small angle to atomic strings or planes, do not come too close to the atoms leads to the fact that stable modes of motion (planar and axial channeling) for positively charged particles in an oriented crystal are significantly more resistant to incoherent scattering of particles on thermal atomic vibrations than in the case of negatively charged particles which are attracted by atomic nuclei. That is why oriented crystals, including bent ones, have recently been more often used to deflect the direction of motion of *positively* charged particles [3–15]. The process of passage of negatively charged particles through oriented crystals is more difficult to describe. At the same time, the relevance of research into this process is determined by the possibility of using oriented crystals to control beams of negatively charged particles, which is an important problem in accelerator physics. Recently, a number of both theoretical [16, 17] and experimental [18–20] studies have been carried out on the process of motion of fast negatively charged particles in oriented crystals. These studies were devoted mainly at finding optimal conditions for deflecting beams of negatively charged particles. Our work aims to expand the study of the process of negatively charged high-energy particles passage through oriented crystals.

In [22] the possess of diffusion of fast negatively charged particles was studied for one given value of the transverse energy of particles in the field of crystal atomic strings. It was shown that diffusion in this case is

anomalous. However, a study of the diffusion process in the case of an arbitrary value of the transverse energy of particles in the field of crystal atomic strings has not yet been carried out. Such a research is the subject of the current article.

2. MOTION OF NEGATIVELY CHANGED PARTICLES IN THE FIELD OF CRYSTAL ATOMIC STRINGS

To find the trajectory of a fast charged particle in a crystal, it is necessary to solve the three-dimensional equation of motion

$$\frac{d\vec{p}}{dt} = -\vec{\nabla}U(\vec{r}), \tag{1}$$

where $\vec{p}$ and $\vec{r}$ are particle momentum and coordinate, $U(\vec{r})$ is particle potential energy in the field of crystal atoms. However, if the particles move at a small angle to one of the main crystalline axes (let's call it the z axis), the atoms along this axis are arranged into strings, and correlations in scattering on neighboring string atoms make it possible to simplify the equation of motion. This simplification consists in the transition from the potential of individual atoms to the continuous potential of atomic strings. In such an averaged field, the potential energy of charged particles is written as follows:

$$U(x, y) = \frac{1}{L} \int_{-\infty}^{\infty} U(x, y, z)\, dz, \tag{2}$$

where L is the thickness of the crystal, x and y are the coordinates of the particle in plane orthogonal to the z axis. In this approximation, we can write the equation of motion of high-energy charged particles in the form of a system of equations

$$\frac{d^2x}{dt^2} = -\frac{c^2}{E_{||}} \frac{\partial}{\partial x} U(x, y),$$

$$\frac{d^2y}{dt^2} = -\frac{c^2}{E_{||}} \frac{\partial}{\partial y} U(x, y),$$

$$\frac{d^2z}{dt^2} = 0, \tag{3}$$

where $E_{||} = c\sqrt{p_z^2 + (mc)^2}$, m is the mass of the particle, and c is the speed of light in vacuum. It can be shown [21] that for system of equations (3) the quantity

$$E_\perp = \frac{pv\psi^2}{2} + U(x, y),$$

is the integral of motion (v is the absolute value of the particle's speed, and ψ is the angle between the speed of the particle and the axis of the atomic strings). This quantity is called the energy of transverse motion.

If we now numerically solve equations (3), then we will find the trajectory of the particle in the field of crystal atomic strings, as was done in [22]. It is important that this approach ignores the incoherent scattering of particles on atomic thermal vibrations and the electronic subsystem. For positively charged particles, such scattering in thin crystals can be neglected due to the fact that, because of repulsion from atomic nuclei, positively charged particles move most of the time in an oriented crystal, not approaching the strings at close distances, at which thermal displacements of atoms relative to the nodes of the crystal lattice are significant. However, negatively charged particles are scattered by thermal vibrations of atoms much more intensely, since these particles are attracted by atomic nuclei. For this reason, for negatively charged particles, incoherent scattering cannot be neglected even in thin crystals, and in equations (3) we must take into account incoherent scattering. This could be done by adding to the equations of motion along the x and y axes a random force [23,24] which is maximum at the points where atomic strings are located in the (x, y) plane and is distributed near these points according to the Gaussian law with a standard deviation equal to the standard deviation of atoms from the nodes of the crystal lattice [25]:

$$\frac{d^2x}{dt^2} = -\frac{c^2}{E_{||}} \frac{\partial}{\partial x} U(x, y) + f_x,$$

$$\frac{d^2y}{dt^2} = -\frac{c^2}{E_{||}} \frac{\partial}{\partial y} U(x, y) + f_y. \tag{4}$$

The explicit form of this force is given in [26].

We calculate the potential of atomic strings in the Doyle-Turner atomic potential model [27], as was done in [17]. In this model potential energy of a particle with a charge, that equals to the charge of an electron, in the field of atomic strings ⟨100⟩ of a silicon crystal can be written as

$$U\left(x,y\right) = -\frac{2\pi\hbar^2}{m_e d d_s^2}\sum_{j=1}^{4}\alpha_j\theta_3\left[\pi\frac{x}{d_s},\exp\left(-\frac{\beta_j+B}{4d_s^2}\right)\right]\theta_3\left[\pi\frac{y}{d_s},\exp\left(-\frac{\beta_j+B}{4d_s^2}\right)\right] + U_0, \qquad (5)$$

where m_e is an electron mass, d is the distance between neighboring atoms in the atomic string, d_s is the distance between closest neighboring atomic strings, α_i and β_i are coefficients found in [27] for a large number of elements, $B = 8\pi^2 r_T^2$, r_T is the rms atomic thermal vibration amplitude in one direction ($r_T \approx 0.075$ Å for Si at 293 K), $\theta_3(u,q) = \sum_{n=-\infty}^{\infty} q^{n^2}\exp(2nui)$ is the Jacobi theta function of the third kind [28], $i^2 = -1$. U_0 is a constant that is determined from the condition that the value of the potential energy of a particle at a point equidistant from the two nearest neighboring atomic strings (i.e. at the saddle point) is taken as zero. Equipotential lines of potential energy (5) are shown in Figure 1.
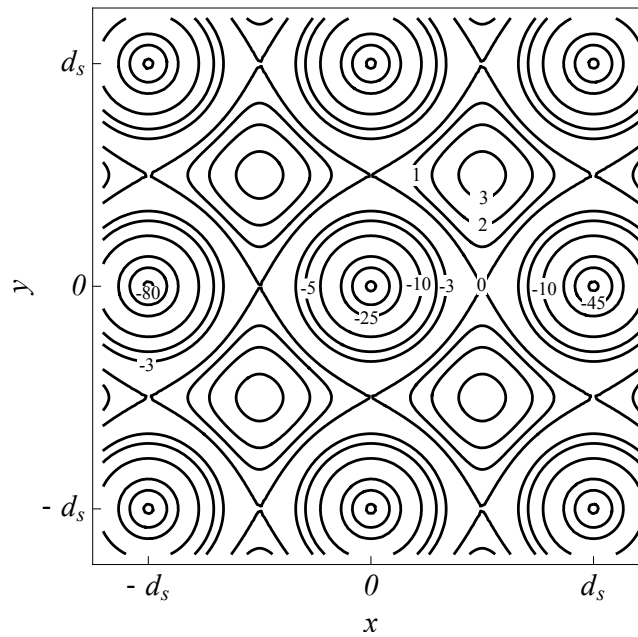
Figure 1. Equipotential lines of continuous potential energy of a π^- meson in the field of ⟨100⟩ atomic strings of a silicon crystal in a plane orthogonal to the ⟨100⟩ crystal axis. The numbers next to the lines show the potential energy value along these lines in eV.

In order to show the importance of taking into account the influence of incoherent scattering on the process of diffusion of negatively charged particles in an oriented crystal, let us consider the trajectories of ten π^- mesons with $p = 100$ GeV/c, which move in the field of ⟨100⟩ atomic strings of a silicon crystal. These trajectories are plotted in the (x, y) plane. The impact parameters and angles of entry of these particles into the crystal are chosen randomly, but so that for every particle the energy of transverse motion immediately after entering the crystal $E_{\perp 0}$ is 1 eV. Figure 2a shows trajectories calculated without taking into account incoherent scattering. These trajectories were found by numerically solving equations (3). Figure 2b shows the trajectories of the same particles, calculated with taking into account incoherent scattering on thermal vibrations of crystal atoms and on electronic subsystem, obtained by solving equations (4). The crystal thickness in both cases was 100 μm. The presence of incoherent scattering leads to the fact that $E_\perp$ ceases to be an integral of motion. This leads to the fact that when incoherent scattering is taken into account, the motion of negatively charged particles in the field of one atomic string becomes unstable and the particles, on average, move faster away from the incidence point in (x, y) plane.

3. DEPENDENCE OF THE DIFFUSION INDEX ON THE ENERGY OF TRANSVERSE PARTICLE MOTION

Knowing the trajectories of a large number of particles in the field of crystal atomic strings, we can determine the diffusion index of a particle beam. In the same way as it was done in [22], we assume that the
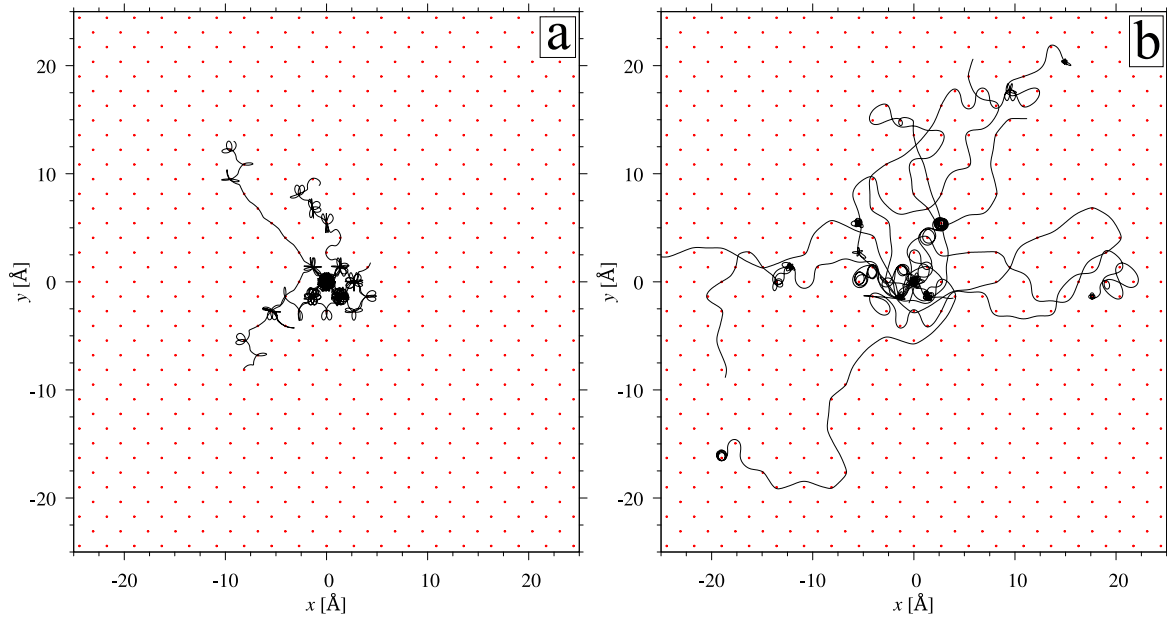
Figure 2. Trajectories of π^- mesons with $p = 100$ GeV/c, which move in the field of $\langle 100 \rangle$ atomic strings of a silicon crystal a) without and b) with taking into account incoherent scattering. $E_{\perp 0} = 1$ eV

mean square distance of particles from the entry points in (x, y) plane can be written as

$$\langle \rho^2 \rangle = a l^\mu, \tag{6}$$

where l is the thickness of the crystal, μ is the diffusion index, a is the proportionality factor. In work [22], the diffusion index was determined from the relation

$$\mu = \frac{\ln\left(\langle \rho^2 \rangle_l / \langle \rho^2 \rangle_{l_0}\right)}{\ln(l/l_0)}, \tag{7}$$

where l_0 is the normalization thickness of the crystal ($l_0 \ll l$). This method of determining μ has a large error, since the diffusion index is determined from the values of the mean square deviation at only two points (at two crystal thicknesses: l and l_0). In the present work, however, we used a different method, namely, we approximated the dependence of $\langle \rho^2 \rangle$ on the crystal thickness by function $a l^\mu$. In this approach the value of the diffusion index is determined taking into account all points of the dependence of $\langle \rho^2 \rangle$ on l, which significantly increases the accuracy of the calculations.

To obtain the dependence of the diffusion index on the initial value of transverse particle motion energy $E_{\perp 0}$ we carried out a number of simulations. In each of them, solving numerically the equations of motion (4), we found the trajectories of 10^5 π^- mesons with $p = 100$ GeV/c and with the same $E_{\perp 0}$ in the field of atomic strings $\langle 100 \rangle$ of a silicon crystal with $l = 100$ μm. Simulations were carried out for 1 eV $\leq E_{\perp 0} \leq 200$ eV with a step of 1 eV. For each value of $E_{\perp 0}$, the dependence of $\langle \rho^2 \rangle$ on the crystal thickness was determined from the found trajectories. To determine μ as a function of $E_{\perp 0}$, each of the obtained dependencies was approximated by the function $a l^\mu$ using the nonlinear least-squares Marquardt-Levenberg algorithm [29, 30]. The results are shown in Figure 3, which shows the dependence of the diffusion index μ on the energy of transverse particle motion. The obtained dependence is not monotonically increasing, as could be expected, taking into account that with increasing the initial value of transverse particle motion energy, particles should move faster in the (x, y) plane. This is indeed the case for $E_{\perp 0} \gtrsim 20$ eV, but for smaller values of $E_{\perp 0}$ there is an increase in μ as $E_{\perp 0}$ decreases. This unusual behavior is explained by the fact that as $E_{\perp 0}$ approaches the value of the potential energy of particles at the saddle point (which we set equal to zero), the rate of exit of particles from the potential well without taking into account incoherent scattering decreases significantly. The motion in this case is similar to the finite motion in the field of one crystal atomic string. In this case, due to the smallness of $E_{\perp 0}$, the particle, with each oscillation in the field of the atomic string, approaches the string at close distances of the order of r_T. At such small distances, there is a high probability of particle scattering at large angles under the influence of incoherent scattering by thermal vibrations of the string atoms. This scattering at large angles leads to an increase in $E_\perp$ and an increase in μ. Note that for channeled particles for which $E_{\perp 0} < 0$, the diffusion index tends to 2 due to incoherent scattering at large angles. At large values of $E_{\perp 0}$, the kinetic

energy of particles in the (x, y) plane becomes much greater than the potential energy and the diffusion index tends to 2 at $E_{\perp 0} \to \infty$, which corresponds to rectilinear motion in this plane.
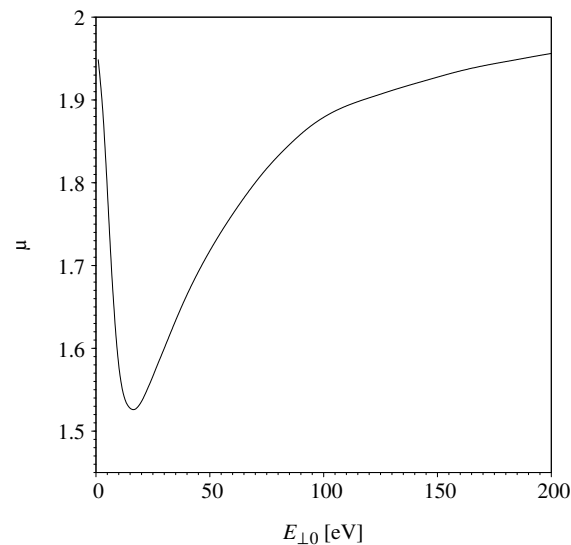

Figure 3. The dependence of the diffusion index on the energy of transverse particle motion

4. CONCLUSIONS

In the article, the dependence of the diffusion index of high-energy negatively charged particles on the energy of the transverse motion in axially oriented crystal was determined. The type of this dependence turned out to be non-monotonic. It has a minimum in the energy region slightly exceeding the value of the potential energy of particles at the saddle point of the potential of crystal atomic strings. At higher values of the energy of transverse motion of particles $E_\perp$, the diffusion index increases with increasing $E_\perp$, since this increases the average absolute value of the velocity of particle motion in the plane orthogonal to the crystal axis, near which motion takes place. The increase in the diffusion index at low values of $E_\perp$ is associated with the manifestation of incoherent scattering of particles on thermal vibrations of crystal atoms. The found dependence is of interest both for a deeper understanding of the process of high-energy negatively charged particle beams passage through oriented crystals, and for improving methods for charged particle beams steering with a help of straight and bent oriented crystals.

ORCID

Igor V. Kyryllin, https://orcid.org/0000-0003-3625-7521; **Mykola F. Shul'ga**, https://orcid.org/0000-0003-1679-6819; **Oleksandr P. Shchus**, https://orcid.org/0000-0001-6063-197X

REFERENCES

[1] M.T. Robinson, and O.S. Oen, Phys. Rev. **132**, 2385 (1963), https://doi.org/10.1103/PhysRev.132.2385

[2] J. Lindhard, Mat. Fys. Medd. Dan. Vid. Selsk. **34**, 1 (1965), http://gymarkiv.sdu.dk/MFM/kdvs/mfm%2030-39/mfm-34-14.pdf

[3] W. Scandale et al., Phys. Lett. B, **760**, 826 (2016), https://doi.org/10.1016/j.physletb.2016.07.072

[4] W. Scandale et al., Eur. Phys. J. C, **78**, 505 (2018), https://doi.org/10.1140/epjc/s10052-018-5985-8

[5] A.G. Afonin et al., Instrum. Exp. Tech. **59**, 196 (2016), https://doi.org/10.1134/S0020441216020019

[6] W. Scandale et al., Phys. Lett. B, **733**, 366 (2014), https://doi.org/10.1016/j.physletb.2014.05.010

[7] I.V. Kyryllin, and N.F. Shul'ga, J. Instrum. **13**, C02020 (2018), https://doi.org/10.1088/1748-0221/13/02/C02020

[8] S. Redaelli et al., Eur. Phys. J. C, **81**, 142 (2021), https://doi.org/10.1140/epjc/s10052-021-08927-x

[9] F.M. Velotti et al., Phys. Rev. Accel. Beams, **22**, 093502 (2019), https://doi.org/10.1103/PhysRevAccelBeams.22.093502

[10] R. Rossi et al. J., Instrum. **18**, P06027 (2023), https://doi.org/10.1103/PhysRevAccelBeams.22.093502

[11] W. Scandale et al., Nucl. Instr. Meth. B, **467**, 118 (2020), https://doi.org/10.1016/j.nimb.2020.01.011

[12] W. Scandale et al., Eur. Phys. J. C, **79**, 993 (2019), https://doi.org/10.1140/epjc/s10052-019-7515-8

[13] W. Scandale et al., Phys. Lett. B, **804**, 135396 (2020), https://doi.org/10.1016/j.physletb.2020.135396

[14] W. Scandale et al., Eur. Phys. J. C, **80**, 27 (2020), https://doi.org/10.1140/epjc/s10052-019-7590-x

[15] W. Scandale et al., Eur. Phys. J. Plus, **137**, 811 (2022), https://doi.org/10.1140/epjp/s13360-022-03034-6

[16] I.V. Kirillin, Phys. Rev. Accel. Beams, **20**, 104401 (2017), https://doi.org/10.1103/PhysRevAccelBeams.20.104401

[17] I.V. Kyryllin, and N.F. Shul'ga, Eur. Phys. J. C, **79**, 1015 (2019), https://doi.org/10.1140/epjc/s10052-019-7517-6

[18] L. Bandiera et al., Eur. Phys. J. C, **81**, 238 (2021), https://doi.org/10.1140/epjc/s10052-021-09021-y

[19] T.N. Wistisen et al. Phys. Rev. Accel. Beams, **19**, 071001 (2016), https://doi.org/10.1103/PhysRevAccelBeams.19.071001

[20] L. Bandiera et al. The Eur. Phys. J. C, **81**, 284 (2021), https://doi.org/10.1140/epjc/s10052-021-09071-2

[21] A.I. Akhiezer, and N.F. Shul'ga, *High energy electrodynamics in matter*, (Gordon and Breach Science Publishers, Amsterdam, 1996).

[22] A.A. Greenenko, A.V. Chechkin, and N.F. Shul'ga. Phys. Lett. A, **324**, 82 (2004), https://doi.org/10.1016/j.physleta.2004.02.053

[23] V.V. Tikhomirov. Probl. Atom. Sci. Tech. **3**, 164 (2007), https://vant.kipt.kharkov.ua/ARTICLE/VANT_2007_3/article_2007_3_164.pdf

[24] N.F. Shul'ga, I.V. Kirillin, and V.I. Truten', J. Surf. Investig. **7**, 398 (2013), https://doi.org/10.1134/S1027451013020468

[25] D.S. Gemmell. Rev. Mod. Phys. **46**, 129 (1974), https://doi.org/10.1103/RevModPhys.46.129

[26] M.F. Shulga, V.I. Truten, I.V. Kirillin, The Journal of Kharkiv National University, physical series: "Nuclei, Particles, Fields", **887**, 54 (2010), https://core.ac.uk/download/pdf/46589346.pdf (in Russian)

[27] P.A. Doyle, and P.S. Turner. Acta Crystallogr. A, **24**, 390 (1968), https://doi.org/10.1107/S0567739468000756

[28] I.S. Gradshteyn, and I.M. Ryzhik, *Table of Integrals, Series, and Products*, 7th ed. (Academic Press, London, 2007).

[29] K. Levenberg. Q. Appl. Math. **2**(2), 164 (1944), https://doi.org/10.1090/qam/10666

[30] D.W. Marquardt. SIAM J. Appl. Math. **11**(2), 431 (1963), https://doi.org/10.1137/0111030

ДИФУЗІЯ ВИСОКОЕНЕРГЕТИЧНИХ ЗАРЯДЖЕНИХ ЧАСТИНОК У ПОЛІ ЛАНЦЮЖКІВ АТОМІВ ОРІЄНТОВАНОГО КРИСТАЛА

Ігор В. Кириллін[a,b], **Микола Ф. Шульга**[a,b], **Олександр П. Щусь**[b,a]

[a] Інститут теоретичної фізики ім. О.І. Ахієзера Національного наукового центру «Харківський фізико-технічний інститут» Академічна вул., 1, Харків, 61108, Україна

[b] Харківський національний університет ім. В.Н. Каразіна, майдан Свободи, 4, 61022, Харків, Україна

У роботі проаналізовано залежність показника дифузії високоенергетичних негативно заряджених частинок від енергії поперечного руху в орієнтованому кристалі. Кристал мав осьову орієнтацію відносно напрямку падіння частинок. Аналіз проводився на прикладі π^--мезонів з імпульсом 100 ГеВ/c, які налітали на кристал кремнію, що відповідає умовам, досяжним на вторинному пучку прискорювача CERN SPS. Аналіз показав, що розглядувана залежність не є монотонною. Вона має мінімум в області енергій, які трохи перевищують значення потенціальної енергії частинок у сідловій точці потенціалу кристалічних атомних ланцюжків. При більших значеннях енергії поперечного руху частинок $E_\perp$ показник дифузії зростає зі збільшенням $E_\perp$, оскільки це збільшує середнє значення модуля швидкості руху частинок у площині, ортогональній до кристалічної осі, біля якої відбувається рух. Збільшення показника дифузії при низьких значеннях $E_\perp$ пов'язане з проявом некогерентного розсіяння частинок на теплових коливаннях атомів кристала. Проведений у роботі аналіз представляє інтерес як для глибшого розуміння процесу проходження пучків високоенергетичних негативно заряджених частинок через орієнтовані кристали, так і для вдосконалення методів керування пучками заряджених частинок за допомогою прямих і зігнутих орієнтованих кристалів.

Ключові слова: *каналювання; заряджена частинка високої енергії; дифузія; орієнтований кристал*

INSTABILITY OF ION CYCLOTRON WAVES(ICWS) AT THE EXPENSE OF LOWER HYBRID DRIFT WAVES (LHDWS) TURBULENCE ENERGY

Raksha Mundhra[*], **P.N. Deka**

Department of Mathematics, Dibrugarh University, Assam, India
[*]*Corresponding Author e-mail: rakshamundhra0308@gmail.com*

Instability of ion cyclotron waves(ICWs) is investigated in presence of lower hybrid drift waves(LHDWs) turbulence. Plasma inhomogeneity in the Earth's magnetopause region supports a range of low frequency drift wave turbulent fields due to gradients in density in different regions of the media. One of these drift phenomena is identified as lower hybrid drift waves(LHDWs)which satisfies resonant conditions $\omega - \mathbf{k} \cdot \mathbf{v} = 0$. We have considered a nonlinear wave-particle interaction model where the resonant wave that accelerates the particle in magnetopause may transfer its energy to ion cyclotron waves through a modulated field. In spite of the frequency gaps between the two waves, energy can be transferred nonlinearly to generate unstable ion cyclotron waves which always do not satisfy the resonant condition $\Omega - \mathbf{K} \cdot \mathbf{v} \neq 0$ and the nonlinear scattering condition $\Omega - \omega - (\mathbf{K} - \mathbf{k}) \cdot \mathbf{v} \neq 0$. Here, ω and Ω are frequencies of the resonant and the nonresonant waves respectively and $\mathbf{k}$ and $\mathbf{K}$ are the corresponding wave numbers. We have obtained a nonlinear dispersion relation for ion cyclotron waves (ICWs) in presence of lower hybrid drift waves (LHDWs) turbulence. The growth rate of the ion cyclotron waves using space observational data in the magnetopause region has been estimated.

Keywords: *Ion Cyclotron Waves; Lower Hybrid Drift Waves; Wave Amplification; Density Gradient; Nonlinear wave-particle interaction*

PACS: 52.35.Hr, 52.35.Qz,52.35.Kt,05.45.-a,52.35.-g

1. INTRODUCTION

Plasma covers nearly 99.9% of the universe. A wide range of electrostatic waves and electromagnetic waves dominate the nature of plasma.But, in general a real plasma can never be entirely homogeneous. Plasma is made up of different boundary layers which are very dynamical and active regions comprising many waves. One of them is the LHDWs which are supported by the free energy reserved in density gradients. The LHDWs are strong plasma waves found in Earth's Magnetosphere. According to some scientists, LHDWs cause anomalous resistivity and thus initiate magnetic reconnection (MR).It transfers the energy stored in the magnetic field to particles, further heating and accelerating them[1]. Many observations of the LHDWs have been made in the magnetosphere [2, 3] as well as in laboratory plasmas [4, 5].

For many decades,electrostatic and electromagnetic ion cyclotron waves have been observed, [cf. Gurnett and Frank, 1972; Kintner *et al.,* 1978] in the terrestrial auroral zones.Recently from the data, [cf. McFadden *et al.,*, 1998; Carlson *et al.,* 1998; Lund *et al.,* 1998; Cattell *et al.,* 1998; Chaston *et al.,* 1998] it was found that these waves are the source ion heating (conics)and parallel electron acceleration in the auroral zone. Ion cyclotron frequency is common in the terrestrial magnetosphere. Broughton *et al.,* has also reported the observation of ion cyclotron harmonically related waves in the vicinity of the plasma sheet boundary layer [6].

In Tokamak, LHDWs heating has attracted maximum attention for heating and toroidal current drive efficiency. Here, the ions are directly heated at the lower hybrid resonance layer where they can convert the ion waves into fast ion waves and the latter are strongly Landau damped on ions. Several experiments of tokamaks have disclosed that LHDWs give rise to parametric excitation of ion cyclotron modes [7].

Huba *et al.,* [2] proposed that in various confinement systems of magnetic fusion [e.g., Davidson *et al.,* 1976; Comrnisso and Griem, 1976], the lower hybrid-drift instability [Krall and Liewer, 1971], operates over a large area of magnetotail.Furthermore, it plays a significant role in the development of field line reconnection as a source of anomalous resistivity.Gurnett *et al.,* carried out some experimental observations [1976] considering the theoretical studies of the lower-hybrid-drift instabilities .He found some strong evidence for the existence of lower hybrid drift instability in terms of existence criteria, spectral characteristics, and amplitude of fluctuations.

In the magnetosphere and plasmasphere very often different wave modes are observed at the same time. For example, in the Freja mission,the data analysis of the waves shows a close relationship between Alfven wave activity and ion acoustic wave activity within auroral energization regions [Wahlund *et al.,* 1994]; similarly,lower hybrid wave (LHW) activity has been observed at the same time with ultralow-frequency waves [Olsen *et al.,*

1987; LaBelle and Treumann, 1988; Pottelette *et al.*, 1990]. Again, simultaneous wave activity has also been observed in the active ionospheric sounding rocket experiments [Arnoldy, 1993; Bale *et al.,* 1998]. Colpitts [2015] reported that the Van Allen Probes observations show very strong modulation of whistler, magnetosonic, and lower hybrid waves by EMIC or ultra low-frequency waves. He relates this modulation to wave-wave and/or wave-particle interactions [8].

The inhomogeneous plasmas like the solar corona or planetary magnetospheres one can observe drift waves to propagate extensively. The electrostatic drift waves propagate perpendicular both to the ambient magnetic field and to the gradient due to density gradients or temperature gradients. But, they become unstable during collisions or electron Landau damping. Hence these waves may play an important role in the destabilization process of the magnetotail before a substorm. Fruit *et al.,* 2017 proposed a kinetic model with trapped bouncing electrons for the electrostatic instabilities in the resonant interactions. Thus, in the period of electron bounce period a linearized Vlasov equation is solved for electrostatic fluctuations and through the quasineutrality condition, a dispersion relation is obtained [9].

Singh and Deka (2005) studied the plasma maser effect in inhomogeneous plasma in the presence of drift wave turbulence. Here,they studied the growth rate of the high frequency Bernstein mode in presence of the spatial density gradient parameter [10].

Borgohain and Deka (2010) studied the instability of electrostatic waves in inhomogeneous plasma in presence of drift wave turbulence. Here, they studied the interaction of ion acoustic waves with drift waves [11]. Deka and Senapati (2018) studied the amplification of upper hybrid waves in presence of lower hybrid waves in an inhomogeneous plasma through a non linear wave particle interaction. Here,they studied the energy transfer from the accelerated electrons which are in phase relation with the LHDWs turbulent field to the unstable upper hybrid through a modulated field nonlinearly. On the other hand, dissipation of unstable upper hybrid wave energy is possible through radiation phenomenon after conversion while propagating through inhomogeneous plasma [12].

Deka and Deka (2022) [13] studied the growth rate of whistler mode in presence of kinetic alfven wave turbulence through nonlinear wave–particle interaction. Here, in this model he considered an external force **F** which helps to create a drifting motion.

Kumar *et al.,* (2022) [14] studied the effect of dust charge fluctuations on the parametric upconversion of a lower hybrid wave into an ion cyclotron wave and a side band wave in a two-ion species tokamak plasma. Here, the lower hybrid wave becomes unstable and decays into two modes: an ion cyclotron wave mode and a low frequency lower hybrid side band wave. Here, the growth rate decreases with the increase in the size of dust grains and electron cyclotron frequency.

Our present investigation is based on the lowest order mode-mode coupling process in a turbulent plasma which was proposed by Nambu [19]. This mode-mode coupling and wave energy conversion process was also suggested by Tsytovich [16] simultaneously. This process suggests that even though there is a large frequency difference, wave energy exchange may be possible. Nambu and Tsytovich proposed that if in a plasma both resonant and non-resonant waves are present, wave energy from resonant mode may be transferred to non-resonant waves. By resonant wave, we mean that the Cherenkov resonant condition $\omega - \mathbf{k} \cdot \mathbf{v} = 0$ is satisfied whereas for non- resonant waves both the resonant condition and nonlinear scattering conditions are not satisfied, i.e. $\Omega - \mathbf{K} \cdot \mathbf{v} \neq 0$ and $\Omega - \omega - (\mathbf{K} - \mathbf{k}) \cdot \mathbf{v} \neq 0$. Here, ω and Ω are frequencies of the resonant and the nonresonant waves respectively and $\mathbf{k}$ and $\mathbf{K}$ are the corresponding wave numbers.The LHDWs operates in the frequency range[1] where both ion and electron dynamics play a crucial role: $\omega_{ci} \ll \omega \ll \omega_{ce}$. The wave oscillate at a frequency in between the ion and electron gyroradius.

In this present paper we have studied the interaction of high frequency ICWs with low frequency LHDWs turbulence. Here, we have used a zeroth- order distribution function that satisfies the time independent Vlasov equation. There is a non zero current associated with the drifts; this current represents a free energy that can drive instabilities and further we obtain the dispersion relation as well as estimate the growth rate of ICWs.

2. FORMULATION

We consider a non-uniform electrostatic LHDWs turbulence to be present in the system with propagation vector $k = (k_\perp, 0, k_{//})$. We consider a weak density gradient perpendicular to B_0 of the form [17]

$$n_j^{(0)}(y) = n_j(1 + \epsilon_n y) \tag{1}$$

So, the density gradient is taken along the $\mathbf{y} - direction$ and the external magnetic field $B = B_0(y)$ is taken in the $\mathbf{z} - direction.$ ϵ_n is the density gradient scale length n.

The particle distribution function is considered as

$$f_{0j}(y, v) = \frac{n_j}{(2\pi v_j^2)^{\frac{3}{2}}} \Big[1 + \epsilon_n \Big(y + \frac{v_x}{\Omega_j} \Big) \Big] exp\Big(\frac{-v^2}{2v_j^2} \Big) \tag{2}$$

The first and second velocity moment of the above distribution are

$$\Gamma_j^{(0)} = n_j v_{nj} \hat{y} \tag{3}$$

$$n_j T_j = n_j T_j (1 + \epsilon_n y) + o(\epsilon_n^2) \tag{4}$$

Where the density gradient drift speed of the jth species [17]is

$$v_{nj} = \frac{\epsilon_n v_j^2}{\Omega_j} \tag{5}$$

Here, $\Omega_j = \frac{eB_0}{mc}$ is the cyclotron frequency.Here the subscript j refers to $j = i$ for ions and $j = e$ for electrons.
Now,

The interaction of the high frequency ICWs with low frequency LHDWs turbulence is well explained by the Vlasov-Poisson's equation

$$\left[\frac{\partial}{\partial t} + \mathbf{v}.\frac{\partial}{\partial \mathbf{r}} - \frac{e}{m}(\mathbf{E} + \frac{\mathbf{v} \times \mathbf{B}}{c}).\frac{\partial}{\partial \mathbf{v}} \right] F_{0i}(\mathbf{r}, \mathbf{v}, \mathbf{t}) = 0 \tag{6}$$

$$\nabla \cdot \mathbf{E} = -4\pi e n_i \int f_{0i}(\mathbf{r}, \mathbf{v}, \mathbf{t}) d\mathbf{v} \tag{7}$$

The non-perturbed distribution function and fields are considered according to the linear response theory of the plasma.

$$F_{0i} = f_{0i} + \epsilon f_{1i} + \epsilon^2 f_{2i} \tag{8}$$
$$\mathbf{E}_{0i} = \epsilon \mathbf{E}_l + \epsilon^2 \mathbf{E}_2 \tag{9}$$
$$B_l = B_0 \tag{10}$$

where ϵ is a small parameter associated with LHDWs turbulence field $E_l = (E_{l\perp}, 0, E_{l//})$. f_{0i} is the space and time average parts, f_{1i} , f_{2i} are the fluctuating parts of the distribution function. $\mathbf{E}_2$ is the second order electric field. B_l is the total magnetic field in the system in presence of LHDWs turbulence.But LHDWs is an electrostatic turbulent that doesnot contribute turbulent to the system.
From eq.(6), we have

$$\left[\frac{\partial}{\partial t} + \mathbf{v}.\frac{\partial}{\partial \mathbf{r}} - \frac{e}{m} \left(\epsilon \mathbf{E}_l + \epsilon^2 \mathbf{E}_2 + \frac{\mathbf{v} \times \mathbf{B}_0}{c} \right).\frac{\partial}{\partial \mathbf{v}} \right] \left[f_{0i}(\mathbf{r}, \mathbf{v}, t) + \epsilon f_{1i}(\mathbf{r}, \mathbf{v}, t) + \epsilon^2 f_{2i}(\mathbf{r}, \mathbf{v}, t) \right] = 0 \tag{11}$$

To the order of ϵ,we have

$$\left[\frac{\partial}{\partial t} + \mathbf{v}.\frac{\partial}{\partial \mathbf{r}} - \frac{e}{m} \left(\frac{\mathbf{v} \times \mathbf{B}_0}{c} \right).\frac{\partial}{\partial \mathbf{v}} \right] f_{1i}(\mathbf{r}, \mathbf{v}, t) = \frac{e}{m} \mathbf{E}_l.\frac{\partial}{\partial \mathbf{v}} f_{0i}(\mathbf{r}, \mathbf{v}, t) \tag{12}$$

To find f_{1i}, we use Fourier transforms of the form

$$H(\mathbf{r}, \mathbf{v}, t) = \sum_{\mathbf{k}, w} H(\mathbf{k}, \omega, \mathbf{v}) exp[i(\mathbf{k}.\mathbf{r} - \omega t)] \tag{13}$$

The Fourier component of $f_{1i}(\mathbf{k}, \omega)$ is given by-

$$f_{1i}(\mathbf{k}, \omega) = \left(\frac{ie}{m}\right) \left[\frac{m}{T_i k_\perp} E_{l\perp} \left\{ 1 + \left(\omega - k_{//} v_{//} - \frac{\epsilon_n T_i k_\perp}{m \Omega_i} \right) P_{a,b} \right\} f_{0i} - E_{l//} \frac{\partial f_{0i}}{\partial v_{//}} P_{a,b} \right] \qquad (14)$$

where

$$P_{a,b} = \sum_{a,b} \frac{J_a(\alpha') J_b(\alpha') exp[i(b-a)\theta]}{\omega - k_{//} v_{//} - a\Omega_i} \qquad (15)$$

$$\alpha' = \frac{k_\perp v_\perp}{\Omega_i} \qquad (16)$$

To this quasi-steady state, we consider high frequency electrostatic ICWs with propagating vector $K = (K_\perp, 0, 0)$ with electric field $\delta E = (\delta E_h, 0, 0)$ and a frequency Ω. So, we have $\Omega \approx \Omega_i$ This high frequency non resonant ICWs acts as the perturbation to the system.

Thus the total perturbed electric field and the distribution function are

$$\delta f = \mu \delta f_h + \mu \epsilon \delta f_{lh} + \mu \epsilon^2 \Delta f \qquad (17)$$

$$\delta \mathbf{E} = \mu \delta \mathbf{E}_h + \mu \epsilon \delta \mathbf{E}_{lh} + \mu \epsilon^2 \Delta \mathbf{E} \qquad (18)$$

$$\delta \mathbf{B} = 0 \qquad (19)$$

where $\delta \mathbf{E}_{lh}, \Delta \mathbf{E}$ are the modulation fields, δf_h is the fluctuating part, $\delta f_{lh}, \Delta f$ are the particle distribution function due to modulating field and μ is the smallest parameter for the perturbed field, which is also smaller in compared to ϵ.

Linearizing the Vlasov-Poisson equation to the order $\mu, \mu \epsilon, \mu \epsilon^2$, we have

$$P \delta f_h = \frac{e}{m} \delta \mathbf{E}_h \cdot \frac{\partial}{\partial \mathbf{v}} f_{0i} \qquad (20)$$

$$P \delta f_{lh} = \frac{e}{m} \delta \mathbf{E}_{lh} \cdot \frac{\partial}{\partial \mathbf{v}} f_{0i} + \frac{e}{m} \delta \mathbf{E}_h \cdot \frac{\partial}{\partial \mathbf{v}} f_{1i} + \frac{e}{m} \mathbf{E}_l \cdot \frac{\partial}{\partial \mathbf{v}} \delta f_h \qquad (21)$$

$$P \Delta f = \frac{e}{m} \mathbf{E}_l \cdot \frac{\partial}{\partial \mathbf{v}} \delta f_{lh} + \frac{e}{m} \delta \mathbf{E}_{lh} \cdot \frac{\partial}{\partial \mathbf{v}} f_{1i} \qquad (22)$$

where the operation P is given by-

$$P \equiv \left[\frac{\partial}{\partial t} + \mathbf{v} \cdot \frac{\partial}{\partial \mathbf{r}} - \frac{e}{m} \left(\frac{\mathbf{v} \times \mathbf{B}_0}{c} \right) \cdot \frac{\partial}{\partial \mathbf{v}} \right] \qquad (23)$$

Now, we evaluate the various fluctuating parts of the perturbed distribution function using the Fourier transform and integrating along the unperturbed orbits to obtain the nonlinear dielectric function of ICWs in presence of the LHDWs turbulence.
Now,

$$\delta f_h = \frac{ie}{m} \delta \mathbf{E}_h \sum_a \sum_b \frac{J_a(\alpha) J_b(\alpha) exp\{i(b-a)\theta\}}{\Omega - a\Omega_i} \cdot \frac{\partial}{\partial v_\perp} f_{0i} \qquad (24)$$

where $\alpha = \frac{K_\perp v_\perp}{\Omega_i}$

Again

$$\delta f_{lh} = I_{lh}^1 + I_{lh}^2 + I_{lh}^3 \qquad (25)$$

where

$$I_{lh}^1 = \left(\frac{ie}{m}\right) \sum_a \sum_b \frac{J_a(\alpha'') J_b(\alpha'') exp\{i(b-a)\theta\}}{k_{//} v_{//} - (\Omega - \omega) - a\Omega_i} \left[E_{l\perp} \left(\frac{a\Omega_i}{(K_\perp - k_\perp) v_\perp} \right) \cdot \frac{\partial \delta f_h}{\partial v_\perp} + E_{//} \frac{\partial \delta f_h}{\partial v_{//}} \right] \qquad (26)$$

$$I_{lh}^2 = \left(\frac{ie}{m}\right) \sum_a \sum_b \frac{J_a(\alpha'')J_b(\alpha'')exp\{i(b-a)\theta\}}{k_{//}v_{//} - (\Omega-\omega) - a\Omega_i} \frac{\delta\overrightarrow{E_{lh}}(\overrightarrow{K}-\overrightarrow{k})}{|\overrightarrow{K}-\overrightarrow{k}|}\left[K_\perp\left(\frac{a\Omega_i}{(K_\perp - k_\perp)v_\perp}\right) \cdot \frac{\partial f_{0i}}{\partial v_\perp} + k_{//}\frac{\partial f_{0i}}{\partial v_{//}}\right] \quad (27)$$

$$I_{lh}^3 = \left(\frac{ie}{m}\right)\delta\mathbf{E}_h\frac{\partial f_{1i}}{\partial v_\perp}\sum_a\sum_b\frac{J_a(\alpha)J_b(\alpha)exp\{i(b-a)\theta\}}{(\Omega-\omega) - a\Omega_i} \quad (28)$$

Here,
$\alpha'' = \frac{(K_\perp - k_\perp)v_\perp}{\Omega_i}$, $\alpha = \frac{K_\perp v_\perp}{\Omega_i}$
Again,

$$\Delta f = \left(\frac{ie}{m}\right)\sum_a\sum_b\frac{J_a(\alpha'')J_b(\alpha'')exp\{i(b-a)\theta\}}{k_{//}v_{//} - a\Omega_i - \Omega}\left[E_{l\perp}\left(\frac{a\Omega_i}{(K_\perp - k_\perp)v_\perp}\right) \cdot \frac{\partial\delta f_{lh}}{\partial v_\perp} + E_{l//}\frac{\partial\delta f_{lh}}{\partial v_{//}}\right]$$

$$+ \left(\frac{ie}{m}\right)\frac{\delta\overrightarrow{E_{lh}}(\overrightarrow{K}-\overrightarrow{k})}{|\overrightarrow{K}-\overrightarrow{k}|}\sum_a\sum_b\frac{J_a(\alpha'')J_b(\alpha'')exp\{i(b-a)\theta\}}{k_{//}v_{//} - a\Omega_i - \Omega}\left[K_\perp\left(\frac{a\Omega_i}{(K_\perp - k_\perp)v_\perp}\right) \cdot \frac{\partial f_{1i}}{\partial v_\perp} + k_{//}\frac{\partial f_{1i}}{\partial v_{//}}\right] \quad (29)$$

Here, from Poisson's equation we find the modulated field $\delta\mathbf{E}_{lh}(\mathbf{K}-\mathbf{k})$,

$$\nabla.\delta\mathbf{E}_{lh} = -4\pi en_i\int\delta f_{lh}d\mathbf{v} \quad (30)$$

$$\therefore \delta\mathbf{E}_{lh}(\mathbf{K}-\mathbf{k}) = \frac{-\omega_{pi}^2}{|\mathbf{K}-\mathbf{k}| \cdot L(\mathbf{K}-\mathbf{k})}\Big[\int\sum_a\sum_b\frac{J_a(\alpha'')J_b(\alpha'')exp\{i(b-a)\theta\}}{k_{//}v_{//} - (\Omega-\omega) - a\Omega_i}\Big\{E_{l\perp}\left(\frac{a\Omega_i}{(K_\perp - k_\perp)v_\perp}\right) \cdot \frac{\partial\delta f_{lh}}{\partial v_\perp}$$

$$+ E_{l//}\frac{\partial\delta f_{lh}}{\partial v_{//}}\Big\} + \int\delta\mathbf{E}_h\sum_a\sum_b\frac{J_a(\alpha)J_b(\alpha)exp\{i(b-a)\theta\}}{(\Omega-\omega) - a\Omega_i} \cdot \frac{\partial f_{1i}}{\partial v_\perp}\Big]d\mathbf{v} \quad (31)$$

where

$$L(\mathbf{K}-\mathbf{k}) = 1 + \frac{\omega_{pi}^2}{|\mathbf{K}-\mathbf{k}|}\int\sum_a\sum_b\frac{J_a(\alpha'')J_b(\alpha'')exp\{i(b-a)\theta\}}{k_{//}v_{//} - (\Omega-\omega) - a\Omega_i}\Big\{K_\perp\left(\frac{a\Omega_i}{(K_\perp - k_\perp)v_\perp}\right) \cdot \frac{\partial f_{0i}}{\partial v_\perp} + k_{//}\frac{\partial f_{0i}}{\partial v_{//}}\Big\}d\mathbf{v} \quad (32)$$

Again, using the Poisson equation we obtain the dielectric response function :

$$\nabla.\delta\mathbf{E}_h = -4\pi en_i\int[\delta f_h + \Delta f]d\mathbf{v} \quad (33)$$

we have

$$\delta E_h(\mathbf{K},\Omega)\epsilon_h(\mathbf{K},\Omega) = 0 \quad (34)$$

The dispersion relation $\epsilon_h(\mathbf{K},\Omega)$ of ion cyclotron wave is evaluated using the equation given as-

$$\epsilon_h(\mathbf{K},\Omega) = \epsilon_0(\mathbf{K},\Omega) + \epsilon_d(\mathbf{K},\Omega) + \epsilon_p(\mathbf{K},\Omega) \quad (35)$$

where $\epsilon_0(\mathbf{K},\Omega)$ is the linear part, $\epsilon_d(\mathbf{K},\Omega)$ is the direct coupling part and $\epsilon_p(\mathbf{K},\Omega)$ is the polarization coupling part.

So, we have

$$\epsilon_0(\mathbf{K}, \Omega) = 1 + \frac{\omega_{pi}^2}{|K_\perp|^2} \int \frac{n_j}{v_j^2} [1 + (\Omega - \frac{v_{nj}K_\perp}{n_j})f_{oi}] \sum_a \sum_b \frac{J_a(\alpha)J_b(\alpha)exp\{i(b-a)\theta\}}{\Omega - a\Omega_i} d\mathbf{v} \tag{36}$$

Here, $v_{nj} = \frac{\epsilon_n v_j^2}{\Omega_j}$ is the density gradient drift speed of the jth species. The subscript j represents ions, $j = i$. v_{nj} bears the sign of e_j , there is a non-zero current J_0 associated with these drifts; this current represents a free energy that can drive instabilities.

$$\epsilon_d(\mathbf{K}, \Omega) = -\frac{\omega_{pi}^2}{|K_\perp|^2} (\frac{e}{m})^2 |E_{l\perp}|^2 P_{a,b}(\frac{a\Omega_i}{(K_\perp - k_\perp)v_\perp}) \frac{\partial}{\partial v_\perp} \Big[Q_{s,t}(\frac{s\Omega_i}{(K_\perp - k_\perp)v_\perp}) \frac{\partial}{\partial v_\perp} \{R_{u,v} \frac{n_j}{v_j} [1 + (\Omega - \frac{v_{nj}K_\perp}{n_j})$$

$$f_{oi}]\} + S_{a,b} \frac{\partial}{\partial v_\perp} \{\frac{m}{T_i k_\perp} \{1 + (\omega - k_{//}v_{//} - \frac{\epsilon T_i K_\perp}{m\Omega_i})\}\} T_{p,q} f_{0i} \Big] d\mathbf{v} - \frac{\omega_{pi}^2}{|K_\perp|^2} (\frac{e}{m})^2 |E_{l//}|^2 P_{a,b} \frac{\partial}{\partial v_{//}}$$

$$\Big[Q_{s,t} \frac{\partial}{\partial v_{//}} \{R_{u,v} \frac{n_j}{v_j} [1 + (\Omega - \frac{v_{nj}K_\perp}{n_j})f_{oi}]\} + S_{a,b} \frac{\partial}{\partial v_\perp} \{T_{p,q} \frac{\partial f_{0i}}{\partial v_{//}}\} \Big] d\mathbf{v} \tag{37}$$

where

$$P_{a,b} = \sum_a \sum_b \frac{J_a(\alpha'')J_b(\alpha'')exp\{i(b-a)\theta\}}{k_{//}v_{//} - a\Omega_i - \Omega} \tag{38}$$

$$Q_{s,t} = \sum_s \sum_t \frac{J_s(\alpha'')J_t(\alpha'')exp\{i(t-s)\theta\}}{k_{//}v_{//} - s\Omega_i - (\Omega - \omega)} \tag{39}$$

$$P_{u,v} = \sum_u \sum_v \frac{J_u(\alpha)J_v(\alpha)\frac{u\Omega_i}{K_\perp v_\perp}exp\{i(v-u)\theta\}}{\Omega - u\Omega_i} \tag{40}$$

$$S_{a,b} = \sum_a \sum_b \frac{J_a(\alpha)J_b(\alpha)\frac{a\Omega_i}{K_\perp v_\perp}exp\{i(b-a)\theta\}}{(\Omega - \omega) - a\Omega_i} \tag{41}$$

$$T_{p,q} = \sum_p \sum_q = \frac{J_p(\alpha)J_q(\alpha)exp\{i(q-p)\theta\}}{\omega - k_{//}v_{//} - a\Omega_i} \tag{42}$$

Again

$$\epsilon_p = -\frac{\omega_{pi}^4}{K_\perp^2} \frac{(\frac{e}{m})^2}{|\mathbf{K} - \mathbf{k}|^2 L(\mathbf{K} - \mathbf{k})} [(A + B) \times (C + D)] \tag{43}$$

where

$$A = |E_{l\perp}|^2 \int \sum_a \sum_b \frac{J_a(\alpha'')J_b(\alpha'')(\frac{a\Omega_i}{(K_\perp - k_\perp)v_\perp})exp\{i(b-a)\theta\}}{k_{//}v_{//} - a\Omega_i - \Omega} \times \frac{\partial}{\partial v_\perp} \Big[\frac{J_s(\alpha'')J_t(\alpha'')exp\{i(t-s)\theta\}}{k_{//}v_{//} - s\Omega_i - (\Omega - \omega)}$$

$$\{K_\perp(\frac{p\Omega_i}{(K_\perp - k_\perp)v_\perp})\frac{\partial f_{0i}}{\partial v_\perp} + k_{//}\frac{\partial f_{0i}}{\partial v_{//}}\} \Big] d\mathbf{v} + \int \sum_a \sum_b \frac{J_a(\alpha'')J_b(\alpha'')exp\{i(b-a)\theta\}}{k_{//}v_{//} - a\Omega_i - (\Omega - \omega)}$$

$$\Big[\sum_u \sum_v \frac{J_u(\alpha)J_v(\alpha)exp\{i(v-u)\theta\}}{\Omega - u\Omega_i} \frac{\partial f_{0i}}{\partial v_\perp} \{|E_{l\perp}|^2(\frac{u\Omega_i}{(K_\perp - k_\perp)v_\perp})\frac{\partial}{\partial v_\perp} + |E_{l//}|^2 \frac{\partial}{\partial v_{//}}\} \Big] d\mathbf{v} \tag{44}$$

$$B = |E_{l//}|^2 \int \sum_a \sum_b \frac{J_a(\alpha'')J_b(\alpha'')exp\{i(b-a)\theta\}}{k_{//}v_{//} - a\Omega_i - \Omega} \times \frac{\partial}{\partial v_{//}} \Big[\frac{J_s(\alpha'')J_t(\alpha'')exp\{i(t-s)\theta\}}{k_{//}v_{//} - s\Omega_i - (\Omega - \omega)}$$

$$\{K_\perp(\frac{p\Omega_i}{(K_\perp - k_\perp)v_\perp})\frac{\partial f_{0i}}{\partial v_\perp} + k_{//}\frac{\partial f_{0i}}{\partial v_{//}}\} \Big] d\mathbf{v} + \int \sum_a \sum_b \frac{J_a(\alpha)J_b(\alpha)exp\{i(b-a)\theta\}}{(\Omega - \omega) - a\Omega_i} \Big[(|E_{l\perp}|^2 + |E_{l//}|^2)$$

$$\frac{\partial}{\partial v_\perp}\Big\{\frac{m}{T_i k_\perp}1 + (\omega - k_{//}v_{//} - \frac{\epsilon_n T_i K_\perp}{m\Omega_i})\sum_p\sum_q\frac{J_p(\alpha)J_q(\alpha)exp\{i(q-p)\theta\}}{\omega - k_{//}v_{//} - a\Omega_i}\}f_{0i}\Big\}$$

$$+ |E_{l//}|^2\frac{\partial}{\partial v_\perp}\{\sum_p\sum_q\}\frac{J_p(\alpha)J_q(\alpha)exp\{i(q-p)\theta\}}{\omega - k_{//}v_{//} - a\Omega_i}\frac{\partial f_{0i}}{\partial v_{//}}\Big]d\mathbf{v} \tag{45}$$

$$C = \int\sum_s\sum_t\frac{J_s(\alpha'')J_t(\alpha'')exp\{i(t-s)\theta\}}{k_{//}v_{//} - s\Omega_i - (\Omega - \omega)}\Big[\{(\frac{s\Omega_i}{(K_\perp - k_\perp)v_\perp})(\frac{\partial}{\partial v_\perp} + \frac{\partial}{\partial v_{//}})$$

$$\sum_u\sum_v\frac{J_u(\alpha)J_v(\alpha)exp\{i(v-u)\theta\}}{\Omega - u\Omega_i}\frac{\partial f_{0i}}{\partial v_\perp}\Big]d\mathbf{v} + K_\perp\int\sum_a\sum_b\frac{J_a(\alpha'')J_b(\alpha'')(\frac{a\Omega_i}{(K_\perp - k_\perp)v_\perp})exp\{i(b-a)\theta\}}{k_{//}v_{//} - a\Omega_i - \Omega}$$

$$\frac{\partial}{\partial v_\perp}(\sum_p\sum_q\frac{J_p(\alpha)J_q(\alpha)exp\{i(q-p)\theta\}}{\omega - k_{//}v_{//} - a\Omega_i}\frac{\partial f_{0i}}{\partial v_{//}})d\mathbf{v} \tag{46}$$

$$D = \int\sum_a\sum_b\frac{J_a(\alpha)J_b(\alpha)exp\{i(b-a)\theta\}}{(\Omega - \omega) - a\Omega_i}\cdot\frac{\partial}{\partial v_\perp}\Big[\frac{m}{T_i K_\perp}\{1 + (\omega - k_{//}v_{//} - \frac{\epsilon T_i K_\perp}{m\Omega_i})$$

$$\sum_p\sum_q\frac{J_p(\alpha)J_q(\alpha)exp\{i(q-p)\theta\}}{\omega - k_{//}v_{//} - a\Omega_i + i0}\}f_{0i} - \sum_p\sum_q\frac{J_p(\alpha)J_q(\alpha)exp\{i(q-p)\theta\}}{\omega - k_{//}v_{//} - a\Omega_i + i0}\frac{\partial f_{0i}}{\partial v_{//}}\Big]d\mathbf{v}$$

$$+ \int\sum_a\sum_b\frac{J_a(\alpha'')J_b(\alpha'')exp\{i(b-a)\theta\}}{k_{//}v_{//} - a\Omega_i - \Omega}\Big[\{K_\perp(\frac{a\Omega_i}{(K_\perp - k_\perp)v_\perp})\cdot\frac{\partial}{\partial v_\perp} + k_{//}\frac{\partial}{\partial v_{//}}\}$$

$$\frac{m}{T_i k_\perp}\{1 + (\omega - k_{//}v_{//} - \frac{\epsilon_n T_i K_\perp}{m\Omega_i})\sum_p\sum_q\frac{J_p(\alpha)J_q(\alpha)exp\{i(q-p)\theta\}}{\omega - k_{//}v_{//} - a\Omega_i}\}f_{0i}\Big]d\mathbf{v} \tag{47}$$

3. GROWTH RATE

We have obtained the growth rate by using the formula:

$$\frac{\gamma_h}{\Omega} = -\Big[\frac{Im\epsilon_p + \frac{1}{2}\frac{\partial^2\epsilon_0}{\partial\Omega\partial t}}{\Omega(\frac{\partial\epsilon_0}{\partial\Omega})}\Big]_{\Omega=\Omega_i} \tag{48}$$

The second part of the expression of the growth rate is due to the reverse absorption effect, which is in our case is given by-

$$\frac{\partial^2\epsilon_0}{\partial\Omega\partial t} = \frac{\omega_{pi}^2}{K_\perp^2}(\frac{n_j}{v_j})\int\Big[\sum_a\sum_b\frac{J_a(\alpha)J_b(\alpha)exp\{i(b-a)\theta\}}{\Omega - a\Omega_i}\times\{(1 - \frac{v_{nj}K_\perp}{n_j})\frac{1}{\Omega - a\Omega_i}\}\frac{\partial f_{0i}}{\partial t}\Big]d\mathbf{v} \tag{49}$$

After partial integration, we find that the contribution of $\frac{\partial^2\epsilon_0}{\partial\Omega\partial t}$ in the growth rate becomes zero due to the reverse absorbtion effect.

Now, we consider the plasma maser interaction between the ICWs and LHDWs turbulence. The condition for the plasma maser is $\omega = k_{//}v_{//}$ and assuming $\Omega < Kv_{//}$. Here, firstly we estimate the linear part of the dielectric function of the ICWs from $eq^n(36)$. Considering the fact that for the ICWs, the most dominant contribution to Bessel sums come from the term $a = b = 1, s = t = u = v = p = q = 1$.

We have evaluated the linear part of the dispersion relation of the ion cyclotron wave as-

$$\epsilon_0 = 1 + \frac{\omega_{pi}^2}{K_\perp^2}\frac{\Omega_i\Lambda_1}{\Omega - \Omega_i} \tag{50}$$

So, we have

$$\frac{\partial\epsilon_0}{\partial\Omega} = \frac{\omega_{pi}^2}{K_\perp^2}\Big(\frac{-\Lambda_1\Omega_i}{(\Omega - \Omega_i)^2}\Big) \tag{51}$$

The imaginary part of the direct coupling term after partial integration, we have obtained-

$$Im\epsilon_d(\mathbf{k},\Omega) = 0 \tag{52}$$

Again,
For evaluating the imaginary part of the polarization coupling term, we have-

$$Im\epsilon_p(\mathbf{K},\Omega) = -\frac{\omega_{pi}^4}{K_\perp^2}\frac{(\frac{e}{m})^2}{|\mathbf{K}-\mathbf{k}|^2 L(\mathbf{K}-\mathbf{k})}\int[A\times ImD + C\times ImB]d\mathbf{v} \tag{53}$$

Now,

$$A = \left[|E_{l\perp}|^2\int P_{a,b}(\frac{a\Omega_i}{(K_\perp - k_\perp)v_\perp})\frac{\partial}{\partial v_\perp}[Q_{s,t}\{K_\perp(\frac{s\Omega_i}{(K_\perp - k_\perp)v_\perp})\frac{n_j}{v_j}[1+(\Omega - \frac{v_{nj}K_\perp}{n_j})f_{0i}] + k_{//}\frac{\partial f_{0i}}{\partial v_{//}}\}]\right.$$
$$\left.+\int Q_{s,t}[\frac{n_j}{v_j}[1+(\Omega - \frac{v_{nj}K_\perp}{n_j})\{|E_{l\perp}|^2(\frac{u\Omega_i}{(K_\perp - k_\perp)v_\perp})\frac{\partial R_{u,v}}{\partial v_\perp} + |E_{l//}|^2\frac{\partial R_{u,v}}{\partial v_{//}}\}]\right]2\pi dv_\perp dv_{//} \tag{54}$$

Here, after partial integration the first part of the product is contributing zero. So, we have-

$$A = 0 \tag{55}$$

Again,

$$ImB = |E_{l//}|^2\frac{\Lambda_2 n_j}{(K_\perp - k_\perp)v_j}\frac{\sqrt{\pi}}{v_e^2|k_{//}|}\left[\{K_\perp\frac{\epsilon}{\Omega_i} + k_{//}\frac{2v_d}{v_e^2}\}\{1+\frac{(K_\perp - k_\perp)^2 v_e^2}{4\Omega_i^2(\Omega_i - \Omega + (K_\perp - k_\perp))}(\Omega - \frac{v_{nj}K_\perp}{n_j})\}\right]$$
$$exp\{-(\frac{v_d}{v_e})^2\} - \frac{\sqrt{\pi}}{v_d|k_{//}|}\frac{\Lambda_2}{v_e^2}\frac{k_{//}v_d - \Omega}{(k_{//}v_d - \Omega)^2 - \Omega_i^2}\{(|E_{l\perp}|^2 + |E_{l//}|^2)\frac{\epsilon}{\Omega_i} + 2|E_{l//}|^2\frac{2v_d}{v_e^2}\} \tag{56}$$

$$C = \frac{4k_{//}}{K_\perp v_e^4}\frac{\Omega_i^2}{(K_\perp - k_\perp)}\frac{(\Omega^2 + \Omega_i^2)}{(\Omega^2 - \Omega_i^2)^3}\Lambda_2\frac{n_j}{v_j}(\Omega - \frac{\epsilon v_j^2 K_\perp}{n_j\Omega_i}) + \frac{\sqrt{\pi}}{v_d|k_{//}|}\frac{4K_\perp}{v_e^4}\Lambda_2\frac{k_{//}v_d - \Omega}{(k_{//}v_d - \Omega)^2 - \Omega_i^2} \tag{57}$$

Where,
$\Lambda_1 = \int_0^\infty 2\pi v_\perp J_0^2(\alpha_i)f_{0e}(v_\perp)dv_\perp$, $\Lambda_2 = \int_0^\infty 2\pi v_\perp^2 J_0^2(\alpha_i)f_{0e}(v_\perp)dv_\perp$

$v_d = \frac{\omega}{k_{//}}$ is the phase velocity.

v_e is the electron thermal velocity.

$Im\int_{-\infty}^\infty\frac{\frac{\partial f_{0e}(v_{//})}{\partial v_{//}}}{-\omega + k_{//}v_{//} + i0^+}dv_{//} = -\int_{-\infty}^\infty \pi\delta(\omega - k_{//}v_{//})\frac{\partial f_{0e}(v_{//})}{\partial v_{//}} = \frac{2\sqrt{\pi}}{v_e^3}\frac{\omega}{k_{//}|k_{//}|exp\{-(\frac{\omega}{k_{//}v_e})^2\}}$

So, we have the growth rate as-

$$\frac{\gamma_p}{\Omega} = \frac{a}{b} \tag{58}$$

where

$$a = -\frac{\omega_{pi}^4}{K_\perp^2}\frac{(\frac{e}{m})^2}{(\mathbf{K}-\mathbf{k})^2|k_{//}|^2}(ImB\times C) \tag{59}$$

$$b = \Omega\frac{\partial\epsilon_0}{\partial\Omega} = \Omega\frac{\omega_{pi}^2}{K_\perp^2}\left(\frac{-\Lambda_1\Omega_i}{(\Omega - \Omega_i)^2}\right) \tag{60}$$

$$L|\mathbf{K}-\mathbf{k}|^2 \sim k_{//}^2 \tag{61}$$

4. DISCUSSIONS AND CONCLUSIONS

In earlier studies, Tang *et al.,* (2015) [28] in the THEMIS observation of electrostatic ion cyclotron(EIC) waves and associated ion heating found that the gradient in plasma density are the possible sources of free energy for the EIC waves. Rosenberg *et al.,* (2009) [29], in his paper discussed that wave frequency increases, the growth rate of higher harmonic EIC waves tends to increase within certain parameter ranges. Khaira *et al.,* (2015) [30], considered the Kappa distribution function and discussed the growth rate with respect to wave vector and its effects.

Here, we have considered the inhomogeneous plasma model for which the particle distribution function is constructed on a zeroth order distribution function that satisfies the time independent Vlasov equation. We assume a weak density gradient perpendicular to B_0 and we may take the magnetic field to be uniform. Here, we have considered v_{nj} is independent of m_j. We have considered the instabilities driven by the ion density drift. v_{nj} carries a nonzero current J_0 which represents free energy that can drive instabilities. The ion density drift wave satisfies $\omega_r \simeq k_y v_{ni}$ at $k_y a_i \leq 1$ and ω_r remains less than Ω_i. At perpendicular propagation, we have ICWs at $\omega_r > \Omega_i$.

Here, we have the effect of density gradient parameter in all the fluctuating parts of the particle distribution function. The study have been performed space plasma and investigated the amplification process of the non-resonant wave by estimating the growth rate considering only the dominant terms, neglecting other terms. Though the wave amplification process is mostly affected by the dominant term but we cannot neglect the influence of other terms involved in the calculation of growth rate.

Now, we consider the observational data in magnetopause of magnetosphere [32], [33]-
$K_\perp = 1.71 m^{-1}$, $\omega_{pi} = 1.32 \times 10^3 Hz$, $\omega_i = 2.1 \times 10^6 Hz$, $v_d \sim 10^6 ms^{-1}$, $E_{l\perp} = 1.4 \times 10^{-4} vm^{-1}$, $E_{l//} = 10^5 vm^{-1}$, $\frac{e}{m} = 1.75 \times 10^{11} Ckg^{-1}$, $k_{//} = 2\pi \times 10^{-5} m^{-1}$, $k_\perp \sim 10^{-3} m^{-1}$, $v_e = 4.19 \times 10^5 ms^{-1}$, $\Omega = 5 \times 10^6 Hz$, $\Omega_i = 5.6 \times 10^6 Hz$, $\Lambda_1 = 1$, $\Lambda_2 = \frac{\sqrt{\pi}}{2} v_e$

For the regions of plasma with very weak density gradient $(\epsilon_n = 0)$ as-

$$\frac{\gamma_p}{\Omega} \sim 10^{-6}. \tag{63}$$

The growth rate with a gradient $(\epsilon_n \neq 0)$, we have
For $(\epsilon_n = 0.1)$,

$$\frac{\gamma_p}{\Omega} \sim 10^{-3}. \tag{64}$$

So, this shows that due to the presence of density gradient, free energy become apparent and thus influences the amplification process of ICWs in presence of LHDWs turbulence.

Now, we have plotted the graph of $\frac{\gamma_p}{\Omega}$ vs $\frac{\omega_{pi}}{\Omega_i}$ for ICWs with different values of the density gradient parameter.
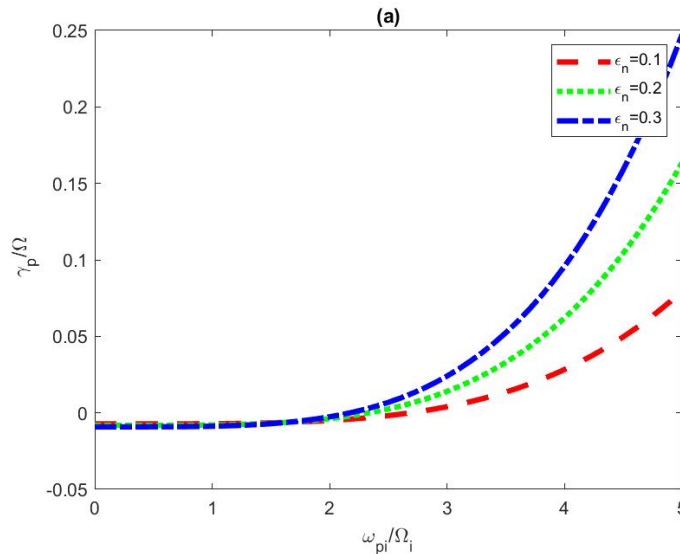
Fig.A.1: *Growth Rate*

Again, we have plotted the graph of $\frac{\gamma_p}{\Omega}$ vs v_{nj} for ICWs with different values of the density gradient parameter.
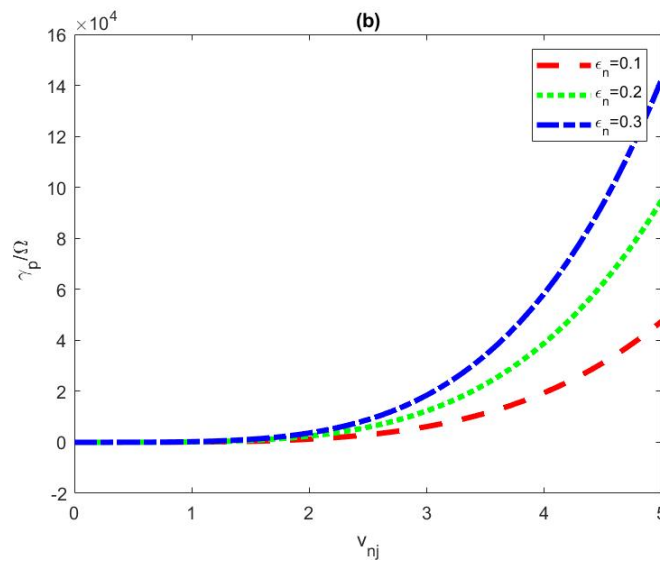
Fig.A.2: *Growth Rate vs density drift speed*

So, it has been clear from the Fig.A.1, that for different values of ϵ_n, we have growth rate increases with the increase in the value of the density gradient parameter. The growth rate is faster with the increase in value of ϵ_n. We can also say from Fig.A.2, that the growth rate increases for different density drift speed. Here, drift speed increases, frequency of the drift wave increases with successively higher ICWs and thus yields larger growth rate with the help of non-linear approach and these agrees with the earlier results of Gary in terms of linear approach [31]. Thus, we can say that there is an amplification of waves due to the interaction of ICWs and LHDWs. So, for the study of ICWs instability, we have identified that the density gradient and the density drift speed may play a significant role.

Data Availability Statement

Data sharing not applicable to this article as no datasets were generated or analysed during the current study.

ORCID

Raksha Mundhra, https://orcid.org/0000-0002-7486-9759; **P.N. Deka**, https://orcid.org/0000-0001-9485-9294

REFERENCES

[1] Cecilia Norgren, Swedish Institute of Space Physics and Department of Physics and Astronomy, Uppsala University, Sweden, ISSN: 1401-5757, UPTEC F 11 057 (2011)

[2] J.D. Huba, N.T. Gladd, and K. Papadopoulos, "Lower-hybrid-drift wave turbulence in the distant magnetotail," J. Geophys. Res. **83**(A11), 5217–5226 (1978).https://doi.org/10.1029/JA083iA11p05217

[3] S.D. Bale, F.S. Mozer, and T. Phan, "Observation of lower hybrid drift instability in the diffusion region at a reconnecting magnetopause," Geophys. Res. Lett. **29**(24), 2180 (2002). https://doi.org/10.1029/2002GL016113

[4] T.A. Carter, M. Yamada, H. Ji, R.M. Kulsrud, and F. Trintchouk, "Experimental study of lower-hybrid drift turbulence in a reconnecting current sheet," Phys. Plasmas, **9**(8), 3272–3288 (2002). https://doi.org/10.1063/1.1494433

[5] W. Fox, M. Porkolab, J. Egedal, N. Katz, and A. Le, "Laboratory observations of electron energization and associated lower-hybrid and Trivelpiece–Gould wave turbulence during magnetic reconnection," Phys. Plasmas, **17**(7), 072303 (2010). https://doi.org/10.1063/1.3435216

[6] J.D. Menietti, P. Schippers, O. Santolík, D.A. Gurnett, F. Crary, and A.J. Coates, "Ion cyclotron harmonics in the Saturn downward current auroral region," J. Geophys. Res. **116**, A12234 (2011). https://doi.org/10.1029/2011JA017102

[7] G. Praburam, Ph.D.Thesis, Department of Physics, Indian Institute of Technology, Delhi, India (1989). http://eprint.iitd.ac.in/handle/2074/4073

[8] G.V. Khazanov, S. Boardsen, E.N. Krivorutsky, M.J. Engebretson, D. Sibeck, S. Chen, and A. Breneman, "Lower hybrid frequency range waves generated by ion polarization drift due to electromagnetic ion cyclotron waves: Analysis of an event observed by the Van Allen Probe B," J. Geophys. Res. Space Physics, **122**, 449–463 (2017). https://doi.org/10.1002/2016JA022814

[9] G. Fruit, P. Louarn, and A. Tur, "Electrostatic drift instability in a magnetotail configuration: The role of bouncing electrons," Phys. Plasmas, **24**(3), 032903 (2017). https://doi.org/10.1063/1.4978566

[10] M. Singh, and P.N. Deka, "Plasma-maser Effect in Inhomogeneous Plasma in the Presence of Drift Wave Turbulence," Phys. Plasmas, **12**(10), 102304 (2005). https://doi.org/10.1063/1.2087587

[11] P.N. Deka, and A. Borgohain, "On unstable electromagnetic radiation through nonlinear wave–particle interactions in presence of drift wave turbulence," J.Plasma Phys. **78**(5), 515-524 (2012). https://doi.org/10.1017/S0022377812000207

[12] P. Senapati, and P.N. Deka, "Instability of Electron Bernstein Mode in Presence of Drift Wave Turbulence Associated with Density and Temperature Gradients," J. Fusion Energy, **39**, 477–490 (2020). https://doi.org/10.1007/s10894-020-00269-y

[13] J.K. Deka, and P.N. Deka, "Emission of whistler mode radiation with kinetic Alfven wave in burning plasma," Eur. Phys. J. Plus, **137**, 1116 (2022). https://doi.org/10.1140/epjp/s13360-022-03330-1

[14] A. Kumar, R. Gupta, and J. Sharma, "Electromagnetic Weibel instability in spatial anisotropic electron–ion plasmas," AIP Advances, **12**(6), 065013 (2022). https://doi.org/10.1063/5.0092835

[15] M. Nambu, Laser Part. Beams, "A new maser effect in plasma turbulence," **1**, 427 (1983). https://doi.org/10.1017/S0263034600000513

[16] V.N. Tsytovich, "Mechanism for wave absorption or amplification in stochastic acceleration of particles," Sov. Phys. JETP, **62**, 483-488 (1985). http://www.jetp.ras.ru/cgi-bin/dn/e_062_03_0483.pdf

[17] S.P. Gary, *Theory of Space Plasma Microinstabilities*, (Cambridge University Press, Cambridge, UK, 1993).

[18] M. Nambu, "Interaction between the Electron-Cyclotron Emissions at $(n+1/2)\Omega_e$ and the Ring-Current Protons in Space," Phys. Rev. Lett. **34**, 387 (1975). https://doi.org/10.1103/PhysRevLett.34.387

[19] M. Nambu, S. Bujarbarua, and S.N. Sarma, "Plasma maser theory for magnetized plasma," Phys. Rev. A, **35**, 798 (1987). https://doi.org/10.1103/PhysRevA.35.798

[20] L.D. Landau, "On the vibration of the electronic plasma," J. Phys. USSR, **10**, 25 (1946).

[21] T.H. Stix, *Waves in Plasma*, ()AIP, New York, 1992).

[22] N.A. Krall, and A.W. Trivelpiece, *Principles of Plasma Physics*, (McGraw Hill Kogakusha Ltd., New York, 1973). https://doi.org/10.1119/1.1987587

[23] S. Ichimaru, *Basic Principles Of Plasma Physics: A Statistical Approach*. 1st ed. (CRC Press, 1973). https://doi.org/10.1201/9780429502118

[24] F. Chen, *Introduction to Plasma Physics*, (Plenum Press, New York, 1974).

[25] M. Singh, P.N. Deka, "Plasma-maser instability of the ion acoustics wave in the presence of lower hybrid wave turbulence in inhomogeneous plasma," Pramana - J. Phys. **66**, 547–561 (2006). https://doi.org/10.1007/BF02704498

[26] T.J. Bradley, S.W. Cowley, G. Provan, G.J. Hunt, E.J. Bunce, *et al.,* "Field-Aligned Currents in Saturn's Nightside Magnetosphere: Subcorotation and Planetary Period Oscillation Components During Northern Spring," J. Geophys. Res. **123**, 3602-3636 (2018). https://api.semanticscholar.org/CorpusID:54949745

[27] P.N. Deka, and A. Borgohain, "Amplification of ion acoustic wave in an inhomogeneous plasma through nonlinear wave-particle interaction with drift wave turbulence," Phys.Plasmas, **18**, 042311 (2011). https://api.semanticscholar.org/CorpusID:120942154

[28] X. Tang, C. Cattell, R. Lysak, L.B. Wilson, L. Dai, and S. Thaller, "THEMIS observations of electrostatic ion cyclotron waves and associated ion heating near the Earth's dayside magnetopause," J. Geophys. Res. Solid Earth, **120**(5), 3380-3392 (2015). https://doi.org/10.1002/2015JA020984

[29] M. Rosenberg, and R. Merlino, "Instability of higher harmonic electrostatic ion cyclotron waves in a negative ion plasma," J. Plasma Phys. **75**, 495-508 (2009). https://api.semanticscholar.org/CorpusID:11846857

[30] V. Khaira, and G. Ahirwar, "Dispersion relation of electrostatic ion cyclotron waves in multi-component magneto-plasma," AIP Conf. Proc. **1670**(1), 030016 (2015). https://doi.org/10.1063/1.4926700

[31] S.P. Gary, "Wave-particle transport from electrostatic instabilities," Phys. Fluids, **23**(6), 1193–1204 (1980). https://doi.org/10.1063/1.863120

[32] M. Malingre, R. Pottelette, N. Dubouloz, P.A. Lindqvist, G. Holmgren, and B. Aparicio, "Sporadic electromagnetic emissions in the Akr frequency range associated with electrostatic plasma turbulence," Geophys. Res. Lett. **19**, 1339-1342 (1992). https://doi.org/10.1029/92GL01154

[33] J. Benáček, M. Karlický and L.V. Yasnov, "Temperature dependent growth rates of the upper-hybrid waves and solar radio zebra patterns," A&A, **598**, A106 (2017). https://doi.org/10.1051/0004-6361/201629717

[34] A.B. Zylstra, O.A. Hurricane, D.A. Callahan, A.L. Kritcher, J.E. Ralph, H.F. Robey, J.S. Ross, *et al.*,, "Burning plasma achieved in inertial fusion," Nature, 601(7894), 542–548 (2022). https://doi.org/10.1038/s41586-021-04281-w

НЕСТАБІЛЬНІСТЬ ІОННИХ ЦИКЛОТРОННИХ ХВИЛЬ (ICW) ЗА РАХУНОК ЕНЕРГІЇ ТУРБУЛЕНТНОСТІ НИЖНІХ ГІБРИДНИХ ДРЕЙФОВИХ ХВИЛЬ (LHDW)

Ракша Мундхра, П.Н. Дека

Факультет математики, Університет Дібругарх, Ассам, Індія

Досліджено нестабільність іонних циклотронних хвиль (ІЦХ) за наявності турбулентності нижньогібридних дрейфових хвиль (НГДХ). Неоднорідність плазми в області магнітопаузи Землі підтримує діапазон низькочастотних хвиль дрейфових турбулентних полів через градієнти густини в різних областях середовища. Одне з цих явищ дрейфу ідентифіковано як нижчі гібридні дрейфові хвилі (LHDWs), які задовольняють умові резонансу $\omega - \mathbf{k} \cdot \mathbf{v} = 0$.ю Ми розглянули нелінійну взаємодію хвилі та частинок модель, де резонансна хвиля, яка прискорює частинку в магнітопаузі, може передавати свою енергію іонним циклотронним хвилям через модульоване поле. Незважаючи на частотні проміжки між двома хвилями, енергія може передаватися нелінійно для генерації нестабільних іонних циклотронних хвиль, які завжди не задовольняють умові резонансу $\Omega - \mathbf{K} \cdot \mathbf{v} \neq 0$ та умові нелінійного розсіювання $\Omega - \omega - (\mathbf{K} - \mathbf{k}) \cdot \mathbf{v} \neq 0$. Тут ω і Ω — це частоти резонансної та нерезонансної хвиль відповідно, а $\mathbf{k}$ та $\mathbf{K}$ — відповідні хвильові числа. Отримано нелінійне дисперсійне співвідношення для іонних циклотронних хвиль (ICW) за наявності турбулентності нижніх гібридних дрейфових хвиль (LHDWs). Оцінено швидкість зростання іонних циклотронних хвиль з використанням даних космічних спостережень в області магнітопаузи.

Ключові слова: *іонні циклотронні хвилі; нижні гібридні дрейфові хвилі; посилення хвиль; градієнт густини; нелінійна взаємодія хвиля-частинка*

NUMERICAL SIMULATION AND ANALYSIS OF THE MODIFIED BURGERS' EQUATION IN DUSTY PLASMAS

 Harekrishna Deka[a], Jnanjyoti Sarma[b]

[a]K.K. Handiqui State Open University, Khanapara, Guwahati, 781022, India
[b]R.G. Baruah College, Fatasil Ambari, Guwahai, 781025, India
[*]Corresponding Author e-mail: harekrishnadeka11@gmail.com

This paper presents a comprehensive study on the numerical simulation of the one-dimensional modified Burgers' equation in dusty plasmas.The reductive perturbation method is employed to derive the equation, and a numerical solution is obtained using the explicit finite difference technique.The obtained results are extensively compared with analytical solutions, demonstrating a high level of agreement, particularly for lower values of the dissipation coefficient.The accuracy and efficiency of the technique are evaluated based on the absolute error.Additionally,the accuracy and effectiveness of the technique are assessed by plotting L_2 and L_∞ error graphs.The technique's reliability is further confirmed through von-Neumann stability analysis, which indicates that the technique is conditionally stable. Overall, the study concludes that the proposed technique is successful and dependable for numerically simulating the modified Burgers' equation in dusty plasmas.

Keywords: *Dusty plamas; Reductive perturbation method; Modified Burgers equation; Finite difference explicit technique; von Neumann stability analysis*

PACS: 02.70Bf, 52.27Lw, 52.35Fp, 52.35Tc

1. INTRODUCTION

Wave propagation in dusty plasmas [1] has gained significant attention in recent years due to its relevance in astrophysical and space environments, as well as in the lower ionosphere of the Earth [2, 3, 4, 5, 6]. The presence of charged dust particles in dusty plasmas has a notable impact on the spectra of normal plasma waves [7], giving rise to the emergence of two kind of low-frequency waves [8] in dusty plasmas, including dust acoustic waves [9, 10] and dust-ion-acoustic waves [8, 9].Dust-acoustic waves (DAWs) have numerous industrial uses, including in laboratory plasma equipment, semiconductor chip manufacturing, and fusion reactor systems [11, 12]. Numerous researchers have investigated the characteristics of nonlinear wave propagation in dusty plasmas. Tamang and Saha [13] presented dynamic transitions of dust acoustic waves in collisional dusty plasmas. Dev et al. [14] have derived the nth-order three-dimensional modified Burgers' equation, considering non-thermal ions with varying temperatures.Tian et al.[15] analyzed a new $(3 + 1)$-dimensional modified Burgers' equation with the electron distribution in the presence of trapping particles and the kinetic equation of charge of dust particle. This paper investigates the one-dimensional modified Burgers' equation in a dusty plasma medium. The MBE has the strong non-linear behaviours and also has widely been utilized in physical phenomena [16].The MBE equation is a nonlinear advection-diffusion equation [17].The primary objective is to numerically solve the equation and explore the diverse characteristics of shock waves. Numerous authors in the literature have suggested and applied diverse numerical techniques to approximate the solution of the modified Burgers' equation.A summary of the suggested numerical techniques for approximating the solution of the modified Burgers' equation includes the following:

Zeytinoglu et al.[18] investigated an efficient numerical method for analyzing the propagation of shock waves in the equation. Bratsos [19] employed a finite difference technique as a computational method to solve the equation. Ramadan et al. [20] employed a septic B-spline collocation approach for solving the equation. Irk [21] have applied the sextic B-spline collocation technique for solving the equation. Saka and Dag [22] used quintic B-splines collocation technique to solve the equation. Duan et al.[23] implemented Lattice Boltzmann method to solve the equation. A Chebyshev spectral collocation method is applied by Temsah [24]. Roshan and Bharma [25] applied the Petrov-Galerkin method for solving the equation. Kutluay et al.[26] implemented a cubic B-spline collocation technique for solving the equation. Also, Ucar et al. [27] used finite difference technique for solving the equation. Gao et al. [28] developed a high bounded upwind scheme within the normalized-variable formulation to approximate the equation. Grienwank et al. [29] introduced a non-polynomial spline-based method for solving the equation. Bratsos et al. [30] employed the explicit finite difference scheme to numerically solve the equation.Numerical solution of nonlinear modified Burgers' equation

is obtained using an improvised collocation technique with cubic B-spline as basis functions in [31]. The authors in [32] provided an orthogonal collocation technique with septic Hermite splines as basis function to obtain the numerical solution of non-linear modified Burgers' equation. A numerical method based on quintic trigonometric B-splines for solving modified Burgers' equation (MBE) is presented in [33]. The arrangement of the manuscript is as follows. Section 2 of the manuscript discusses the governing equations of the dusty plasma model, along with the derivation of the modified Burgers' equation in dusty plasmas. Section 3 presents the explicit finite difference technique. The stability analysis of this technique is presented in Section 4. Section 5 includes the results and discussion, while the conclusion is provided in Section 6.

2. GOVERNING EQUATIONS AND DERIVATION OF MODIFIED BURGERS' EQUATION

The governing equations for the dusty plasma model are:

$$\frac{\partial n_d}{\partial t} + \nabla \cdot (n_d u_d) = 0 \tag{1}$$

$$\frac{\partial u_d}{\partial t} + (u_d \cdot \nabla) u_d = \frac{Z_d e}{m_d} \nabla \Psi - \frac{\nabla p_d}{m_d n_d} \tag{2}$$

The Poisson equation is expressed as follows

$$\nabla^2 \Psi = 4\pi e [n_e + Z_d n_d - n_{il} - n_{ih}] \tag{3}$$

where u_d represents the fluid speed, Z_d denotes the dust charge number, m_d represents the mass of the dust particle, Ψ represents the electrostatic potential, and n_d represents the dust particle number density. Additionally, n_{il} represents the ion particle number density at lower temperature, n_{ih} represents the ion particle number density at higher temperature, and n_e represents the electron particle number density.

The electron density, as well as the ion densities at both low and high temperatures, are provided as follows:

$$n_e = \left(\frac{1}{\sigma_1 + \sigma_2 - 1} \right) e^{\left(\frac{s\theta_1 \Psi}{K_B T_e} \right)} \tag{4}$$

$$n_{il} = \left(\frac{\sigma_1}{\sigma_1 + \sigma_2 - 1} \right) \left(1 + \eta g\varphi + \eta (g\varphi)^2 \right) exp \left(\frac{-g\Psi}{K_B T_{il}} \right) \tag{5}$$

$$n_{ih} = \left(\frac{\sigma_1}{\sigma_1 + \sigma_2 - 1} \right) \left(1 + \eta g\rho\varphi + \eta (g\theta\varphi)^2 \right) exp \left(\frac{-g\rho\Psi}{K_B T_{ih}} \right) \tag{6}$$

where $\theta_1 = \frac{T_{il}}{T_e}$, $\theta_2 = \frac{T_{ih}}{T_e}$, $\theta = \frac{\theta_1}{\theta_2} = \frac{T_{il}}{T_{ih}}$, $\sigma_1 = \frac{n_{il0}}{n_{e0}}$, $\sigma_2 = \frac{n_{ih0}}{n_{e0}}$, $g = \frac{T_{eff}}{T_{il}} = \frac{\sigma_1 + \sigma_2 - 1}{\sigma_1 + \sigma_2 \theta + \theta_1}$, $\varphi = \frac{e\Psi}{K_B T_{eff}}$ and $\eta = \frac{4\kappa}{1 + 3\kappa}$.

The charge equation is written as [35, 36]

$$\frac{d\bar{Q}_d}{dt} + \nu \bar{Q}_d = |I_{e0}| n_{d0} Z_{d0} \left(\frac{\bar{n}_{il}}{n_{il0}} + \frac{\bar{n}_{ih}}{n_{ih0}} - \frac{\bar{n}_e}{n_{e0}} \right) \tag{7}$$

with $Q_d = \bar{Q}_d + Q_{d0}$ where $\bar{Q}_d$ and Q_{d0} are the charged of the dust particle at perturbed and equilibrium states respectively. The natural decay rate ν is defined as $\nu = \frac{e|I_{e0}|}{C} \left[\frac{1}{K_B T_{eff}} + \frac{1}{\aleph_0} \right]$ and $\aleph_0 = k_B T_{eff} - e\Psi_{f0}$, with Ψ_{f0} is the floating potential at equilibrium.

The effective temperatures T_{eff} for two types of ions, namely, ions at low temperature and ions at high temperature, are provided.

$$T_{eff} = \left[\frac{1}{n_{d0} Z_{d0}} \left(\frac{n_{e0}}{T_e} + \frac{n_{il0}}{T_{il}} + \frac{n_{ih0}}{T_{ih}} \right) \right]^{-1} \tag{8}$$

The equations 1, 2, 3 and 7 can be expressed in their normalized form as follows:

$$\frac{\partial N_d}{\partial T} + \nabla (N_d U_d) = 0 \tag{9}$$

$$\left(\frac{\partial}{\partial T} + U_d \nabla \right) U_d = Z_d \nabla \psi - \Omega \frac{5}{3} N_d^{-1} \nabla N_d{}^\xi \tag{10}$$

$$\nabla^2\psi = \Upsilon_1\psi + \Upsilon_2\psi^2 + (Z_dN_d - 1) \tag{11}$$

$$\frac{dZ_d}{d\iota} + \nu' Z_d = r + r_1\psi + r_2\psi^2 \tag{12}$$

where $\Upsilon_1 = \frac{\theta_1 + (\sigma_1 + \sigma_2\theta)(1-\eta)}{\sigma_1 + \sigma_2 - 1}g$, $\Upsilon_2 = \frac{\theta_1{}^2 - \sigma_1 - \sigma_2\theta^2}{2(\sigma_1 + \sigma_2 - 1)}g^2$, $\Omega = \frac{T_d}{T_{eff}}$, $r = \frac{|I_{e0}|}{ez_{d0}\omega_{pd}}$, $r_1 = \frac{|I_{e0}|[(\eta-1)(1+\theta)-\theta_1]}{ez_{d0}\omega_{pd}}$, $r_2 = \frac{|I_{e0}|(1+\theta^2-\theta_1{}^2)}{2ez_{d0}\omega_{pd}}g^2$, $\nu' = \frac{\nu}{\omega_{pd}}$ and N_d is the number density of dust particle and is normalized by n_{d0}, U_d is the fluid velocity which is normalized by $c_d = \sqrt{\frac{Z_{d0}k_B T_{eff}}{m_d}}$, ψ is the electrostatic potential which is normalized by $\psi = \frac{e\Psi}{K_B T_{eff}}$ and charge density Z_d is normalized by $Z_{d0}.x$ is normalized by the dust $\lambda_D = \left(\frac{K_B T_{eff}}{4\pi n_{d0}e^2 Z_{d0}}\right)^{\frac{1}{2}}$ and time variable t is normalized by the dust plasma frequency $\omega_{pd} = \left(\frac{4\pi Z_{d0}{}^2 n_{d0}e^2}{m_d}\right)^{\frac{1}{2}}$. The adiabatic index $\xi = 3$ for the one dimensional geometry of the system.

For employing reductive perturbation theory, the space and time stretched coordinates are as follows:

$$\zeta = \epsilon^3(x - V_p t); \iota = \epsilon^6 t \tag{13}$$

where ϵ represents a small quantity that characterizes the nonlinearity in the system, and V_p is the phase speed of the wave. The variables N_d, Z_d, ψ and U_{dx} are expanded as power series in terms of ϵ as shown below:

$$N_d = 1 + \epsilon N_d^{(1)} + \epsilon^2 N_d^{(2)} + \epsilon^3 N_d^{(2)} + \dots \tag{14}$$

$$Z_d = 1 + \epsilon Z_d^{(1)} + \epsilon^2 Z_d^{(2)} + \epsilon^3 Z_d^{(2)} + \dots \tag{15}$$

$$\psi = \epsilon\psi^{(1)} + \epsilon^2\psi^{(2)} + \epsilon^3\psi^{(3)} + \dots \tag{16}$$

$$U_{dx} = \epsilon U_{dx}^{(1)} + \epsilon^2 U_{dx}^{(2)} + \epsilon^3 U_{dx}^{(3)} + \dots \tag{17}$$

After substituting the relations 13-17 into equations 9-12 and performing some algebraic manipulations, the following equation has been obtained [14] as:

$$\frac{\partial\psi^{(1)}}{\partial\iota} + A\left[\psi^{(1)}\right]^3\frac{\partial\psi^{(1)}}{\partial\zeta} = B\frac{\partial^2\psi^{(1)}}{\partial\zeta^2} \tag{18}$$

The nonlinear coefficient A is given in the form

$$A = \frac{e^2 z_{d0}(z_{d0} + r_1)}{V_p^3 m_d^2} - \frac{e^2 r_1 z_{d0}}{V_p^3 m_d^2\theta} - \frac{4}{3}\frac{er_2}{m_d V_P} + \frac{e^3(z_{d0})^3}{4V_p^5 m_d^3} - \frac{r_1^2 e}{4m_d V_p z_d^{(0)}\theta^2} + \frac{r_2 e^2}{V_p m_d\theta}$$
$$- \frac{e}{2m_d V_p z_{d0}\theta^2} + \frac{r_1 r_2 V_p}{4\theta^2(z_{d0})^2} + \frac{r_1^2 V_p}{16\theta^3(z_{d0})^2} \tag{19}$$

and the dissipation coefficient B is represented by

$$B = \frac{V_p^4 r}{2\omega_{pd}^2\theta^2} \tag{20}$$

The equation 18 is commonly referred to as the one-dimensional modified Burgers' equation in dusty plasmas. It serves as a fundamental model for describing various phenomena, including shock wave solutions, mass transport, gas dynamics in plasma, and fluid dynamics.

The travelling wave solution [14] of 18 is derived as

$$\psi^{(1)} = \left\{\psi_m\left[1 - tanh\left(\frac{\upsilon}{\delta}\right)\right]\right\}^{\frac{1}{3}} \tag{21}$$

Here, $\psi_m = \frac{4Vl}{2Al^2} = \frac{2V}{Al}$ represents the amplitude of the shock wave, and $\delta = \frac{2Bl^3}{Vl} = \frac{2Bl^2}{V}$ represents its width. In these equations, l denotes the direction cosines, and V is the speed of the shock wave. Substituting $\upsilon = \zeta l - V\iota, \psi_m = \frac{2V}{Al}$ and $\delta = \frac{2Bl^2}{V}$ in 21, the travelling wave solution of modified Burgers' equation becomes

$$\psi^{(1)}(\zeta,\iota) = \left\{\frac{2V}{Al}\left[1 - tanh\left(\frac{\zeta l - V\iota}{\frac{2Bl^2}{V}}\right)\right]\right\}^{\frac{1}{3}} \tag{22}$$

3. EXPLICIT FINITE DIFFERENCE METHOD

For convenience, we consider $\psi^{(1)}(\zeta,\iota) = u(x,t)$ and $l = 1$. The equation 18 is rewritten as

$$\frac{\partial u}{\partial t} + Au^3\frac{\partial u}{\partial x} = B\frac{\partial^2 u}{\partial x^2} \tag{23}$$

The travelling wave solution of equation is written by

$$u(x,t) = \left\{\frac{2V}{A}\left[1 - tanh\frac{V}{4B}\left(x - \frac{t}{2}\right)\right]\right\}^{\frac{1}{3}} \tag{24}$$

with the initial condition,

$$u(x,0) = \left\{\frac{2V}{A}\left[1 - tanh\left(\frac{Vx}{4B}\right)\right]\right\}^{\frac{1}{3}} \tag{25}$$

and the boundary conditions

$$u(0,t) = \left\{\frac{2V}{A}\left(1 + tanh\frac{Vt}{8B}\right)\right\}^{\frac{1}{3}} \tag{26}$$

$$u(1,t) = \left\{\frac{2V}{A}\left[1 - tanh\frac{V}{4B}\left(1 - \frac{t}{2}\right)\right]\right\}^{\frac{1}{3}} \tag{27}$$

In order to discretize the modified Burgers' equation 23, we apply the forward difference approximation to replace the partial derivative $\frac{\partial u}{\partial t}$ and the central difference approximation to replace the partial derivatives $\frac{\partial u}{\partial x}$ and $\frac{\partial^2 u}{\partial x^2}$, as described in reference[34], i.e.

$$\frac{\partial u}{\partial t} \approx \frac{u_{i,j+1} - u_{i,j}}{k} \tag{28}$$

$$\frac{\partial^2 u}{\partial x^2} \approx \frac{u_{i+1,j} - 2u_{i,j} + u_{i-1,j}}{h^2} \tag{29}$$

$$\frac{\partial u}{\partial x} \approx \frac{u_{i+1,j} - u_{i-1,j}}{2h} \tag{30}$$

thus 23 becomes

$$\frac{u_{i,j+1} - u_{i,j}}{k} + Au_{i,j}^3\left[\frac{u_{i+1,j} - u_{i-1,j}}{2h}\right] = B\left[\frac{u_{i+1,j} - u_{i,j} + u_{i-1,j}}{h^2}\right] \tag{31}$$

which simplifies

$$u_{i,j+1} = u_{i,j} + \frac{kA}{2h}u_{i,j}^3\left[u_{i-1,j} - u_{i+1,j}\right] + \frac{kB}{h^2}\left[u_{i+1,j} - 2u_{i,j} + u_{i-1,j}\right] \tag{32}$$

4. STABILITY ANALYSIS OF THE EXPLICIT FINITE DIFFERENCE METHOD

The von Neumann analysis method is employed to assess the stability of a numerical approach for both linear initial value problems and linearized nonlinear boundary value problems [37]. The Von Neumann stability theory in which the growth factor ξ is defined as

$$u_{i,j} = \xi^j e^{Ikhi} = \xi^j e^{I\theta i} \tag{33}$$

where $I = \sqrt{-1}$,ξ^j is the amplitude at time level k and $h = \Delta x$.The equation 32 has been linearized by putting $u^3 = M$ to check the stability.

$$u_{i,j+1} = u_{i,j} + \frac{kAM}{2h}\left[u_{i-1,j} - u_{i+1,j}\right] + \frac{kB}{h^2}\left[u_{i+1,j} - 2u_{i,j} + u_{i-1,j}\right] \tag{34}$$

$$u_{i,j+1} = (1 - \frac{2kB}{h^2})u_{i,j} + (\frac{kAM}{2h} + \frac{kB}{h^2})u_{i-1,j} + (\frac{kB}{h^2} - \frac{kAM}{2h})u_{i+1,j} \tag{35}$$

Substitute 33 in 35, we get

$$\xi^j e^{I\theta i}\xi = \xi^j e^{I\theta i}\left[\left(1 - \frac{2kB}{h^2}\right) + \left(\frac{kAM}{2h} + \frac{kB}{h^2}\right)e^{-I\theta} + \left(\frac{kB}{h^2} - \frac{kAM}{2h}\right)e^{I\theta}\right]$$

$$\xi = \left(1 - \frac{2kB}{h^2}\right) + \left(\frac{kAM}{2h} + \frac{kB}{h^2}\right)e^{-I\theta} + \left(\frac{kB}{h^2} - \frac{kAM}{2h}\right)e^{I\theta}$$

$$\xi = \left(1 - \frac{2kB}{h^2}\right) + \frac{kAM}{2h}\left(e^{-I\theta} - e^{I\theta}\right) + \frac{kB}{h^2}(e^{I\theta} + e^{-I\theta})$$

$$\xi = \left(1 - \frac{2kB}{h^2}\right) + \frac{kAM}{2h}\left(-2Isin\theta\right) + \frac{kB}{h^2}(2cos\theta)$$

$$\xi = \left(1 - \frac{2kB}{h^2}\right) - \frac{kAM}{h}sin\theta + \frac{2kB}{h^2}cos\theta$$

The stability criteria for the numerical technique is $|\xi| \leq 1$,which means $-1 \leq \xi \leq 1$ where

$$|\xi| = \left|\left(1 - \frac{2kB}{h^2}\right) - \frac{kAM}{h}sin\theta + \frac{2kB}{h^2}cos\theta\right| \leq 1 \tag{36}$$

So the stability condition is $\frac{2kB}{h^2} \leq 1$ or $\frac{kB}{h^2} \leq \frac{1}{2}$

$$k \leq \frac{h^2}{2B} \tag{37}$$

5. RESULTS AND DISCUSSION

Upon evaluating the von Neumann stability condition, we explore different values of B (specifically, $B = 0.001, 0.005, 0.01, 0.05, 0.1, 0.5$) for given step sizes $h = 0.001, 0.01$ and $k = 0.01, 0.05, 0.0001, 0.0005$. The coefficient A is influenced by various plasma parameters, and within these parameters, we consider a specific range of A values, namely $A = 0.2$ to $A = 4$. The validity of the present technique is evaluated using the absolute error which is defined by

$$\left|u_i^{Analytical} - u_i^{Numerical}\right| \tag{38}$$

Also,L_2 and L_∞ error norms, defined by

$$L_2 = \sqrt{h\sum_{j=1}^{N}\left|u_j^{analytical} - u_j^{numerical}\right|^2} \tag{39}$$

$$L_\infty = max\left|u_j^{analytical} - u_j^{numerical}\right| \tag{40}$$

are presented graphically for various values of nonlinear coefficient and dissipation coefficient for chosen space and time steps to check the accuracy and effectiveness of the method.
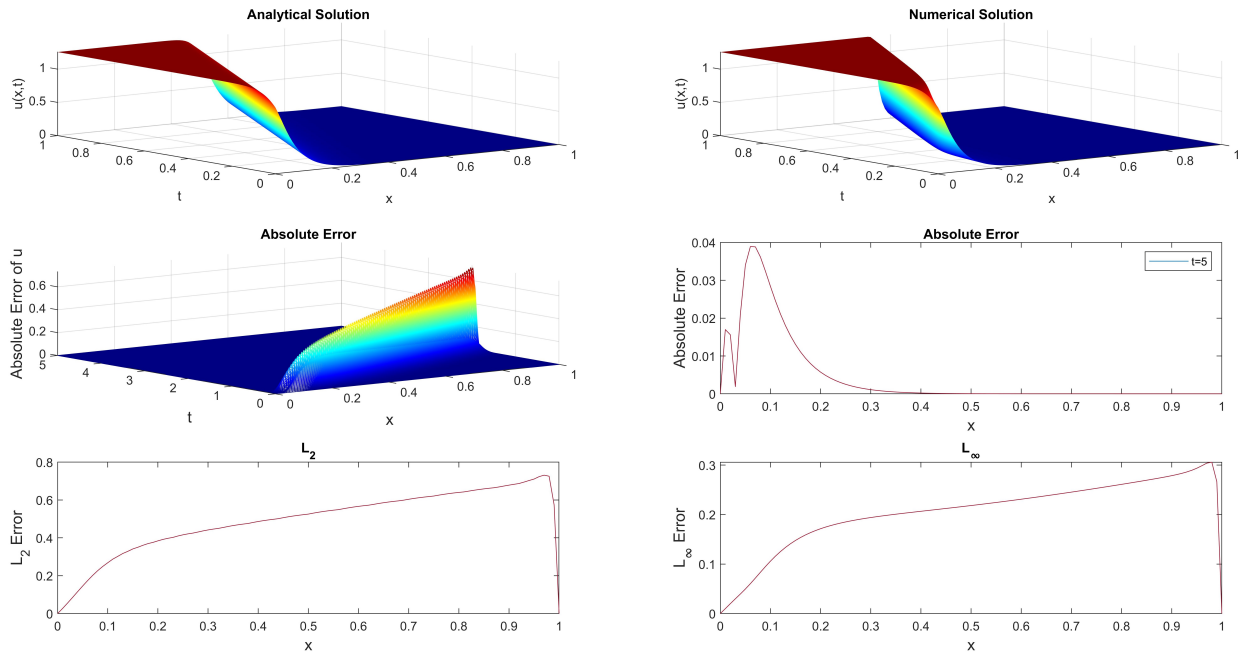
Figure 1. Analytical and numerical solutions, as well as the absolute error, L_2 error norm, and L_∞ error norm, at $A = 1$, $B = 0.01$, $h = 0.01$, and $k = 0.005$.
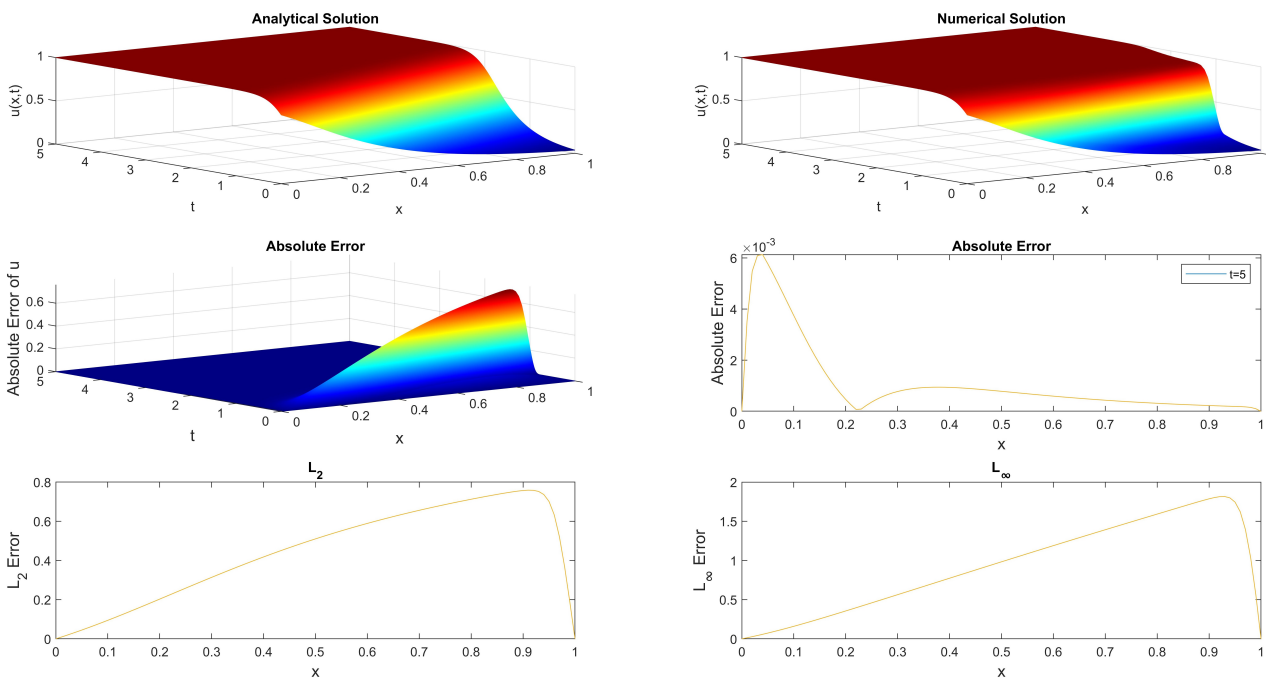
Figure 2. Analytical and numerical solutions, as well as the absolute error, L_2 error norm, and L_∞ error norm, at $A = 2$, $B = 0.05$, $h = 0.01$, $k = 0.001$.
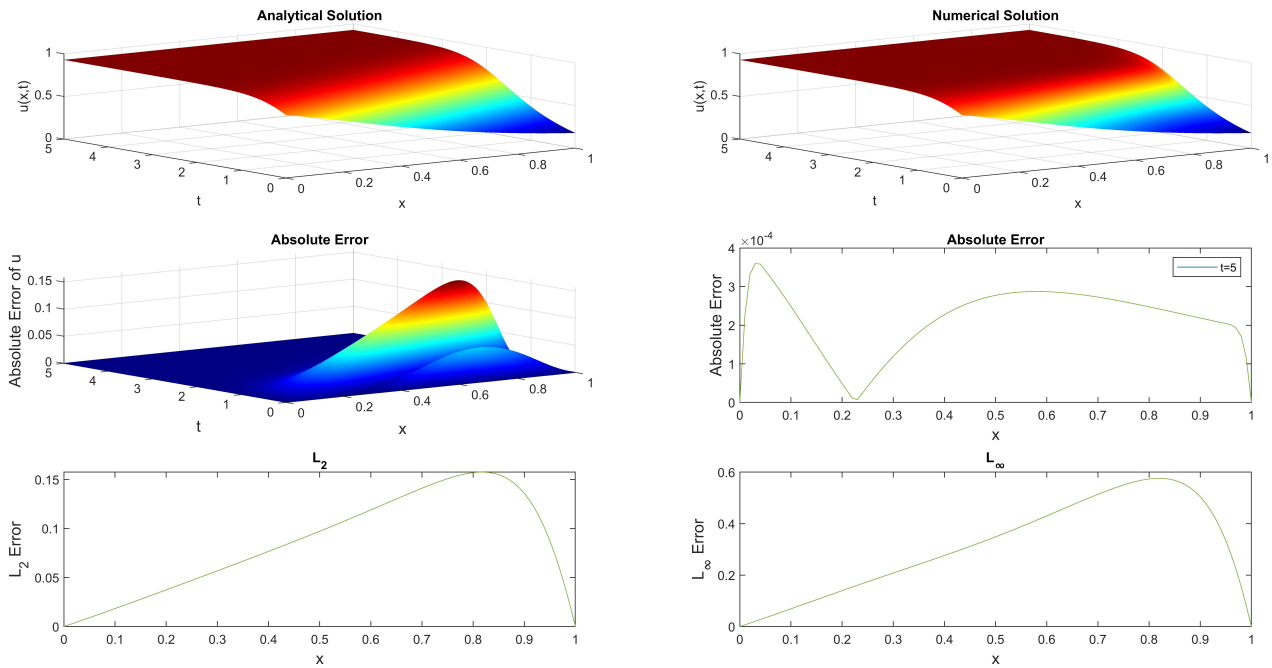
Figure 3. Analytical and numerical solutions, as well as the absolute error, L_2 error norm, and L_∞ error norm, at $A = 2.5, B = 0.1, h = 0.1, k = 0.0005$.

Figures 1-3 demonstrate that the greatest absolute error is observed on the left side of the solution domain for $B = 0.01$ and $B = 0.05$. This suggests that there is a significant discrepancy between the numerical and analytical solutions in that region for these specific values of B. Conversely, the highest error for both the L_2 and L_∞ norms is found on the right side of the solution domain, again for $B = 0.01$ and $B = 0.05$. This implies that the overall accuracy of the numerical solution deteriorates more prominently towards the right side for these particular values of B. Furthermore, by examining Figures 1-3, it can be concluded that as the dissipation coefficient decreases, the wave curves exhibit interesting behavior. Specifically, they become progressively flatter and steeper. This observation suggests that reducing the dissipation coefficient has a noticeable impact on the shape and steepness of the wave curves, indicating a stronger influence of convection effects in the system. Therefore, it can be concluded from the analysis of Figures 1-3 that the dissipation coefficient plays a crucial role in shaping the behavior of the wave curves.
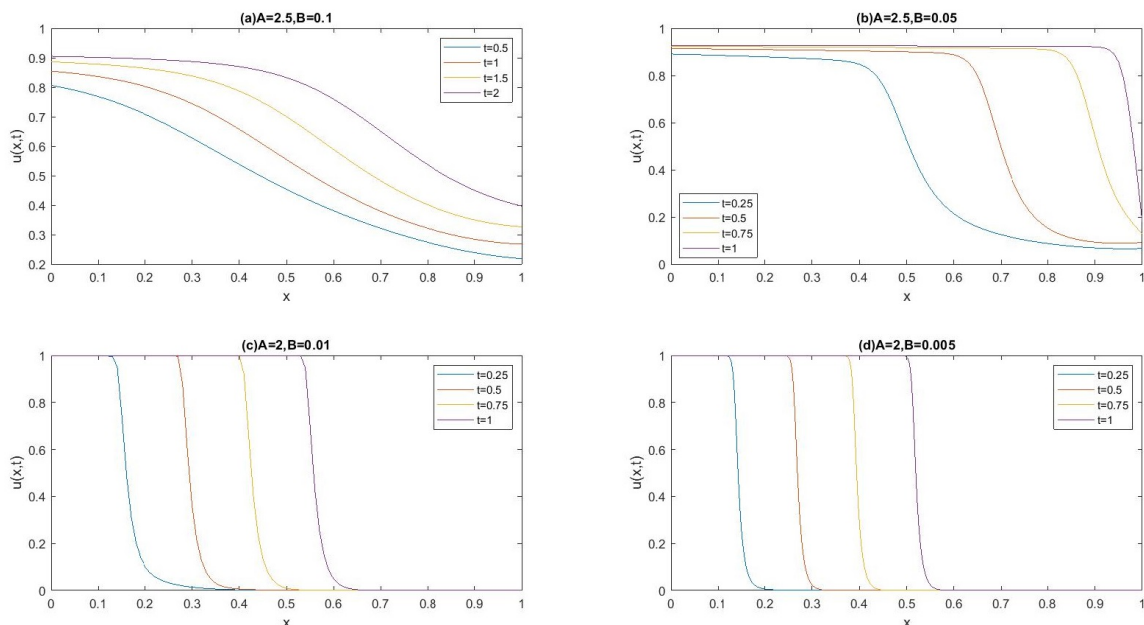
Figure 4. The numerical solution at various time stages using different values for A and B.

Figure 4 demonstrates that the wave propagation accelerates as the dissipation coefficient decreases. Furthermore, the figure also illustrates that as the value of the dissipative coefficient decreases, the wave front tends to exhibit a sharper steepness. In other words, with lower values of the dissipation coefficient, the wave profile becomes more pronounced and intense, indicating a stronger and more distinct wavefront. Figure 4 provides a visual representation of the behavior of shock wave profiles at different time intervals, while considering various values of the dissipation coefficient.
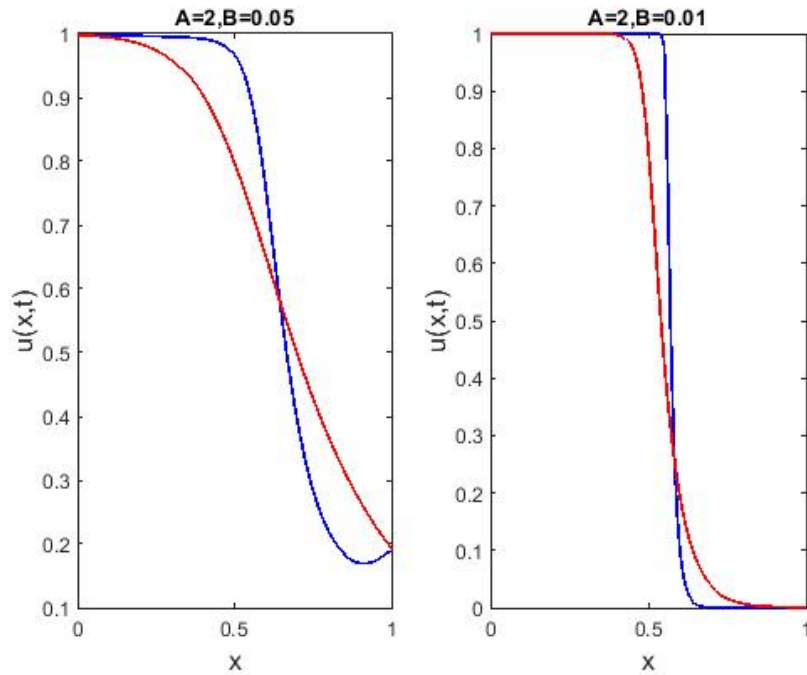
Figure 5. The numerical and analytical solution for various values of A and B (red - analytical, blue - numerical)
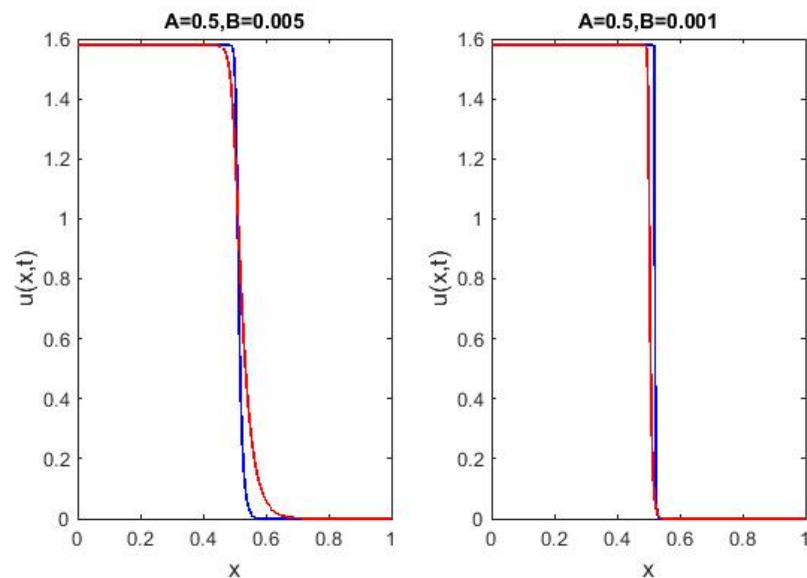
Figure 6. The numerical and analytical solution for various values of A and B (red - analytical, blue - numerical)

Figure 5 and 6 present a comparison between the numerical and analytical solutions at different time points, considering various values of A and B. Upon examination, it can be observed that the graphs representing the

numerical results closely align with the analytical results, particularly when B takes on the values of 0.005 and 0.001.

6. CONCLUSION

In this research, we numerically solve the one-dimensional modified Burgers' equation in dusty plasmas, considering the presence of non-thermal ions with different temperatures. The explicit finite difference technique is employed to solve the equation and investigate the characteristics of shock wave profiles. To assess the accuracy of our approach, we compare the numerical results with analytical results and find that the numerical graphs closely match the analytical ones. Moreover, our numerical solutions outperform those obtained by other methods described in the literature. The results indicate that the accuracy and efficiency of the technique depend on the value of the dissipation coefficient. Specifically, smaller values of the dissipation coefficient yield better results. The research also explores the behavior of shock wave propagation for varying values of the nonlinear coefficient and dissipation coefficient. It is observed that as the dissipation coefficient decreases, the wave front becomes sharper. To assess the accuracy and efficiency of the proposed technique, the absolute error is calculated. The findings indicate that the technique's accuracy and efficiency depend on the value of the dissipation coefficient, with improved results obtained when the dissipation coefficient is smaller.

ORCID

 Harekrishna Deka, https://orcid.org/0000-0003-4280-3728; **Jnanjyoti Sarma**, https://orcid.org/0000-0002-0793-5680

REFERENCES

[1] S. Raut, K.K. Mondal, P. Chatterjee, and A. Roy, "Propagation of dust-ion-acoustic solitary waves for damped modified Kadomtsev–Petviashvili–Burgers equation in dusty plasma with a q-nonextensive nonthermal electron velocity distribution," SeMA Journal, **78**, 571-593 (2021). https://doi.org/10.1007/s40324-021-00242-5

[2] C. Goertz, "Dusty plasmas in the solar system," Reviews of Geophysics, **27**(2), 271–292 (1989). https://doi.org/10.1029/RG027i002p00271.

[3] D.A. Mendis, and M.Rosenberg, "Cosmic Dusty Plasma," Annual Review of Astronomy and Astrophysics, **32**(1), 419-463 (1994). https://doi.org/10.1146/annurev.aa.32.090194.002223.

[4] P.K. Shukla, "A survey of dusty plasma physics," Physics of Plasmas, **8**(5), 1791–1803 (2001). https://doi.org/10.1063/1.1343087.

[5] M. Horanyi, and D.A. Mendis, "The dynamics of charged dust in the tail of comet Giacobini Zinner," Journal of Geophysical Research: Space Physics, **91**(A1), 355-361 (1986). https://doi.org/10.1029/SP027p0313.

[6] M. Horányi, "Charged dust dynamics in the solar system," Annual review of astronomy and astrophysics, **34**(1), 383-418 (1996). https://doi.org/10.1146/annurev.astro.34.1.383.

[7] P.K. Shukla, and L. Stenflo, "Stimulated scattering of electromagnetic waves in dusty plasmas," Astrophysics and space science, **190**(1), 23-32 (1992). https://doi.org/10.1063/1.871450.

[8] J. Tamang, and A. Saha, "Phase plane analysis of the dust-acoustic waves for the Burgers equation in a strongly coupled dusty plasma,", Indian Journal of Physics, **95**(4), 749-757 (2021). https://DOI:10.1007/s12648-020-01733-3.

[9] A. Barkan, A.N. D'angelo, and R.L. Merlino, "Experiments on ion-acoustic waves in dusty plasmas," Planetary and Space Science, **44**(1), 239-242 (1996). https://doi.org/10.1016/0032-0633(95)00109-3.

[10] P.K. Shukla, and V.P.Silin, "Dust ion-acoustic wave," Physica Scripta, **45**(5), 508 (1992). DOI10.1088/0031-8949/45/5/015.

[11] R. Merlino, "Dusty plasmas: From Saturn's rings to semiconductor processing devices," Advances in Physics: X, **6**(1), 1873859 (2021). https://doi.org/10.1080/23746149.2021.1873859.

[12] S. Ratynskaia, A. Bortolon, and S.I. Krasheninnikov, "Dust and powder in fusion plasmas: Recent developments in theory, modeling, and experiments," Reviews of Modern Plasma Physics, **6**(1), 20 (2022). https://doi.org/10.1007/s41614-022-00081-5.

[13] J. Tamang, and A. Saha, "Influence of dust-neutral collisional frequency and nonextensivity on dynamic motion of dust-acoustic waves," Waves in Random and Complex Media," **31**(4), 597-617 (2021). https://doi.org/10.1080/17455030.2019.1605230.

[14] A.N. Dev, J. Sarma, and M.K. Deka, "Dust acoustic shock waves in arbitrarily charged dusty plasma with low and high temperature non-thermal ions," Canadian Journal of Physics, **93**(10), 1030-1038 (2015). https://doi.org/10.1139/cjp-2014-0391.

[15] R. Tian, L. Fu, Y. Ren, and H. Yang, "(3+1)-Dimensional time-fractional modified Burgers equation for dust ion-acoustic waves as well as its exact and numerical solutions," Mathematical Methods in the Applied Sciences, **44**(10), 8177-8196 (2021). https://doi.org/10.1002/mma.5823.

[16] U. Yusuf, M. Yağmurlu, and A. Bashan, "Numerical solutions and stability analysis of modified Burgers equation via modified cubic B-spline differential quadrature methods," Sigma Journal of Engineering and Natural Sciences, **37**(1), 129-142 (2019). https://sigma.yildiz.edu.tr/storage/upload/pdfs/1635837147-en.pdf

[17] O. Oruç, Two meshless methods based on pseudo spectral delta-shaped basis functions and barycentric rational interpolation for numerical solution of modified Burgers equation. International Journal of Computer Mathematics, **98**(3), 461-479 (2021). https://doi.org/10.1080/00207160.2020.1755432.

[18] A. Zeytinoglu, M. Sari, and B. Allahverdiev, "Numerical simulations of shock wave propagating by a hybrid approximation based on high-order finite difference schemes," Acta Physica Polonica A, **133**(1), 140-151 (2018). https://doi.org/10.12693/aphyspola.133.140.

[19] A.G. Bratsos, "A fourth-order numerical scheme for solving the modified Burgers' equation," Computers and Mathematics with Applications, **60**(5), 1393-1400 (2010). https://doi.org/10.1016/j.camwa.2010.06.021.

[20] M.A. Ramadan, T.S. El-Danaf, and F.E. Abd Alaal, "A numerical solution of the Burgers' equation using septic B-splines," Chaos, Solitons and Fractals, **26**(4), 1249-1258 (2005). https://doi.org/10.1016/j.chaos.2005.01.054.

[21] D. Irk, "Sextic B spline collocation method for the modified Burgers' equation," Kybernetes, **38**(9), 1599-1620 (2009). https://doi.org/10.1108/03684920910991568.

[22] B. Saka, and I. Dag, "A numerical study of the Burgers' equation," Journal of the Franklin Institute, **345**(4), 328-348 (2008). https://doi.org/10.1016/j.jfranklin.2007.10.004.

[23] Y. Duan, R. Liu, and Y. Jiang, "Lattice Boltzmann model for the modified Burgers' equation," Applied Mathematics and Computation, **202**(2), 489-497 (2008). https://doi.org/10.1016/j.amc.2008.01.020

[24] R.S. Temsah, "Numerical solutions for convection-diffusion equation using El-Gendi method," Communications in Nonlinear Science and Numerical Simulation, **14**(3), 760-769 (2009). https://doi.org/10.1016/j.cnsns.2007.11.004

[25] T. Roshan, and K.S. Bhamra, "Numerical solutions of the modified Burgers' equation by Petrov-Galerkin method," Applied Mathematics and Computation, **218**(7), 3673-3679 (2011). https://doi.org/10.1016/j.amc.2011.09.010

[26] S. Kutluay, Y. Ucar, and N.M. Yagmurlu, "Numerical solutions of the modified Burgers' equation by a cubic B-spline collocation method," Bulletin of the Malaysian Mathematical Sciences Society, **39**(4), 1603-1614 (2016). https://doi.org/10.1016/j.amc.2012.01.059

[27] Y. Ucar, N.M. Yagmurlu, and O. Tasbozan, "Numerical solutions of the modified Burgers' equation by finite difference methods," Journal of applied mathematics, statistics and informatics, **13**(1), 19-30 (2017). https://doi.org/10.1515/jamsi-2017-0002

[28] W. Gao, Y. Liu, B. Cao, and H. Li, "A High-Order NVD/TVD-Based Polynomial Upwind Scheme for the Modified Burgers' Equations," Advances in Applied Mathematics and Mechanics, **4**(5), 617-635 (2012). https://doi.org/10.4208/aamm.10-m1139

[29] A. Griewank, and T.S. El-Danaf, "Efficient accurate numerical treatment of the modified Burgers' equation," Applicable Analysis, **88**(1), 75-87 (2009). https://doi.org/10.1080/00036810802556787

[30] A.G. Bratsos, and L.A. Petrakis, "An explicit numerical scheme for the modified Burgers' equation," International Journal for Numerical Methods in Biomedical Engineering, **27**(2), 232-237 (2011). https://doi.org/10.1002/cnm.1294

[31] Shallu, and V.K. Kukreja, "An improvised collocation algorithm with specific end conditions for solving modified Burgers equation," Numerical Methods for Partial Differential Equations, **37**(1), 874-896 (2021). https://doi.org/10.1002/num.22557

[32] A. Kumari, and V.K. Kukreja, "Error bounds for septic Hermite interpolation and its implementation to study modified Burgers' equation," Numerical Algorithms, **89**(4), 1799-1821 (2022). https://doi.org/10.1007/s11075-021-01173-y

[33] L. Chandrasekharan Nair, and A. Awasthi, "Quintic trigonometric spline based numerical scheme for nonlinear modified Burgers' equation," Numerical Methods for Partial Differential Equations, **35**(3), 1269-1289 (2019). https://doi.org/10.1002/num.22349

[34] G.W. Recktenwald, "Finite-difference approximations to the heat equation," Mechanical Engineering, **10** (01) (2004). https://webspace.science.uu.nl/~zegel101/MOLMODWISK/FDheat2.pdf

[35] M.R. Jana, A. Sen, and P.K. Kaw, "Collective effects due to charge-fluctuation dynamics in a dusty plasma," Physical review E, **48**(5), 3930 (1993). https://doi.org/10.1103/PhysRevE.48.3930

[36] J.R. Bhatt, and B.P. Pandey, "Self-consistent charge dynamics and collective modes in a dusty plasma," Phys. Rev. E, **50**(5), 3980–3983 (1994). https://doi.org/10.1103/PhysRevE.50.3980

[37] N. Parumasur, R.A. Adetona, and P. Singh, "Efficient solution of burgers', modified burgers' and KdV–burgers'," Mathematics, **11**(8), 1847 (2023). https://doi.org/10.3390/math11081847

ЧИСЕЛЬНЕ МОДЕЛЮВАННЯ ТА АНАЛІЗ МОДИФІКОВАНОГО РІВНЯННЯ БЮРГЕРСА В ЗАПОРОШЕНІЙ ПЛАЗМІ

Харекрішна Дека[a], **Джнандйоті Сарма**[b]

[a]*Державний відкритий університет К.К. Хандікі, Ханапара, Гувахаті, 781022, Індія*
[b]*Коледж Р.Г. Баруа, Фатасил Амбарі, Гувахаті, 781025, Індія*

У цьому документі представлено всебічне дослідження чисельного моделювання одновимірного модифікованого рівняння Бюргерса в запорошеній плазмі. Для виведення рівняння використовується метод відновних збурень, а числове рішення отримано за допомогою явного методу кінцевих різниць. Отримані результати детально порівнюються з аналітичними рішеннями, демонструючи високий рівень узгодженості, особливо для менших значень коефіцієнта дисипації. Точність і ефективність методики оцінюють за абсолютною похибкою. Крім того, точність і ефективність методики оцінюється шляхом побудови графіків похибок L_2 і L_∞. Надійність методики додатково підтверджується аналізом стабільності за фон-Нейманом, який вказує на те, що методика умовно стабільна. Загалом дослідження робить висновок, що запропонована методика є успішною та надійною для чисельного моделювання модифікованого рівняння Бюргерса в запиленій плазмі.

Ключові слова: *пилова плазма; редуктивний метод збурень; модифіковане рівняння Бюргерса; метод скінченної різниці в явному вигляді; аналіз стійкості фон Неймана*

THE EFFECT OF THERMAL STRATIFICATION ON UNSTEADY PARABOLIC FLOW PAST AN INFINITE VERTICAL PLATE WITH CHEMICAL REACTION

◉ **Rupam Shankar Nath***, ◉ **Rudra Kanta Deka**, ◉ **Himangshu Kumar**

Department of Mathematics, Gauhati University, Guwahati-781014, Assam, India
*Corresponding Author e-mail: rupamnath23@gmail.com

This research paper investigates the effects of thermal stratification on unsteady parabolic flow past an infinite vertical plate with chemical reaction. Using the Laplace transform method, analytical solutions are derived to simulate the physical process of the flow. The study considers the effects of thermal stratification on the flow field, as well as the effects of chemical reaction on the velocity, and temperature field. The results of the stratification case are then compared to the case of no stratification of a similar flow field. The results of this research can be used to improve understanding of the unsteady parabolic flow in thermal stratified environments and provide valuable insight into the effects of chemical reactions on the temperature field.

Keywords: *Thermal Stratification; Chemical Reaction; Parabolic Flow; Vertical plate*

PACS: 47.55.P-, 44.25.+f, 44.05.+e, 47.11.-j

NOMENCLATURE

α	Thermal Diffusivity	K	Non-Dimensional Chemical Reaction Parameter
β	Volumetric Coefficient of Thermal Expansion	K_1	Chemical Reaction Parameter
β^*	Volumetric Coefficient of Expansion with Concentration	Pr	Prandtl Number
η	Similarity Parameter	S	Non-Dimensional Thermal Stratification Parameter
γ	Thermal Stratification Parameter	Sc	Schimdt Number
ν	Kinematic Viscosity	t	Non-Dimensional Time
τ	Non-Dimensional Skin-Friction	T'	Temperature of the fluid
θ	Non-Dimensional Temperature	t'	Time
C	Non-Dimensional Concentration	T'_∞	Temperature of the fluid far away from the Plate
C'	Species Concentration in the fluid		
C'_∞	Concentration of the fluid far away from the Plate	T'_w	Temperature of the Plate
		U	Non-Dimensional Velocity
C'_w	Concentration of the Plate	u'	Velocity of the fluid in x' direction
D	Mass Diffusion Coefficient	u_0	Velocity of the Plate
g	Acceleration due to gravity		
Gc	Mass Grashof Number	y	Non-Dimensional Coordinate Normal to the plate
Gr	Thermal Grashof Number	y'	Coordinate Normal to the Plate

1. INTRODUCTION

The study of parabolic flow is significant because it helps to reduce energy losses in flowing fluids by decreasing viscous interactions between neighboring layers of fluid and the pipe wall. Additionally, parabolic flow is simpler to model and calculate than unstable flow, which includes the fluid's random and unpredictable
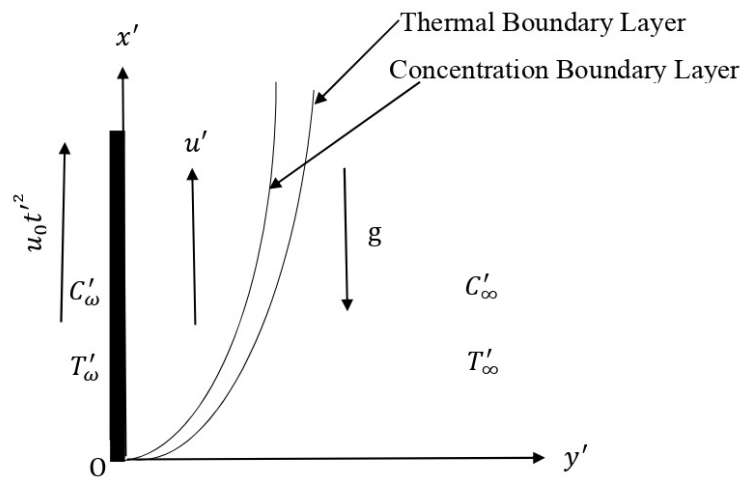
Figure 1. Physical Model and coordinate system

motion. One of the uses for parabolic flow is in mass and heat transfer procedures using an infinite vertical plate. The plate may be subjected to a variety of boundary conditions, including constant or variable temperature, constant or variable heat flow, constant or variable concentration, etc. The study of these problems has a lot of attention because they are important in engineering and industrial processes, such as cooling electronic devices, sun collectors, chemical reactors, combustion chambers, etc.

The first study on the parabolic starting flow past an infinite vertical plate was done by [1]. In addition, the MHD Parabolic flow for an infinite vertical plate was investigated by [2], while [3] studied the flow around an accelerating vertical plate. The present research is the first work to look into the combined effects of thermal stratification and chemical reaction on parabolic flow past an infinite vertical plate. [4, 5] and [6] investigated unsteady flows in a stably stratified fluid, focusing on infinite plates. Furthermore, buoyancy-driven flows in a stratified fluid were examined by [7, 8]. [9] came up with an analytical solution to describe how fluid would flow past an infinite vertical plate that had been affected chemically. In their studies, [10] and [11] examine the results of applying a chemical reaction to an infinite vertical plate under different situations. The articles [12] and [13] investigate the impacts of chemical reaction and thermal stratification on MHD flow for vertical stretching surfaces. In a similar manner, [14] investigated the effects of non-Newtonian fluid flow across a porous material on both effects. The study conducted by [15] focuses on analysing the collective influence of thermal stratification and chemical reaction on the flow of a fluid relative to an infinitely vertical plate. Furthermore, [16] conducted an investigation to examine the impact of thermal stratification on the unsteady flow of fluid past an accelerated vertical plate, while also considering the presence of a first-order chemical reaction. [17] conducted an investigation to analyse the impact of thermal stratification with velocity slip, and changing viscosity on the magnetohydrodynamic (MHD) flow of a nanofluid across a disc.

The work presents the derivation of the special solutions for the situation $Sc = 1$ and the classical solutions for the case $S = 0$, where no stratification is present. In order to compare these solutions to the original solutions, graphs are utilized to show the variations. Physical parameters that affect the concentration, temperature, and velocity profiles are discussed and illustrated graphically. These parameters include the S, K, Gr, Gc, and time t. The conclusions of this study have numerous uses across several industries and chemical plants.

2. MATHEMATICAL ANALYSIS

We examine at the unstable parabolic flow over an infinite vertical plate of a viscous, in-compressible, stratified fluid with first order chemical reaction effects. To study the flow situation, we employ a coordinate system in which the y' axis is perpendicular to the plate and the x' axis is chosen vertically upward along the plate. At first, both the plate's initial temperature T'_∞ and fluid's initial concentration C'_∞ are the same. At time $t' > 0$, the plate is moving at the velocity $u_0 t'^2$ in its own plane relative to the gravitational field. Additionally, at time $t' > 0$, the concentration level is raised to C'_w and the plate temperature is raised to T'_w. All flow variables are independent of x' and only affected by y' and t' since the plate has an infinite length. As a result, we are left with a flow that is only one dimension and has one non-zero vertical velocity component, u'. The Boussinesqs' approximation is then used to represent the equations for motion, energy, and concentration as follows:

$$\frac{\partial u'}{\partial t'} = g\beta(T' - T'_\infty) + g\beta^*(C' - C'_\infty) + \nu\frac{\partial^2 u'}{\partial y'^2} \tag{1}$$

$$\frac{\partial T'}{\partial t'} = \alpha\frac{\partial^2 T'}{\partial y'^2} - \gamma u' \tag{2}$$

$$\frac{\partial C'}{\partial t'} = D\frac{\partial^2 C'}{\partial y'^2} - K_1 C' \tag{3}$$

with the following initial and boundary Conditions:

$$
\begin{array}{llll}
u' = 0 & T' = T'_\infty & C' = C'_\infty & \forall y', t' \le 0 \\
u' = u_0 t'^2 & T' = T'_w & C' = C'_w & \text{at } y' = 0, t' > 0 \\
u' = 0 & T' \to T'_\infty & C' \to C'_\infty & \text{as } y' \to \infty, t' > 0
\end{array}
$$

where, $\gamma = \frac{dT'_\infty}{dx'} + \frac{g}{C_p}$ denotes the thermal stratification parameter and $\frac{dT'_\infty}{dx'}$ denotes the vertical temperature convection known as thermal stratification. In addition, $\frac{g}{C_p}$ represents the rate at which particles in a fluid do reversible work due to compression, often known as work of compression. The variable (γ) will be referred to as the thermal stratification parameter in our research because the compression work is relatively minimal. For the purpose of testing computational methods, compression work is kept as an additive to thermal stratification. And we provide non-dimensional quantities in the following:

$$U = u'\left(\frac{u_0}{\nu^2}\right)^{1/3}, \quad t = t'\left(\frac{u_0^2}{\nu}\right)^{1/3}, \quad y = y'\left(\frac{u_0}{\nu^2}\right)^{1/3}, \quad \theta = \frac{T' - T'_\infty}{T'_w - T'_\infty}, \quad C = \frac{C' - C'_\infty}{C'_w - C'_\infty}, \quad Pr = \frac{\nu}{\alpha}$$

$$Gr = \frac{g\beta(T'_w - T'_\infty)}{(\nu u_0)^{1/3}}, \quad Gc = \frac{g\beta^*(C'_w - C'_\infty)}{(\nu u_0)^{1/3}}, \quad Sc = \frac{\nu}{D}, \quad K = K_1\left(\frac{\nu}{u_0^2}\right)^{1/3}, \quad S = \frac{\gamma\nu}{u_0(T'_w - T'_\infty)}$$

The non-dimensional forms of the equations (1)-(3) are given by

$$\frac{\partial U}{\partial t} = Gr\theta + GcC + \frac{\partial^2 U}{\partial y^2} \tag{4}$$

$$\frac{\partial \theta}{\partial t} = \frac{1}{Pr}\frac{\partial^2 \theta}{\partial y^2} - SU \tag{5}$$

$$\frac{\partial C}{\partial t} = \frac{1}{Sc}\frac{\partial^2 C}{\partial y^2} - KC \tag{6}$$

Non-dimensional form of initial and boundary Conditions are:

$$
\begin{array}{llll}
U = 0 & \theta = 0 & C = 0 & \forall y, t \le 0 \\
U = t^2 & \theta = 1 & C = 1 & \text{at } y = 0, t > 0 \\
U = 0 & \theta \to 0 & C \to 0 & \text{as } y \to \infty, t > 0
\end{array} \tag{7}
$$

3. METHOD OF SOLUTION

The non-dimensional governing equations (4)-(6) with boundary conditions (7) are solved using Laplace's transform method for $Pr = 1$. Hence, the expressions for concentration, velocity and temperature with the help of [18] and [19] are given by

$$C = \frac{1}{2}\left[e^{-2\eta\sqrt{ScKt}}erfc\left(\eta\sqrt{Sc} - \sqrt{Kt}\right) + e^{2\eta\sqrt{ScKt}}erfc\left(\eta\sqrt{Sc} + \sqrt{Kt}\right)\right] \tag{8}$$

$$U = [f_4(iA) + f_4(-iA)] + \frac{iA}{2S}\{f_1(iA) - f_1(-iA)\} + \frac{Gc}{2(Sc-1)}[C_1\{f_1(iA) + f_1(-iA)\}]$$

$$+(C_2 - iC_3)\{f_2(iA, B + iB_1) + f_2(-iA, B + iB_1)\} + (C_2 + iC_3)\{f_2(iA, B - iB_1)$$

$$+f_2(-iA, B - iB_1)\}] + \frac{Gc}{2iA}[(D_1 - 1)\{f_1(iA) - f_1(-iA)\} + (D_2 + iD_3)\{f_2(iA, B + iB_1)$$

$$-f_2(-iA, B + iB_1)\} + (D_2 - iD_3)\{f_2(iA, B - iB_1) - f_2(-iA, B - iB_1)\}]$$

$$-\frac{Gc}{(Sc-1)}\left[\frac{C_1}{2}\left\{e^{-2\eta\sqrt{ScKt}}erfc\left(\eta\sqrt{Sc} - \sqrt{Kt}\right) + e^{2\eta\sqrt{ScKt}}erfc\left(\eta\sqrt{Sc} + \sqrt{Kt}\right)\right\}$$

$$+(C_2 - iC_3)\{f_3(K, B + iB_1)\} + (C_2 + iC_3)\{f_3(K, B - iB_1)\}] \tag{9}$$

$$\theta = \frac{S}{iA}[f_4(iA) - f_4(-iA)] + \frac{1}{2}\{f_1(iA) + f_1(-iA)\} + \frac{SGc}{2iA(Sc-1)}[C_1\{f_1(iA) - f_1(-iA)\}$$

$$+(C_2 - iC_3)\{f_2(iA, B + iB_1) - f_2(-iA, B + iB_1)\} + (C_2 + iC_3)\{f_2(iA, B - iB_1)$$

$$-f_2(-iA, B - iB_1)\}] + \frac{SGc}{2(Sc-1)^2}[E_1\{f_1(iA) + f_1(-iA)\} + (E_2 - iE_3)\{f_2(iA, B + iB_1)$$

$$+f_2(-iA, B + iB_1)\} + (E_2 + iE_3)\{f_2(iA, B - iB_1) + f_2(-iA, B - iB_1)\}]$$

$$-\frac{SGc}{(Sc-1)^2}\left[\frac{E_1}{2}\left\{e^{-2\eta\sqrt{ScKt}}erfc\left(\eta\sqrt{Sc} - \sqrt{Kt}\right) + e^{2\eta\sqrt{ScKt}}erfc\left(\eta\sqrt{Sc} + \sqrt{Kt}\right)\right\}$$

$$+(E_2 - iE_3)f_3(K, B + iB_1) + (E_2 + iE_3)f_3(K, B - iB_1) \tag{10}$$

where,

$$\eta = \frac{y}{2\sqrt{t}}, \quad A = \sqrt{SGr}, \quad B = \frac{ScK}{Sc-1}, \quad B_1 = \frac{A}{Sc-1} = \frac{\sqrt{SGr}}{Sc-1}, \quad C_1 = \frac{B}{(B^2 + B_1^2)}$$

$$C_2 = \frac{-B}{2(B^2 + B_1^2)}, \quad C_3 = \frac{-B_1}{2(B^2 + B_1^2)}, \quad D_1 = \frac{B^2}{(B^2 + B_1^2)}, \quad D_2 = \frac{B_1^2}{2(B^2 + B_1^2)}$$

$$D_3 = \frac{BB_1}{2(B^2 + B_1^2)}, \quad E_1 = \frac{1}{(B^2 + B_1^2)}, \quad E_2 = \frac{-1}{2(B^2 + B_1^2)}, \quad E_3 = \frac{B}{2B_1(B^2 + B_1^2)}$$

Also, f_i's are inverse Laplace's transforms given by

$$f_1(ip) = L^{-1}\left\{\frac{e^{-y\sqrt{s+ip}}}{s}\right\}, \quad f_2(ip, q_1 + iq_2) = L^{-1}\left\{\frac{e^{-y\sqrt{s+ip}}}{s + q_1 + iq_2}\right\}$$

$$f_3(p, q_1 + iq_2) = L^{-1}\left\{\frac{e^{-y\sqrt{Sc(s+p)}}}{s + q_1 + iq_2}\right\}, \quad f_4(ip) = L^{-1}\left\{\frac{e^{-y\sqrt{s+ip}}}{s^3}\right\}$$

We separate the complex arguments of the error function contained in the previous expressions into real and imaginary parts using the formulas provided by [18].

4. SPECIAL CASE [FOR $Sc = 1$]

We came up with answers for the special case where $Sc = 1$. Hence, the solutions for the special case are as follows:

$$C^* = \frac{1}{2}\left[e^{-2\eta\sqrt{Kt}}erfc\left(\eta - \sqrt{Kt}\right) + e^{2\eta\sqrt{Kt}}erfc\left(\eta + \sqrt{Kt}\right)\right] \tag{11}$$

$$U^* = \frac{KGc}{2(K^2 + A^2)}\{f_1(iA) + f_1(-iA)\} + \frac{iA}{2}\left(\frac{1}{S} + \frac{Gc}{K^2 + A^2}\right)\{f_1(iA) - f_1(-iA)\}$$

$$-\frac{KGc}{2(K^2 + A^2)}\left[e^{-2\eta\sqrt{Kt}}erfc\left(\eta - \sqrt{Kt}\right) + e^{2\eta\sqrt{Kt}}erfc\left(\eta + \sqrt{Kt}\right)\right]$$

$$+\{f_4(iA) + f_4(-iA)\} \tag{12}$$

$$\theta^* = \frac{SKGc}{2iA(K^2 + A^2)}\{f_1(iA) - f_1(-iA)\} + \frac{1}{2}\left(1 + \frac{SGc}{K^2 + A^2}\right)\{f_1(iA) + f_1(-iA)\}$$

$$-\frac{SGc}{2(K^2 + A^2)}\left\{e^{-2\eta\sqrt{Kt}}erfc\left(\eta - \sqrt{Kt}\right) + e^{2\eta\sqrt{Kt}}erfc\left(\eta + \sqrt{Kt}\right)\right\}$$

$$+\frac{S}{iA}\{f_4(iA) - f_4(-iA)\} \tag{13}$$

5. CLASSICAL CASE ($S = 0$)

We derived solutions for the classical case of no thermal stratification ($S = 0$). We want to compare the results of the fluid with thermal stratification to the case with no stratification. Hence, the corresponding solutions for the classical case is given by :

$$\theta_c = erfc(\eta) \tag{14}$$

$$
\begin{aligned}
U_c = \ & \frac{Gc}{2KSc}\left[2erfc(\eta) - e^{-Bt}\left\{e^{-2\eta\sqrt{-Bt}}erfc\left(\eta - \sqrt{-Bt}\right) + e^{2\eta\sqrt{-Bt}}erfc\left(\eta + \sqrt{-Bt}\right)\right\}\right. \\
& - \left\{e^{-2\eta\sqrt{ScKt}}erfc\left(\eta\sqrt{Sc} - \sqrt{Kt}\right) + e^{2\eta\sqrt{ScKt}}erfc\left(\eta\sqrt{Sc} + \sqrt{Kt}\right)\right\} \\
& + e^{-Bt}\left\{e^{-2\eta\sqrt{Sc(K-B)t}}erfc\left(\eta\sqrt{Sc} - \sqrt{(K-B)t}\right)\right. \\
& \left.\left. + e^{2\eta\sqrt{Sc(K-B)t}}erfc\left(\eta\sqrt{Sc} + \sqrt{(K-B)t}\right)\right\}\right] + 2t\eta Gr\left\{\frac{e^{-\eta^2}}{\sqrt{\pi}} - \eta\ erfc(\eta)\right\} \\
& + \frac{t^2}{3}\left\{\left(3 + 12\eta^2 + 4\eta^4\right)erfc(\eta) - \frac{\eta}{\sqrt{\pi}}\left(10 + 4\eta^2\right)e^{-\eta^2}\right\}
\end{aligned} \tag{15}
$$

5.1. Skin-Friction

The non-dimensional Skin-Friction, which is determined as shear stress on the surface, is obtained by

$$\tau = -\left.\frac{dU}{dy}\right|_{y=0}$$

The solution for the Skin-Friction is calculated from the solution of Velocity profile U, represented by (9), as follows:

$$
\begin{aligned}
\tau = \ & t\sqrt{\frac{t}{\pi}}\cos At + t^2\sqrt{\frac{A}{2}}(r_1 - r_2) + \frac{t(r_1 + r_2)}{\sqrt{2A}} + \frac{(r_1 - r_2)}{4A\sqrt{2A}} - \frac{\sin At}{2A}\sqrt{\frac{t}{\pi}} \\
& + \frac{Gc}{Sc-1}\left[C_1\left\{\frac{\cos At}{\sqrt{\pi t}} + \sqrt{\frac{A}{2}}(r_1 - r_2) - \sqrt{ScK}\ erf(\sqrt{Kt}) - \sqrt{\frac{Sc}{\pi t}}e^{-Kt}\right\}\right. \\
& + 2C_2\left\{\frac{\cos At}{\sqrt{\pi t}} - \sqrt{\frac{Sc}{\pi t}}e^{-Kt}\right\} \\
& + e^{-Bt}\left\{(C_2P_1 + C_3Q_1)(r_3\cos B_1t + r_4\sin B_1t) + (C_3P_1 - C_2Q_1)(r_4\cos B_1t - r_3\sin B_1t)\right\} \\
& + e^{-Bt}\left\{(C_2P_2 - C_3Q_2)(r_5\cos B_1t - r_6\sin B_1t) - (C_3P_2 + C_2Q_2)(r_6\cos B_1t + r_5\sin B_1t)\right\} \\
& \left. - 2e^{-Bt}\sqrt{Sc}\left\{(C_2P_3 - C_3Q_3)(r_7\cos B_1t - r_8\sin B_1t) - (C_3P_3 + C_2Q_3)(r_8\cos B_1t + r_7\sin B_1t)\right\}\right] \\
& + \frac{A}{S}\left\{\frac{\sin At}{\sqrt{\pi t}} - \sqrt{\frac{A}{2}}(r_1 + r_2)\right\} + \frac{Gc}{A}\left[(D_1 - 1)\left\{\frac{-\sin At}{\sqrt{\pi t}} + \sqrt{\frac{A}{2}}(r_1 + r_2)\right\} - \frac{2D_2\sin At}{\sqrt{\pi t}}\right. \\
& + e^{-Bt}\left\{(D_2P_1 - D_3Q_1)(r_4\cos B_1t - r_3\sin B_1t) + (D_3P_1 + D_2Q_1)(r_3\cos B_1t + r_4\sin B_1t)\right\} \\
& \left. + e^{-Bt}\left\{(D_2P_2 + D_3Q_2)(r_6\cos B_1t + r_5\sin B_1t) - (D_3P_2 - D_2Q_2)(r_5\cos B_1t - r_6\sin B_1t)\right\}\right]
\end{aligned}
$$

The solution for the Skin-Friction for the special case is given from the expression (12), which is represented by

$$
\begin{aligned}
\tau^* = \ & t\sqrt{\frac{t}{\pi}}\cos At + t^2\sqrt{\frac{A}{2}}(r_1 - r_2) + \frac{t(r_1 + r_2)}{\sqrt{2A}} + \frac{(r_1 - r_2)}{4A\sqrt{2A}} - \frac{\sin At}{2A}\sqrt{\frac{t}{\pi}} + \frac{KGc}{K^2 + A^2}\left\{\frac{\cos At}{\sqrt{\pi t}}\right. \\
& \left. + \sqrt{\frac{A}{2}}(r_1 - r_2) - \sqrt{K}\ erf(\sqrt{Kt}) - \frac{e^{-Kt}}{\sqrt{\pi t}}\right\} + A\left(\frac{1}{S} + \frac{Gc}{K^2 + A^2}\right)\left\{\frac{\sin At}{\sqrt{\pi t}} - \sqrt{\frac{A}{2}}(r_1 + r_2)\right\}
\end{aligned}
$$

The solution for the Skin-Friction for the classical case is given from the expression (15), which is represented by

$$
\tau_c = \frac{Gc}{KSc}\left[e^{-Bt}\left\{\sqrt{Sc(K-B)}\ erf(\sqrt{(K-B)t}) - \sqrt{-B}\ erf(\sqrt{-Bt})\right\} - \sqrt{ScK}\ erf(\sqrt{Kt})\right]
$$

$$+\left(\frac{8t}{3} - Gr\right)\sqrt{\frac{t}{\pi}}$$

where,

$$B_2 = \sqrt{B^2 + (A - B_1)^2}, \quad B_3 = \sqrt{B^2 + (A + B_1)^2}, \quad B_4 = \sqrt{(K - B)^2 + B_1^2}, \quad P_1 = \sqrt{\frac{B_2 - B}{2}},$$

$$Q_1 = \sqrt{\frac{B_2 + B}{2}}, \quad P_2 = \sqrt{\frac{B_3 - B}{2}}, \quad Q_2 = \sqrt{\frac{B_3 + B}{2}}, \quad P_3 = \sqrt{\frac{B_4 - (K - B)}{2}},$$

$$Q_3 = \sqrt{\frac{B_4 + (K - B)}{2}}, \quad \sqrt{-B + i(A - B_1)} = P_1 + iQ_1, \quad \sqrt{-B + i(A + B_1)} = P_2 + iQ_2,$$

$$\sqrt{K - B + iB_1} = P_3 + iQ_3, \quad erf(\sqrt{iAt}) = r_1 + ir_2, \quad erf(P_1\sqrt{t} + iQ_1\sqrt{t}) = r_3 + ir_4,$$

$$erf(P_2\sqrt{t} + iQ_2\sqrt{t}) = r_5 + ir_6, \quad erf(P_3\sqrt{t} + iQ_3\sqrt{t}) = r_7 + ir_8$$

5.2. Nusselt Number

The non-dimensional Nusselt number, which is determined as the rate of heat transfer, is obtained by

$$Nu = -\frac{d\theta}{dy}\bigg|_{y=0}$$

The solution for the Nusselt number is calculated from the solution of Temperature profile θ, represented by (10), as follows:

$$
\begin{aligned}
Nu =\ & \frac{\cos At}{\sqrt{\pi t}} + \sqrt{\frac{A}{2}}\,(r_1 - r_2) - \frac{S}{A}\left[t\sqrt{\frac{t}{\pi}}\sin At - t^2\sqrt{\frac{A}{2}}\,(r_1 + r_2) + \frac{t(r_1 - r_2)}{\sqrt{2A}} - \frac{(r_1 + r_2)}{4A\sqrt{2A}}\right. \\
& + \frac{\cos At}{2A}\sqrt{\frac{t}{\pi}}\Bigg] + \frac{Gc}{A(Sc - 1)}\left[C_1\left\{\frac{-\sin At}{\sqrt{\pi t}} + \sqrt{\frac{A}{2}}\,(r_1 + r_2)\right\} - \frac{2C_2\sin At}{\sqrt{\pi t}}\right. \\
& + e^{-Bt}\{(C_2P_1 + C_3Q_1)(r_4\cos B_1 t - r_3\sin B_1 t) - (C_3P_1 - C_2Q_1)(r_3\cos B_1 t + r_4\sin B_1 t)\} \\
& + e^{-Bt}\{(C_2P_2 - C_3Q_2)(r_6\cos B_1 t + r_5\sin B_1 t) + (C_3P_2 + C_2Q_2)(r_5\cos B_1 t - r_6\sin B_1 t)\}\Bigg] \\
& + \frac{SGc}{(Sc-1)^2}\left[E_1\left\{\frac{\cos At}{\sqrt{\pi t}} + \sqrt{\frac{A}{2}}\,(r_1 - r_2) - \sqrt{ScK}\,erf(\sqrt{Kt}) - \sqrt{\frac{Sc}{\pi t}}e^{-Kt}\right\}\right. \\
& + 2E_2\left\{\frac{cos At}{\sqrt{\pi t}} - \sqrt{\frac{Sc}{\pi t}}e^{-Kt}\right\} + e^{-Bt}\{(E_2P_1 + E_3Q_1)(r_3 cos B_1 t + r_4\sin B_1 t)\} \\
& + (E_3P_1 - E_2Q_1)(r_4 cos B_1 t - r_3\sin B_1 t) + e^{-Bt}\{(E_2P_2 - E_3Q_2)(r_5 cos B_1 t - r_6\sin B_1 t) \\
& - (E_3P_2 + E_2Q_2)(r_6 cos B_1 t + r_5\sin B_1 t)\} - 2e^{-Bt}\sqrt{Sc}\{(E_2P_3 - E_3Q_3)(r_7 cos B_1 t - r_8\sin B_1 t) \\
& - (E_3P_3 + E_2Q_3)(r_8 cos B_1 t + r_7\sin B_1 t)\}\Bigg]
\end{aligned}
$$

The solution for the Nusselt number for the special case is given from the expression (13), which is represented by

$$
\begin{aligned}
Nu^* =\ & \frac{SKGc}{A(K^2 + A^2)}\left\{\frac{-\sin At}{\sqrt{\pi t}} + \sqrt{\frac{A}{2}}\,(r_1 + r_2))\right\} + \left(1 + \frac{SGc}{K^2 + A^2}\right)\left\{\frac{\cos At}{\sqrt{\pi t}} + \sqrt{\frac{A}{2}}\,(r_1 - r_2)\right\} \\
& - \frac{S}{A}\left[t\sqrt{\frac{t}{\pi}}\sin At - t^2\sqrt{\frac{A}{2}}\,(r_1 + r_2) + \frac{t(r_1 - r_2)}{\sqrt{2A}} - \frac{(r_1 + r_2)}{4A\sqrt{2A}} + \frac{\cos At}{2A}\sqrt{\frac{t}{\pi}}\right] \\
& - \frac{SGc}{K^2 + A^2}\left\{\sqrt{K}\,erf(\sqrt{Kt}) + \frac{e^{-Kt}}{\sqrt{\pi t}}\right\}
\end{aligned}
$$

The solution for the Nusselt number for the classical case is given from the expression (14), which is represented by

$$Nu_c = \frac{1}{\sqrt{\pi t}}$$

5.3. Sherwood Number

The non-dimensional Sherwood number, which is determined as the rate of mass transfer, is obtained by

$$Sh = -\frac{dC}{dy}\bigg|_{y=0}$$

The solution for the Sherwood number is calculated from the solution of Concentration profile C, represented by (8), as follows:

$$Sh = \sqrt{ScK}\ erf(\sqrt{Kt}) + \sqrt{\frac{Sc}{\pi t}}e^{-Kt}$$

The solution for the Sherwood number for the special case is given from the expression (11), which is represented by

$$Sh^* = \sqrt{K}\ erf(\sqrt{Kt}) + \frac{1}{\sqrt{\pi t}}e^{-Kt}$$

6. RESULT AND DISCUSSIONS

We calculated the velocity, temperature, concentration, Skin friction, Nusselt number, and Sherwood number for various values of the physical parameters S, Gr, Gc, Sc, K and time t from the solutions we obtained in the previous sections. This allowed us to get a better understanding of the physical significance of the problem. Additionally, we portrayed them graphically in Figures 2- 15.
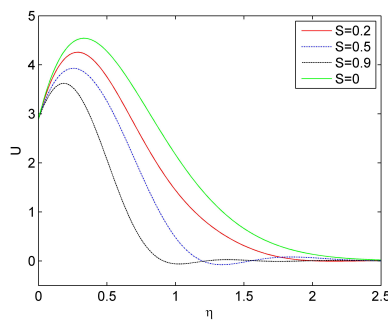
Figure 2. Effects of S on Velocity Profile for $Gr = 5, Gc = 5, t = 1.7, Sc = 0.6, K = 0.2$
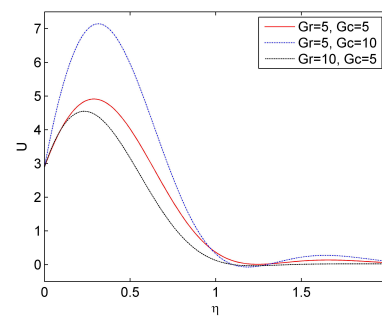
Figure 3. Effects of Gr and Gc on Velocity Profile for $S = 0.4, Sc = 0.6, t = 1.7, K = 0.2$
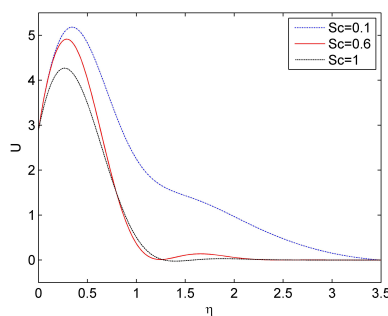
Figure 4. Effects of Sc on Velocity Profile for $Gr = 5, Gc = 5, S = 0.4, t = 1.7, K = 0.2$
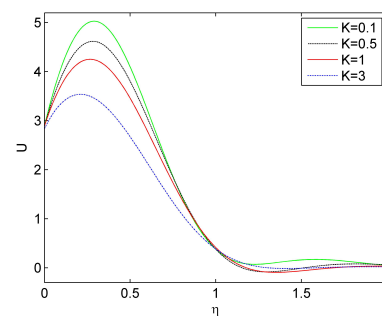
Figure 5. Effects of K on Velocity Profile for $Gr = 5, Gc = 5, S = 0.4, Sc = 0.6, t = 1.7$

The Figure 2 displays the changes in velocity profiles brought upon by thermal stratification (S). It can be seen that thermal stratification decrease the velocity. An increase in the thermal stratification parameter(S) leads to a decrease in the convective potential efficiency between the hot plate and the surrounding fluid. The reduction in the buoyancy force consequently leads to a decrease in the flow velocity. As seen in Figure 3, a rise in Gc results in a rise in velocity, but a rise in Gr results in a decline in velocity. The fluid's velocity for various values of Sc and K are represented in figures 4 and 5. As Sc and K values grow, the fluid velocity falls.
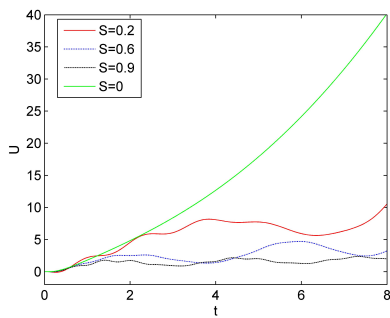
Figure 6. Effects of S on Velocity Profile against time for $Gr = 5, Gc = 5, Sc = 0.6, y = 1.6, K = 0.2$
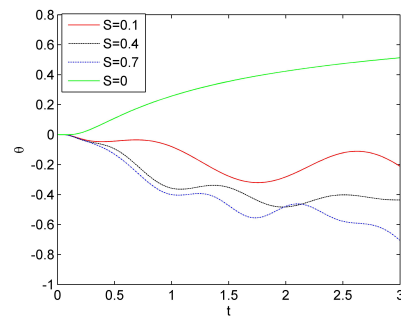
Figure 7. Effects of S on Temperature Profile against time for $Gr = 5, Gc = 5, Sc = 0.6, y = 1.6, K = 0.2$
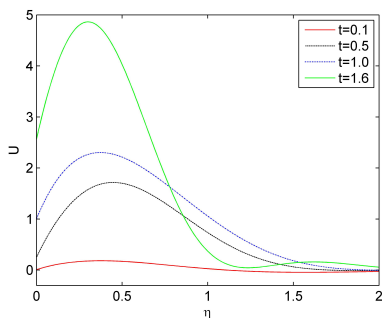
Figure 8. Velocity Profile at different time for $Gr = 5, Gc = 5, S = 0.4, Sc = 0.6, K = 0.2$
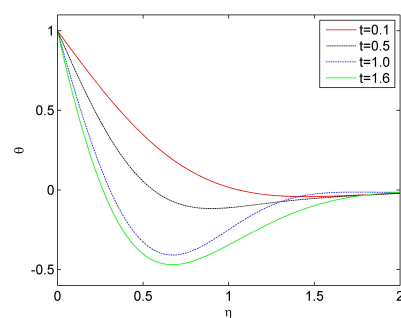
Figure 9. Temperature Profile at different time for $Gr = 5, Gc = 5, S = 0.4, Sc = 0.6, K = 0.2$

The impact of thermal stratification (S) on fluid velocity and temperature are plotted against time in Figures 6 and 7. When there is no stratification, the velocity increases indefinitely with time; but, when stratification exists, the velocity progressively approaches a stable state. The present research is more realistic than earlier ones without stratification because it applies thermal stratification, which lowers velocity and temperature in comparison to the classical scenario $(S = 0)$. The figures 8 and 9 represent time-varying velocity and temperature characteristics. We have seen that the velocity rises with time and falls to zero as the distance from the plate increases. On the other hand, Temperatures decrease with time and eventually attain absolute zero as one moves away from the plate.
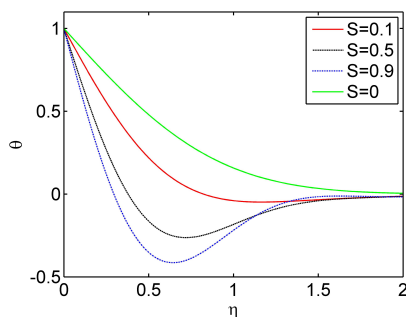
Figure 10. Effects of S on Temperature Profile for $Gr = 5, Gc = 5, , Sc = 0.6, t = 0.6, K = 0.2$
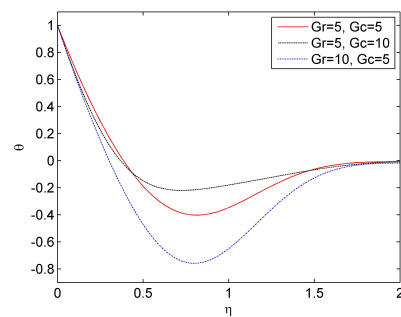
Figure 11. Effects of Gr and Gc on Temperature Profile for $S = 0.5, Sc = 0.6, t = 1.1, K = 0.2$

The impact of thermal stratification (S) on the temperature distribution is seen in Fig. 10. The presence of thermal stratification(S) will result in a decrease in the temperature gradient between the heated plate and the surrounding fluid. Therefore, the thermal boundary layer experiences an increase in thickness, resulting in a decrease in temperature. As the value of thermal stratification parameters (S) increases, it has been observed that the temperature drops. The impacts of $Gr, Gc, Sc,$ and K are displayed in 11, 12, and 13, respectively. The temperature decreases as the value of $Gr, Sc,$ and K is reduced, while the value of Gc is increased. The results of thermal stratification (S) on skin friction and Nusselt number are presented in Fig. 14 and 15, respectively.

They increase in presence of thermal stratification (S) compared to special case with no stratification. Thermal Stratification (S) contributes to an increase in the oscillation of the Nusselt number.
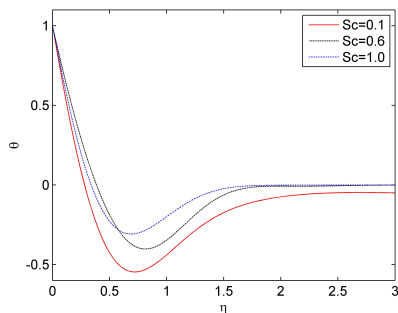
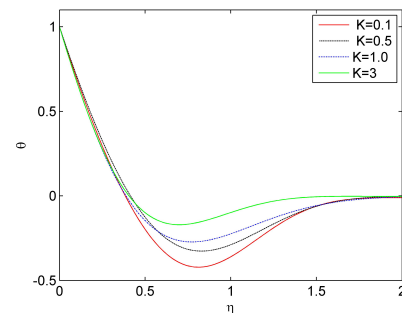**Figure 12.** Effects of Sc on Concentration Profile for $Gr = 5, Gc = 5, S = 0.5, t = 1.1, K = 0.2$

Figure 13. Effects of K on Temperature Profile for $Gr = 5, Gc = 5, S = 0.5, Sc = 0.6, t = 1.1$
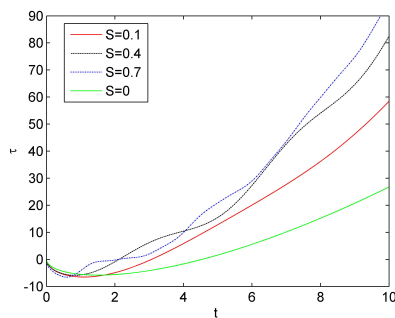

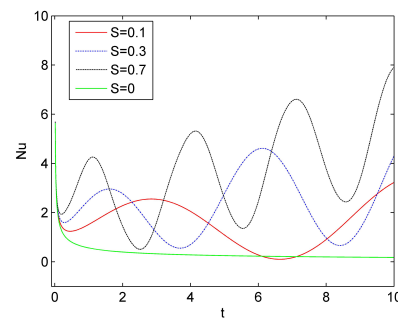**Figure 14.** Effects of S on Skin friction for $Gr = 5, Gc = 5, Sc = 0.1, K = 0.2$

Figure 15. Effects of S on Nusselt Number for $Gr = 5, Gc = 5, Sc = 0.1, K = 0.2$

7. CONCLUSION

We looked at the effect of thermal stratification (S) on the parabolic flow through an infinite vertical plate when a chemical reaction is present. The outcomes of the current investigation have been compared with those of the classic case, which assumes that there is no stratification. The velocity of the fluid reduces as the values of S, K, and Gr grows, but it increases as the value of Gc grows. The use of thermal stratification, which reduces velocity and temperature compared to the classical situation $(S = 0)$, makes this study more applicable than earlier ones. Temperature drops as K, Sc, and Gc go down; it rises when S, Gr, and time go up. The temperature is highest at the plate and then drops till it becomes zero farther away. The existence of stratification raises both the skin friction and the Nusselt number in contrast to a situation with no stratification. Furthermore, thermal Stratification (S) causes the Nusselt number to oscillate more frequently.

ORCID

Rupam Shankar Nath, https://orcid.org/0009-0002-2352-0538; **Rudra Kanta Deka**, https://orcid.org/0009-0007-1573-4890; **Himangshu Kumar**, https://orcid.org/0009-0008-9784-650X

REFERENCES

[1] R. Muthucumaraswamy, and E. Geetha, "Effects of parabolic motion on an isothermal vertical plate with constant mass flux," Ain Shams Engineering Journal, **5**(4), 1317–1323 (2014). https://doi.org/10.1016/j.asej.2014.05.011

[2] R. Muthucumaraswamy, and P. Sivakumar, "Hydro magnetic effects on parabolic flow past an infinite isothermal vertical plate with variable mass diffusion in the presence of thermal radiation and chemical reaction," International Journal of Recent Technology and Engineering, **4**(2), 5–10 (2015).

[3] A. Selvaraj, S.D. Jose, R. Muthucumaraswamy, and S. Karthikeyan, "Mhd-parabolic flow past an accelerated isothermal vertical plate with heat and mass diffusion in the presence of rotation," Materials Today: Proceedings, **46**, 3546–3549 (2021). https://doi.org/10.1016/j.matpr.2020.12.499

[4] E. Magyari, I. Pop, and B. Keller, "Unsteady free convection along an infinite vertical flat plate embedded in a stably stratified fluid-saturated porous medium," Transport in porous media, **62**, 233–249 (2006). https://doi.org/10.1007/s11242-005-1292-6

[5] A. Bhattacharya, and R.K. Deka, "Theoretical study of chemical reaction effects on vertical oscillating plate immersed in a stably stratified fluid," Research Journal of Applied Sciences, Engineering and Technology, **3**(9), 887–898 (2011). https://maxwellsci.com/print/rjaset/v3-887-898.pdf

[6] A. Shapiro, and E. Fedorovich, "Unsteady convectively driven flow along a vertical plate immersed in a stably stratified fluid," Journal of Fluid Mechanics, **498**, 333–352 (2004). https://doi.org/10.1017/S0022112003006803

[7] J.S. Park, and J.M. Hyun, "Technical note transient behavior of vertical buoyancy layer in a stratified fluid," International journal of heat and mass transfer, **41**(24), 4393–4397 (1998). https://doi.org/10.1016/S0017-9310(98)00175-6

[8] J.S. Park, "Transient buoyant flows of a stratified fluid in a vertical channel," KSME International Journal, 15, 656–664 (2001). https://doi.org/10.1007/BF03184382

[9] U.N. Das, R. Deka, and V.M. Soundalgekar, "Effects of mass transfer on flow past an impulsively started infinite vertical plate with constant heat flux and chemical reaction," Forschung im Ingenieurwesen, **60**(10), 284–287 (1994). https://doi.org/10.1007/BF02601318

[10] F.M.N. El-Fayez, "Effects of chemical reaction on the unsteady free convection flow past an infinite vertical permeable moving plate with variable temperature," Journal of surface engineered materials and advanced technology, **2**(2), 100-109 (2012). http://dx.doi.org/10.4236/jsemat.2012.22016

[11] B.P. Reddy, and J. Peter, "Effects of chemical reaction on mhd flow past an impulsively started infinite vertical plate with variable temperature and mass diffusion in the presence of hall current," Journal of the Serbian Society for Computational Mechanics, **13**(1), 92–108 (2019). http://doi.org/10.24874/jsscm.2019.13.01.06

[12] M.A. Mansour, N.F. El-Anssary, and A.M. Aly, "Effects of chemical reaction and thermal stratification on mhd free convective heat and mass transfer over a vertical stretching surface embedded in a porous media considering soret and dufour numbers," Chemical engineering journal, **145**(2), 340–345 (2008). https://doi.org/10.1016/j.cej.2008.08.016

[13] R. Kandasamy, K. Periasamy, and K.K.S. Prabhu, "Chemical reaction, heat and mass transfer on mhd flow over a vertical stretching surface with heat source and thermal stratification effects," International Journal of Heat and Mass Transfer, **48**(21-22), 4557–4561 (2005). https://doi.org/10.1016/j.ijheatmasstransfer.2005.05.006

[14] A.M. Megahed, and W. Abbas, "Non-newtonian cross fluid flow through a porous medium with regard to the effect of chemical reaction and thermal stratification phenomenon," Case Studies in Thermal Engineering, **29**, 101715 (2022). https://doi.org/10.1016/j.csite.2021.101715

[15] R.S. Nath, and R.K. Deka, "The effects of thermal stratification on flow past an infinite vertical plate in presence of chemical reaction," East European Journal of Physics, **3**, 23–232 (2023). https://doi.org/10.26565/2312-4334-2023-3-19

[16] N. Kalita, R.K. Deka, and R.S. Nath, "Unsteady flow past an accelerated vertical plate with variable temperature in presence of thermal stratification and chemical reaction," East European Journal of Physics, **3**, 441–450 (2023). https://doi.org/10.26565/2312-4334-2023-3-49

[17] K. Rafique, Z. Mahmood, U. Khan, S.M. Eldin, M. Oreijah, K. Guedri, and H.A. El-Wahed Khalifa, "Investigation of thermal stratification with velocity slip and variable viscosity on MHD flow of Al_2O_3-Cu-TiO_2/H_2O nanofluid over disk," Case Studies in Thermal Engineering, **49**, 103292 (2023). https://doi.org/10.1016/j.csite.2023.103292

[18] M. Abramowitz, and I.A. Stegun, editors, *Handbook of mathematical functions with Formulas, Graphs, and Mathematical Tables*, Ninth Printing, (Dover Publications Inc., NY, 1970).

[19] R.B. Hetnarski, "An algorithm for generating some inverse laplace transforms of exponential form," Zeitschrift f¨ur angewandte Mathematik und Physik ZAMP, **26**, 249–253 (1975). https://doi.org/10.1007/BF01591514

ВПЛИВ ТЕРМІЧНОЇ СТРАТИФІКАЦІЇ НА НЕСТАЦІОНАРНИЙ ПАРАБОЛІЧНИЙ ПОТІК ПОВЗ НЕСКІНЧЕННУ ВЕРТИКАЛЬНУ ПЛАСТИНУ З ХІМІЧНОЮ РЕАКЦІЄЮ

Рупам Шанкар Нат, **Рудра Канта Дека**, **Хімангшу Кумар**

Факультет математики, Університет Гаухаті, Гувахаті-781014, Ассам, Індія

У цій дослідницькій статті досліджується вплив термічної стратифікації на нестаціонарний параболічний потік повз нескінченну вертикальну пластину з хімічною реакцією. Використовуючи метод перетворення Лапласа, отримані аналітичні рішення для моделювання фізичного процесу потоку. Дослідження розглядає вплив термічної стратифікації на поле течії, а також вплив хімічної реакції на поле швидкості та температури. Результати випадку стратифікації потім порівнюються з випадком відсутності стратифікації подібного поля потоку. Результати цього дослідження можуть бути використані для покращення розуміння нестаціонарного параболічного потоку в теплових стратифікованих середовищах і надання цінного розуміння впливу хімічних реакцій на температурне поле.

Ключові слова: *термічна стратифікація; хімічна реакція; параболічний потік; вертикальна плита*

THERMAL AND MASS STRATIFICATION EFFECTS ON UNSTEADY FLOW PAST AN ACCELERATED INFINITE VERTICAL PLATE WITH VARIABLE TEMPERATURE AND EXPONENTIAL MASS DIFFUSION IN POROUS MEDIUM

 Himangshu Kumar*, Rudra Kanta Deka

Department of Mathematics, Gauhati University, Guwahati-781014, Assam, India
Corresponding Author e-mail: himangshukumar307@gmail.com

This study looks at how thermal and mass stratification affect the unsteady flow past an infinitely fast-moving vertical plate when the temperature is changing and there is exponential mass diffusion in a porous medium. By applying the Laplace transformation method, we determine the solutions to the equations that govern the system for the case of unitary Prandtl and Schmidt numbers. Graphical representations of the concentration, temperature, and velocity profiles, as well as the Nusselt Number, Sherwood number, and the Skin friction are provided to facilitate discussion of the cause of the different variables. To see the effects of thermal and mass stratification on the fluid flow, we compare the classical solution (Fluid with out stratification) with the primary solution (Fluid with the stratification) by using graph. The combined effects of the two stratification lead to a quicker approach to steady states. The outcomes can be helpful for heat exchange design and other engineering applications.

Keywords: *Unsteady flow; Porous Medium; Thermal Stratification; Mass Stratification; Accelerated plate*

PACS: 47.55.P-, 44.25.+f, 44.05.+e, 47.11.-j

NOMENCLATURE

α	Thermal Diffusivity	g	Acceleration due to gravity
β	Volumetric Coefficient of Thermal Expansion	Gc	Mass Grashof Number
β^*	Volumetric Coefficient of Expansion with Concentration	Gr	Thermal Grashof Number
γ	Thermal Stratification Parameter	Pr	Prandtl Number
ν	Kinematic Viscosity	S	Non-Dimensional Thermal Stratification Parameter
τ	Non-Dimensional Skin-Friction	t	Non-Dimensional Time
θ	Non-Dimensional Temperature	T'	Temperature of the fluid
ξ	Mass Stratification Parameter	t'	Time
A, a, a'	Constant	T'_∞	Temperature of the fluid far away from the Plate
C	Non-Dimensional Concentration		
C'	Species fluid concentration	T'_w	Temperature at the Plate
C'_∞	Concentration of the fluid far away from the Plate	U	Non-Dimensional Velocity
		u'	Velocity of the fluid in x' direction
C'_w	Concentration at the Plate	u_0	Acceleration of the Plate
D	Mass Diffusion Coefficient		
Da	Darcy number	y	Non-Dimensional Coordinate which is Normal to the plate
F	Non-Dimensional Mass Stratification Parameter		
		y'	Coordinate which is Normal to the Plate

1. INTRODUCTION

Many fields, including geology, thermal hydraulics, combustion, and environmental engineering, are profoundly affected by the phenomenon of mass and heat movement in porous material. The discovery of new energy sources has sparked a growing interest in the challenge of controlling the flow of mass and heat through porous materials. The focus of this work is to investigate the influences of thermal and mass stratification on the dynamics of unstable flow across an infinite vertical plate moving at high speed through a material that is permeable with changing temperature and exponential mass diffusion. Analytical approaches are applied to determine the solutions to the problem's governing equations. The outcomes are carefully examined and discussed. The paper also sheds light on the relevant physical processes that control the flow's behavior.

Natural convection of MHD mass and heat transport, when a chemical reaction is present was explored by Hemant Poonia and R.C. Chaudhary [1] through the use of an infinitely accelerated plate in a porous material that is positioned vertically. A. Selvaraj and E. Jothi [2] studied MHD and the absorption of radiation of a stream of fluid passing a vertical plate moving at an exponentially increasing rate, when warmth and mass diffuse exponentially across a porous material, and the influences of the source of heat on these variables. R.K. Deka and B.C. Neog [3] conducted research to find a precise solution to the problem of natural convection movement that fluctuates in one dimension passing an endless vertically accelerated plate while the plate was immersed in a thick fluid with layers of different temperatures. Researchers Kumar A.V., S.V.K. Varma, and R. Mohan [4] studied how the chemical processes and radiation affect the flow of MHD free convection through a plate that is vertical and accelerating at an exponential rate, where both the temperature and the rate of mass diffusion were variable. Using a porous materials and a magnetic field, Mondal S., Parvin S., and Ahmmed S. [5] examined the impact of chemical processes and radiation on the transfer of mass in unstable natural convection flow across an infinite perpendicular plate moving at an exponential pace. The unstable, incompressible, one-dimensional natural convective flow across an indefinitely rotating vertical cylinder with combined buoyancy effects of mass and heat transfer along with thermal and mass stratification was investigated by Deka R.K. and Paul A. [6]. Muthucumaraswamy R. and Visalakshi V. [7] investigated the impact of heat radiation on the motion of a fluid with a high viscosity and low compressibility through a vertically infinite plate moving at an exponential rate, subject to a homogeneous mass diffusion and changeable temperature. Rajesh V., Varma S.V.K. [8] did a study to find out how heat radiation affects the flow of natural convection over an infinitely long perpendicular plate that is speed up exponentially in a magnetic field and with mass transfer. Rajesh V. and S. Varma [9] considered the impact of a heat source on MHD flow. The flow was studied as it went through a porous medium at several temperatures and past an exponentially accelerating vertical plate. R.S. Nath and R.K. Deka [18] looked into how thermal stratification affected a fluid's ability to pass through an infinite vertical plate while experiencing a first-order chemical reaction.

Since no studies have been conducted on the impact of mass and thermal stratification on an infinite vertical plate started by an impulse in a porous material with exponential mass diffusion and temperature change, we were inspired to fill this area of knowledge.

2. MATHEMATICAL ANALYSIS

The fundamental equations of momentum, energy, and mass conservation are used to develop the system of equations that describes unsteady flow via a porous materials with exponential mass diffusion and fluctuating temperatures across an indefinitely accelerated vertical plate. Fig. 1 depicts the problem's physical layout. We assume a Cartesian coordinate system to discuss the flow problem where the infinite plate is to be the $x' - axis$, and the $y' - axis$ to be transverse to it. At the start, the fluid and plate are both at the identical temperature, T'_∞, and the concentration, C'_∞, is uniform across the entire surface. At time t', the plate began to speed up with a velocity of $u' = u_0 t'$ in its own path. The plate's temperature grew in a linear fashion with time t', while the level of concentration close to the plate achieved a value $C'_\infty + (c'_w - c'_\infty)e^{a't'}$. Therefore, the following equations characterize the unsteady flow using the standard Boussinesq approximation:

$$\frac{\partial u'}{\partial t'} = g\beta(T' - T'_\infty) + g\beta^*(C' - C'_\infty) + \nu\frac{\partial^2 u'}{\partial y'^2} - \frac{\nu}{k'}u' \tag{1}$$

$$\frac{\partial T'}{\partial t'} = \alpha\frac{\partial^2 T'}{\partial y'^2} - \gamma u' \tag{2}$$

$$\frac{\partial C'}{\partial t'} = D\frac{\partial^2 C'}{\partial y'^2} - \xi u' \tag{3}$$

with the following initial and boundary Conditions:

$$u' = 0 \qquad T' = T'_\infty \qquad C' = C'_\infty \qquad \forall y', t' \le 0$$
$$u' = u_0 t' \qquad T' = T'_\infty + (T'_w - T'_\infty)At' \qquad C' = C'_\infty + (C'_w - C'_\infty)e^{a't'} \qquad \text{at } y' = 0, t' > 0$$

$$u' = 0 \qquad T' \to T'_\infty \qquad\qquad C' \to C'_\infty \qquad\qquad \text{as } y' \to \infty, t' > 0 \quad (4)$$

Non-Dimensional Quantities:

$$U = \frac{u'}{(u_0\nu)^{\frac{1}{3}}}, \quad t = \frac{t'u_0^{\frac{2}{3}}}{\nu^{\frac{1}{3}}}, \quad y = \frac{y'u_0^{\frac{1}{3}}}{\nu^{\frac{2}{3}}}, \quad \theta = \frac{T' - T'_\infty}{T'_w - T'_\infty}, \quad C = \frac{C' - C'_\infty}{C'_w - C'_\infty}, \quad Gr = \frac{g\beta(T'_w - T'_\infty)}{u_0}$$

$$Gc = \frac{g\beta^*(C'_w - C'_\infty)}{u_0}, \quad Pr = \frac{\nu}{\alpha}, \quad Sc = \frac{\nu}{D}, \quad a = \frac{\nu^{\frac{1}{3}}a'}{u_0^{\frac{2}{3}}}, \quad S = \frac{\gamma\nu^{\frac{2}{3}}}{u_0^{\frac{1}{3}}(T'_w - T'_\infty)}, \quad F = \frac{\xi\nu^{\frac{2}{3}}}{u_0^{\frac{1}{3}}(C'_w - C'_\infty)}$$

$$Da = \frac{k'u_0^{\frac{2}{3}}}{\nu^{\frac{4}{3}}}$$

where, $A = \left(\frac{u_0^2}{\nu}\right)^{\frac{1}{3}}$ is the constant.

Using the non-dimensional quantities, equation (1) to (3) reduces to

$$\frac{\partial U}{\partial t} = Gr\theta + GcC + \frac{\partial^2 U}{\partial y^2} - \frac{1}{Da}U \tag{5}$$

$$\frac{\partial \theta}{\partial t} = \frac{1}{Pr}\frac{\partial^2 \theta}{\partial y^2} - SU \tag{6}$$

$$\frac{\partial C}{\partial t} = \frac{1}{Sc}\frac{\partial^2 C}{\partial y^2} - FU \tag{7}$$

Boundary and initial conditions in dimensionless form are:

$$\begin{aligned}
u = 0 & \qquad \theta = 0 & \qquad C = 0 & \qquad \forall y, t \le 0 \\
u = t & \qquad \theta = t & \qquad C = e^{at} & \qquad \text{at } y = 0, t > 0 \\
u = 0 & \qquad \theta \to 0 & \qquad C \to 0 & \qquad \text{as } y \to \infty, t > 0
\end{aligned} \tag{8}$$

3. METHOD OF SOLUTION

The Laplace Transform is implemented to find the solutions of the coupled equations mentioned above. Using Laplace transform technique for Pr=Sc=1 and with the help of (8), equation (5) to (7) reduces to,

$$\frac{d^2\overline{U}}{dy^2} - \left(s + \frac{1}{Da}\right)\overline{U} + Gr\overline{\theta} + Gc\overline{C} = 0 \tag{9}$$
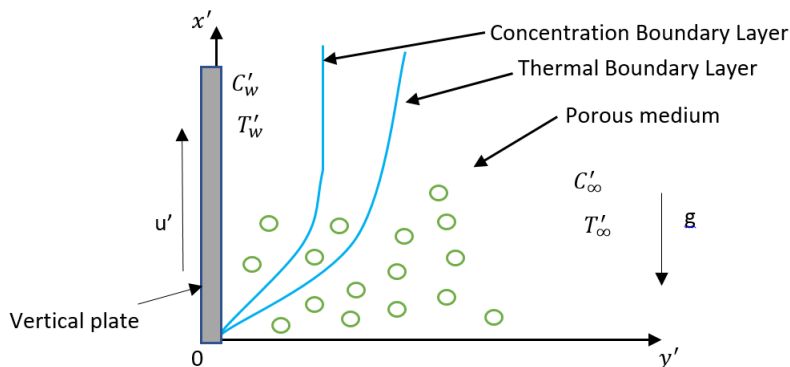
Figure 1. Physical model of the problem

$$\frac{d^2\overline{\theta}}{dy^2} - s\overline{\theta} = S\overline{U} \tag{10}$$

and

$$\frac{d^2\overline{C}}{dy^2} - s\overline{C} = F\overline{U} \tag{11}$$

Where 's' is the Parameter for the Laplace transform and $\overline{U}, \overline{\theta}$ and $\overline{C}$ are the Laplace transform of U, Θ and C respectively.

Now this set of differential equations were solved using boundary and initial conditions and taking inverse Laplace technique we obtained the expression for velocity, concentration and temperature as follows:

$$U \;=\; \frac{1}{B-R}\{Bh_1(B) - Rh_1(R)\} - \frac{Gr}{B-R}\{h_1(B) - h_1(R)\} - \frac{Gc}{B-R}\{h_2(B) - h_2(R)\} \tag{12}$$

$$
\begin{aligned}
C \;=\;& \frac{SGre^{at}}{2BR}\left[e^{-2\eta\sqrt{at}}erfc\left(\eta - \sqrt{at}\right) + e^{2\eta\sqrt{at}}erfc\left(\eta + \sqrt{at}\right)\right] - \frac{FGrt}{BR}\left[\left(1+2\eta^2\right)erfc(\eta) - \frac{ye^{-\eta^2}}{\sqrt{\pi t}}\right] \\
&+ \frac{F}{B-R}\{h_1(B) - h_1(R)\} - \frac{FGr}{BR(B-R)}\{Rh_1(B) - Bh_1(R)\} \\
&- \frac{FGc}{BR(B-R)}\{Rh_2(B) - Bh_2(R)\}
\end{aligned} \tag{13}
$$

and

$$
\begin{aligned}
\theta \;=\;& \frac{FGct}{BR}\left[\left(1+2\eta^2\right)erfc(\eta) - \frac{ye^{-\eta^2}}{\sqrt{\pi t}}\right] - \frac{SGce^{at}}{2BR}\left[e^{-2\eta\sqrt{at}}erfc\left(\eta - \sqrt{at}\right) + e^{2\eta\sqrt{at}}erfc\left(\eta + \sqrt{at}\right)\right] \\
&+ \frac{S}{B-R}\{h_1(B) - h_1(R)\} - \frac{SGr}{BR(B-R)}\{Rh_1(B) - Bh_1(R)\} \\
&- \frac{SGc}{BR(B-R)}\{Rh_2(B) - Bh_2(R)\}
\end{aligned} \tag{14}
$$

Where,

$$B = \frac{\frac{1}{Da} + \sqrt{\frac{1}{Da^2} - 4(SGr + FGc)}}{2}, \quad R = \frac{\frac{1}{Da} - \sqrt{\frac{1}{Da^2} - 4(SGr + FGc)}}{2},$$

$$\eta = \frac{y}{2\sqrt{t}}, \quad BR = SGr + FGc, \quad B + R = \frac{1}{Da}, \quad B - R = \sqrt{\frac{1}{Da^2} - 4(SGr + FGc)}$$

Also h_i's are inverse Laplace's transforms given by

$$h_1(P) = L^{-1}\left\{\frac{e^{-y\sqrt{s+P}}}{s^2}\right\} \quad and \quad h_2(P) = L^{-1}\left\{\frac{e^{-y\sqrt{s+P}}}{s-a}\right\}$$

3.1. Classical Case ($S = 0, F = 0$)

For classical solution, we first put $\gamma = 0$ in equation (2) and $\xi = 0$ in equation (3). After that they are non-dimensionalized by using same group of dimensionless parameters. Thus the solutions of concentration, temperature and velocity are obtained as follows:

$$C^* \;=\; \frac{e^{at}}{2}\left[e^{-2\eta\sqrt{at}}erfc\left(\eta - \sqrt{at}\right) + e^{2\eta\sqrt{at}}erfc\left(\eta + \sqrt{at}\right)\right] \tag{15}$$

$$\theta^* \;=\; t\left[\left(1+2\eta^2\right)erfc(\eta) - \frac{ye^{-\eta^2}}{\sqrt{\pi t}}\right] \tag{16}$$

$$
\begin{aligned}
U^* \;=\;& \left(1 - \frac{Gr}{B+R}\right)h_1(B+R) - \frac{Gc}{(B+R)}h_2(B+R) + \frac{Gr.t}{B+R}\left[\left(1+2\eta^2\right)erfc(\eta) - \frac{ye^{-\eta^2}}{\sqrt{\pi t}}\right] \\
&+ \frac{Gc\,e^{at}}{2(B+R)}\left\{e^{-2\eta\sqrt{a.t}}erfc\left(\eta - \sqrt{a.t}\right) + e^{2\eta\sqrt{a.t}}erfc\left(\eta + \sqrt{a.t}\right)\right\}
\end{aligned} \tag{17}
$$

3.2. Skin-Friction

Non-dimensional determinations of the plate's skin friction (relative to momentum transfer) is given by:

$$\tau = -\frac{dU}{dy}\bigg|_{y=0}$$

So, using the expression of velocity profile in equation (12) we get,

$$
\begin{aligned}
\tau &= \frac{1}{B-R}\left[t\left(B^{3/2}\,erf\left(\sqrt{B.t}\right) - R^{3/2}\,erf\left(\sqrt{R.t}\right) + \frac{B.e^{-B.t} - R.e^{-R.t}}{\sqrt{\pi t}}\right)\right.\\
&\quad\left. + \frac{\sqrt{B}erf\left(\sqrt{B.t}\right) - \sqrt{R}erf\left(\sqrt{R.t}\right)}{2}\right] - \frac{Gr}{B-R}\left[t\left(\sqrt{B}\,erf\left(\sqrt{B.t}\right) - \sqrt{R}\,erf\left(\sqrt{R.t}\right)\right.\right.\\
&\quad\left.\left. + \frac{e^{-B.t} - e^{-R.t}}{\sqrt{\pi t}}\right) + \frac{erf\left(\sqrt{B.t}\right)}{2\sqrt{B}} - \frac{erf\left(\sqrt{R.t}\right)}{2\sqrt{R}}\right] - \frac{Gc}{B-R}\left[e^{a.t}\left(\sqrt{a+B}\,erf\left(\sqrt{(a+B)t}\right)\right.\right.\\
&\quad\left.\left. - \sqrt{a+R}\,erf\left(\sqrt{(a+R)t}\right)\right) + \frac{e^{-B.t} - e^{-R.t}}{\sqrt{\pi t}}\right]
\end{aligned}
\tag{18}
$$

Similarly the expression of skin friction for Classical case is given by -

$$
\begin{aligned}
\tau^* = -\frac{dU^*}{dy}\bigg|_{y=0} &= \left(1 - \frac{Gr}{B+R}\right)\left[t\sqrt{B+R}\,erf\left(\sqrt{(B+R)t}\right) + \frac{te^{-(B+R)t}}{\sqrt{\pi t}}\right.\\
&\quad\left. + \frac{erf\left(\sqrt{(B+R)t}\right)}{2\sqrt{B+R}}\right] + \frac{2Gr}{(B+R)}\sqrt{\frac{t}{\pi}}\\
&\quad - \frac{Gc}{(B+R)}\left[e^{a.t}\sqrt{a+B+R}\,erf\left(\sqrt{(a+B+R)t}\right) + \frac{e^{-(B+R)t}}{\sqrt{\pi t}}\right]\\
&\quad + \frac{Gc}{(B+R)}\left[e^{a.t}\sqrt{a}\,erf\left(\sqrt{at}\right) + \frac{1}{\sqrt{\pi t}}\right]
\end{aligned}
\tag{19}
$$

3.3. Nusselt Number

Non-dimensional determinations of the plate's Nusselt number (relative to heat transfer) is given by:

$$Nu = -\frac{d\theta}{dy}\bigg|_{y=0}$$

So, using expression of temperature in equation (14) we get,

$$
\begin{aligned}
Nu &= \frac{2FGc}{BR}\sqrt{\frac{t}{\pi}} - \frac{SGc}{BR}\left[e^{at}\sqrt{a}\,erf\left(\sqrt{at}\right) + \frac{1}{\sqrt{\pi t}}\right] + \frac{S}{B-R}\left[t\left(\sqrt{B}\,erf\left(\sqrt{B.t}\right)\right.\right.\\
&\quad\left.\left. - \sqrt{R}\,erf\left(\sqrt{R.t}\right) + \frac{e^{-B.t} - e^{-R.t}}{\sqrt{\pi t}}\right) + \frac{1}{2}\left(\frac{erf\left(\sqrt{B.t}\right)}{\sqrt{B}} - \frac{erf\left(\sqrt{R.t}\right)}{\sqrt{R}}\right)\right]\\
&\quad - \frac{SGr}{BR(B-R)}\left[t\left(R\sqrt{B}\,erf\left(\sqrt{B.t}\right) - B\sqrt{R}\,erf\left(\sqrt{R.t}\right) + \frac{R.e^{-B.t} - B.e^{-R.t}}{\sqrt{\pi t}}\right)\right.\\
&\quad\left. + \frac{1}{2}\left(\frac{R.erf\left(\sqrt{B.t}\right)}{\sqrt{B}} - \frac{B.erf\left(\sqrt{R.t}\right)}{\sqrt{R}}\right)\right] - \frac{SGc}{BR(B-R)}\left[\frac{R.e^{-B.t} - B.e^{-R.t}}{\sqrt{\pi t}}\right.\\
&\quad\left. + e^{at}\left\{R\sqrt{a+B}\,erf\left(\sqrt{(a+B)t}\right) - B\sqrt{a+R}erf\left(\sqrt{(a+R)t}\right)\right\}\right]
\end{aligned}
\tag{20}
$$

Similarly the expression of nusselt number for Classical case is given by -

$$Nu^* = -\frac{d\theta^*}{dy}\bigg|_{y=0} = 2\sqrt{\frac{t}{\pi}}$$

3.4. Sherwood Number

In non-dimensional form, expression for the Sherwood number (relative to mass transfer) is given by,

$$Sh = -\frac{dC}{dy}\bigg|_{y=0}$$

So, using expression of concentration in equation (13) we get,

$$
\begin{aligned}
Sh \;=\; & \frac{SGr}{BR}\left[e^{at}\sqrt{a}\; erf(\sqrt{at}) + \frac{1}{\sqrt{\pi t}}\right] - \frac{2FGr}{BR}\sqrt{\frac{t}{\pi}} \\
& + \frac{F}{B-R}\left[t\left(\sqrt{B}\; erf(\sqrt{B.t}) - \sqrt{R}\; erf(\sqrt{R.t}) + \frac{e^{-B.t} - e^{-R.t}}{\sqrt{\pi t}}\right)\right. \\
& + \frac{1}{2}\left(\frac{erf(\sqrt{B.t})}{\sqrt{B}} - \frac{erf(\sqrt{R.t})}{\sqrt{R}}\right)\bigg] \\
& - \frac{FGr}{BR(B-R)}\left[t\left(R\sqrt{B}\; erf(\sqrt{B.t}) - B\sqrt{R}\; erf(\sqrt{R.t}) + \frac{R.e^{-B.t} - B.e^{-R.t}}{\sqrt{\pi t}}\right)\right. \\
& + \frac{1}{2}\left(\frac{R.erf(\sqrt{B.t})}{\sqrt{B}} - \frac{B.erf(\sqrt{R.t})}{\sqrt{R}}\right)\bigg] - \frac{FGc}{BR(B-R)}\left[\frac{R.e^{-B.t} - B.e^{-R.t}}{\sqrt{\pi t}}\right. \\
& + e^{at}\left\{R\sqrt{a+B}\; erf(\sqrt{(a+B)t}) - B\sqrt{a+R}\; erf(\sqrt{(a+R)t})\right\}\bigg]
\end{aligned}
$$

(21)

Similarly the expression of Sherwood number for Classical case is given by -

$$Sh^* = -\frac{dC^*}{dy}\bigg|_{y=0} = e^{at}\sqrt{a}\; erf(\sqrt{at}) + \frac{1}{\sqrt{\pi t}}$$

4. RESULT AND DISCUSSIONS

We computed numerical values of temperature, concentration, velocity, Nusselt number, Skin friction, and Sherwood Number from the solutions obtained in the sections that came before this one, for a variety of values of the physical parameters Gr, Gc, S, F, Da and time t. This allowed us to get a better understanding of the physical significance of the problem. In addition to this, we showed them using graphs, which can be found in Figures 2 through 22.

The velocity profile with and without stratification for various values of S, F, Gr, Gc, Da and time (t) are shown in the Figures 2 to 6. A stratified fluid is observed to move more slowly than a comparable volume of unstratified fluid. The velocity diminishes as the values of S and F, which represent the temperature and mass stratification, are raised. The increase in velocity is proportional to the rise in thermal Grashof number (Gr) and mass Grashof number (Gc). The rise in velocity is caused by an increase in buoyancy forces. With time, the classical velocity keeps on rising, but in the presence of stratification, it stabilises. All of these results were found to be similar to those obtained by Deka RK and Paul A. [6]. Figure 6 clearly shows that the velocity grows up with the growing Darcy number(Da). The reason behind this is that a higher Darcy number indicates a more permeable porous material, which in turn reduces the resistance to the flow of the fluid and increases its velocity.

The temperature and concentration profile (with stratification and with no stratification) against y for various values of S, F, Gr, Gc, Da and t are depicted graphically in Figures 7 to 16. Diagrams show that at the plate, the concentration and temperature are at their highest, and as time progresses, they decline toward zero. Concentration reduces with rising F but increases with rising S, and temperature rises with rising F but drops with rising S. Compared to the non-stratified fluid, the stratified fluid has been found to have lower concentration and temperature. As the thermal and mass Grashof numbers $(Gr$ and $Gc)$ go up, it is also evident that both concentration and temperature fall. In the absence of stratification, the traditional concentration and temperature also increase gradually over time. From Figures 9 and 14 it is seen that as Darcy number(Da) grow up, temperature and concentration fall down.

For a set of variables governing the mass and temperature stratification, Figures 17, 19, and 21 shows the time-dependent pattern of the momentum transfer rate, the Nusselt number, and the rate of mass transfer, including the classical case. While skin friction steadily decreases for an unstratified fluid, it approaches a steady state for a stratified one and as the temperature and mass stratification parameters rise, so does skin friction. Plate and fluid interaction generates skin friction. More extreme differences in fluid temperature or density from the plate surface are observed when the thermal or mass stratification parameter rises. Skin friction increases

as a result of increased fluid interaction with a plate as a result of a change in fluid temperature or density. The Nusselt number increases over time, and the Sherwood number initially drops before rising again. Also with the increase in S, Nusselt number increases but it decreases as mass stratification parameter (F) increases and the result is opposite for Sherwood number. Skin friction decrease as Gr and Gc increases. All of these results were earlier predicted by Deka RK and Paul A. [6]. However, the Nusselt and Sherwood numbers are decreases with increasing Gc but increases as Gr increase.
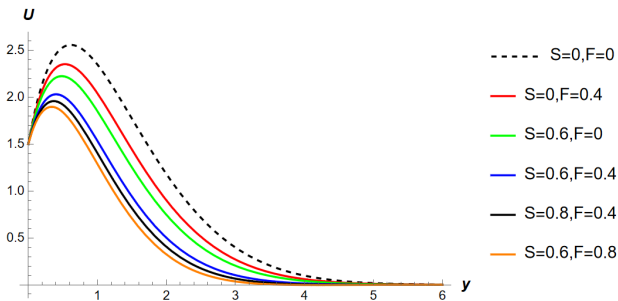
Figure 2. Influences of S and F on velocity profile for $Gr = 5, Gc = 5, Da = 1, a = 0.1, t = 1.5$
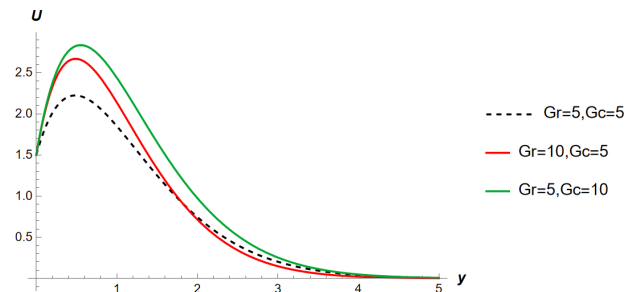
Figure 3. Influences of Gr and Gc on velocity profile for $S = 0.4, F = 0.2, Da = 1, a = 0.1, t = 1.5$
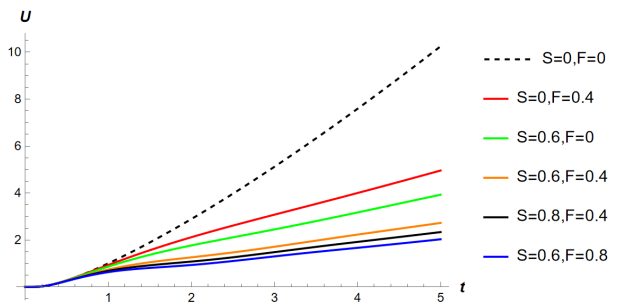
Figure 4. Influences of S and F on velocity profile against time for $Gr = 5, Gc = 5, y = 1.4, Da = 1, a = 0.1$
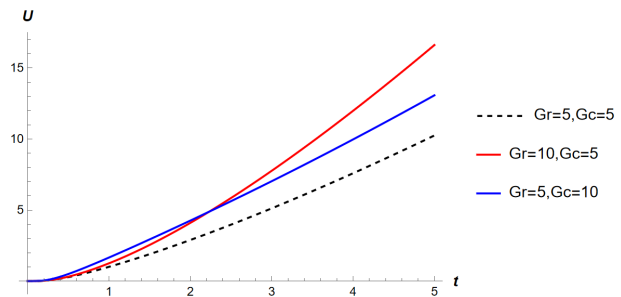
Figure 5. Influences of Gr and Gc on velocity against time for $S = 0.4, F = 0.2, Da = 1, y = 1.4, a = 0.1$
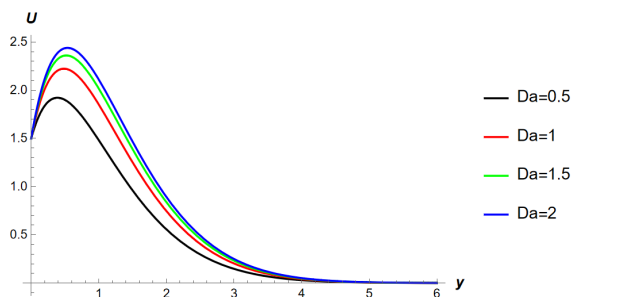
Figure 6. Influences of Da on velocity profile for $Gr = 5, Gc = 5, S = 0.4, F = 0.2, a = 0.1, t = 1.5$
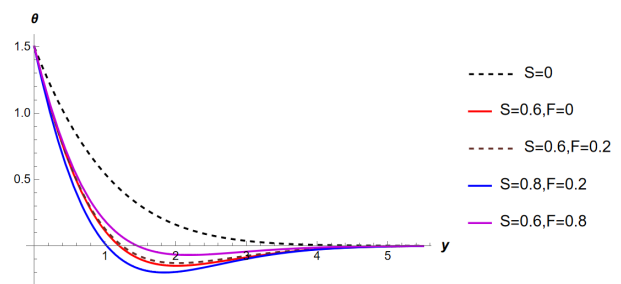
Figure 7. Influences of S and F on temperature profile for $Gr = 5, Gc = 5, t = 1.5, Da = 1, a = 0.1$

5. CONCLUSION

Based on the results derived from the preceding discussion, the following are the conclusions of this study:

(i) As S and F grow, velocity drops, while rises with Gr, Gc and Da. Compared to unstratified fluid, the speed of thermally and mass-stratified fluid is slower.
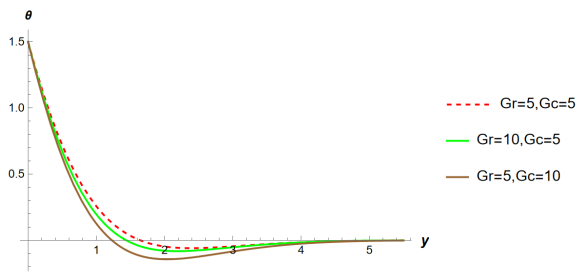
Figure 8. Influences of Gr and Gc on temperature for $S = 0.4, F = 0.2, a = 0.1, Da = 1, t = 1.5$
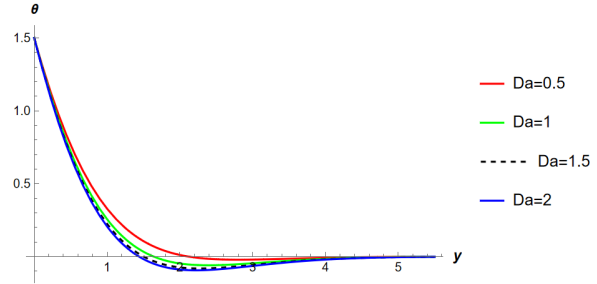

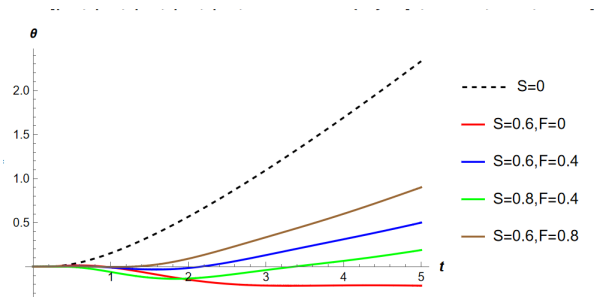**Figure 9.** Influences of Da on temperature for $S = 0.4, F = 0.2, a = 0.1, t = 1.5, Gr = 5, Gc = 5$

Figure 10. Influences of S and F on temperature profile against time for $Gr = 5, Gc = 5, Da = 1, y = 1.4, a = 0.1$
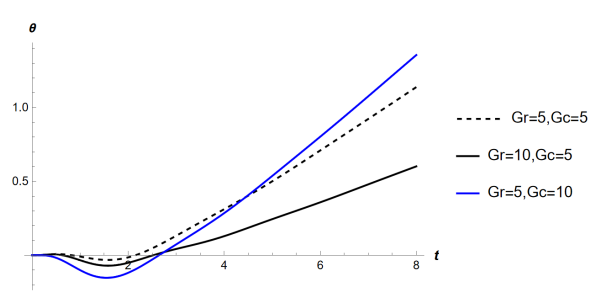

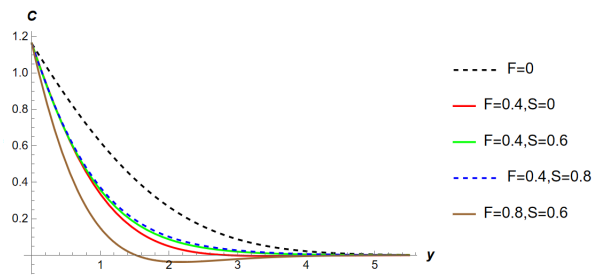**Figure 11.** Influences of Gr and Gc on temperature profile for $S = 0.4, F = 0.2, Da = 1, y = 1.4, a = 0.1$

Figure 12. Influences of S and F on concentration profile for $Gr = 5, Gc = 5, t = 1.5, a = 0.1, Da = 1$
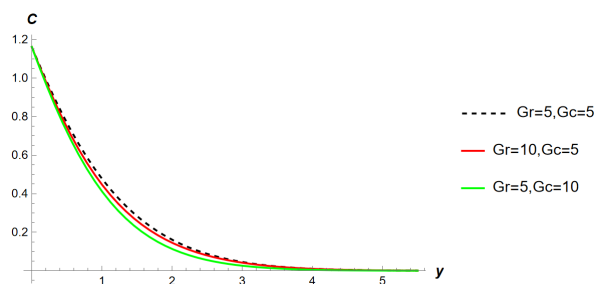
Figure 13. Influences of Gr and Gc on concentration for $S = 0.4, F = 0.2, a = 0.1, Da = 1, t = 1.5$
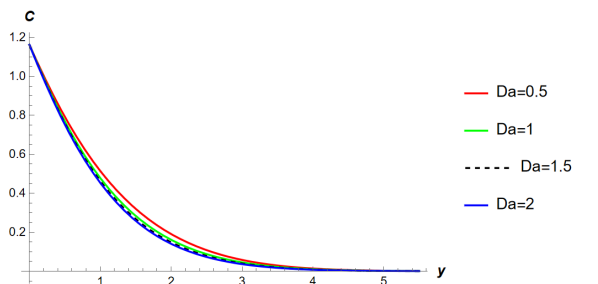
Figure 14. Influences of Da on concentration profile for $S = 0.4, F = 0.2, a = 0.1, Da = 1, t = 1.5, Gr = 5, Gc = 5$
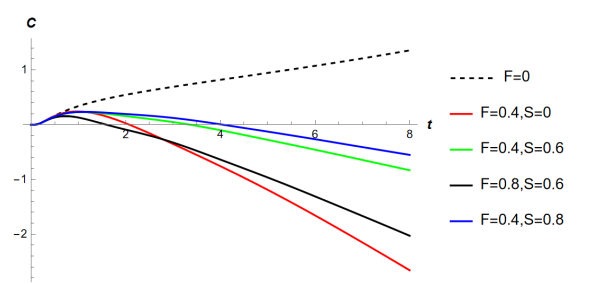

Figure 15. Influences of S and F on concentration against time for $Gr = 5, Gc = 5, a = 0.1, Da = 1, y = 1.4$

(ii) Increasing Gr, and Gc causes temperature and concentration to drop. The temperature falls as S rise and rises as F rise, the result is opposite for concentration. Fluid that is stratified has a lower temperature and concentration than fluid that is not stratified.
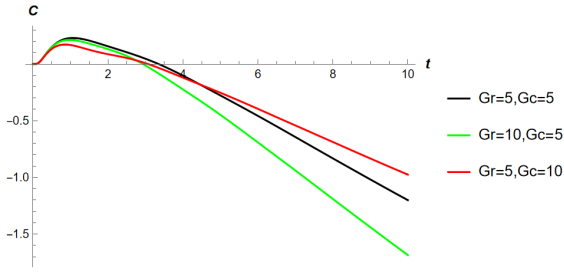
Figure 16. Influences of Gr and Gc on concentration against time for $S = 0.4$, $F = 0.2$, $y = 1.4$, $a = 0.1$, $Da = 1$
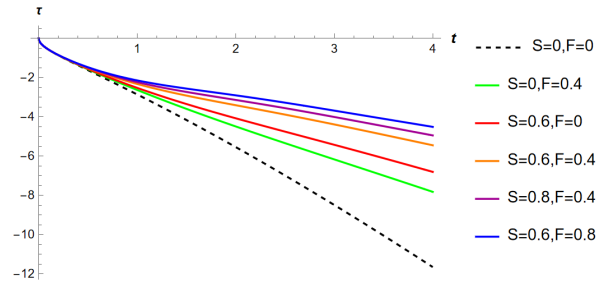

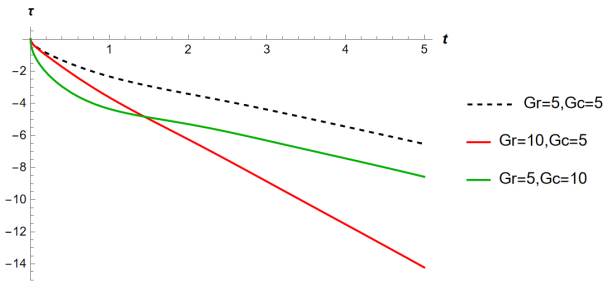**Figure 17.** Influences of S and F on Skin friction for $Gr = 5$, $Gc = 5, a = 0.1$, $Da = 1$

Figure 18. Influences of Gr and Gc on Skin friction for $S = 0.4, F = 0.2, a = 0.1, Da = 1$
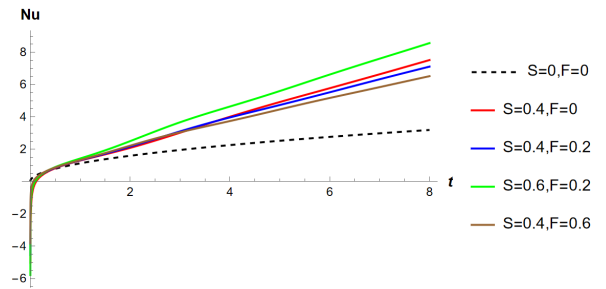

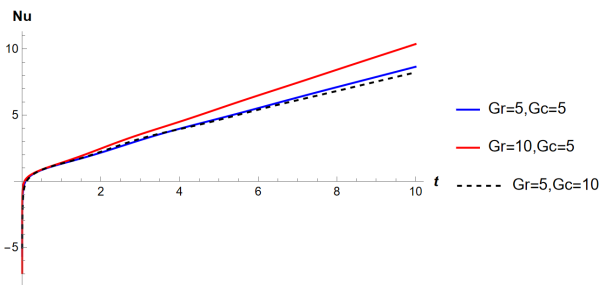**Figure 19.** Influences of S and F on Nusselt number for $Gr = 5, Gc = 5, a = 0.1, Da = 1$

Figure 20. Influences of Gr and Gc on Nusselt number for $S = 0.4, F = 0.2, Da = 1, a = 0.1$
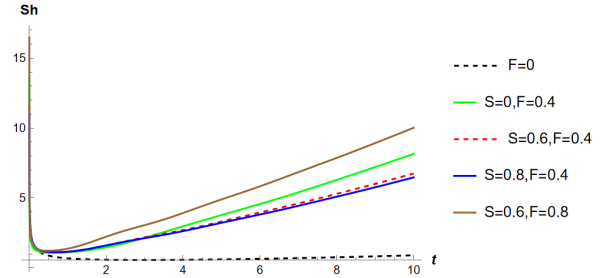

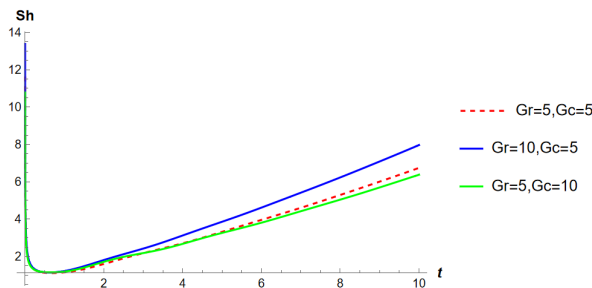**Figure 21.** Influences of S and F on Sherwood number for $Gr = 5, Gc = 5, Da = 1, a = 0.1$

Figure 22. Influences of Gr and Gc on Sherwood number for $S = 0.4, F = 0.2, a = 0.1, Da = 1$

(iii) When stratification is present, the velocity, temperature, and concentration progressively stabilise, whereas without it, they continue to increase gradually with time. A more rapid approach to steady states is achieved due to the cumulative impacts of the two stratification.

(iv) It is shown that, unlike in the classical condition, skin friction approaches a fixed value as time progresses for stratified fluid. When S and F are both high, skin friction rises. Additionally, as Gr and Gc grow, skin friction decreases.

(v) Increasing the thermal stratification value leads to a greater Nusselt number, whereas increasing the mass stratification parameter causes a decline in the Nusselt number; however, the inverse is true for the Sherwood number. Increasing Gc reduces the Nusselt number and the Sherwood number, but increasing Gr raises them.

ORCID

 Himangshu Kumar, https://orcid.org/0009-0008-9784-650X; **Rudra Kanta Deka**, https://orcid.org/0009-0007-1573-4890

REFERENCES

[1] H. Poonia, and R.C. Chaudhary, "Mass transfer with chemical reaction effects on MHD free convective flow past an accelerated vertical plate embedded in a porous medium," Int. J. of Applied Mathematics & Statistical Sciences, **5**(4), 33-46 (2016).

[2] A. Selvaraj, and E. Jothi, "Heat source impact on MHD and radiation absorption fluid flow past an exponentially accelerated vertical plate with exponentially variable temperature and mass diffusion through a porous medium," Materials Today: Proceedings, **46**, 3490-3494 (2021). https://doi.org/10.1016/j.matpr.2020.11.919.

[3] R.K. Deka, and Bhaben Ch Neog, "Unsteady natural convection flow past an accelerated vertical plate in a thermally stratified fluid," Theoretical and Applied Mechanics, **36**(4), 261-274 (2009). https://doi.org/10.2298/TAM0904261D

[4] A.G.V. Kumar, S.V.K. Varma, and R. Mohan, "Chemical reaction and radiation effects on MHD free convective flow past an exponentially accelerated vertical plate with variable temperature and variable mass diffusion," Annals of the Faculty of Engineering Hunedoara, **10**(2), 195 (2012). https://annals.fih.upt.ro/pdf-full/2012/ANNALS-2012-2-32.pdf

[5] S. Mondal, S. Parvin, and S.F. Ahmmed, "Effects of radiation and chemical reaction on MHD free convection flow past a vertical plate in the porous medium," American Journal of Engineering Research, **3**(12), 15-22 (2014).

[6] R.K. Deka, and A. Paul, "Convectively driven flow past an infinite moving vertical cylinder with thermal and mass stratification," Pramana, **81**, 641-665 (2013). https://doi.org/10.1007/s12043-013-0604-6

[7] R. Muthucumaraswamy, and V. Visalakshi, "Radiative flow past an exponentially accelerated vertical plate with variable temperature and mass diffusion," Int. J. of Enng. Annals. of Faculty Engineering Hunedoara, **9**, 137-140 (2011). https://annals.fih.upt.ro/pdf-full/2011/ANNALS-2011-2-26.pdf

[8] V. Rajesh, and S.V.K. Varma, "Radiation and mass transfer effects on MHD free convection flow past an exponentially accelerated vertical plate with variable temperature," ARPN Journal of Engineering and Applied Sciences, **4**(6), 20-26 (2009). https://www.arpnjournals.com/jeas/research_papers/rp_2009/jeas_0809_222.pdf

[9] V. Rajesh, and S.V.K. Varma, "Heat source effects on MHD flow past an exponentially accelerated vertical plate with variable temperature through a porous mediumm," International Journal of Applied Mathematics and Mechanics, **6**(12), 68-78 (2010).

[10] S. Sarma, and A. Nazibuddin, "Thermal diffusion effect on unsteady MHD free convective flow past a semi-infinite exponentially accelerated vertical plate in a porous medium," Canadian Journal of Physics, **100**(10), 437-451 (2022). https://doi.org/10.1139/cjp-2021-0361

[11] M.V. Krishna, and A.J. Chamkha, "Hall and ion slip effects on MHD rotating flow of elastico-viscous fluid through porous medium," International Communications in Heat and Mass Transfer, **113**, 104494 (2020). https://doi.org/10.1016/j.icheatmasstransfer.2020.104494

[12] M.V. Krishna, K. Jyothi, and A.J. Chamkha, "Heat and mass transfer on MHD flow of second-grade fluid through porous medium over a semi-infinite vertical stretching sheet," Journal of Porous media, **23**(8), (2020). https://doi.org/10.1615/JPorMedia.2020023817

[13] M.V. Krishna, N.A. Ahamad, and A.J. Chamkha, "Hall and ion slip effects on unsteady MHD free convective rotating flow through a saturated porous medium over an exponential accelerated plate," Alexandria Engineering Journal, **59**(2), 565-577 (2020). https://doi.org/10.1016/j.aej.2020.01.043

[14] M.V. Krishna, and A.J. Chamkha, "Hall and ion slip effects on magnetohydrodynamic convective rotating flow of Jeffreys fluid over an impulsively moving vertical plate embedded in a saturated porous medium with Ramped wall temperature," Numerical Methods for Partial Differential Equations, **37**(3), 2150-2177 (2021). https://doi.org/10.1002/num.22670

[15] M.V. Krishna, and A.J. Chamkha, "Hall and ion slip effects on MHD rotating boundary layer flow of nanofluid past an infinite vertical plate embedded in a porous medium," Results in Physics, **15**, 102652 (2019). https://doi.org/10.1016/j.rinp.2019.102652

[16] R.B. Hetnarski, "An algorithm for generating some inverse Laplace transforms of exponential form," Zeitschrift für angewandte Mathematik und Physik ZAMP, **26**, 249-253 (1975). https://doi.org/10.1007/BF01591514.

[17] M. Abramowitz, I.A. Stegun, and R.H. Romer, "Handbook of mathematical functions with formulas, graphs, and mathematical tables," American Journal of Physics, **56**(10), 958 (1988). https://doi.org/10.1119/1.15378

[18] R.S. Nath, and R.K. Deka, "The Effects of Thermal Stratification on Flow Past an Infinite Vertical Plate in Presence of Chemical Reaction," East European Journal of Physics, **3**, 223-232 (2023). https://doi.org/10.26565/2312-4334-2023-3-19

[19] N. Kalita, R.K. Deka, and R.S. Nath, "Unsteady Flow Past an Accelerated Vertical Plate with Variable Temperature in Presence of Thermal Stratification and Chemical Reaction," East European Journal of Physics, **3** 441-450 (2023). https://doi.org/10.26565/2312-4334-2023-3-49

ВПЛИВ ТЕРМІЧНОЇ ТА МАСОВОЇ СТРАТИФІКАЦІЇ НА НЕСТАЦІОНАРНИЙ ПОТІК ПОВЗ ПРИСКОРЕНУ НЕСКІНЧЕННУ ВЕРТИКАЛЬНУ ПЛАСТИНУ ЗІ ЗМІННОЮ ТЕМПЕРАТУРОЮ ТА ЕКСПОНЕНЦІАЛЬНОЮ МАСОВОЮ ДИФУЗІЄЮ В ПОРИСТОМУ СЕРЕДОВИЩІ

Хімангшу Кумар, **Рудра Канта Дека**

Факультет математики, Університет Гаухаті, Гувахаті-781014, Ассам, Індія

У цьому дослідженні розглядається, як термічна та масова стратифікація впливає на нестаціонарний потік повз вертикальну пластину, що нескінченно швидко рухається, коли температура змінюється та відбувається експоненціальна дифузія маси в пористому середовищі. Застосовуючи метод перетворення Лапласа, ми визначаємо розв'язки рівнянь, що керують системою, для випадку унітарних чисел Прандтля та Шмідта. Графічне представлення профілів концентрації, температури та швидкості, а також числа Нуссельта, числа Шервуда та поверхневого тертя надаються для полегшення обговорення причин різних змінних. Щоб побачити вплив термічної та масової стратифікації на потік рідини, ми порівнюємо класичне рішення (рідина без стратифікації) з первинним рішенням (рідина з стратифікацією) за допомогою графіка. Комбінований ефект двох стратифікацій призводить до швидшого наближення до стійких станів. Результати можуть бути корисними для проектування теплообміну та інших інженерних застосувань.

Ключові слова: *нестабільний потік; пористе середовище; термічна стратифікація; масове розшарування; прискорена пластина*

EFFECT OF ARRHENIUS ACTIVATION ENERGY IN MHD MICROPOLAR NANOFLUID FLOW ALONG A POROUS STRETCHING SHEET WITH VISCOUS DISSIPATION AND HEAT SOURCE

Keshab Borah[a]*, Jadav Konch[b†], Shyamanta Chakraborty[c§]

ᵃ Department of Mathematics, Gauhati University, Guwahati-781014, Assam, India
ᵇ Department of Mathematics, Dhemaji College, Dhemaji-787057, Assam, India
ᶜ UGC-HRDC, Gauhati University, Guwahati-781014, Assam, India
*Corresponding Author e-mail: keshabborah388@gmail.com
†E-mail: jadavkonch@gmail.com; §E-mail: schakrabortyhrdc@gauhati.ac.in

A numerical study of the heat and mass transfer of a micropolar nanofluid flow over a stretching sheet embedded in a porous medium is carried out in this investigation. The main objective of this work is to investigate the influence of Arrhenius activation energy, heat source and viscous dissipation on the fluid velocity, microrotation, temperature, and concentration distribution. The equations governing the flow are transformed into ordinary differential equations using appropriate similarity transformations and solved numerically using bvp4c solver in MATLAB. Graphs are plotted to study the influences of important parameters such as magnetic parameter, porosity parameter, thermophoresis parameter, Brownian motion parameter, activation energy parameter and Lewis number on velocity, microrotation, temperature and concentration distribution. The graphical representation explores that the velocity of the liquid diminishes for increasing values of magnetic parameter, whereas the angular velocity increases with it. This study also reports that an enhancement of temperature and concentration distribution is observed for the higher values of activation energy parameter, whereas the Lewis number shows the opposite behavior. The effects of various pertinent parameters are exposed realistically on skin friction coefficient, Nusselt and Sherwood numbers via tables. A comparison with previous work is conducted, and the results show good agreement.

Keywords: *Arrhenius activation energy; Viscous dissipation; Brownian motion; Thermophoresis; Micropolar nanofluid; Porous medium*
PACS: 44.05.+e; 44.30.+v; 44.20.+b;47.85.-g

INTRODUCTION

The flow and heat transfer characteristics of specific fluids such as polymeric fluids, colloidal fluids, fluids with additives, animal blood, paints, and fluids with suspensions cannot be adequately explained using conventional Newtonian or non-Newtonian fluid flow theories. As a result, Eringen [1] introduced the concept of microfluids, which focuses on a particular category of fluids that demonstrate specific microscopic effects originating from the local structure and micro-motions of the fluid elements. These fluids have the capability to accommodate stress moments and body moments, and their behavior is influenced by spin inertia. Subsequently, Eringen [2] further developed a subclass of these fluids known as micropolar fluids. These fluids exhibit micro-rotational effects and micro-rotational inertia, but they do not possess the ability to undergo stretch.

The study of magnetohydrodynamics (MHD) focuses on the interaction between the fluid velocity field and the electromagnetic field. In recent years, numerous authors have studied about MHD due to its various applications in engineering and industry. For instance, MHD can be utilized in power generators, accelerators, harnessing energy from geothermal sources, and crystal growth. Eldabe *et al.* [3] conducted a numerical study on the heat transfer in magnetohydrodynamic (MHD) flow of a micropolar fluid over a stretching sheet with suction and blowing through a porous medium. They employed the Chebyshev finite difference method (ChFD) to obtain the solution. Using the same method, they [4] also investigated the heat and mass transfer in a hydromagnetic flow of a micropolar fluid past a stretching surface in presence of Ohmic heating and viscous dissipation. Nadeem and Hussain [5] examined the motion of a viscous fluid in a magnetically induced shear field towards a nonlinear porous stretching sheet. Bhattacharyya [6] investigated reactive mass transfer and stable boundary layer flow in an exponentially flowing free stream. Muhaimin and Khamis [7] investigated the heat and mass transport in the context of nonlinear MHD flow of the boundary layer over a shrinking sheet, considering the influence of suction. Mandal and Mukhopadhyay [8] studied the impact of surface heat flux on fluid flow through an exponentially stretching porous sheet. Elbashbeshy [9] examined the heat and mass transfer over a vertical surface with varying temperature in presence of magnetic field.

Hassanien and Gorla [10] conducted a study on the numerical solution for heat transfer in a micropolar fluid over a non-isothermal stretching sheet. Pal and Chatterjee [11] observed the flow of a micropolar fluid in a porous medium toward a heated stretched sheet considering the influence of thermal radiation. Abd El-Aziz [12] examined the influence of viscous dissipation on the mixed convection flow of a micropolar fluid past over an exponentially stretched sheet. Hussain *et al.* [13] investigated the effect of radiation on the thermal boundary layer flow of a micropolar fluid towards a

stretched sheet with permeability. Pal and Mandal [14] investigated the effects of thermal radiation and MHD on the boundary layer flow of a micropolar nanofluid over a stretching sheet with a non-uniform heat sink/source. Kumar [15] performed research on a stretched sheet, employing finite element analysis to examine the heat and mass transfer in a hydromagnetic micropolar flow. Goud *et al.* [16] studied Ohmic heating and the influence of chemical reactions on the MHD flow of a micropolar fluid over a stretching surface.

Micropolar nanofluid is a unique and fascinating class of fluid that combines the characteristics of micropolar fluids and nanofluids. It is a fluid that consists of a base fluid, such as water or oil, in which tiny nanoparticles are dispersed. The presence of nanoparticles in the micropolar nanofluid alters its thermophysical properties, such as thermal conductivity and viscosity. The nanoparticles, due to their small size and large surface area, significantly enhance heat transfer and fluid flow characteristics compared to conventional fluids. This makes micropolar nanofluids highly attractive for various applications involving heat transfer, such as cooling systems, thermal management, and energy conversion devices. Atif *et al.* [17] examined the characteristics of a bio-convective MHD micropolar nanofluid with stratification. They observed that the density distribution decreases when both the density stratification and mixed number parameter are increased. Zemedu and Ibrahim [18] investigated the flow of a micropolar nanofluid with nonlinear convection and multiple slip effects. They concluded that increasing the solutal nonlinear convection parameter results in an increase in velocity.

The flow and heat transport phenomena of nanofluids have attract the researchers due to its various applications in science and engineering. The results of viscous dissipation in a hybrid nanofluid flow with magnetic effects were analyzed by Waini *et al.* [19]. The study found that the Nusselt number decreases for higher values of the Eckert number and radiation parameter in a hybrid nanofluid. In their research, Sharma *et al.* [20] investigated the combined effect of thermophoresis and Brownian motion on magnetohydrodynamic mixed convective flow over an inclined stretching surface, considering the influence of thermal radiation and chemical reaction. Bhatti *et al.* [21] investigated the electro-magneto-hydrodynamic Eyring-Powell fluid flow through microparallel plates, considering heat transfer and non-Darcy effects. Khan *et al.* [22] conducted an investigation on the flow of micropolar base nanofluid over a stretching sheet in the presence of thermal radiation and a magnetic dipole. Recently, Khan *et al.* [23] studied the unsteady micropolar hybrid nanofluid flow past a permeable stretching/shrinking vertical plate. Kausar *et al.* [24] investigated the impact of thermal radiation and viscous dissipation on the boundary layer flow of micropolar nanofluid towards a permeable stretching sheet in porous medium. The influence of thermal radiation and viscous dissipation on a three-dimensional MHD viscous flow were examined by Akbar and Sohail [25].

Activation energy is a critical threshold that must be reached for a chemical reaction to occur. It represents the minimum energy required for the reactants to form products and can be found in the form of kinetic or potential energy. Without this energy, the reaction cannot proceed. Activation energy finds diverse applications in various fields such as geothermal engineering, chemical engineering, oil emulsions, and food processing. In recent years, several researchers have explored their research on the influence of Arrhenius activation energy in boundary layer flow, particularly in the context of non-Newtonian fluid flow, considering different physical aspects. Devi *et al.* [26] studied the impact of various factors, including thermal radiation, buoyancy force, chemical reaction, and activation energy, on the behavior of MHD nanofluid flow past a vertically stretching surface. Li *et al.* [27] observed chemical reaction and activation energy effects on unsteady MHD dissipative Darcy-Forchheimer squeezed flow along a horizontal channel in the context of Casson fluid. In the study conducted by Dessie [28], this study aims to investigate the effects of heat radiation, activation energy and chemical reactions on MHD Maxwell fluid flow in a rotating frame. In a MHD nanofluid flow with double stratification, binary chemical reactions were studied by Anjum *et al.* [29]. Gautam *et al.* [30] explored their investigation on the influence of binary chemical reaction and activation energy in a porous medium for the MHD flow of Williamson nanofluid.

Motivated by the above study, our objective is to investigate the effects of activation energy, viscous dissipation and magnetic field on boundary layer flow of micropolar nanofluid in a porous medium along a stretching sheet in the presence of a heat source. The study of combined influences of activation energy and viscous dissipation in micropolar nanofluid flow induced by a stretching sheet in the presence of heat source and magnetic field is quite a novel problem. The introduction of porous medium along with a magnetic field and heat source makes the physical problem more interesting and attractive in scientific and application viewpoints. Also, numerical solutions are obtained for the governing equations using MATLAB inbuilt function 'bvp4c'. The graphical and tabular form of the computed results shall be presented and discussed.

MATHEMATICAL FORMULATION

We have considered a steady two-dimensional laminar flow of an incompressible micropolar nanofluid caused by the motion of a stretching sheet. The sheet is immersed in a quiescent, electrically conducting fluid with an electric conductivity represented by σ. A magnetic field B_0 is applied to the stretching sheet. We neglect the influence of the induced magnetic field due to the assumption that the magnetic Reynolds number is too small. Additionally, we assume that there is no impressed electric field and neglect the Hall effect.

Let us define the coordinates such that the *x*-axis aligns with the sheet and the *y*-axis is perpendicular to it. The surface originates from a narrow opening at the origin. The velocity components in the *x* and *y* directions are represented

by u and v, respectively while N represents the microrotation component. It is assumed that the speed of a point on the sheet is inversely proportional to its distance from the opening. Furthermore, we consider the fluid properties to be isotropic and constant. The flow geometry of the problem is depicted in Figure 1.
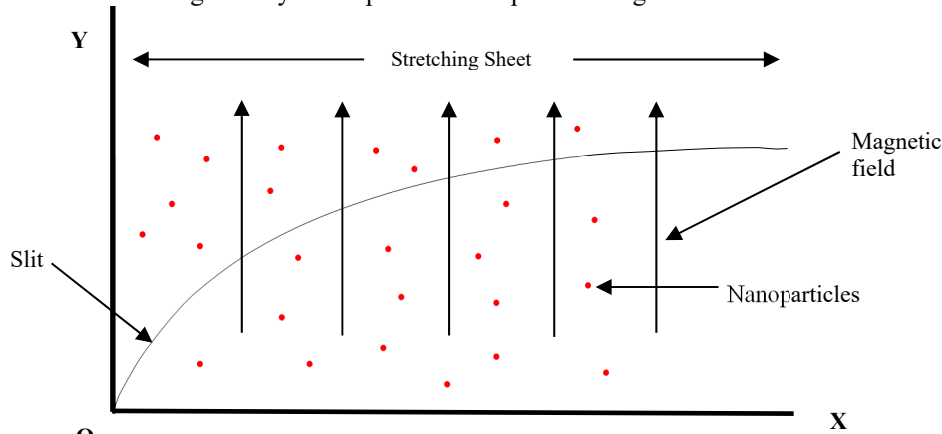

Figure 1. Flow geometry of the problem

Using the typical boundary layer approximation and following Saidulu *et al.* [31] and Rehman *et al.* [32], the governing equations can be expressed as follows:
Continuity Equation:

$$\frac{\partial u}{\partial x} + \frac{\partial v}{\partial y} = 0 \tag{1}$$

Momentum Equation:

$$u \frac{\partial u}{\partial x} + v \frac{\partial u}{\partial y} = \left(\frac{\mu + \kappa}{\rho} \right) \frac{\partial^2 u}{\partial y^2} + \frac{\kappa}{\rho} \frac{\partial N}{\partial y} - \frac{\sigma B_0^2 u}{\rho} - \frac{v}{k_p'} u \tag{2}$$

Angular momentum Equation:

$$u \frac{\partial N}{\partial x} + v \frac{\partial N}{\partial y} = \frac{\gamma}{\rho j} \frac{\partial^2 N}{\partial y^2} - \frac{\kappa}{\rho j} \left(2N + \frac{\partial u}{\partial y} \right) \tag{3}$$

Energy Equation:

$$u \frac{\partial T}{\partial x} + v \frac{\partial T}{\partial y} = \frac{k_f}{\rho C_p} \frac{\partial^2 T}{\partial y^2} + \left(\frac{\mu + \kappa}{\rho C_P} \right) \left(\frac{\partial u}{\partial y} \right)^2 + \frac{\sigma B_0^2}{\rho C_p} u^2 + \frac{Q_0}{\rho C_p} (T - T_\infty) + \tau \left(D_B \frac{\partial C}{\partial y} \frac{\partial T}{\partial y} + \frac{D_T}{T_\infty} \left(\frac{\partial T}{\partial y} \right)^2 \right) \tag{4}$$

Concentration Equation:

$$u \frac{\partial C}{\partial x} + v \frac{\partial C}{\partial y} = D_B \frac{\partial^2 C}{\partial y^2} + \frac{D_T}{T_\infty} \frac{\partial^2 T}{\partial y^2} - k_r^2 \left(\frac{T}{T_\infty} \right)^n e^{-\frac{E_a}{\xi T}} (C - C_\infty) \tag{5}$$

The suitable physical boundary conditions are:

$$\left. \begin{array}{l} u = u_w = bx, \ v = 0, \ N = -s \frac{\partial u}{\partial y}, \ T = T_w, \ C = C_w \qquad \text{at} \quad y = 0 \\[2mm] u = 0, \qquad N = 0, \qquad T = T_\infty, \qquad C = C_\infty \qquad \text{as} \quad y \to \infty \end{array} \right\} \tag{6}$$

In the above governing equations (4) and (5), the term $\dfrac{\sigma B_0^2}{\rho C_p} u^2$ represent Ohmic heating effect and the term

$k_r^2 \left(\dfrac{T}{T_\infty} \right)^n e^{-\frac{E_a}{\xi T}} (C - C_\infty)$ depicts the modified Arrhenius function, in which the reaction rate is provided by k_r^2, the

activation energy by E_a, the Boltzmann constant by $\xi = 8.61 \times 10^{-5} \, eV/K$, and the fitted rate constant by 'n', which ranges between –1 and 1. Also the spin gradient viscosity, given by Rees and Pop [33], is $\gamma = (\mu + \kappa/2) j$, where j is the microinertia density given by $j = v/b$ that represent the reference length.

To convert the governing equations into a system of ordinary differential equations, we will employ similarity transformations and introduce dimensionless variables as follows:

$$\eta = \sqrt{\frac{b}{\upsilon}}\, y \,, \quad f(\eta) = \frac{\psi}{x\sqrt{b\upsilon}} \,, \quad G(\eta) = \sqrt{\frac{\upsilon}{b}}\frac{N}{bx} \,, \quad \theta(\eta) = \frac{T - T_\infty}{T_w - T_\infty} \,, \quad \phi(\eta) = \frac{C - C_\infty}{C_w - C_\infty} \tag{7}$$

We have $u = \dfrac{\partial \psi}{\partial y}$, $v = -\dfrac{\partial \psi}{\partial x}$, where ψ is the stream function, which gives $u = xbf'(\eta)$ and $v = -\sqrt{b\upsilon}\, f(\eta)$.

We observe that equation (1) is satisfied automatically and equations (2) – (5) are simplified to the following

$$(1+K)f''' - (f')^2 + ff'' + KG' - \left(M + \frac{1}{K_p}\right)f' = 0 \tag{8}$$

$$\left(1 + \frac{K}{2}\right)G'' + fG' - f'G - K(2G + f'') = 0 \tag{9}$$

$$\theta'' + \Pr f\theta' + (1+K)\Pr Ec(f'')^2 + \Pr Ec M(f')^2 + \Pr Q\theta + \Pr N_b\,\theta'\phi' + \Pr N_t(\theta')^2 = 0 \tag{10}$$

$$\phi'' + Le\, f\,\phi' + \frac{N_t}{N_b}\theta'' - Le \wedge (1+\delta\theta)^n Exp\left(-\frac{E}{1+\delta\theta}\right)\phi = 0 \tag{11}$$

Corresponding boundary conditions are reduced to the following:

$$\left.\begin{array}{l} f(\eta) = 0 \,,\ f'(\eta) = 1 \,,\ G(\eta) = -s\,f''(\eta) \,,\ \theta(\eta) = 1 \,,\ \phi(\eta) = 1\ \text{at}\ \eta = 0 \\ f'(\eta) = 0 \,, \qquad G(\eta) = 0, \qquad \theta(\eta) = 0 \,, \qquad \phi(\eta) = 0\ \text{ as }\ \eta \to \infty \end{array}\right\} \tag{12}$$

The non-dimensional parameters are defined as follows:

$$K = \frac{\kappa}{\mu} \,,\ M = \frac{\sigma B_0^2}{\rho b} \,,\ K_p = \frac{k_p' b}{\upsilon} \,,\ \Pr = \frac{\mu C_p}{k_f} \,,\ Ec = \frac{u_w^2}{C_P(T_w - T_\infty)} \,,\ N_b = \frac{\tau D_B(C_w - C_\infty)}{\upsilon} \,,$$

$$N_t = \frac{\tau D_T(T_w - T_\infty)}{\upsilon T_\infty} \,,\qquad Le = \frac{\upsilon}{D_B} \,,\qquad \wedge = \frac{k_r^2}{b} \,,\qquad \delta = \frac{T_w - T_\infty}{T_\infty} \,,\qquad E = \frac{E_a}{\xi T_\infty} \,.$$

K is the material parameter, M is the magnetic parameter, K_p is the porosity parameter, $\Pr$ is the Prandtl number, Ec is the Eckert number, N_t is the thermophoresis parameter, N_b is the Brownian motion parameter, Le is the Lewis number, $\wedge$ is the reaction rate parameter, E is the activation energy parameter, δ is the temperature difference parameter.

PHYSICAL QUANTITIES

In this problem, the important engineering physical quantities are C_f (=skin friction coefficient), Nu (=local Nusselt number) and Sh (=local Sherwood number) respectively are defined below with $Re = \dfrac{bx^2}{\upsilon}$ as local Reynolds number.

The shear stress at the surface is determined by the equation $\tau_w = \left[(\mu + \kappa)\dfrac{\partial u}{\partial y} + \kappa N\right]_{y=0}$.

The skin friction coefficient (C_f) can be defined as $C_f = \dfrac{\tau_w}{\rho u_w^2}$, where $u_w = bx$ is characteristic velocity.

This gives

$$C_f = \frac{[1 + (1-s)K]f''(0)}{\sqrt{Re}}$$

The couple stress (M_w) at the surface is defined by the following equation:

$$M_w = \left(\gamma\frac{\partial N}{\partial y}\right)_{y=0} = \mu u_w\left(1 + \frac{K}{2}\right)G'(0).$$

The local surface heat flux $q_w(x)$ can be expressed using Fourier's law as:

$$q_w(x) = -k_f\left(\frac{\partial T}{\partial y}\right)_{y=0} = -k_f(T_w - T_\infty)\sqrt{\frac{b}{\upsilon}}\,\theta'(0).$$

The local surface heat flux transfer coefficient $h(x)$ can be given by:

$$h(x) = \frac{q_w(x)}{(T_w - T_\infty)} = -k_f\sqrt{\frac{b}{\upsilon}}\,\theta'(0).$$

The local Nusselt number can be expressed as:

$$Nu = \frac{x\,h(x)}{k_f} = -x\sqrt{\frac{b}{\upsilon}}\,\theta'(0) \quad \text{which gives} \quad \frac{Nu}{\sqrt{Re}} = -\theta'(0)$$

The local mass flux J_w is given by $J_w = -D\left(\dfrac{\partial C}{\partial y}\right)_{y=0}$.

The Sherwood number can be expressed as follows:

$$Sh = \frac{x\,J_w}{D\left(C_w - C_\infty\right)} = -x\sqrt{\frac{b}{\upsilon}}\,\phi'(0) \quad \text{which gives} \quad \frac{Sh}{\sqrt{Re}} = -\phi'(0)$$

METHOD OF SOLUTION

The nonlinear ordinary differential equations, represented by equations (8) to (11) and subject to the boundary conditions (12) are numerically solved using MATLAB inbuilt function 'bvp4c'. It utilizes a finite difference approach with fourth-order accuracy.

To employ the solver effectively, the equations need to be transformed into a system of equivalent first-order ordinary differential equations. This transformation is achieved through the following substitutions:

$$y(1) = f$$
$$y(1)' = f' = y(2)$$
$$y(2)' = f'' = y(3)$$
$$y(3)' = f''' = \frac{[\,y(2)^2 - y(1)\,y(2) - K\,y(5) + (M+1/Kp)\,y(2)]}{(1+K)}$$
$$y(4) = G$$
$$y(4)' = G' = y(5)$$
$$y(5)' = G'' = \frac{[\,y(4)y(2) - y(1)y(5) + K(2y(4) + y(3))]}{\left(1+\dfrac{K}{2}\right)}$$
$$y(6) = \theta$$
$$y(6)' = \theta' = y(7)$$
$$y(7)' = \theta'' = -\Pr y(1)y(7) - (1+K)\Pr Ec\,y(3)^2 - \Pr Ec\,M\,y(2)^2 - \Pr Q\,y(6) - \Pr Nb\,y(7)\,y(9) - \Pr Nt\,y(7)^2$$
$$y(8) = \phi$$
$$y(8)' = \phi' = y(9)$$
$$y(9)' = \phi'' = -Le\,y(1)\,y(9) - (Nt/Nb)\big(y(7)'\big) + y(8)\,e^{\left(-\frac{E}{1+\delta y(6)}\right)}Le \wedge (1+\delta y(6))^n$$

The corresponding boundary conditions are reduced to:
$$y0(1)-0;\ y0(2)-1;\ y0(4)+s\,y0(3);\ y0(6)-1;\ y0(8)-1;\ y1(2)-0;\ y1(4)-0;\ y1(6)-0;\ y1(8)-0\,.$$

RESULTS AND DISCUSSION

The system of non-linear coupled governing boundary layer equations (8)–(11) along with the corresponding boundary conditions (12) is numerically solved using the 'bvp4c' solver in MATLAB. The 'bvp4c' solver is a commonly used tool for solving boundary value problems. This solution satisfies the specified boundary conditions and provides an approximation for the desired variables in the problem. The findings are compared with the findings obtained by Saidulu *et al*. [31], Grubka and Bobba [34] and Seddeek and Salem [35] to verify the accuracy of the present numerical scheme as shown in Table 1 and Table 2.

Figures (2) to (17) depict the variation in velocity distribution, angular velocity distribution, temperature distribution, and species concentration distribution for various flow parameter.

Figures (2) to (5) illustrate the effect of magnetic parameter M on the velocity, angular velocity, temperature and species concentration profile respectively. Figure 2 shows that as the magnetic parameter M increases, the velocity decreases. This is due to the presence of a transverse magnetic field, which creates a resistive force called Lorentz force that acts in the opposite direction to the fluid motion. This observation indicates that a stronger magnetic field has the effect of slowing down the movement of the fluid. Consequently, the thickness of the velocity boundary layer decreases with an increasing M. Figure 3 indicates that angular velocity increases with the increasing values of M. Figure 4 depicts the temperature Distribution with respect to the magnetic field parameter. It is observed that the temperature increases as

M increases. This observed phenomenon can be attributed to the influence of the Lorentz force, which resist velocity of the fluid, as a result a rise in temperature. Figure 5 depicts the influence of magnetic parameters on the concentration profile. It is found that the fluid concentration is rising as the magnetic parameter rises.
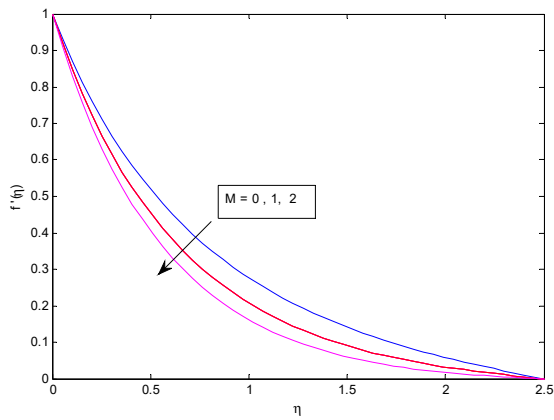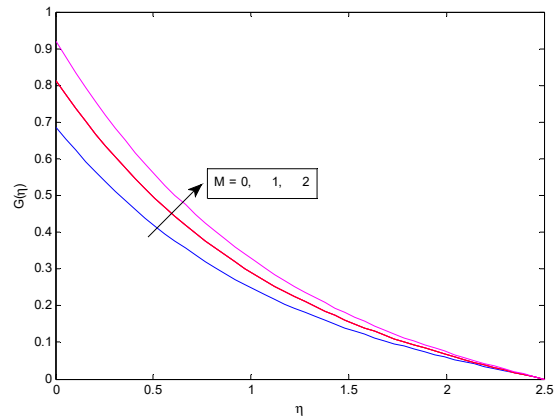

Figure 2. Velocity profile for different M.

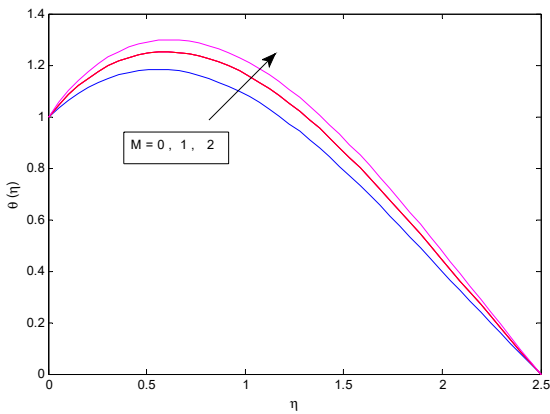**Figure 3.** Angular velocity profile for different M

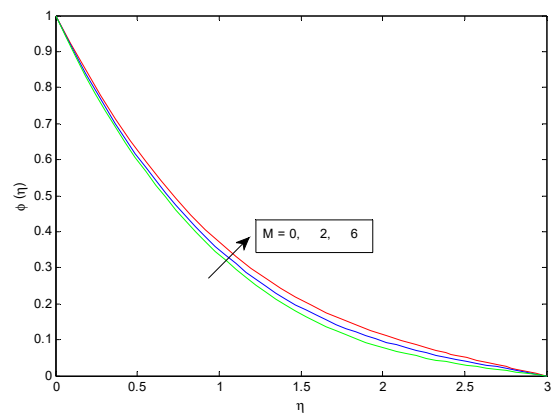**Figure 4.** Temperature profile for different M

Figure 5. Concentration profile for different M

Figures 6–9 illustrate the impact of the porosity parameter Kp on various fluid properties, including fluid velocity, angular velocity, fluid temperature, and fluid concentration respectively. It can be observed from figure 6 that as the porosity parameter increases, the fluid is provided with more space to flow, resulting in an increase in fluid velocity. On the other hand, Figures 7–9 clearly demonstrate that an increase in the porosity parameter leads to a decrease in the flow profiles of the micro-rotation, temperature and concentration. Physically, the porosity parameter influences the generation of internal heat within the flow, which contributes to the observed trends in temperature profiles. Additionally, the rotational effects in the flow can contribute to the depreciation observed in the temperature and concentration fields.
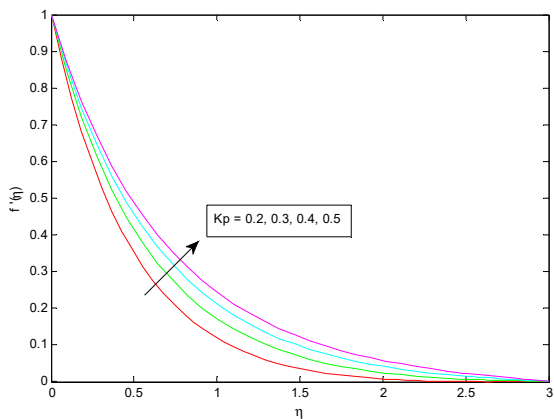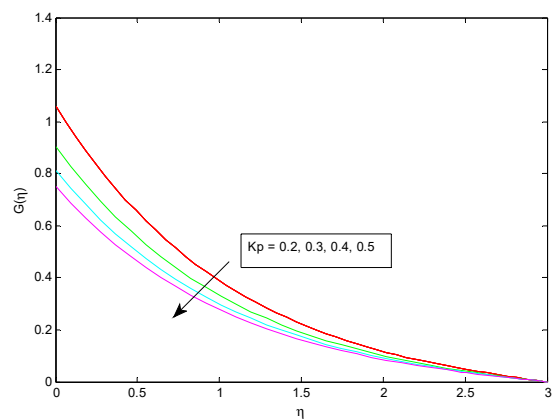

Figure 6. Velocity profile for different Kp

Figure 7. Angular velocity profile for different Kp

Figures 10 and 11 depicts the impact of activation energy (E) on fluid temperature and fluid concentration, respectively. From Figure 10, it can be observed that an increase in activation energy (E) leads to an increase in the

temperature profile. As the temperature increases, the speed of molecular motion increases, resulting in more frequent collisions between molecules. Additionally, the molecules possess higher kinetic energy at higher temperatures. Consequently, the proportion of collisions capable of surpassing the activation energy for the reaction also increases with temperature. Also Figure 11 exhibits that activation energy (E) enhances the fluid concentration. The increasing values of activation energy (E) retard the Arrhenius energy function, which result, increasing the rate of the generative chemical reaction that enhances the concentration.
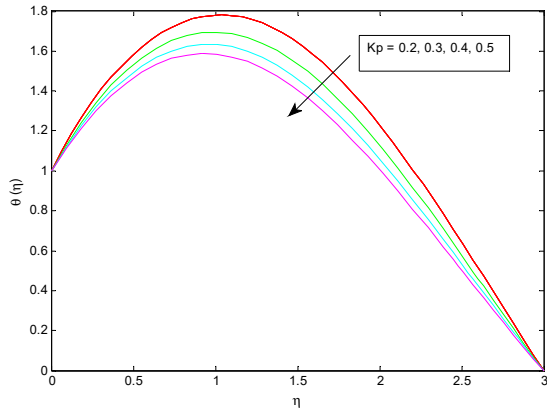
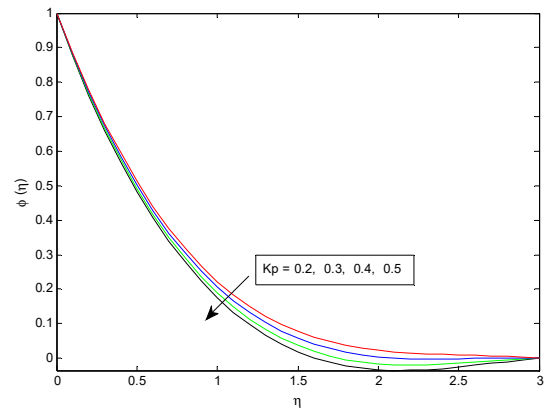**Figure 8.** Temperature profile for different Kp

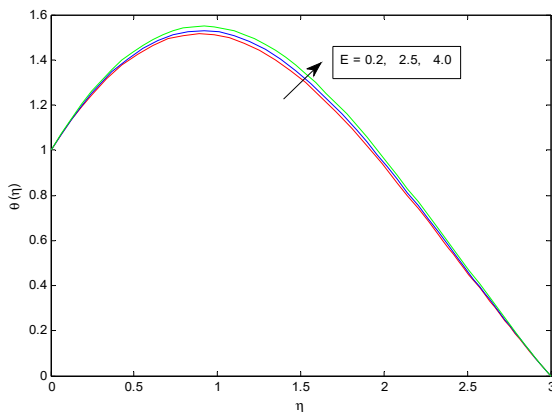**Figure 9.** Concentration profile for different Kp

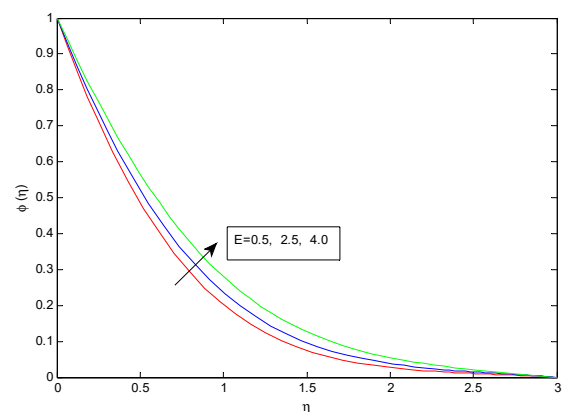**Figure 10.** Temperature profile for different E

Figure 11. Concentration profile for different E

The Lewis number, which is a dimensionless quantity measuring the rate of temperature spread compared to mass diffusivity, plays a role in the temperature and concentration profiles. In Figure 12 and 13, it can be observed that as the Lewis number (Le) increases, the temperature and concentration profiles decrease. Higher values of Le indicate stronger molecular motions, which ultimately lead to an enhancement in fluid temperature.
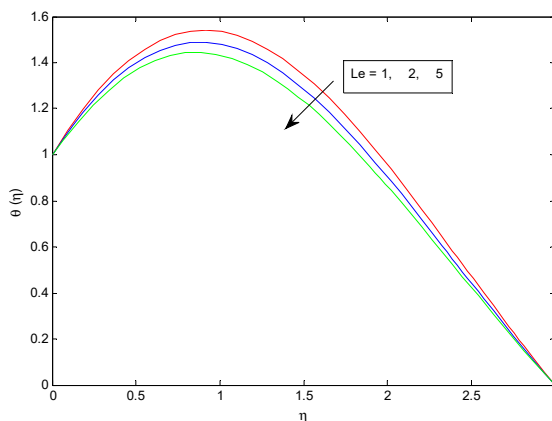
Figure 12. Temperature profile for different Le
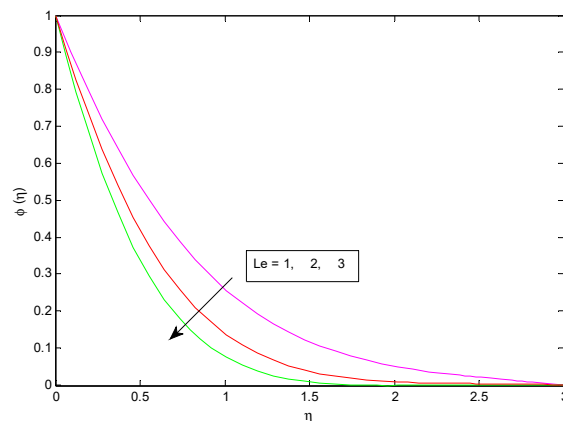
Figure 13. Concentration profile for different Le

Thermophoresis refers to the particle diffusion phenomenon resulting from a temperature gradient. The thermophoretic force is the force that causes nanoparticles to deposit into the surrounding fluid due to the temperature

gradient. For higher values of the thermophoresis parameter N_t, it is observed from the graphs 14 and 15 that both the concentration and temperature profiles are increases. Physically, when $\theta(\eta)$ increases, it leads to a higher thermal gradient, which in turn increases the intermediate force. This relationship is evident in the increasing values of the thermophoresis parameter.
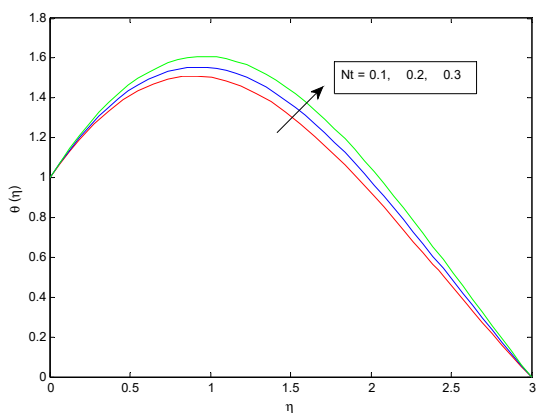

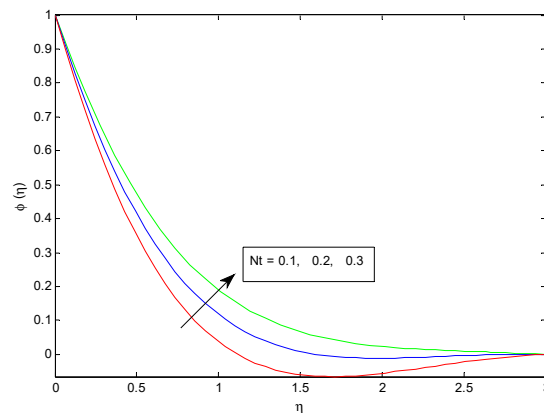**Figure 14.** Temperature profile for different N_t

Figure 15. Concentration profile for different N_t

The Brownian motion is created by the random collisions between small particles. The parameter N_b quantifies the level of random motion of suspended nanoparticles within the nanofluid. It is observed that increasing convection leads to enhanced heat transfer, as depicted in Fig. 16. Moreover, the concentration profile decreases as the distance from the surface increases, as shown in Fig. 17. Physically, an increase in temperature results in higher particle energy, leading to greater random movement and faster collisions, thereby increasing the Brownian motion. Conversely, increasing the concentration reduces the available space for particle movement, thereby decreasing the probability of collision.
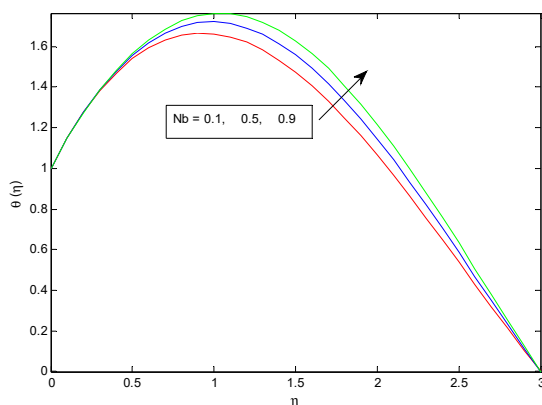

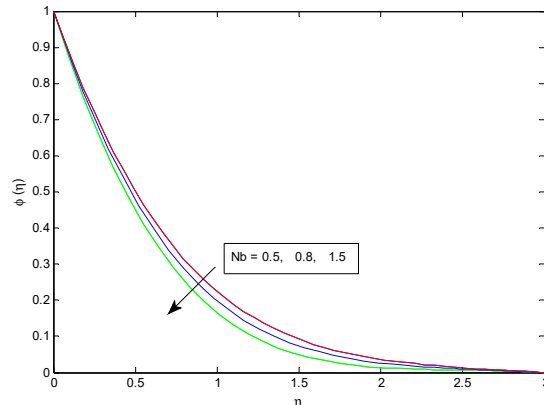**Figure 16.** Temperature profile for different N_b

Figure 17. Concentration profile for different N_b

Table 1 illustrates the changes in skin friction coefficient, Nusselt number and Sherwood number due to the parameter M, K and s. It is found that the skin friction coefficient increases with higher values of M, K and s, while opposite effect is observed for the Nusselt number. Also, Sherwood number decreases with an increase in M, but increases with K and s. Table 2 provides a comparison of $-\theta'(0)$ for various values of Pr in the absence of other influencing factors. It is observed that Nusselt number increases with Pr.

Table 1. Comparison of skin friction coefficient, Nusselt number, and Sherwood number for various parameters.

M	K	s	$-(1+K)f''(0)$		$-\theta'(0)$		$-\phi'(0)$	
			Saidulu *et al.* [31]	Present Study	Saidulu *et al.* [31]	Present Study	Saidulu *et al.* [31]	Present Study
0.5	0.5	0.5	1.632309	1.632313	0.301208	0.301234	0.418950	0.418943
1			1.874420	1.874426	0.223923	0.223941	0.400290	0.400297
2			2.276598	2.276568	0.104321	0.104335	0.375010	0.375025
0.5	1		1.983995	1.983981	0.293786	0.293759	0.430439	0.430424
	2		2.576759	2.576779	0.280081	0.280065	0.448508	0.448521
	0.5	0.7	1.983995	1.983967	0.293786	0.293771	0.430439	0.430446
		1	2.295365	2.295332	0.286817	0.286829	0.440171	0.440147

Table 2. Comparison of $-\theta'(0)$ for different values of *Pr*

Pr	Grubka and Bobba [34]	Seddeek and Salem [35]	Saidulu and Reddy [31]	Present Study
0.72	0.4631	0.46134	0.4632	0.4637
1	0.582	0.58197	0.5819	0.58192
3	1.1652	1.16524	1.1652	1.16528

CONCLUSIONS

In this study, the two-dimensional MHD micropolar nanofluid flow over a stretching sheet embedded in a porous medium in the presence of Arrhenius activation energy, heat source is studied. The governing partial differential equations were transformed into a system of ordinary differential equations using a set of similarity transformations. These equations were then solved numerically using the 'bvp4c' solver available in MATLAB. The results of the study led to the following conclusions**:**

- For increasing values of the magnetic field parameter (*M*), the velocity profile decreases. However, the microrotation, temperature, and concentration profiles are strengthened.
- The fluid temperature and concentration profile are enhanced with the increasing values of thermophoresis parameter (*N*$_t$).
- The temperature profile increases with the strengthening of the Brownian motion parameter (N_b), while the concentration profile decreases with N_b.
- An increase in activation energy (*E*) leads to an increase in the concentration and temperature profiles.
- Increasing values of the Lewis number (*Le*) result in decreasing temperature and concentration profiles.
- The rate of heat transfer decreases with an enhancement of the magnetic parameter and material parameter.
- The rate of mass transfer, in terms of Sherwood number, decreases with an increase in *M*, but an opposite effect is observed with *K*.

ORCID
Ⓘ**Keshab Borah,** https://orcid.org/0009-0005-5486-5784; Ⓘ**Jadav Konch,** https://orcid.org/0000-0002-6953-3679
Ⓘ**Shyamanta Chakraborty,** https://orcid.org/0000-0001-5839-4856

REFERENCES
[1] A.C. Eringen, "Simple Microfluids," International Journal of Engineering Science, **2**(2), 205-217 (1964). https://doi.org/10.1016/0020-7225(64)90005-9
[2] A.C. Eringem, "Theory of Micropolar Fluids," Journal of Mathematics and Mechanics, **16**(1), 1–18 (1966). http://dx.doi.org/10.1512/iumj.1967.16.16001
[3] N.T. Eldabe, E.F. Elshehawey, M.E. Elbarbary, and N.S. Elgazery, "Chebyshev Finite Difference Method for MHD Flow of a Micropolar Fluid past a Stretching Sheet with Heat Transfer," Journal of Applied Mathematics and Computation, **160**, 437-450 (2005). https://doi.org/10.1016/j.amc.2003.11.013
[4] N.T. Eldabe, and E.M.O. Mahmoud, "Chebyshev Finite Difference Method for Heat and Mass Transfer in a Hydromagnetic Flow of a Micropolar Fluid Past a Stretching Surface with Ohmic Heating and Viscous Dissipation," Applied Mathematics and Computation, **177**, 561-571 (2006). https://doi.org/10.1016/j.amc.2005.07.071
[5] S. Nadeem, and A. Hussain, "MHD flow of a viscous fluid on a nonlinear porous shrinking sheet with homotopy analysis method," Appl. Math. Mech.-Engl. **30**, 1569–1578 (2009). https://doi.org/10.1007/s10483-009-1208-6
[6] K. Bhattacharyya, "Steady boundary layer flow and reactive mass transfer past an exponentially stretching surface in an exponentially moving free stream," Journal of the Egyptian Mathematical Society, **20**(3), 223-228 (2012). https://doi.org/10.1016/j.joems.2012.08.018.
[7] R. Muhaimin, Kandasamy, and A.B. Khamis, "Effects of heat and mass transfer on nonlinear MHD boundary layer flow over a shrinking sheet in the presence of suction," Applied Mathematics and Mechanics, **29**, 1309–1317 (2008). https://doi.org/10.1007/s10483-008-1006-z
[8] I.C. Mandal, and S. Mukhopadhyay, "Heat transfer analysis for fluid flow over an exponentially stretching porous sheet with surface heat flux in porous medium," Ain Shams Engineering Journal, **4**(1), 103-110 (2013). https://doi.org/10.1016/j.asej.2012.06.004.
[9] E.M. Elbashbeshy, "Heat and mass transfer along a vertical plate with variable surface tension and concentration in the presence of the magnetic field," International Journal of Engineering Science, **35**, 515-522 (1997). https://doi.org/10.1016/S0020-7225(96)00089-4
[10] I.A. Hassanien, and R.S.R. Gorla, "Heat transfer to a micropolar fluid from a non-isothermal stretching sheet with suction and blowing," Acta Mechanica, **84**, 191–199 (1990). https://doi.org/10.1007/BF01176097
[11] D. Pal, and S. Chatterjee, "MHD mixed convection stagnation-point flow of a micropolar fluid in a porous medium towards a heated stretching sheet with thermal radiation," Mathematical Modelling and Analysis, **17**(4), 498-518 (2012). https://doi.org/10.3846/13926292.2012.706653

[12] M.A. El-Aziz, "Viscous dissipation effect on mixed convection flow of a micropolar fluid over an exponentially stretching sheet," Canadian Journal of Physics, **87**(4), 359-368 (2009). https://doi.org/10.1139/P09-047

[13] M. Hussain, M. Ashraf, S. Nadeem, and M. Khan, "Radiation effects on the thermal boundary layer flow of a micropolar fluid towards a permeable stretching sheet," Journal of the Franklin Institute, **350**(1), 194-210 (2013). https://doi.org/10.1016/j.jfranklin.2012.07.005

[14] D. Pal, and G. Mandal, "Thermal radiation and MHD effects on boundary layer flow of micropolar nanofluid past a stretching sheet with non-uniform heat source/sink," International Journal of Mechanical Sciences, **126**, 308-318 (2017). https://doi.org/10.1016/j.ijmecsci.2016.12.023

[15] L. Kumar, "Finite Element Analysis of Combined Heat and Mass Transfer in Hydromagnetic Micropolar Flow along a Stretching Sheet," Computational Materials Science, **46**, 841-848 (2009). http://dx.doi.org/10.1016/j.commatsci.2009.04.021

[16] B.S. Goud, and M.M. Nandeppanavar, "Ohmic heating and chemical reaction effect on MHD flow of micropolar fluid past a stretching surface," Partial Differential Equations in Applied Mathematics, **4**, 100104 (2021). https://doi.org/10.1016/j.padiff.2021.100104

[17] S.M. Atif, S. Hussain, and M. Sagheer, "Magnetohydrodynamic stratified bioconvective flow of micropolar nanofluid due to gyrotactic microorganisms," AIP Advances, **9**(2), 025208 (2019). https://doi.org/10.1063/1.5085742

[18] C. Zemedu, and W. Ibrahim, "Nonlinear Convection Flow of Micropolar Nanofluid due to a Rotating Disk with Multiple Slip Flow," Mathematical Problems in Engineering, **2020**, 4735650 (2020). https://doi.org/10.1155/2020/4735650

[19] I. Waini, A. Ishak, and I. Pop, "Radiative and magnetohydrodynamic micropolar hybrid nanofluid flow over a shrinking sheet with Joule heating and viscous dissipation effects," Neural Comput & Applic, **34**, 3783–3794 (2022). https://doi.org/10.1007/s00521-021-06640-0

[20] B.K. Sharma, U. Khanduri, N.K. Mishra, and K.S. Mekheimer, "Combined effect of thermophoresis and Brownian motion on MHD mixed convective flow over an inclined stretching surface with radiation and chemical reaction," International Journal of Modern Physics B, **37**, 2350095 (2022). http://dx.doi.org/10.1142/S0217979223500959

[21] M.M. Bhatti, M.H. Doranehgard, and R. Ellahi, "Electro-magneto-hydrodynamic Eyring-Powell fluid flow through micro-parallel plates with heat transfer and non-Darcian effects," Mathematical Methods in the Applied Sciences, **46**(1), 11642-11656 (2022). http://dx.doi.org/10.1002/mma.8429

[22] S.A. Khan, B. Ali, C. Eze, K.T. Lau, L. Ali, J. Chen, and J. Zhao, "Magnetic dipole and thermal radiation impacts on stagnation point flow of micropolar based nanofluids over a vertically stretching sheet: finite element approach," Processes, **9**(7), 1089 (2021). https://doi.org/10.3390/pr9071089

[23] U. Khan, A. Zaib, I. Pop, S.A. Bakar, and A. Ishak, "Unsteady micropolar hybrid nanofluid flow past a permeable stretching/shrinking vertical plate," Alexandria Engineering Journal, **61**(12), 11337-11349 (2022). https://doi.org/10.1016/j.aej.2022.05.011

[24] M.S. Kausar, A. Hussanan, M. Waqas, and M. Mamat, "Boundary layer flow of micropolar nanofluid towards a permeable stretching sheet in the presence of porous medium with thermal radiation and viscous dissipation," Chinese Journal of Physics, **78**(6), 435–452 (2022). http://dx.doi.org/10.1016/j.cjph.2022.06.027

[25] S. Akbar, and M. Sohail, "Three Dimensional MHD Viscous Flow under the Influence of Thermal Radiation and Viscous Dissipation," International Journal of Emerging Multidisciplinaries: Mathematics, **1**(3), 106–117 (2022). https://doi.org/10.54938/ijemdm.2022.01.3.122

[26] G.L. Devi, H. Niranjan, and S. Sivasankaran, "Effects of chemical reactions, radiation, and activation energy on MHD buoyancy induced nanofluid flow past a vertical surface," Scientia Iranica, **29**(1), 90-100 (2022). https://doi.org/10.24200/sci.2021.56835.4934

[27] S. Li, K. Raghunath, A. Alfaleh, F. Ali, A. Zaib, M.I. Khan, S. M. ElDin, and V. Puneeth, "Effects of activation energy and chemical reaction on unsteady MHD dissipative Darcy–Forchheimer squeezed flow of Casson fluid over horizontal channel," Scientific Reports, **13**, 2666, (2023). https://doi.org/10.1038/s41598-023-29702-w

[28] H. Dessie, "Effects of Chemical Reaction, Activation Energy and Thermal Energy on Magnetohydrodynamics Maxwell Fluid Flow in Rotating Frame," Journal of Nanofluids, **10**(1), 67–74 (2021). https://doi.org/10.1166/jon.2021.1767

[29] A. Anjum, S. Masood, M. Farooq, N. Rafiq, and M.Y. Malik, "Investigation of binary chemical reaction in magnetohydrodynamic nanofluid flow with double stratification," Adv. Mech. Eng. **13**(5), (2021). https://doi.org/10.1177/16878140211016264

[30] A.K. Gautam, A.K. Verma, K. Bhattacharyya, S. Mukhopadhyay, and A.J. Chamkha, "Impacts of activation energy and binary chemical reaction on MHD flow of Williamson nanofluid in Darcy–Forchheimer porous medium: a case of expanding sheet of variable thickness," Waves in Random and Complex Media, (2021). https://doi.org/10.1080/17455030.2021.1979274

[31] B. Saidulu, and K.S. Reddy, "Evaluation of Combined Heat and Mass Transfer in Hydromagnetic Micropolar Flow along a Stretching Sheet when Viscous Dissipation and Chemical Reaction Is Present," Partial Differential Equations in Applied Mathematics, **7**, 100467 (2023). https://doi.org/10.1016/j.padiff.2022.100467

[32] S.U. Rehman, A. Mariam, A. Ullah, M.I. Asjad, M.Y. Bajuri, B.A. Pansera, and A. Ahmadian, "Numerical Computation of Buoyancy and Radiation Effects on MHD Micropolar Nanofluid Flow over a Stretching/Shrinking Sheet with Heat Source," Case Studies in Thermal Engineering, **25**, 100867 (2021). https://doi.org/10.1016/j.csite.2021.100867

[33] D. Rees, and I. Pop, "Free convection boundary-layer flow of a micropolar fluid from a vertical flat plate," IMA Journal of Applied Mathematics, **61**(2), 179-197 (1998). https://doi.org/10.1093/imamat/61.2.179

[34] L.J. Grubka, and K.M. Bobba, "Heat Transfer Characteristics of a Continuous, Stretching Surface with Variable Temperature". ASME J. Heat Transfer, **107**, 248-250 (1985). http://dx.doi.org/10.1115/1.3247387

[35] M.A. Seddeek, and A.M. Salem, "Laminar mixed convection adjacent to vertical continuously stretching sheets with variable viscosity and variable thermal diffusivity," Heat Mass Transf. **41**, 1048–1055 (2005). http://dx.doi.org/10.1007/s00231-005-0629-6

ВПЛИВ ЕНЕРГІЇ АКТИВАЦІЇ АРРЕНІУСА В МГД ПОТОЦІ МІКРОПОЛЯРНОЇ НАНОРІДИНИ ВЗДОВЖ ПОРИСТОГО РОЗТЯГНУТОГО ЛИСТА З В'ЯЗКОЮ ДИСИПАЦІЄЮ І ДЖЕРЕЛОМ ТЕПЛА

Кешаб Борах[a], Джадав Конч[b], Шьяманта Чакраборти[c]

[a] Департамент математики, Університет Гаухаті, Гувахаті-781014, Ассам, Індія
[b] Департамент математики, коледж Демаджі, Демаджі-787057, Ассам, Індія
[c] UGC-Центр розвитку персоналу, Університет Гаухаті, Гувахаті-781014, Ассам, Індія

У цьому дослідженні проведено чисельне дослідження тепло- та масообміну потоку мікрополярного нанофлюїду над розтягнутим листом, вбудованим у пористе середовище. Основною метою цієї роботи є дослідження впливу енергії активації Арреніуса, джерела тепла та в'язкої дисипації на швидкість рідини, мікрообертання, температуру та розподіл концентрації. Рівняння, що керують потоком, перетворюються на звичайні диференціальні рівняння за допомогою відповідних перетворень подібності та розв'язуються чисельно за допомогою розв'язувача bvp4c у MATLAB. Графіки будуються для вивчення впливу важливих параметрів, таких як магнітний параметр, параметр пористості, параметр термофорезу, параметр броунівського руху, параметр енергії активації та число Льюїса на швидкість, мікрообертання, температуру та розподіл концентрації. Графічне представлення показує, що швидкість рідини зменшується зі збільшенням значень магнітного параметра, тоді як кутова швидкість збільшується разом із ним. Це дослідження також повідомляє, що посилення розподілу температури та концентрації спостерігається для більш високих значень параметра енергії активації, тоді як число Льюїса демонструє протилежну поведінку. Вплив різних відповідних параметрів реалістично відображено на коефіцієнті поверхневого тертя, числах Нуссельта та Шервуда за допомогою таблиць. Проведено порівняння з попередньою роботою, і результати показали хороший збіг.

Ключові слова: *енергія активації Арреніуса; в'язке розсіювання; броунівський рух; термофорез; мікрополярний нанофлюїд; пористе середовище*

ANALYSIS OF THE HEAT TRANSFER PERFORMANCE OF NANOFLUIDS IN MICRO-CYLINDER GROUPS

Lina Wafaa Belhadj Senini, Mustpaha Boussoufi, ⦿Amina Sabeur*

Laboratoire des Sciences et Ingénierie Maritimes, Faculté de Génie Mécanique,
Université des Sciences et de la Technologie d'Oran Mohammed Boudiaf,
BP 1505 El M'Naouer Oran 31000, Algérie
*Corresponding Author e-mail: sabeuramina@hotmail.com

The objective of this study is to investigate, through numerical simulations, the flow and heat transfer characteristics of Al_2O_3, Cu, TiO_2, and SiC water-based nanofluids flowing over micro-cylinder groups arranged in an inline configuration. The simulations were carried out under laminar flow conditions, and the analysis considered seven different low values of the Reynolds number, with a constant volume fraction of 2 %. The aim of this investigation was to determine how nanofluids, i.e., suspensions of nanoparticles in water as the base fluid, can affect the pressure drop and heat transfer performance in micro-cylinder groups. To accomplish this, the finite volume method was employed to evaluate the impact of the nanofluids on pressure drop and heat transfer characteristics in the micro-cylinder groups. The study results demonstrate that, for all the nanofluids studied, the pressure drop and friction factor of the micro-cylinder groups increased with increasing Reynolds number. This behavior can be attributed to the interaction between the nanoparticles and the wall, which results in an increase in friction. Furthermore, the Nusselt number was found to increase with increasing Reynolds number. The SiC/Water nanofluid exhibited the highest Nusselt numbers among the four nanofluids tested, indicating that it provides better heat transfer performance than the other nanofluids. These results are consistent with experimental findings, indicating that the numerical simulations were accurate and reliable.

Keywords: *Nanoparticles; Micro-cylinder-group; Heat transfer enhancement; Convection; Laminar regime*
PACS: 02.70.−c, 02.60.Cb, 05.70.−a, 44.15.+a, 44.27.+g, 47.10.A−, 47.11.Df, 47.15.−x, 47.15.Rq, 47.27.Te

INTRODUCTION

The electronics industry is a constantly growing industry worldwide. With the increasing demand for energy-efficient technologies, research in this field has focused on minimizing the heat generated by electronic chips and maximizing their efficiency. Several innovative technologies have been developed to enhance heat transfer, including microchannel cooling technology and nano-technology. Microchannel cooling technology was first introduced by Tuckerman and Pease [1] in an attempt to transfer maximum heat in minimum volume. The technology uses micro-sized channels to circulate cooling fluids close to the heat source, which results in an effective cooling system. In addition to microchannel cooling technology, researchers have explored the use of micro-finned surfaces to improve heat transfer efficiency. Mizunuma et al. [2] conducted experimental and numerical studies to investigate the forced convective heat transfer from a micro-finned surface. They found that micro-finned surfaces can be effective in improving heat transfer performance in microchannels. Overall, the development of innovative technologies such as microchannel cooling and micro-finned surfaces has opened up new possibilities for enhancing heat transfer and improving the energy efficiency of electronic devices. Kosar et al. [3] conducted an experimental investigation on the pressure drops and friction factors associated with the forced flow of de-ionized water over staggered and in-line circular/diamond-shaped micro pin-fin bundles. The study aimed to determine the pressure drops and friction factors in micro pin-fin heat exchangers. In a similar vein, Galvis et al. [4] have studied several models of pin-fin heat exchangers. The results show that the micro pin-fin heat exchanger's thermal performance always exceeded that of the smooth channel and that pin-fin heat exchangers can be highly effective in enhancing heat transfer in electronic cooling systems. Moreover, Ohadi et al. [5] have investigated thermal managements techniques for cooling high-flux electronics. The techniques included immersion cooling, jet impingement, spray cooling, and ultra-thin film evaporation (UTF), which are used primarily for hot spot cooling of the chip. The study aimed to develop effective cooling techniques that can prevent overheating and improve the overall performance of electronic devices. Liu and Guan et al. [6,7] conducted a numerical analysis of the relationship between vortex and temperature distributions in in-line and staggered arranged micro-cylinder groups. They suggested that the end wall effect and the vortex distribution have a significant impact on the thermal performance of micro-cylinder groups. This study aims to improve the understanding of the heat transfer mechanisms in micro-cylinder groups to optimize their thermal performance. In addition, nano-technology has become an important area in the field of heat transfer. Nanofluids are fluids containing nano-scale particles added to a base fluid such as water, ethylene glycol, or oil. They have various applications in microelectronics, fuel cells, heat exchangers, micro-electro-mechanical systems, and pharmaceutical devices. Choi [8] conducted a theoretical examination of the thermal conductivity of a fluid with Cu nanoparticles, which is later referred to as a nanofluid. The study aimed to enhance the understanding of the thermal conductivity of nanofluids, which is crucial for designing efficient heat transfer systems. Furthermore, Abu-Nada et al. [9] carried out a numerical

study on the natural convection of different nanofluids in horizontal concentric annuli. They found that the addition of nanoparticles to the base fluid leads to higher thermal conductivity and better heat transfer, especially at high Rayleigh numbers. Mohammed et al. [10] performed a numerical study on the flow and heat transfer of an alumina-water nanofluid in a microchannel heat sink. Their results showed that increasing the volume fraction of nanoparticles led to an increase in both heat transfer coefficient and wall shear stress, while the thermal resistance decreased. In another study, Akbani et al. [11] compared single-phase and two-phase models of a nanofluid for turbulent forced convection. They concluded that the single-phase model was more suitable due to its less expensive numerical integration and its simplicity of implementation. Moraveji et al. [12] developed a numerical model of the flow of nanofluids in a mini-channel heat exchanger with TiO_2 and SiC nanoparticles, considering various concentrations. Their study found that heat transfer extended with increasing volume fraction and Reynolds number.

Adriana [13] conducted a numerical analysis of the flow and heat transfer characteristics of water- Al_2O_3 nanofluid in a horizontal tube. They found that the heat transfer coefficient increased by 2.33% to 26.45% compared to pure water and that uncertainties in the properties of the nanofluid have a significant effect on the results. Said et al. [14] investigated the thermal performance of TiO_2-water nanofluid for different mass flow rates and volume fractions. They concluded that an increase in energy efficiency of up to 76.6% was observed for a volume fraction of 0.1% and a flow rate of 0.5 kg/min. In a study by Bouhazza et al. [15], the heat transfer of nanofluids containing Cu and TiO_2 nanoparticles was simulated at various volume fractions. The results revealed that increasing the volume fraction led to enhanced heat transfer and that the Cu-water nanofluid exhibited the best heat conductivity. Dabiri [16] conducted experiments and found that using SiC nanofluid in a circular tube led to an increase of up to 8.88% in the Nusselt number. Bowers [17] experimentally investigated the flow and heat transfer of silica and alumina nanofluids in micro-channels and found that at low volume fractions of both nanofluids, there was an improvement in heat transfer which increased with rising Reynolds number and hydraulic diameter. Goodarzi [18] employed the finite volume method to investigate the natural convection of nanofluids containing Cu, MWCNT, and Al_2O_3 nanoparticles in a two-dimensional closed cavity. The study revealed that the presence of nanofluids led to heat transfer in the cavity with distinct regions of low and high temperatures. On the other hand, Zhang et al. [19] utilized both nanofluid and micro-channel technologies to experimentally investigate the heat transfer of SiC-water nanofluid in micro-cylinder-groups under laminar flow with varying volume fractions and two different arrangements. The results indicated a decrease in the Nusselt number with increasing volume fraction and a heat transfer enhancement factor above 1 for volume fractions of 0.02 and 0.05. Kamini et al. [20] conducted an experimental study on the convective heat transfer of SiC-water nanofluid in a shell and tube heat exchanger. The results showed that the presence of SiC nanoparticles increased heat transfer by 19.8%. Zheng et al. [21] also carried out an experimental investigation on the flow and heat transfer of nanofluids containing Al_2O_3, SiC, Cu, and Fe_3O_4 in water. They found that the Fe_3O_4-water nanofluid had the greatest thermal enhancement, and empirical relations were developed to predict the thermal behavior of nanofluids. Ahmad [22] performed a simulation and experimental analysis on the effect of twisted tape and nanofluids on heat transfer in a circular tube at high Reynolds numbers. Two types of nanofluids (SiC/Water and Al_2O_3/Water) at various volume fractions were used, and the results showed that the heat transfer efficiency was improved by up to 10% with the use of SiC/Water nanofluid. Presently, there has been significant scholarly interest in exploring the flow and heat transfer characteristics of nanofluids in microchannels. Researchers from various fields have conducted investigations to understand how nanofluids behave in different types of microchannels. However, there remains a noticeable gap in the literature regarding the heat transfer behavior of nanofluids in micro-channels that consist of micro-cylinder groups. This specific configuration has received limited attention in research studies thus far. Moreover, the existing studies that have examined the heat transfer phenomena in micro-cylinder groups using nanofluids have primarily relied on experimental approaches [19] rather than numerical simulations or modeling. Furthermore, there is a dearth of conclusive evidence regarding the accuracy and reliability of numerical models in replicating the flow and heat transfer characteristics of nanofluids in micro-cylinder groups. The capability of numerical models to accurately predict the behavior of nanofluids in this particular micro-channel configuration has not been firmly established. As a result, further research and investigation are needed to evaluate and enhance the performance of numerical models in capturing the intricate flow and heat transfer phenomena exhibited by nanofluids in micro-cylinder groups.

In the current study, the four different water-based nanofluids containing SiC, Cu, Al_2O_3, and TiO_2 nanoparticles were simulated numerically to investigate their flow and heat transfer characteristics in the micro-cylinder groups arranged in an inline configuration. The simulations were conducted under laminar flow conditions, with low Reynolds numbers. The volume fraction of the nanoparticles was set to 0.02. This work also examines the agreement between the experimental and numerical results and the ability of these simulations to reproduce the physical phenomena acting in this geometry in the presence of nanofluids. Conducting this research will also help to provide prime predictions on the potential applications of these different nanofluids in such heat transfer systems. The effects of the nanoparticles on the flow and heat transfer characteristics, such as velocity profiles, temperature distributions, and heat transfer coefficients, were analyzed and compared to those of pure water.

PHYSICAL MODEL AND MATHEMATICAL FORMULATION

The physical domain of the micro-cylinder groups is shown in Figure (1). It consists of thirty circular cylinders arranged in line, placed in a micro-channel filled with four different water-based nanofluids in a laminar flow regime. The dimensions of the micro-cylinder-groups, including the diameter of the micro-cylinders (d), the length and width of

the micro-channel (L and W, respectively), and the height of the micro-cylinders (M), are presented in Table 1. To analyze the forced convection of the nanofluids, the continuity, momentum, and energy equations were solved using both the single-phase approach and the two-phase mixture approaches.
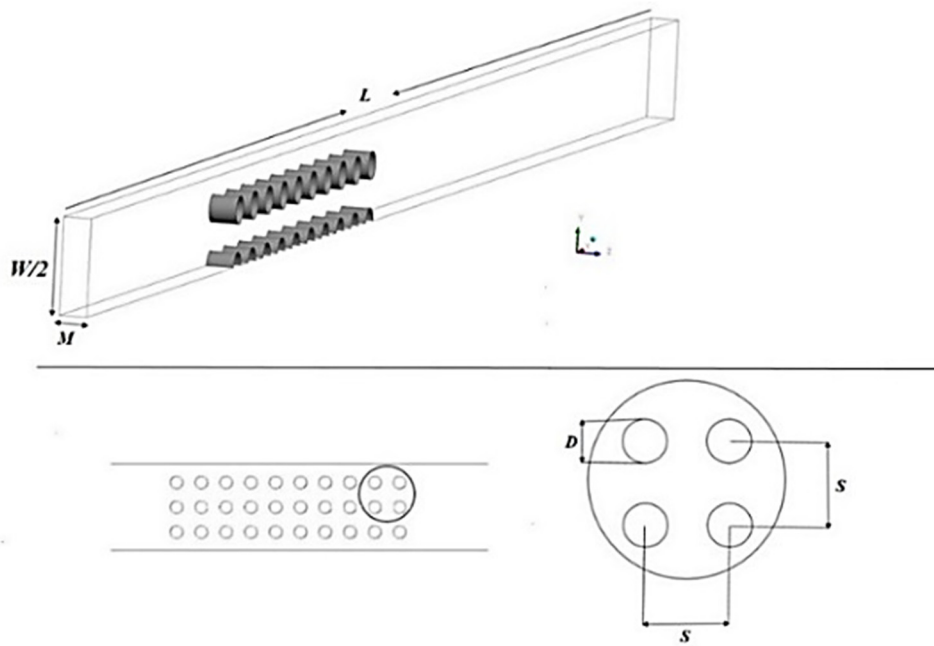

Figure 1. The physical domain of the micro-cylinder-group

Table 1. Detailed dimensions of the micro-cylinder-groups

d(mm)	S/d	N	M(mm)	L(mm)
0.5	2	10	0.5	40

Single Phase Approach

The single-phase approach is a modeling approach that treats nanofluids as a single homogeneous liquid with effective thermophysical properties. In this approach, the continuity, momentum, and energy equations are solved for the nanofluid as a single-phase fluid. The effective properties of the nanofluid are obtained by using the volume fraction of nanoparticles and the properties of the base fluid. The equations are:

Continuity:

$$\nabla.(\rho\vec{V}) = 0 \tag{1}$$

Momentum:

$$\nabla.(\rho\vec{V}\vec{V}) = -\nabla.P + \nabla.(\mu\nabla.\vec{V}) + \rho g \tag{2}$$

Energy equation:

$$\nabla.(\rho\vec{V}H) = -\nabla.q - \tau : \nabla.\vec{V} \tag{3}$$

Reynolds number

$$Re = \frac{\rho_{nf}U_{max}d}{\mu_{nf}} \tag{4}$$

In order to solve the above equations, accurate effective thermo-physical properties must be involved. The literature contains various models allowing us to theoretically calculate the nanofluid's hydrothermal properties. The expressions used to define these properties used in this work are: for the homogeneous single-phase model with constant properties, density and heat capacity of nanofluid, are estimated by using classical models [23,24,25] as follows:

Density:

$$\rho_{nf} = (1-\varphi)(\rho Cp)_f + \varphi(\rho Cp)_p \tag{5}$$

Specific heat:

$$(\rho Cp)_{nf} = (1-\varphi)(\rho Cp)_f + \varphi(\rho Cp)_p \tag{6}$$

Thermal expansion coefficient:

$$(\rho\beta)_{nf} = (1-\varphi)(\rho\beta)_f + \varphi(\rho\beta)_p \tag{7}$$

Dynamic viscosity (Brinkman [26]):

$$\mu_{nf} = \frac{\mu_f}{(1-\varphi)^{2.5}} \tag{8}$$

On the other hand, nanofluid thermal conductivity is determined by the correlation reported by Maxwell [27]

Thermal conductivity (Maxwell [27]):

$$\frac{k_{nf}}{k_f} = \frac{(1-\varphi)(k_p + 2k_f) + 3\varphi k_p}{(1-\varphi)(k_p + 2k_f) + 3\varphi k_f} \tag{9}$$

Table 2. Thermo-physical properties of water and nanoparticles **[28], [29], [30], [31]**

Thermo-physical properties	Density (Kg/m³)	Specific heat	Thermal conductivity
Water	997	4179	0.673
Al2O3	3970	765	40
Cu	8933	385	401
TiO2	4250	686.2	8.4
SiC	3160	723	490

Mixture Two-Phase Approach

The mixture model considers the nanofluid as a two-phase fluid where water is considered as the continuous liquid first phase while the nanoparticles as the dispersed solid secondary phase. The continuity, momentum, and energy equations are solved for the mixture at the same time an additional equation: the mass conservation equation or volume fraction equation is solved only for the second phase.

Continuity equation for the mixture:

$$\nabla.(\rho_m \vec{V}_m) = 0 \tag{10}$$

Momentum equation of the mixture:

$$\nabla.\left(\rho_m \vec{V}_m \vec{V}_m\right) = -\nabla.P_m + \nabla.\left(\mu_m \nabla.\vec{V}_m + \sum_{k=1}^{n} \varphi_k \rho \overline{v_k v_k}\right) + \rho_m g + \nabla.\left(\sum_{k=1}^{n} \varphi_k \rho_k V_{dr,k} \vec{V}_{dr,k}\right) \tag{11}$$

Energy equation of the mixture:

$$\nabla.(\sum_{k=1}^{n} \varphi_k \rho_k \vec{V}_k H_k) = -\nabla.q_m - \tau : \nabla \vec{V}_m \tag{12}$$

Volume fraction equation of the secondary phase:

$$\nabla.\left(\varphi_p \rho_p \vec{V}_m\right) = -\nabla.\left(\varphi_p \rho_p \vec{V}_{dr,p}\right) \tag{13}$$

The mixture velocity, density and viscosity are:

$$\vec{V}_m = \frac{\sum_{k=1}^{n} \varphi_k \rho_k \vec{V}_k}{\rho_m} \tag{14}$$

$$\rho_m = \sum_{k=1}^{n} \varphi_k \rho_k \tag{15}$$

$$\mu_m = \sum_{k=1}^{n} \varphi_k \mu_k \tag{16}$$

The kth phase's drift velocity is:

$$\vec{V}_{dr,k} = \vec{V}_k - \vec{V}_m \tag{17}$$

Where φ_k is the volume fraction of the phase k.
The formulation of friction factor is given by:

$$f = \frac{2H\Delta p}{L\rho U^2_{max}} \tag{18}$$

Nusselt number:

$$Nu = \frac{hD}{\mu_{nf}} \tag{19}$$

Convective heat transfer coefficient:

$$h = \frac{Q}{\Delta T} \tag{20}$$

Thermal enhancement factor:

$$TEF = \frac{Nu_{nf}/Nu_f}{\left(f_{nf}/f_f\right)^{1/3}} \tag{21}$$

Boundary conditions

The physical problem's boundary conditions consist of various components, such as adiabatic walls, heating walls, a velocity inlet, a fully developed outlet, and a symmetry plane as presented in Figure (2). These components are crucial for the analysis of the flow and heat transfer of the nanofluids within the micro-cylinder groups.
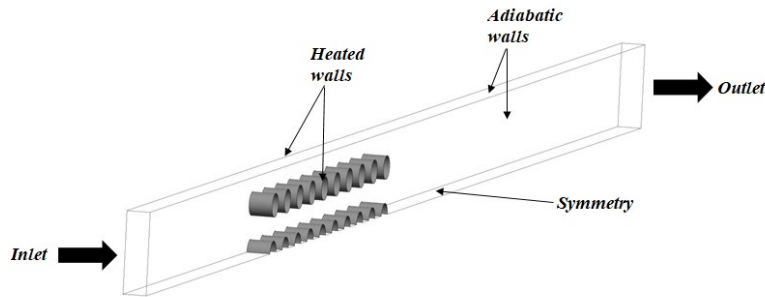

Figure 2. Boundary conditions

Heated walls: $u,v,w_{wall-h} = 0, \frac{\partial T}{\partial \vec{n}}_{wall-h} = q$.

Adiabatic walls: $u,v,w_{wall-ad} = 0, \frac{\partial T}{\partial \vec{n}}_{wall-ad} = 0$.

Inlet: $u = u_{in,}, v, w = 0, T_{in} = 293.15K$.

Outlet: $\frac{\partial u}{\partial x}_{out} = 0, \frac{\partial v}{\partial y}_{out} = 0, \frac{\partial w}{\partial z}_{out} = 0, \frac{\partial T}{\partial \vec{n}}_{out} = 0$.

Symmetry: $\frac{\partial u}{\partial x}_{sym} = 0, \frac{\partial v}{\partial y}_{sym} = 0, \frac{\partial w}{\partial z}_{sym} = 0, \frac{\partial T}{\partial \vec{n}}_{sym} = 0$.

The resolution of the equations cited above allowed the analysis of the variations in the pressure drops, the Nusselt numbers as well as the temperature distributions, and their influence on the thermal performance of the nanofluids.

MESH AND VALIDATION

The simulation considers the flow to be three-dimensional, and a 3D hexahedral mesh is generated based on half of the physical model, taking into account the structural symmetry of the micro-cylinder groups. Preliminary calculations are carried out to evaluate the mesh sensitivity, and three meshes (800000, 1700000, and 2300000) are employed. Table 3 summarizes the sensitivity measures, which are the obtained values of the average Nusselt numbers and the pressure drop. The deviation of the pressure drops and Nusselt number among the three different grids is less than 0.6% and 2.5%, respectively. Consequently, the mesh containing 1700000 elements is deemed satisfactory for the simulation of flow and heat transfer characteristics.

Table 3. Comparison of average Nusselt number and pressure drop among different grids tested for **Re = 236**

Grid	Nusselt number	Err %	Pressure drop	Eerr %
Grid 1 (800000)	9,7574037		1221,7252	
Grid 2 (1700000)	10,00619	2,486323965	1215,6107	0,500480796
Grid 3 (2300000)	10,04324	0,368904855	1215,2634	0,028578167

In order to validate the numerical predictions with the experimental results **[19],** both single phase approach and mixture two phase approach were employed.

Figures (3) and (4) provide a comparison between the experimental and numerical results obtained through both approaches for the pressure drop and Nusselt number. As indicated in Figure (3), the three graphs have consistent trends. However, at low Reynolds numbers, the mixture two-phase model yielded results that were closer to the experimental findings. In contrast, at higher Reynolds numbers, the single-phase model was more accurate. Figure (4) shows that the mixture approach overestimated the Nusselt number, while the single-phase approach produced results that were close to the experimental findings. These comparisons provide validation for the numerical model proposed in this study and demonstrate its accuracy.
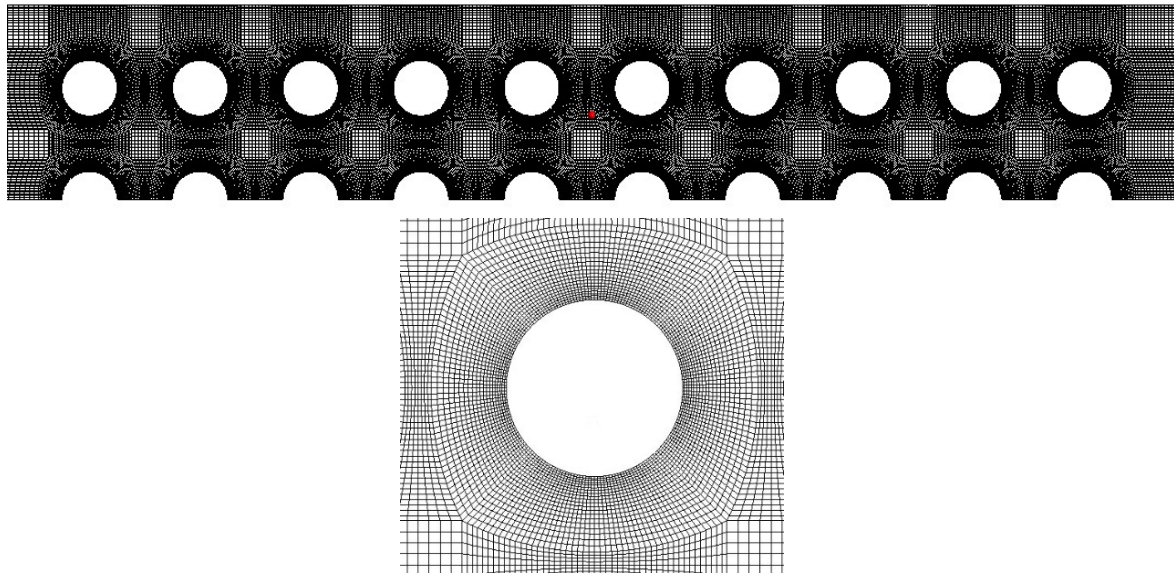

Figure 3. View of the grid distribution of the physical domain

NUMERICAL METHODS

To solve the governing equations that describe the flow and heat transfer characteristics in the micro-cylinder groups, the finite volume method was used. This method involves dividing the computational domain into a grid of discrete cells and evaluating the variables at specific locations within each cell. The differential equations were then converted to algebraic equations that can be solved numerically. By resolving these equations, it was possible to analyze the influence of the nanoparticles on the pressure drop, heat transfer, and efficiency of the system. The resolution of the equations was carried out using the second-order upwind scheme, which is a numerical scheme commonly used for the discretization of the energy and momentum equations. The coupling between the pressure and velocity fields was achieved using the SIMPLE algorithm, which is a well-established approach for solving the Navier-Stokes equations in computational fluid dynamics. To ensure the accuracy and reliability of the numerical simulations, a convergence criterion of 10^{-6} was used for all computations. This criterion ensures that the solution has converged to a stable and consistent solution. With these numerical tools and techniques, it was possible to gain insights into the flow and heat transfer characteristics of the micro-cylinder groups and understand how the nanoparticles affect these characteristics.
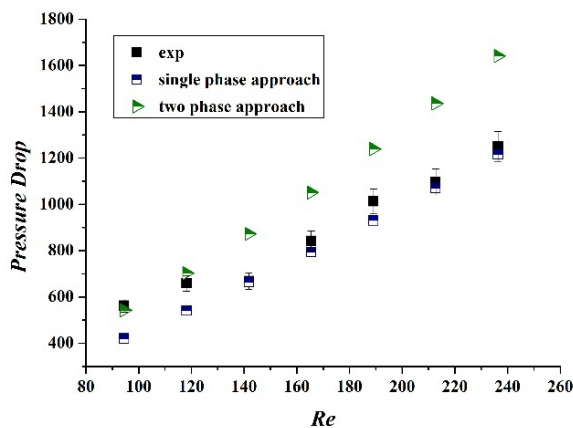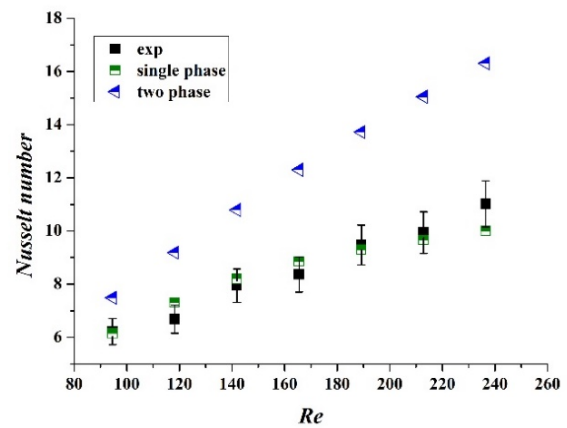

Figure 4. Comparison of pressure drop variation

Figure 5. Comparison of Nusselt number variation

RESULTS AND DISCUSSION

In this study, the thermal performance of four different water-based nanofluids in micro-cylinder groups was numerically analyzed to assess the enhancement of heat transfer. The simulations were performed in a laminar regime with Reynolds numbers below 300 and a volume concentration of 2%. Figure 6 depicts the variation of pressure drop for each nanofluid. It can be observed that the pressure drop increases with increasing Reynolds number, and this is primarily attributed to the increase in velocity. In this micro-flow, the boundary layer between the micro-cylinders is thin, and the presence of solid particles disturbs this layer, exacerbating the pressure drop. The presence of nanoparticles in the nanofluids has a significant effect on the pressure drop, and this effect increases with increasing Reynolds number.
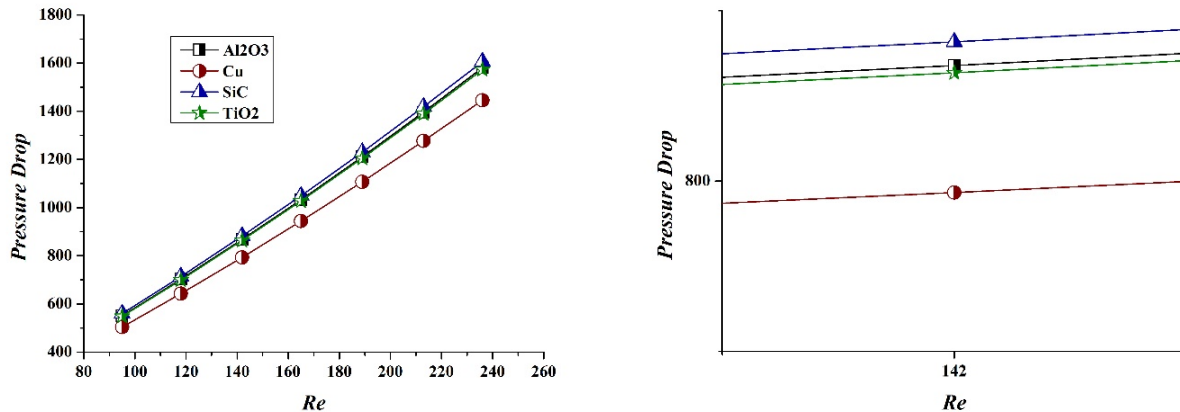

Figure 6. variation of pressure drops

In Figure 7, the velocity fields of SiC/water nanofluid at a specific location (z=0.25 mm) along the x-direction are depicted for two different Reynolds numbers, namely a low and a high value. Upon analysis, it becomes apparent that there are two distinct regions of intensified velocity located in the upper section of the geometry, positioned between the two columns of micro-cylinders. With an increase in the Reynolds number, these high-speed regions not only expand in size but also exhibit an augmentation in the maximum velocity magnitude within those areas. This observation suggests that the flow behavior and characteristics are strongly influenced by the Reynolds number. The occurrence of these high-speed narrow regions can be attributed to multiple factors. Firstly, viscous forces play a significant role in shaping the flow patterns. The presence of the micro-cylinders causes the fluid to experience changes in momentum, resulting in localized regions with elevated velocities. These regions are confined and exhibit a narrow shape due to the influence of the micro-cylinder geometry. Secondly, the superposition of velocity fields contributes to the formation of these high-speed regions. As the fluid flows past the micro-cylinders, the velocity fields from different regions combine, leading to regions of accelerated flow. It is important to note that the expansion and intensification of these high-speed regions are directly associated with the Reynolds number. As the Reynolds number increases, the impact of viscous forces and the superposition of velocity fields become more pronounced, resulting in larger and more energetic high-speed regions. In summary, the appearance of the two high-speed narrow regions in the upper part of the geometry, positioned between the micro-cylinders, can be attributed to the interplay between viscous forces and the superposition of velocity fields. These regions expand and exhibit higher velocities with increasing Reynolds numbers, indicating the significant influence of fluid dynamics on the flow behavior within micro-channel configurations.
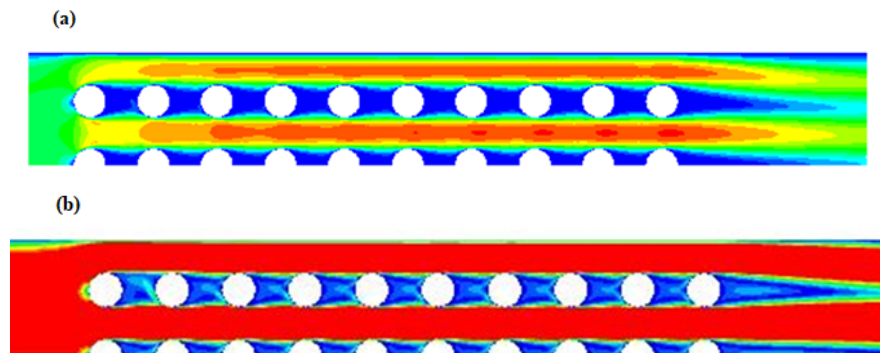

Figure 7. Velocity fields (a) Re= 94, (b) Re=212

Furthermore, Figure 8 displays the variation of Nusselt number for the nanofluids studied, with a heat flux of 15 W/cm2 and under laminar flow conditions. All the graphs show a consistent trend in which the Nusselt number increases with the rise of Reynolds number. This increase in Nusselt number is an indication of enhanced heat transfer, which is produced by the disturbance or separation of the boundary layer caused by the increasing velocity. The presence of nanoparticles in the nanofluids has a significant effect on the improvement and increase of thermal conductivity, which in turn enhances the heat transfer.
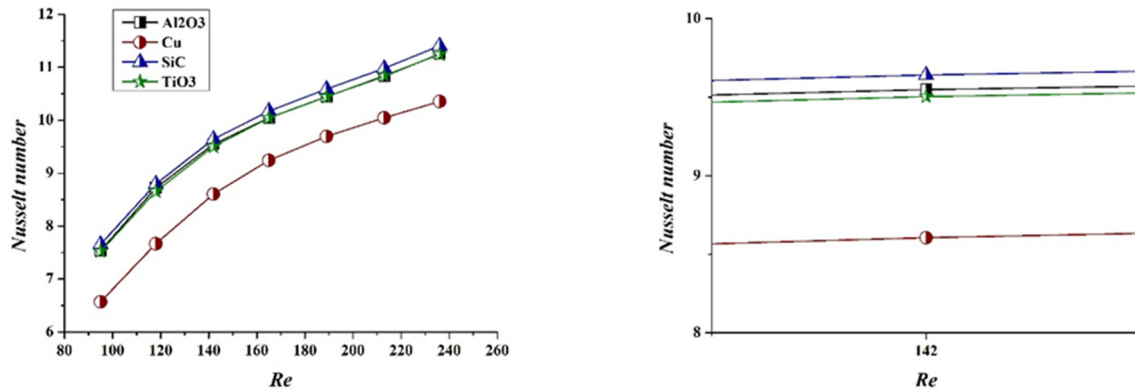
Figure 8. Variation of Nusselt Number

Figure 9 shows the temperature distributions of SiC/water nanofluid for two different Reynolds numbers: a low Reynolds number of 94 and a high Reynolds number of 212. The analysis reveals that there is a prominent low-temperature region upstream of the micro-cylinders. This behavior is due to an increased heat transfer resulting from the separation of the boundary layer in this region. Conversely, in the downstream region of each micro-cylinder, there is a decrease in the heat transfer coefficient, leading to a high-temperature region. These regions become larger with an increase in the Reynolds number, thereby significantly impacting the overall temperature distribution of the system.

It's worth noting that the temperature downstream of the micro-cylinder is higher than the temperature upstream, which is in agreement with the theory of boundary layer flow. The separation of the boundary layer creates a wake vortex downstream of the micro-cylinder, which leads to a decrease in flow velocity and, consequently, an increase in temperature. The present analysis of temperature distributions for different Reynolds numbers provides valuable insights into the flow dynamics and heat transfer in this complex system.

The thermal enhancement factor is a key parameter that measures the relative effectiveness of nanofluids compared to the base fluid. It is defined as the ratio of the heat transfer coefficient and friction factor of the nanofluid to those of the base fluid. When this factor is above 1, the nanofluid is considered to be effective, which means that the growth of heat transfer is greater than the loss of pressure drops. This factor is an essential tool used in this study to evaluate the thermal efficiency of nanofluids inside micro-cylinder groups. It provides insights into the performance of nanofluids in terms of heat transfer and fluid flow. Furthermore, it offers a useful means of comparing the thermal performance of different nanofluids and identifying the most effective nanofluid for a specific application.
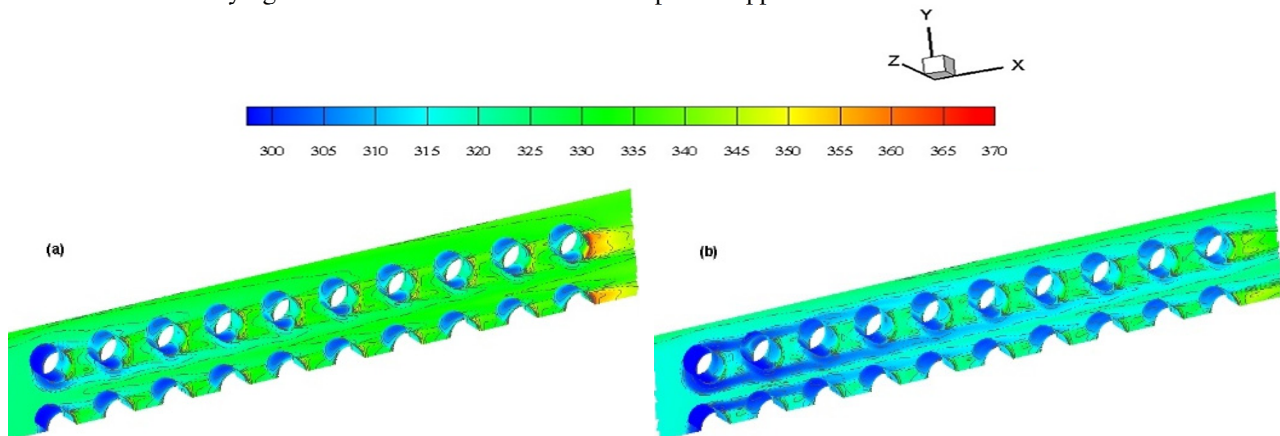

Figure 9. Temperature distributions at **(a)** Re=94 and **(b)** Re=212

Figure 10 depicts the variation of thermal enhancement factor with the Reynolds number for various nanofluids containing metallic oxide nanoparticles. The graph reveals a positive correlation between the Reynolds number and the thermal enhancement factor, suggesting an increase in heat transfer performance with an increase in Reynolds number. However, the nanofluids containing metallic oxide nanoparticles exhibit better performance under specific conditions, including geometry, volume fraction, and Reynolds number. In these conditions, the presence of metallic oxide nanoparticles can improve heat transfer, resulting in a thermal enhancement factor greater than 1 for SiC nanoparticles. Nevertheless, in general, the introduction of metallic oxide nanoparticles does not have a positive impact on heat transfer, as indicated by thermal enhancement factors below 1. These findings indicate the need for further investigations to explore the influence of various parameters on the heat transfer performance of nanofluids. The parameters to be considered in such studies include particle size, shape, and concentration, among others. An in-depth understanding of the effect of these parameters on the performance of nanofluids could lead to the development of optimized nanofluid formulations for various engineering applications.
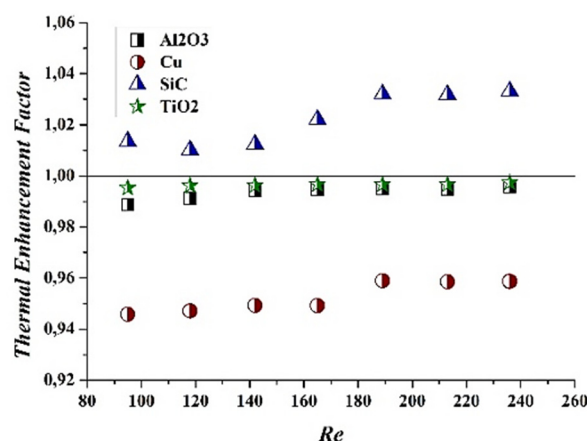
Figure 10. variation of the Thermal Enhancement Factor

CONCLUSIONS

The objective of this research was to examine the heat transfer and flow properties of four types of nanofluids in micro-cylinder groups operating under laminar conditions and a volume fraction of 0.02.

In order to validate the new numerical findings, a comparison was made between the results obtained in this study and the experimental data from a previous work conducted by Zhang et al. [19]. Remarkably, the two sets of results exhibited strong agreement, further corroborating the validity and accuracy of the numerical findings in this study.

- The obtained results clearly indicate that an elevation in Reynolds number corresponds to amplified values of both pressures drop and Nusselt number. This observation can be attributed to the escalating disturbance of the boundary layer as the Reynolds number increases.
- Under the specific conditions considered, the SiC/water nanofluid demonstrated the highest Nusselt number among the Cu, Al2O3, and TiO2 nanofluids. The SiC/water nanofluid exhibited superior heat transfer performance compared to the other nanofluids in terms of convective heat transfer efficiency.
- The increased viscosity of nanofluids compared to the base fluid can limit their effectiveness in certain applications. However, an analysis of the thermal enhancement variation reveals that only SiC nanofluids, at the specific concentration studied, exhibit significant and effective performance with thermal enhancement factors exceeding 1.

Further study into this issue is still required in order to check the enhancement of the heat transfer processes in such geometries. A more detailed research effort that will consider different factors, such as volume fraction and micro-cylinder arrangements, to expand our understanding of the flow and heat transfer properties of nanofluids.

List of abbreviations

Re	Reynolds number	**Greek letters**	
d	Micro-cylinders diameter (mm)	ρ	Density (kg m-3)
S	Space between micro-cylinders (mm)	μ	Dynamic viscosity (N s m-2)
N	Micro-cylinders column number	τ	Stress tensor (N m-2)
M	Microchannel height (mm)	φ	Volume fraction
L	Microchannel length (mm)	β	Thermal expansion factor (k)
V	Velocity (m s-1)	**Subscripts**	
P	Pressure (pa)	Nf	Nanofluid
g	Gravity (m s-2)	Max	maximum
Q, q	Heat flux (W m-2)	F	fluid
H	Entropy (J k-1)	P	particle
U	X velocity (m s-1)	M	mixture
Cp	Specific heat (j kg-1 k-1)	N	Nth phase
k	Thermal conductivity (W m-1 k-1)	K	Kth phase
Nu	Nusselt number	dr	Drift
f	Friction factor	Wall-h	Heated wall
h	Convective heat transfer coefficient	Wall-ad	Adiabatic wall
T	Temperature (k)	In	Inlet
TEF	Thermal enhancement factor	out	Outlet
		sym	symmetry

Authors' contributions.

Lina Wafaa Belhadj Senini: conceived of the presented idea, developed the theory and performed the computations and contributed to the final version of the manuscript. **Mustapha Boussoufi**: performed the analytic calculations and the numerical simulations. **Amina Sabeur**: developed the theoretical formalism, discussed the results, and contributed to the final manuscript

ORCID

ⓘ**Amina Sabeur,** https://orcid.org/0000-0001-6972-4136

REFERENCES

[1] D.B. Tuckerman, and R.F.W. Pease, "High Performance Heat Sinking for VLSI," IEEE Electron Device Letters, **2**(5), 126-129 (1981). https://doi.org/10.1109/EDL.1981.25367

[2] H. Mizunuma, M. Behnia, and W. Nakayama, "Heat transfer from micro-finned surfaces to flow of fluorine coolant in reduced-size channels," IEEE Transactions on Components, Packaging, and Manufacturing Technology: Part A, **20**(2), 138–145 (1997). https://doi.org/10.1109/95.588565

[3] A. Koşar, C. Mishra, and Y. Peles, "Laminar flow across a bank of low aspect ratio micro pin fins," J. Fluids Eng. **127**, 419–430 (2005). https://doi.org/10.1115/1.1900139

[4] E. Galvis, B.A. Jubran, F.Xi.K. Behdinan, and Z. Fawaz, "Numerical modeling of pin-fin micro heat exchangers," Heat Mass Transfer, **44**, 659–666 (2008). https://doi.org/10.1007/s00231-007-0291-2

[5] M. Ohadi, J. Qi, and J. Lawler, "Ultra-Thin Film Evaporation (UTF) – Application to Emerging Technologies in Cooling of Microelectronics," in: Microscale Heat Transfer Fundamentals and Applications. NATO Science Series II: Mathematics, Physics and Chemistry, vol. 193, edited by S. Kakaç, L. Vasiliev, Y. Bayazitoğlu, and Y. Yener (Springer, Dordrecht, 2005). pp. 321–338. https://doi.org/10.1007/1-4020-3361-3_17

[6] N. Guan, Z.G. Liu, and C.W. Zhang, "Numerical investigation on heat transfer of liquid flow at low Reynolds number in micro-cylinder-groups," Heat Mass Transfer, **48**, 1141–1153 (2012). https://doi.org/10.1007/s00231-011-0956-8

[7] N. Guan, and Z.G. Liu, "Numerical investigation of laminar flow and heat transfer in micro-cylinder-groups," in: *Proceedings of the 8th International Conference on Nanochannels, Microchannels and Mini channels*, (ASME, Montreal, Canada, 2010) pp. 645–654. https://doi.org/10.1115/FEDSM-ICNMM2010-30423

[8] S.U.S. Choi, and J.A. Eastman, "Enhancing thermal conductivity of fluids with nanoparticles," in: *ACME International Mechanical Engineering Congress & Exposition* (San Francisco, Ca, 1995). https://www.osti.gov/servlets/purl/196525

[9] E. Abu-Nada, Z. Masoud, and A. Hijazi, "Natural convection heat transfer enhancement in horizontal concentric annuli using nano-fluids," International Communications in Heat and Mass Transfer, **35**, 657–665 (2008). https://doi.org/10.1016/j.icheatmasstransfer.2007.11.004

[10] H.A. Mohammed, P. Gunnasegaran, and N.H. Shuaib, "Heat transfer in rectangular micro-channels heat sink using nano-fluids," International Communications in Heat and Mass Transfer, **37**, 1496–1503 (2010). https://doi.org/10.1016/j.icheatmasstransfer.2010.08.020

[11] M. Akbari, N. Galanis, and A. Behzadmehr, "Comparative assessment of single and two-phase models for numerical studies of nano-fluid turbulent forced convection," International Journal of Heat and Fluid Flow, **37**, 136–146 (2012). https://doi.org/10.1016/j.ijheatfluidflow.2012.05.005

[12] M.K. Moraveji, R.M. Ardehali, and A. Ijam, "CFD investigation of nano-fluid effects (cooling performance and pressure drop) in mini-channel heat sink," International Communications in Heat and Mass Transfer, **40**, 58–66 (2013). https://doi.org/10.1016/j.icheatmasstransfer.2012.10.021

[13] A. Adriana, "Simulation of Nano-fluids Turbulent Forced Convection at High Reynolds Number: A Comparison Study of Thermophysical Properties Influence on Heat Transfer Enhancement," Flow Turbulence Combust, **94**, 555–575 (2015) https://doi.org/10.1007/s10494-014-9590-0

[14] Z. Said, M.A. Sabiha, R. Saidur, A. Hepbasli, N.A. Rahim, S. Mekhilef, and T.A. Ward, "Performance enhancement of a Flat Plate Solar collector using Titanium dioxide nano-fluid and Polyethylene Glycol dispersant," Journal of Cleaner Production, **92**, 343-353 (2015). https://doi.org/10.1016/j.jclepro.2015.01.007

[15] A. Bouhezza, S. Boubeggar, and K. Boukerma, "Simulation numérique du transfert de chaleur de nano-fluide dans un canal," in: *Third International Conference on Energy, Materials, Applied Energetics and Pollution*, (Constantine, Algeria, 2016). pp. 302-307. https://www.umc.edu.dz/images/50-BOUHEZZA.pdf

[16] E. Dabiri, F. Bahrami, and S.M. Zadeh, "Experimental investigation on turbulent convection heat transfer of SiC/W and MgO/W nanofluids in a circular tube under constant heat flux boundary condition," J. Therm. Anal. Calorim. **131**, 2243–2259 (2018). http://dx.doi.org/10.1007/s10973-017-6791-5

[17] J. Bowers, H. Cao, and G. Qiao, "Flow and heat transfer behavior of nano-fluids in micro-channels," Prog. Nat. Sci.: Mater. Int. **28**, 225–234 (2018). https://doi.org/10.1016/j.pnsc.2018.03.005

[18] H. Goodarzi, O.A. Akbari, M.M. Sarafraz, M. Mokhtari, M.R. Safaei, and G.A.S. Shabani, "Numerical Simulation of Natural Convection Heat Transfer of Nanofluid with Cu, MWCNT And Al$_2$O$_3$ Nanoparticles in A Cavity with Different Aspect Ratios," Journal of Thermal Science and Engineering Application, **11**(6), 061020 (2019). https://doi.org/10.1115/1.4043809

[19] X. Zhang, G. Meng, and Z. Wang, "Experimental study on flow and heat transfer characteristics of SiC-water Nanofluids in micro-cylinder-groups," International Journal of Heat and Mass Transfer, **147**, 118971 (2020). https://doi.org/10.1016/j.ijheatmasstransfer.2019.118971

[20] S. Karimi, M.M. Heyhat, A.H.M. Isfahani, and A. Hosseinian, "Experimental investigation of convective heat transfer and pressure drop of SiC/water nanofluid in a shell and tube heat exchanger," Heat and Mass Transfer **56**, 2325–2331 (2020). https://link.springer.com/article/10.1007/s00231-020-02844-7

[21] D. Zheng, J. Wang, Z. Chen, J. Baleta, and B. Sundén, "Performance analysis of a plate heat exchanger using various nanofluids," International Journal of Heat and Mass Transfer, **158**, 119993 (2020). https://doi.org/10.1016/j.ijheatmasstransfer.2020.119993

[22] S. Ahmad, S. Abdullah, and K. Sopian, "Numerical and Experimental Analysis Of The Thermal Performances of Si'/Water and Al₂O₃/Water Nanofluid Inside A Circular Tube with Constant-Increased-PR Twisted Tape," Energies, **13**, 2095 (2020). https://doi.org/10.3390/en13082095

[23] B.C. Pak, and Y.I. Cho, "Hydrodynamic and heat transfer study of dispersed fluids with submicron metallic oxide particles," Exp. Heat Transf. **11**, 151-170 (1998). https://doi.org/10.1080/08916159808946559

[24] S.E.B. Maiga, C.T. Nguyen, N. Galanis, and G. Roy, "Heat transfer behaviours of nanofluids in a uniformly heated tube," Superlattices Microstruct. **35**, 543-557 (2004). https://doi.org/10.1016/j.spmi.2003.09.012

[25] V. Bianco, F. Chiacchio, O. Manca, and S. Nardini, "Numerical investigation of nanofluids forced convection in circular tubes," Appl. Therm. Eng. **29**, 3632-3642 (2009). https://doi.org/10.1016/j.applthermaleng.2009.06.019

[26] H.C. Brinkman, "The viscosity of concentrated suspensions and solution," J. Chem. Phys. **20**, 571–581 (1952). https://doi.org/10.1063/1.1700493

[27] J.C. Maxwell, *A Treatise on Electricity and Magnetism*, (Clarendon Press, 1881).

[28] G.A. Slack, "Thermal Conductivity of MgO, Al₂O₃, MgAl₂O₄, and Fe₃O₄ Crystals from 3 to 300 K," Phys. Rev. **126**, 427 (1962). https://doi.org/10.1103/PhysRev.126.427

[29] H. Kim, S.R. Choi, and D. Kim, "Thermal conductivity of metal-oxide nanofluids: particle size dependence and effect of laser irradiation," J. Heat Transf. **129**, 298-307 (2007). https://doi.org/10.1115/1.2427071

[30] International Atomic Energy Agency, Vienna International Centre, PO Box 100, A-1400 Vienna, Austria, *Thermo-physical properties of materials for nuclear engineering: a tutorial and collection of data*. (2008). https://www-pub.iaea.org/MTCD/Publications/PDF/IAEA-THPH_web.pdf

[31] D.W. Green, and R.H. Perry, *Perry's Chemical Engineers' Handbook*, (McGraw-Hill Professional, 1999).

АНАЛІЗ ХАРАКТЕРИСТИК ТЕПЛООБМІНУ НАНОРІДИН В МІКРОЦИЛІНДРИЧНИХ ГРУПАХ

Ліна Вафаа Белхадж Сеніні, Мустпаха Буссуфі, Аміна Сабер

Лабораторія морських наук та інженерії факультету машинобудування, Університет науки і технологій Орана Мохаммеда Будіафа, ВР 1505 Ель М'Науэр Оран 31000, Алжир

Мета цього дослідження полягає в дослідженні за допомогою чисельного моделювання характеристик потоку та теплопередачі нанофлюїдів на водній основі Al₂O₃, Cu, TiO₂ та SiC, що протікають через групи мікроциліндрів, розташовані в рядній конфігурації. Моделювання проводилося в умовах ламінарного потоку, і аналіз враховував сім різних низьких значень числа Рейнольдса з постійною об'ємною часткою 2%. Метою цього дослідження було визначити, як нанофлюїди, тобто суспензії наночастинок у воді як базовій рідині, можуть впливати на перепад тиску та тепловіддачу в групах мікроциліндрів. Щоб досягти цього, був застосований метод кінцевого об'єму для оцінки впливу нанофлюїдів на перепад тиску та характеристики теплообміну в групах мікроциліндрів. Результати дослідження демонструють, що для всіх досліджуваних нанофлюїдів перепад тиску та коефіцієнт тертя груп мікроциліндрів зростали зі збільшенням числа Рейнольдса. Таку поведінку можна пояснити взаємодією між наночастинками та стінкою, що призводить до збільшення тертя. Крім того, було виявлено, що число Нуссельта зростає зі збільшенням числа Рейнольдса. Нанорідина SiC/вода продемонструвала найвищі числа Нуссельта серед чотирьох протестованих нанорідини, що вказує на те, що вона забезпечує кращі показники теплопередачі, ніж інші нанорідини. Ці результати узгоджуються з експериментальними висновками, вказуючи на те, що чисельне моделювання було точним і надійним.

Ключові слова: *наночастинки; мікроциліндрична група; посилення тепловіддачі; конвекція; ламінарний режим*